DESIGN AND ANALYSIS OF A NOVEL HIGH SPEED SHAPE-TRANSITIONED WAVERIDER INTAKE

by

Mark Noftz

A Thesis

Submitted to the Faculty of Purdue University

In Partial Fulfillment of the Requirements for the degree of

Master of Science in Aeronautics and Astronautics

School of Aeronautics and Astronautics

West Lafayette, Indiana

May 2022

THE PURDUE UNIVERSITY GRADUATE SCHOOL
STATEMENT OF COMMITTEE APPROVAL

Dr. Joseph S. Jewell, Chair

School of Aeronautics and Astronautics

Dr. Jonathan Poggie

School of Aeronautics and Astronautics

Dr. Steven P. Schneider

School of Aeronautics and Astronautics

Dr. Brian E. Rice

Air Force Research Laboratory

Approved by:

Dr. Gregory A. Blaisdell

For Colin and grandma.

ACKNOWLEDGMENTS

This project would not have been possible without the helpful guidance, feedback, and support from my advisor, Dr. Jewell. I also thank Dr. Rice, who kick-started the inlet idea by spearheading the transfer of HIFiRE-6 from AFRL to Purdue's BAM6QT group. The idea of this project was spawned by the need to create an in-house geometry similar to this sugar-scoop inlet model. Additionally, the combined Purdue - Notre Dame - AFRL team has been an invaluable resource to test, refine, and present our ideas. Dr. Poggie and Andrew Shuck assisted with inlet computations that brought this project to the next level. Dr. Juliano and Andrew Bustard provided much help with the mechanical design and data analysis garnered from the test campaign. Andrew Bustard and Andrew Shuck importantly share credit with me for the Streamtracing Design Code. We spent many nights troubleshooting and diagnosing errors. The code is now a powerful multi-faceted tool. Dr. Bisek has provided important feedback, kept our focus, but also unwaveringly backed the novel streamtracing idea. Dr. Schneider and Dr. Heister peaked my interest in inlets before the conceptualization of this project. I especially thank Dr. Schneider and Dr. Jewell for their encouragement to pursue outside internships, which has caused a butterfly-effect that cascaded into a sizable project.

I would like to express my immense gratitude to Chris O'Bryan and Jerry Hahn for providing effective and timely design feedback for all of my submitted designs. Special thanks is also in-store for J. Scott Williams, who has effectively machined a 4-axis geometry with a 3-axis CNC. Last but not least, I would like to thank the entire BAM6QT team - including Dr. Chynoweth, A. Carson Lay, Katie Gray, Dr. Turbeville - for their continuous feedback on my ideas, models, and presentations.

I would like to thank my mom, uncle, and dog Ginger for their encouragement to pursue a graduate degree. Lastly, I could not have completed this degree without the emotional support from my amazing and lovely girlfriend, Margaret.

TABLE OF CONTENTS

LIST OF TABLES

LIST OF FIGURES

LIST OF SYMBOLS

a	acoustic speed
A	area
c^*	characteristic velocity
C_f	thrust coefficient
$E(x)$	transition function
f	cavity frequency
g	gravitational constant
G_θ	Görtler Number
$h, R_\circ$	throat height
H	boundary layer shape factor
I_{SP}	specific impulse
L	cavity length
$\dot{m}$	massflow rate
M	Mach number
n	super-ellipse exponent
P, P_s	static pressure
$\bar{P}$	area-averaged pressure
$\langle P \rangle$	time-averaged pressure
$P'_\circ$	recovery pressure
P_∞	freestream pressure
$P_{\mathrm{i+1}}$	post-shock pressure
P_{i}	pre-shock pressure
$P_t, P_\circ$	stagnation pressure
Pr	Prandtl Number
r	radial variable
R	specific gas constant
Re	Reynolds Number
Re_θ	Momentum Reynolds Number

Re_m	Unit Reynolds Number
$T_t, T_\circ$	stagnation temperature
u	angular Mach
α	transition parameter
β	shock wave angle
δ	deflection angle
δ^*	displacement thickness
γ	ratio of specific heats
λ	recovery factor
ϕ	osculating plane angle
θ	polar angle
Θ	momentum thickness

ABBREVIATIONS

AFOSR	Air Force Office of Scientific Research
AR	Aspect Ratio
BAM6QT	Boeing-AFOSR Mach 6 Quiet Tunnel
BLDT	Boundary Layer Displacement Thickness
BLVC	Boundary Layer Viscous Correction
BPP	Back Pressure Port
BUSE	Busemann Streamtracing Design Code
CAD	Computer Aided Design
CFD	Computational Fluid Dynamics
CNC	Computer Numerical Control
CR	Total Contraction Ratio
DAQ	Data Acquisition System
DLS	Digital Light Synthesis
EC	External Contraction
FDM	Fused Deposition Modeling
FEA	Finite Element Analysis
FoS	Factory of Safety
HF	Hot Film
HIFiRE	Hypersonic International Flight Research Experimentation Program
IC	Internal Contraction
ICFA/B/C	Internal Conical Flow - A/B/C
ICR	Internal Contraction Ratio
IML	Inner Mold Line
INlet	Indiana Intake Testbed
MC	Mixed Contraction
MoC	Method of Characteristics
NACA	National Advisory Committee for Aeronautics
NASA	National Aeronautics and Space Administration

NWK	Nozzle Wall Kulite
OIWPS	Osculating Internal Waverider Intake with Parallel Streamlines
OML	Outer Mold Line
OP	Osculating Planes
PM	Prandtl-Meyer
PS	Parallel Streamlines
PSD	Power Spectral Density
PSP	Pressure Sensitive Paint
REST	Rectangular to Elliptical Shape Transition
RMS	Root Mean Squared
SABRE	Synergetic Air Breathing Rocket Engine
SSTO	Single Stage to Orbit
SWBLI	Shock Wave Boundary Layer Interaction
TBCC	Turbine Based Combined Cycle
TM	Taylor-Maccoll
TSP	Temperature Sensitive Paint

ABSTRACT

Air intakes are a fundamental part of all high speed airbreathing propulsion concepts. The main purpose of an intake is to capture and compress freestream air for the engine. At hypersonic speeds, the intake's surface and shock structure effectively slow the airflow through ram-air compression. In supersonic-combustion ramjets, the captured airflow remains supersonic and generates complicated shock structures. The design of these systems require careful evaluation of proposed operating conditions and relevant aerodynamic phenomena. The physics of these systems, such as the intake's operability range, mass capture efficiency, back-pressure resiliency, and intake unstart margins are all open areas of research.

A high speed intake, dubbed the Indiana Intake Testbed, was developed for experimentation within the Boeing-AFOSR Mach 6 Quiet Tunnel at Purdue University. This inward-turning, mixed compression intake was developed from osculating axisymmetric theory and uses a streamtracing routine to create a shape-transitioned geometry. To account for boundary layer growth, a viscous correction was implemented on the intake's compression surfaces. This comprehensive independent design code was pursued to generate an unrestricted geometry that satisfies academic inquiry into fluid dynamic interactions relevant to intakes. Additionally, the design code contains built-in analysis tools that are compared against CFD calculations and experimental data.

Two blockage models were constructed and outfitted with Kulite pressure transducers to detect possible intake start and unstart effects. Due to an error in the design code, the preliminary blockage models' lower surfaces were oversized. The two intake models were tested over a freestream Reynolds number sweep, under noisy and quiet flow, at one non-zero angle of attack, and at a singular back-pressure condition. Back-pressure effects acted to unstart the intake and provide a comparison between forced-unstart and started states. The experimental campaign cataloged both tunnel starting and inlet starting conditions, which informed the design of the finalized model. The finalized model is presented herein. Future experiments to study isolator shock-trains, shock-wave boundary layer interactions, and possible instances of boundary layer transition on the intake's compression surface are planned.

1. AIR INTAKES

The first, and arguably most critical, component of an airbreathing engine is the air intake. Air intakes, also known as inlets, supply and slow down captured air to downstream components in an airbreathing engine, such as the compressor, combustor, and nozzle. An inlet can consist of a supersonic diffuser, subsonic diffuser, or both, depending on design and mission. The consistent, uninterrupted supply of air ensures sustained combustion occurs within the engine. As such, the primary design factor for a generic inlet is the mass flow requirement. The second most important factor is to design an inlet with low total pressure losses [1]–[3]. These losses affect efficiency of the engine, and they are caused by a variety of different fluid dynamic phenomena. The characteristic velocity ($c^\star$), defined in equation (1.1), is useful tool to measure a rocket or airbreathing engine's combustion efficiency [4]–[6]. Parameters in the equation, such as total stagnation pressure ($P_\circ$) and mass flow rate ($\dot{m}$), are variables directly influenced by the intake's properties. The throat area (A_t) is a design parameter.

$$c^\star = \frac{P_\circ A_t}{\dot{m}} \tag{1.1}$$

Airbreathing engines hold a significant advantage over rocket propelled alternatives. Since airbreathing engines use captured atmospheric oxygen for combustion, they do not need to carry their own oxidizer. These vehicles are lighter, smaller, and less complex overall. Additionally, airbreathing engines have higher specific impulse (I_{SP}) values versus rockets. This is because the ratio of thrust produced (F_T) per amount of on-board fuel consumed ($\dot{m}_f$) is higher. A comparison of various airbreathing engine concepts and their efficiencies are shown in Figure 1.1. High-speed airbreathing engines are an attractive alternative to rockets for large March numbers. However, several key aerodynamic and thermodynamic challenges remain before consistent and robust hypersonic flight becomes reality. Specific impulse is determined through the characteristic velocity (c^*) and the thrust coefficient (C_f), which is the nozzle efficiency term dictated by pressure and area ratios [5].

$$I_{SP} = \frac{F_T}{\dot{m}_f} = \frac{c^\star C_f}{g} \tag{1.2}$$

In order to minimize losses, engineers need to understand the underlying physics of the intake system. There is an extensive list of flow phenomena that negatively impact performance: boundary layer separation, flow distortion, shock-shock interaction, shock wave-boundary layer interaction, back pressure induced intake unstart, boundary layer ingestion, intake buzz, boundary layer transition, off-design operation, and boundary layer suction or blowing. Additionally, engineers must compromise on the overall performance of the intake with other design factors that may include intake shape transition, aircraft integration, total size and weight limits, variable geometry, flow control capability, minimizing aerodynamic drag, noise suppression, minimizing radar cross section, and active cooling requirements [2], [3], [7]–[9]. Considering all the challenges, air intakes quickly become one of the more difficult subsystems to design, analyze, and test. Thus, intakes play a pivotal role in defining the performance of an airbreathing engine and remain at the forefront of scientific research.

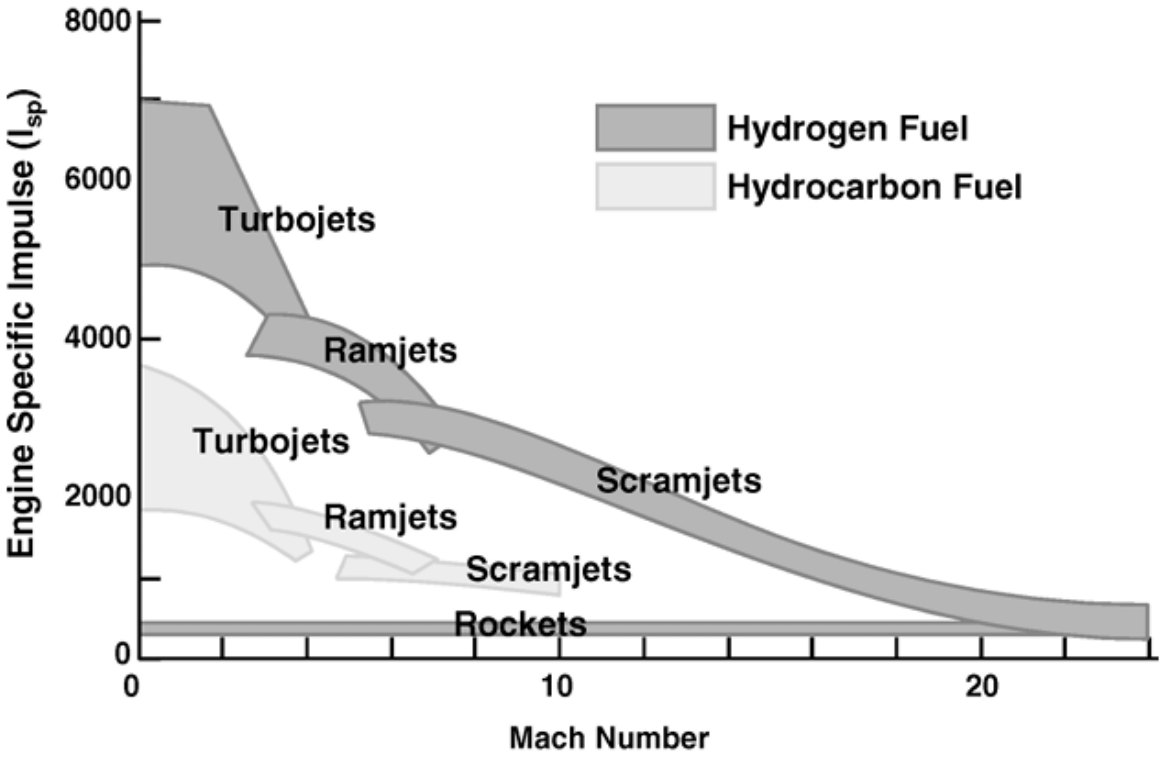

Figure 1.1. Performance of various airbreathing engines types. From ref. [10]; reprinted by permission of the American Institute of Aeronautics and Astronautics, Inc.

1.1 Flight Regimes of Air Intakes

Depending on the operating design requirements, such as altitude and Mach number, an intake's geometry and design methodology can vary substantially. For example, subsonic passenger airplanes often use a form of pitot inlet. Pitot intakes are unviable for high supersonic flight due to the creation of standing normal shockwaves that adversely impact performance. Thus, aircraft that operate in both the supersonic and subsonic regime require special design considerations. Since intake geometry is one of the most important factors influencing performance, variable geometric inlets were used extensively on a variety of airplanes. This includes, but is not limited to, fighter aircraft such as the F-14, F-15, MiG-21, and MiG-25, bombers like the XB-70A and Tu-160, and the Concorde passenger aircraft [3], [11], [12]. Variable geometric cones and ramps allow a finer tuning of shockwave positions within an intake, enhancing pressure recovery and increasing mass capture ability. The same principles are applied to supersonic and hypersonic platforms. However, these intakes may require additional systems to stay operational, such as flow bypass doors, boundary layer bleed slots, and unstart detection sensors. The importance of the intake's validation throughout the flight envelope is critical to the engine as a whole [9].

1.1.1 Subsonic Inlets

Low speed aircraft, such as the conventional turbojet or turbofan powered passenger planes, almost universally use the pitot intake design. Pitot intakes are often optimized for cruise condition at a high altitude, but they are still designed to provide reasonable capability at lower altitudes. For instance, thrust demands are higher at takeoff, so the intake must supply more massflow than at the cruise condition. Performance is determine by a corrected massflow parameter for the different conditions experienced by the intake [8]. If a subsonic inlet deviates from an on-design condition, such as during excessive yaw or pitch maneuvers, high-pressure regions in the intake duct may cause flow separation in the duct or on the compressor blades. The imbalance necessarily effects engine thrust by disrupting mass flow requirements, but it might also damage other components through dangerous vibrations, back-flow, and pressure fluctuations [13].

The pitot intake supplies air to a diffuser, which provides area relief to the captured streamtube. A streamtube is the volumetric region of all captured streamlines that enter the inlet. The diffuser acts to increase static pressure and straighten the flow before it enters the compressor face. If diffusion is very rapid, then adverse pressure gradients may separate the boundary layer along the wall. This leads to downstream flow distortion, loss of total pressure, and an area of recirculation that acts as a blockage. Compressor stall, where the demand for air outpaces the supplied airflow, often occurs due to this process. Balancing separation risk with wall frictional losses play an important part of the diffuser's geometric design, whether its 2D, conical, or annular in shape [14].

Other subsonic designs, such as the submerged intake (S-duct) and NACA style internal intakes, exist on platforms such as drones and missiles. These intakes use a face that is flush with the host aircraft which improve drag margins. Additionally, internal ducts shield rotating compressor blades from radar, improving stealth characteristics [3]. However, internal S-ducts pose additional challenges to keeping flow uniform and mitigating boundary layer growth or separation [15]. The external capture shape of the pitot and internal area profile of the diffuser are an inherently coupled problem that requires extensive testing and validation.

1.1.2 Transonic and Supersonic Inlets

For transonic and supersonic capable aircraft, such as fighter jets, the core design principle of an inlet, to capture airflow, remains the same. However, the oncoming airflow must be sufficiently slowed from supersonic speeds to subsonic speeds. In order to accomplish this task, a supersonic inlet is usually composed of two parts: a supersonic and subsonic diffuser. The job of a supersonic diffuser is to slow the captured air stream down to a subsonic Mach number. However, establishing subsonic flow in the engine necessitates the formation of a normal shock. By reducing the Mach number upstream of a normal shock, the associated pressure losses can be mitigated. Upstream oblique shocks caused from ramps, wedges, bumps, or cowls can be used for this effect. Multiple shock systems or isentropic compression

surfaces can further reduce pressure losses [8], [16]. Therefore, controlling the formation of shock waves on the intake surface becomes a primary design consideration.

Poor design and shock placement can cause shock reflections and distorted flow profiles which result in compressor stall. Therefore, judicial design of leading edge geometries and turns inside the intake allow convenient shockwave positions. Since shockwave angles are dependent on Mach number, variable geometry systems can be devised to control shock placement. Aircraft such as the Concorde, F-15 Eagle, MiG-25 Foxbat, and F-14 Tomcat use ramp style variable geometric intakes to ensure minimal shock losses throughout a given flight envelope [9], [11]. After the shock system, an attached subsonic diffuser would act to raise the flow's static pressure, drop the incoming Mach number, and create a uniform stream of air to the compressor face. This ensures subsonic flow is provided to the engine for all designed flight conditions [16].

1.1.3 Ramjet Inlets

For high supersonic conditions, jet engines become less efficient due to the increased rate of fuel consumption and corresponding drop in specific impulse. The temperature rise through compressors operating at highly supersonic conditions would also exceed the material's thermo-structural limitations. It becomes economical to use ramjets, which are airbreathing engines that use the ram-compression of air at high speeds. These systems do not need mechanical compressors. Instead, the shock waves and intake surfaces provide the airflow compression. However, these simple duct geometries do not produce static thrust and must be boosted to an operable flight condition. Intakes for ramjets are usually designed by combining a supersonic diffuser with a subsonic diffuser. The supersonic diffuser acts to control shock placement and capture the necessary airflow for the engine [6]. After passing through a normal shock at the inlet throat, the airflow is then turned and expanded in a subsonic diffuser. Similarly to a supersonic aircraft, this subsonic diffuser provides area relief, slows the airflow, increases static pressure, and creates a uniform velocity profile before the subsonic isobaric combustion process [8], [16].

1.1.4 Scramjet Inlets

As flight Mach number continues to increase, the ramjet no longer becomes viable. Terminal normal shocks at the throat in ramjets would cause immense stagnation pressure losses in hypersonic conditions. Additionally, the temperature rise caused by strong shocks would make combustion impossible. High static temperatures dissociate most practical hydrocarbon fuels. To create meaningful energy release into the flow, these extreme temperatures must be avoided. The normal shock is replaced by a series of oblique shocks, which also reduces total pressure losses. The trade-off, however, is that the airflow will remain supersonic throughout the inner flowpath and combustor. Hence, the ramjet becomes a scramjet, or a supersonic-combustion ramjet. The heat release inside the combustor becomes a Rayleigh-flow problem, which also causes pressure losses. Thus, the losses from the combustion process must be balanced in tandem with intake compression losses [4]. Figure 1.2 shows a representative scramjet with labeled flows stations. Station 0 references the freestream flow values, which determines the total pressure and total temperature properties. Station 1 is beginning of the intake geometry. It generally references flow properties directly behind the leading edge shock. The captured streamtube is turned into the isolator at the throat, which is station 2. Fuel is injected, mixed, and burned within the combustor, which starts at station 3. Flow enters the nozzle at station 4. Flow expansion along the surface provides meaningful thrust to the vehicle. The flow exits the vehicle at station 9.

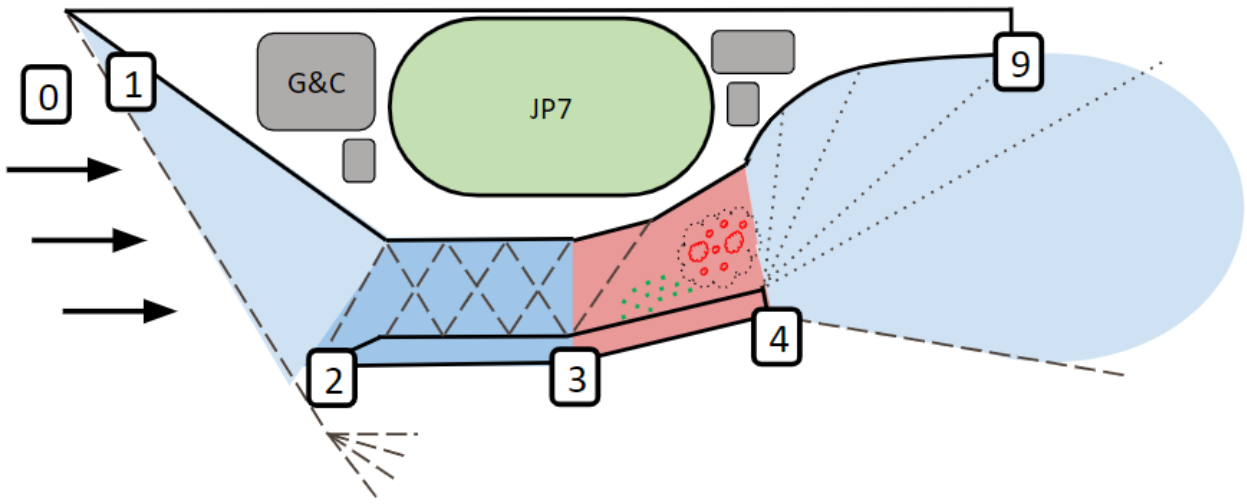

Figure 1.2. Common diagram of the different flow stations for a generic scramjet vehicle.

The scramjet has a supersonic diffuser similarly to a ramjet, but the subsonic diffuser is now replaced with an isolator. The isolator acts to separate the effects of combustion induced back-pressure from the inlet. A shock train develops in the isolator, which may expand or retract based on the flight conditions and back-pressure levels. Non-optimal flight conditions or excessive back-pressure spikes may contract and expel the isolator shock train. When the shock train is disgorged from the inlet throat, the inlet is said to undergo "unstart" [4]. This phenomenon causes a normal shock to develop near the beginning of an intake's internal contraction. This normal shock establishes subsonic flow through the inner flow path of the scramjet. Additionally, large amounts of freestream airflow are rerouted around the engine, dropping the massflow and capture efficiency. [17]. This is often catastrophic for the vehicle, since the loss of massflow may cause a flame-out condition in the combustor. Sudden deceleration of the aircraft may cause structural failure. Also, the spike in static pressure from the standing normal shock at the inlet may cause large aerodynamic moments and loss of pitch control. Area constriction due to boundary layer growth, boundary layer separation, off-design operation, and thermal choke from combustion are common causes of unstart. The dynamics of coupled inlet unstart and shock-train behavior are a major field of scientific interest within the high-speed flow community [17]–[19].

1.1.5 Exotic Inlets

Other exotic airbreathing engine designs rely upon a combination of different cycles, namely: turbojets, ramjets, rockets, and scramjets. The SR-71 Blackbird is a prime example of an aircraft that uses an exotic, variable-geometric intake for its after-burning turboramjet engine. This aircraft essentially used a jet engine for low-speed flight, but it transitioned to a bypassed ramjet after-burner for speeds over Mach 2. The axisymmetric, isentropic spike intake used on the Blackbird family had to adequately supply airflow to the engines over a wide range of Mach numbers and flight regimes. As such, the inlet design required clever use of flow control technologies to successfully operate the J-58 engine. Flow control technologies such as boundary layer suction ducts, bypass doors to reroute core airflow, and a retractable spike system to control shock placement all had to work in tandem to sufficiently control the captured airflow, cool the engine, and mitigate intake-unstart events [20], [21].

Newer concepts, such as dual-mode ramjets, seek to merge the ramjet and scramjet design. Inlets in these cases need to be carefully tailored to produce uniform subsonic flow in ramjet mode, but also stable shock trains when in scramjet mode. The turbine-based combined cycle (TBCC) is a development that seeks to combine a jet engine and ramjet with a common inlet but separate internal flowpaths. Single-stage to orbit (SSTO) concepts, such as Skylon, and exotic rocket-based combined cycle engines are also under development [22], [23]. At hypersonic speeds, flow compression results in very high gas temperatures that can melt compressor and turbine blades. Hot gases may also dissociate the injected fuel, effectively neutralizing the engine's thrust capabilities. In-situ air cooling before critical components can essentially trick the airflow by allowing compressors, combustors, and turbines to operate in unconventional flight regimes. The SABRE engine seeks to incorporate these advanced heat exchangers, and they may prove the key to sustainable and reusable hypersonic flight [22]. Thus, integration of different engine cycles and unconventional technologies onto one aircraft remain an open area of research for scientists and engineers.

1.2 Types of Intake Compression

As previously discussed, intakes range widely in terms of geometric shape and targeted flight condition. The routing of captured flow is accomplished in a few key ways depending on the design methodology. This directly influences whether the flow is captured and compressed externally, internally, or in a mixed fashion. The capability of the design tool and available computational power also play a critical role. Early intake designs were mostly based on axisymmetric conical flow solutions. For instance, many Soviet-era aircraft used retractable external-compression cone intakes on their supersonic capable fighters. Simple 2D ramp intakes were also prevalent on numerous U.S. fighters and even the experimental X-43 and X-51 scramjet flight vehicles [24]. Modern computing techniques allow designers to pursue more advanced designs, which include swept and inward-turning surfaces. The inherent advantages and disadvantages of these different intake compression methods are presented below.

1.2.1 Internal Compression

Internal compression intakes are mechanically simple and operate well within the subsonic range. One such example, the pitot intake, often operates as a subsonic diffuser. However, in the supersonic realm, internal compression intakes must swallow a normal shock that forms at the intake capture plane. The normal shock sits within the intake duct, slowing the air to subsonic speeds before it reaches downstream components. Since flow is decelerated through the use of a normal shock, pressure losses become untenable at highly supersonic conditions. The internal contraction ratio (ICR), or internal area change, also determines the total amount of flow compression the intake can achieve. If the exit area is too greatly restricted, then the intake will be unable ingest the massflow required for the engine [25]. If the normal shock is swallowed, but a downstream blockage causes excessive back-pressure, then the shock may be expelled upstream. The intake is said to operate in an "unstarted" spill mode. The increase in total pressure losses and reduction of mass capture renders the inlet ineffective [4]. These geometries are usually fixed, so the internal area ratio is usually optimized for a specific flight condition. Restarting the intake requires either overspeeding

the engine, reducing the flow blockage (mechanical or thermal), or opening the internal area with variable geometry [14]. These mechanisms are either too complex or require tailored control laws [8], [21]. Internal compression intakes, for these reasons, are rarely the only compression mechanism used in high speed engines.

1.2.2 External Compression

External compression intakes rectify many of the starting problems and flight regime limitations encountered by internal compression intakes. External compression intakes, such as 2D ramp intakes, use a series of oblique shocks to slow down incoming air. By compressing the flow through a series of shocks, pressure losses are mitigated by reducing total Mach number before the terminal normal shock at the intake's face. Figure 1.3, reproduced from Goldsmith, shows how pressure loss can be mitigated by increasing the amount of oblique shocks processing the captured flow [1]. This plot includes the military standard for total pressure recovery in subsonic and supersonic air intakes. Since shock angles change with Mach number, external ramps can adjust their position to retain optimal shock placement. External compression inlets often utilize some form of variable geometry for this reason. If generated shocks miss the inlet cowling, then flow in the captured streamtube will escape before engine ingestion - dropping the capture efficiency. Loss of massflow to the engine is a critical issue that may lead to flame-out or critical loss of thrust [8].

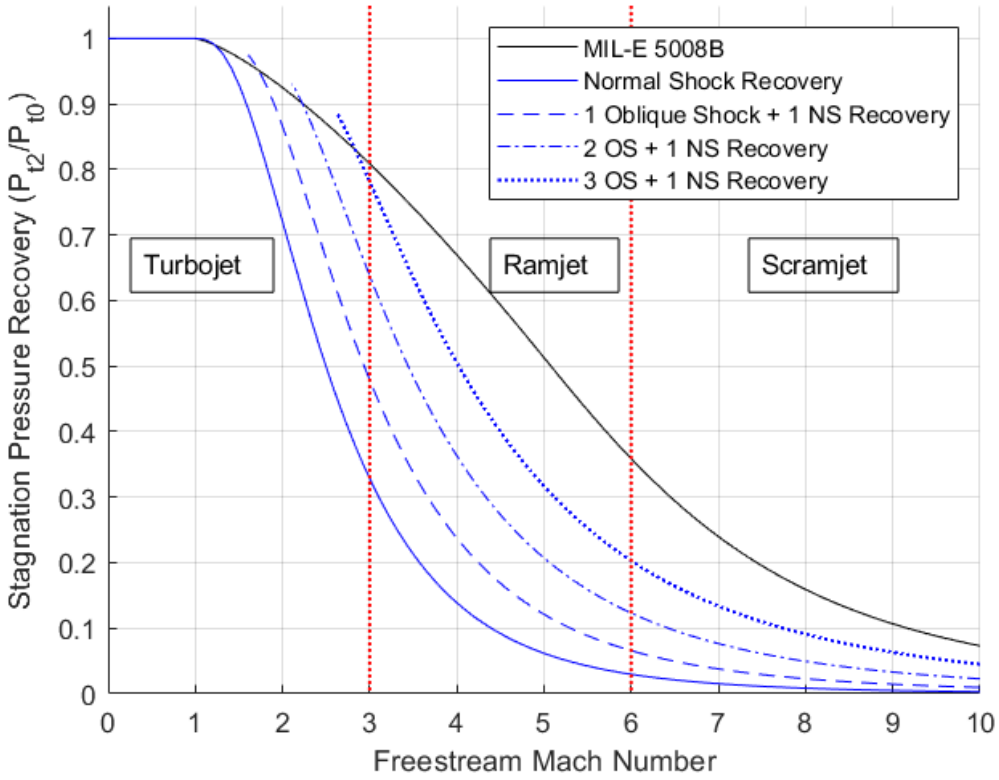

Figure 1.3. Total pressure recovery as a function of freestream Mach number with equal strength oblique shocks and a terminating normal shock. Approximately reproduced from Goldsmith [1].

The isentropic spike intake slows the captured streamtube by gradually changing the streamtube's area over a fixed distance. The geometry's curvature compresses the air by generating a continuous amount of Mach waves focused at the cowl focal point, simultaneously turning the flow and creating an isentropic compression process. Pressure losses are mitigated from shocks, but frictional losses may supersede shock losses if the geometry becomes prohibitively long. There is a limit to the isentropic compression that could be applied to a given flow. Connors noted that a reflected throat shock has to balance the pressure rise provided by the isentropic compression. If compression is too great, then the necessary reflected throat shock would have to exceed the strength of a normal shock - which is nonphysical [26]. Thus, there is a practical limit to the amount of possible isentropic compression to a captured airflow in a supersonic diffuser.

1.2.3 Mixed Compression

Mixed compression intakes, as the name implies, provide both internal and external compression to captured air. These intakes become a necessity in highly supersonic conditions. Similarly to the external compression intakes, mixed compression intakes usually pre-compresses the air before ingestion into a duct. The difference is that the captured flow duct airflow is supersonic. An oblique shock train and a subsequent normal shock develops within the internal compression portion of inlet duct [14]. These intakes provide better pressure recovery, startability, and provide better off-design performance compared with purely internal intakes [27].

The internal location of the normal shock is an important design parameter that balances total pressure losses with flow compression. The location and stability of the terminating normal shock is an important factor for engine operability, and it may change based on flight Mach number, wind gusts, or angle of attack. Boundary layer suction, bypass doors, and geometric notches may all serve as shock guides, and are important in preventing unexpected shock expulsion [6], [28]. These intake types are the most complex to develop, but are often necessary to sustain flight beyond Mach 3 where intake stability and total pressure recovery become paramount design drivers.

Mixed compression intakes can also be designed by utilizing a vehicle's forebody for pre-compression of the airflow. Wedges, canards, or bumps can act as istenropic compression surfaces that guide the flow into the internal duct. A common issue with inlet-forebody integration is the ingestion of the low momentum boundary layer. Careful design of external features, such as bumps, can effectively route the boundary layer flow around the intake by creating a localized adverse wall pressure gradient [9], [29]. This theory has been tried and tested for a variety of supersonic fighter aircraft, but is also under consideration for hypersonic intakes [30].

1.3 Intake Starting

Air intakes are fundamentally designed to capture as much massflow for the engine as possible. This requirement is usually defined as the ratio between the intake's internal

capture and throat areas. This area ratio defines the overall flow contraction applied to the captured streamtube. However, there are theoretical limits on the amount of contraction possible for a compressible gas. The isentropic limit, which assumes no thermal or total pressure losses, is derived by the maximum amount of contraction possible for a streamtube before it reaches the sonic point. The total area contraction under isentropic conditions is specified in equation (1.3) as a function of freestream Mach number. Viscous and shock losses act to make this value a theoretical upper limit. A second limit, called the Kantrowitz criterion, is derived from quasi-one-dimensional flow for a normal shock. Under a worst case scenario, a high-speed intake will be required to swallow a normal shock to establish internal supersonic flow [25]. The normal shock causes total pressure losses that reduce the amount of possible flow compression and massflow ingestion. In order to swallow this normal shock, a reduction in contraction is necessary compared to isentropic theory. The Kantrowitz limit is defined in equation (1.4) as a function of freestream Mach number. For these equations A_e is the exit area of the intake, A_c is the capture area of the intake, γ is the ratio of specific heats, and M is the Mach number at the exit area.

$$CR_{Isen.} = \left(\frac{A_e}{A_c}\right) = \frac{1}{M}[\frac{2}{\gamma+1}(1+\frac{\gamma-1}{2}M^2)]^{\frac{\gamma+1}{2(\gamma-1)}} \tag{1.3}$$

$$CR_{Kant.} = \left(\frac{A_e}{A_c}\right) = M\left[\frac{(\gamma+1)M^2}{(\gamma-1)M^2+2}\right]^{\frac{-\gamma}{\gamma-1}}\left[\frac{\gamma+1}{2\gamma M^2-(\gamma-1)}\right]^{\frac{-1}{\gamma-1}}\left[\frac{\gamma+1}{2+(\gamma-1)M^2}\right]^{\frac{\gamma+1}{2(\gamma-1)}} \tag{1.4}$$

The Kantrowitz limit, although useful for initial analysis, does not adequately predict the starting limits for complex three-dimensional intakes. Starting limits for these intakes differ substantially throughout the literature, and much work has been done to create more useful semi-empirical relationships that better match experiment [7], [18], [31]–[33]. A plot of some well known starting limits are presented in figure 1.4. The startability index (SI = 0.6) correlation developed by Mölder predicts starting well for 2D intake geometries [34]. The semi-empirical method calculates the steepest shock angle that may occur within an intake before shock detachment [31]. This semi-empirical method matches experimental data better

than the startability index method for high Mach numbers. For inward turning intakes ingested shocks during start-up may be conical or oblique, meaning that the Kantrowitz limit becomes a conservative worst-case limit for self-starting.

Intake starting is an important design parameter that determines the viability and efficiency of the intake. If the flow contraction is too great, then the shock system is unstable and a standing normal shock will form upstream of the intake's cowl enclosure. On the contrary, too little contraction results in a loss of compression and engine efficiency. This tradeoff is compounded by several other factors. For instance, strong shocks near the throat region may induce boundary layer separation. A separation event will restrict the core flow area, artificially increasing the area constriction that might induce an intake unstart [18]. Unstarts due to separation events are referred to as "soft" unstarts in the literature, while "hard" unstarts occur from flow reaching the sonic point at the throat [33]. For this reason, boundary layer bleed mechanisms near the throat region are a useful tool to improve starting robustness.

Several other options exist to enhance intake startability. Due to the non-linear behavior of the Kantrowitz limit, over-speeding an intake may allow an intake to ingest a normal shock during starting. Over-speeding is a temporary increase in freestream Mach number that allows the intake to pass the Kantrowitz limit. If the normal shock is passed and the flow path successfully starts, then the intake can decelerate to a lower Mach number. Over-speeding is not usually viable in flight, but intakes can be designed for a lower freestream Mach number than a predicted cruise condition. For instance, operating a Mach 5 intake at Mach 6 cruise may be worth the loss of pressure recovery for a gain in starting robustness. Other methods to improve starting include selective mass spillage through perforations, but this leads to downstream flow non-uniformity [35]. A standing throat shock can also be swallowed by increasing a intake's throat area that reduces the total contraction ratio. Variable geometric ramps, throats, and perforation spillage methods are mechanically complex, but are all proven methods to increase intake startability [36].

Intake design is often complicated by the non-linear behavior of restart behavior after an unstart. Many intakes exhibit a hysteresis phenomena that acts to keep an intake unstarted even when optimal conditions are re-established. This is not to be confused with the hystere-

sis effect associated with over-speeding intakes above the Kantrowitz line. Over-speeding is an invisicd mechanism to pass a normal shock, while this effect occurs due to the formation of a separation bubble at the intake's throat. The removal of the separation bubble cannot be accomplished through the same control route in which it was developed [37]. Since it is a viscous phenomena, it is possible for a self-startable intake with a low internal contraction ratio to exhibit this hysteresis effect. For example, the HIFIRE-6 intake is shown to unstart in Mach 4.3 flow at 8.7° angle of attack during a continuous pitch-up progression. However, the intake does not restart until it is lowered to a -2.7° angle of attack [38]. This effect complicates intake control schemes and reinforces the need for extensive ground-based testing and validation of intake designs.

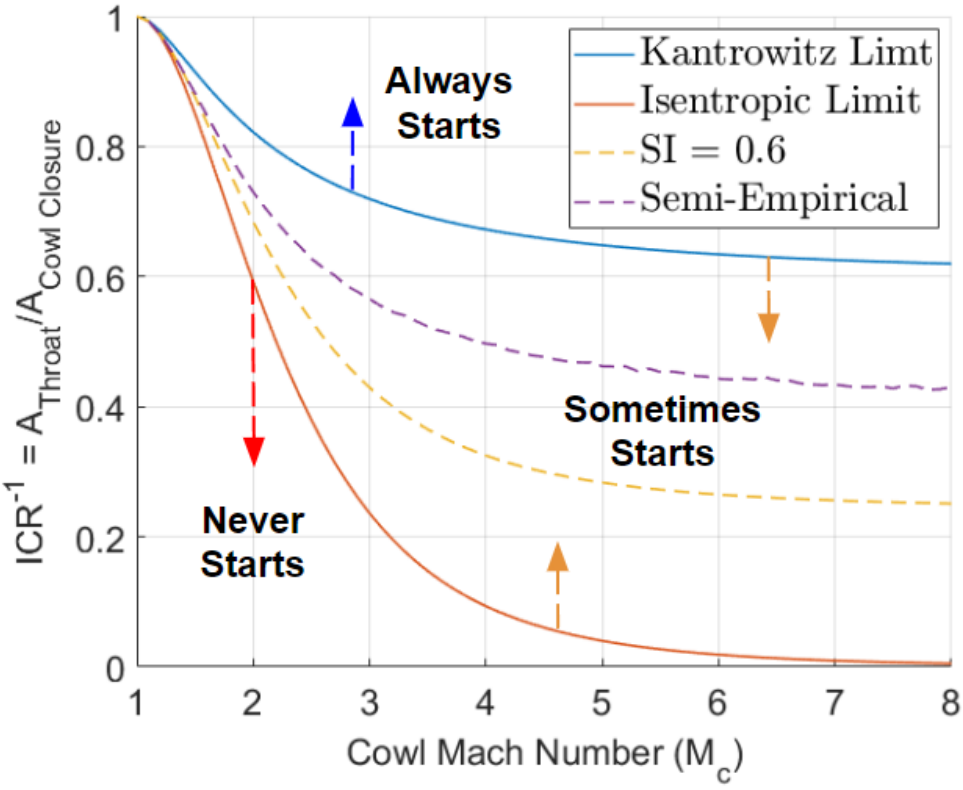

Figure 1.4. Inlet contraction limits from various analytical and empirical correlations.

2. HYPERSONIC INTAKE DESIGN METHODS

The design of hypersonic intakes requires special attention to compressible flow effects and generated shock structure. The goal of the intake is to sufficiently slow the ingested oncoming streamtube. However, this captured airflow is still supersonic throughout the entirety of the internal flowpath. As mentioned in the "Scramjet Inlets" section 1.1.4, these intakes do not need a subsonic diffuser. Instead, a section called the isolator conditions the flow and raises the static pressure through a series of shocks. This shock train resists downstream changes in back pressure by allowing the shock train to expand or compress. As such, it acts as a buffer for the intake, isolating it from the effects of most fluctuations. However, unstart is still possible under extreme conditions. Sudden spikes in back pressure can force the shock train out the front of the intake, causing a standing normal shock at the start of the inlet's internal contraction [4]. Real-world systems often carry isolator length margin due to no active shock-train control method. Better understanding of isolator shock dynamics and active control would lead to shorter isolators, reduce weight, and improvements in performance.

In order to adequately perform its mission, several requirements must be satisfied by the hypersonic intake. It must start easily, especially at off-design Mach numbers, to ensure that the supersonic core flow stays established within the internal ducts of the engine. The captured streamtube should be captured efficiently by providing as much flow compression as possible while mitigating total pressure losses. Care should be taken to mitigate flow distortion and keep the Mach number distribution uniform. Additionally, there should be minimal flow spillage at an on-design condition. This ensure as much massflow enters into the engine as possible. Other considerations include minimizing external drag and reducing mechanical complexity [36].

Several different methods exist to design hypersonic intakes. In the past, expanding flowfields were derived from nozzle design codes to create a shape-transitioned geometry. The nozzle geometry was truncated and the flow reversed to create the intake [39], [40]. More conventional designs rely on the familiar 2D ramp style, external-turning isentropic spike method, or an inward-turning scoop designs. The following sections will analyze streamtraced

inward-turning designs, as they allow several advantages over normal 2D, axisymmetric, and outward-turning designs [41].

2.1 Classic Designs

There are a variety of different legacy designs that have been extensively studied in the open the literature. Each method provides a unique advantage, whether it may be analytical simplicity or a staging concept to improve startability. The work done with these intakes provide the foundation for the more advanced streamtraced methods, which are described in following sections.

2.1.1 Prandtl-Meyer Intake

The Prandtl-Meyer intake is a two-dimensional design that uses an isentropic compression fan to compress and turn the captured freestream flow. The isentropic compression consists of an infinite amount of Prandtl-Meyer compression waves that are focused at the intake's throat. The curved ramp, which provides the flow turning and compression, is designed by discretizing the flow turning angle and back-solving the Prandtl-Meyer function to determine local ramp slope. The design accounts for the focused compression waves that reflect off the centerline into an oblique shock at the throat. Flow entering the isolator is turned and compressed by the throat shock. The strength of the throat shock is solvable by the amount of flow turning created by the forebody [26]. Since the design is only two-dimensional, sidewalls are necessary to prevent the flow from spilling out of the intake. Although the design performs better than discrete 2D wedge compression ramps, it losses performance from sidewall effects and viscous losses from surface friction. Modifications to this design exist within the literature, such as intakes with improved sidewall geometries [8], [42].

2.1.2 Oswatitsch Intake

The Oswatitch intake design method is based on a staging concept that splits compression into a series of equal strength shocks. Processing the flow through several equal strength shock waves was mathematically proven by Oswatitch to out-perform concepts that used

dissimilar strength shocks [43]. The oncoming flow is routed outward and turned through oblique shocks which provide the flow compression. This intake is radially symmetric and most of the compression is done externally. Since the compressed streamlines move radially outward, the flow is divergent [6], [42]. The Oswatitch design is similar to the isentropic spike example used on the SR-71 engine. The difference, however, is that the intermediate shock compression process is replaced by an isentropic compression ramp similar to the Prandtl-Meyer intake concept. The Oswatitch intake staging processes has also been applied with Busemann diffuser geometries to enhance starting. Low contraction Busemann diffusers can be successively stitched together so that each Busemann stage satisfies the starting criterion [36]. A 2D view of Prandtl-Meyer, Oswatitsch, and Buesmann intakes are presented in Figure 2.1. Highlighted grey regions are the surfaces of the intake.

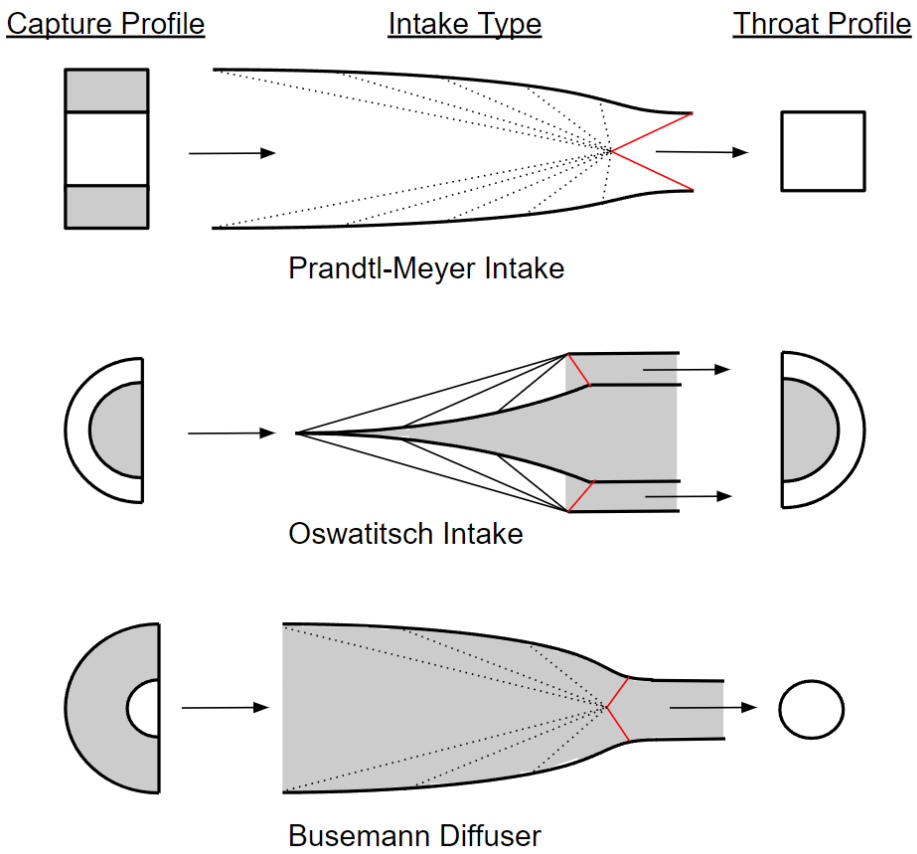

Figure 2.1. Classic designs of hypersonic intakes. © 2018, Sannu Mölder. Adapted from [42]; originally published under CC BY 3.0 license. Available from: 10.5772/intechopen.82736

2.1.3 Busemann Diffuser

The classic inward-turning intake from inviscid, compressible flow theory is the Busemann diffuser [44]. This intake is one of four solutions to the Taylor Maccoll equations [45]. It is a conically axisymmmeric, isentropic, irrotational, and internally converging flowfield [46]. The solution does not account for wall friction, body forces, entropy gradients, and assumes constant specific heats along the streamline. The final streamline is assumed to contain perfectly sharp leading edges, straight shocks, uniform and steady oncoming flow. The second-order differential equations for axisymmetric conical flow can be integrated, in polar coordinates, from a known throat shock angle to a freestream condition. This condition can either be specified by a truncation angle or when radial flow velocity becomes negligible. Figure 2.3 shows a 3D view of a complete, untruncated Busemann diffuser. Instead of shock angle, a compression ratio or total pressure loss value can be substituted as a design variable, which is a standard design procedure in the streamtracing BUSE code [47]. The freestream Mach number is not known a priori and is only known post integration. Iteration is required to obtain a desired contraction ratio or targeted freestream Mach number [36].

The Busemann solution provides higher compression efficency and lower stagnation pressure losses than simple two-dimensional ramp style intakes. This holds even for modest truncation angles [48]. Although the diffuser provides excellent flow compression and mass capture efficiency, it is quite impractical. The weak-shock Busemann contour allows for supersonic core flow to exist in the isolator, but the high internal contraction of the geometry means it will never successfully start in practice. For an on-design solution, this geometry would constrict the flow beyond its startability criterion and would never establish supersonic flow beyond the cowl internal enclosure [49]. A strong shock Busemann diffuser is possible, but it does not provide enough flow compression to be viable for hypersonic flight. Additionally, it establishes subsonic flow in the diffuser, which is suitable for ramjets, not scramjets.

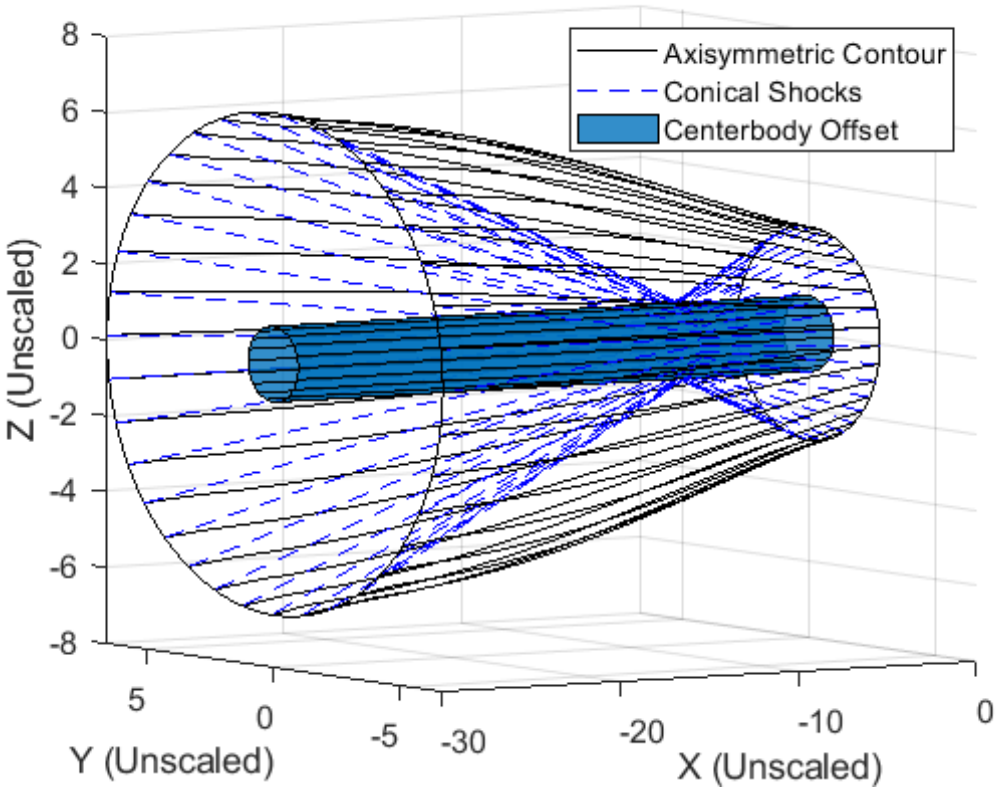

Figure 2.2. 3D untruncated Buseman contour with a defined centerbody.

The starting issues stem from the internal compression nature of the intake. If parts of the intake could be cut-away, then the flow would have area relief and allow flow spillage at off-design flight Mach numbers. The reduced internal contraction allows the intake to ingest the starting normal shock and to establish supersonic flow past the throat. The starting criterion, called the Kantrowitz limit, is discussed in chapter 1 in detail [42]. Staging methodologies, similar to the Oswatitsch intake, have also been applied to pure Busemann intakes flowfields. In these designs, each stage satisfies the Kantrowitz limit for starting. The downside to these designs is the excessive length requirement to adequately stage the intake [36].

2.2 Practical Design Considerations

Intake designs are often constrained in shape, length, and weight during integration onto a physical vehicle or test article. Additionally, many design tools only solve inviscid

flow profiles and assume infinitely thin leading edges. For example, a Busemann diffuser streamline is prohibitively lengthy for real world application. A trade-off exists where losses become dominated by skin friction for untruncated geometries [36]. Thus, some truncation or stunting is usually applied to the contours, even with the loss of some isentropic compression [50].

2.2.1 Truncation Effects

Truncation of a Busemann diffuser is accomplished by terminating the streamline integration along a specific polar angle or targeted leading edge deflection angle. Multiple authors have studied different truncation and stunting strategies. Slight truncation, in the realm of 3°-5°, has shown to significantly reduce total length while minimizing pressure losses [51]–[53]. The truncated Busemann streamline was compared to several different polynomial and quadratically defined curved streamlines. Studies showed that truncated Busemann flowfields out-performed these other options when accounting for viscous losses [54]. Truncation strategies limit the contour's vertical height, causing a drop in total contraction ratio that might be detrimental to design. Stunting of a Busemann contour is accomplished by contracting the length of the intake in the axial distance. Oncoming flow is subjected to aggressive turning angles and leads to stronger leading-edge shocks that reduce total pressure recovery. Stunting mitigates viscous losses and preserves the contour's total contraction ratio since contour height is unchanged [55]. Trade studies are often required to satisfy these competing factors.

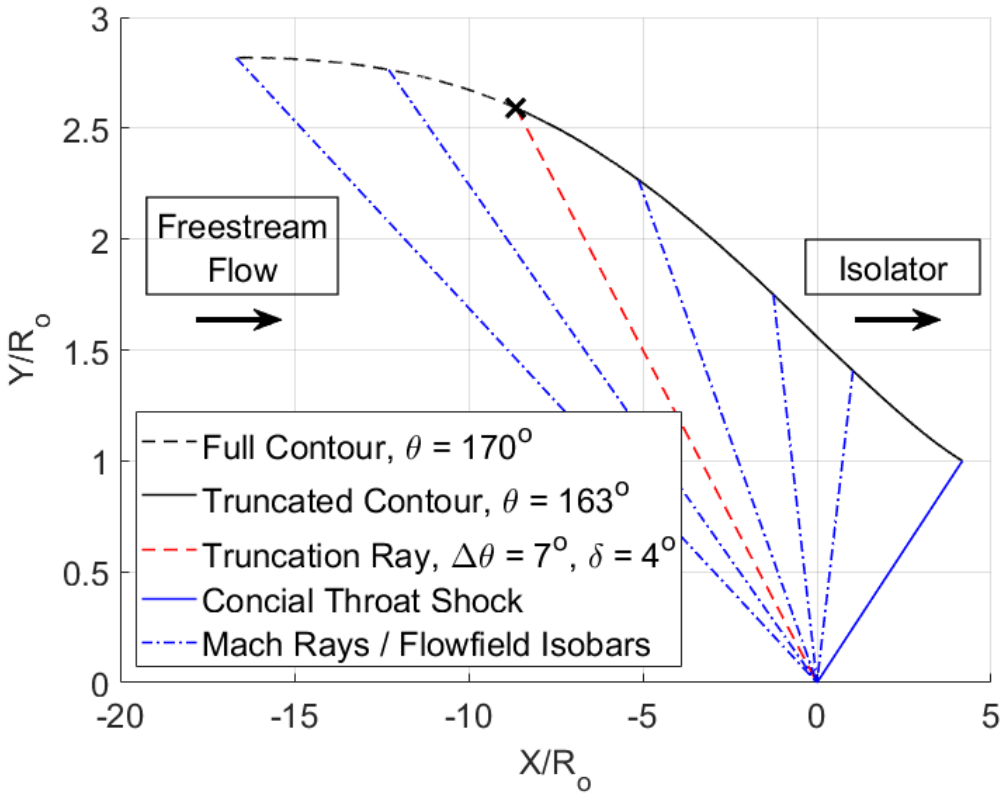

Figure 2.3. Generic truncated Busemann contour.

Leading edge shocks on truncated Busemann contours are steeper than the radiated characteristic lines generated from the isentropic compression process. The shock wave and these infinitesimal Mach waves intersect, and the shock becomes increasingly curved as it approaches the centerline. The shock curvature causes the shock to change strength radially, and the flow becomes distorted at the inlet's exit [50]. Shock curvature can be detrimental to downstream flow uniformity. Progress has been made to purposefully design curved intake shockwaves and quantify their effects on performance [56]. Lastly, shock curvature causes rotational flow, which violates the original Taylor-Maccoll assumptions.

2.2.2 Blunting Effects

Excessively sharp leading edges are not machinable or practical on most geometries. Blunting is often necessary to reduce stagnation point heat transfer on leading edge geome-

tries. Blunting causes strong bow shocks near the leading edges that cause the development of entropy layers [57]. Thus, blunting and contour thickness lead to bow shock formation that has greater strength and shallower angle than predicted oblique shocks. The effects of blunting have also been investigated analytically and numerically. Many analytical techniques fail to capture the complicated bow shock formation associated with blunting. Results often over-predict pressure recovery due to adverse shock placement and reflection [58]. Lastly, blunting causes significant drag and range reduction for the host aircraft.

2.2.3 Off-Design Effects

Off-design conditions are also considered when designing and analyzing intakes. Fixed geometry intakes perform most optimally at zero angle-of-attack and at a specified freestream Mach number. These design point conditions allow favorable shock placement and optimal mass capture of the oncoming air flow. Deviations from these conditions may occur in flight due to wind gusts, aerial maneuvers, and acceleration. So, intake designs must retain stability and provide sufficient performance margin for these off design conditions. Intakes on vehicles with accelerator mission profiles must operate over a range of Mach numbers. These intakes require less severe internal contractions, spillage zones to satisfy the Kantrowitz criterion, or boundary-layer bleed that reduces the effective contraction ratio. Spillage is often necessary to retain a started inner flowpath. However, shock reflections will act to increase flow non-uniformity at the throat [59]. Numerical studies show that pressure recovery drops with lower off-design freestream Mach numbers [60]. Angle of attack causes adverse changes to shock structure and other performance parameters. For streamtraced Busemann intakes, mass capture efficiency and total pressure recovery was found to follow a linear trend for angles of attack below 10°[60]. Overall, there are a host of real world loss-related mechanisms that act to decrease performance on intakes. These effects are hard to model analytically, and CFD is often required to validate and close the design loop.

2.2.4 Viscous Effects

Intake designs are generated from compressive parent flowfields that are often calculated using an inviscid analytical flow solutions or method-of-characteristics codes. These streamlines do not account for the growth of the boundary layer on the intake's surfaces. The growth of boundary layers displaces surface streamlines and causes a shift in the generation of the characteristic lines which govern the isentropic compression process. The displacement caused by the boundary layer leads to adverse shock placement and drop in pressure recovery, leading to intake design inefficiencies [61]. Fortunately, correction procedures have been developed that recover the behavior and performance targets of the inviscid design codes. For instance, a 16% increase in pressure recovery has been measured when a viscous correction is applied to elliptical streamtraced Busemann intakes [62].

Surface correction for boundary layer growth is accomplished by moving the inviscid surface outward by some percentage of the predicted boundary layer displacement thickness. Various methods at predicting the boundary layer displacement thickness have been pursued. Smart modified each inviscid streamline of the REST intake by the boundary layer displacement thickness (BLDT) from a 2D finite-element boundary layer solver. The method assumed an axisymmetric boundary layer profile with assumed boundary-layer transition to occur 12 mm downstream of leading edges [39]. Jones used a flat-plate turbulent boundary-layer solution from the momentum equation with local boundaries to compute the BLDT on a modular waverider intake [63]. An osculating axisymmetric waverider intake devloped by You used the White and Christoph inner-variable method to calcualte the BLDT [64]. The method solves the compressible momentum differential equation for the skin friction coefficient, which can then be used to find momentum and displacement thickness [65]. Additionally, other studies have investigated different levels of displacement offset percentages. Drayna et al. discovered that a 50% displacement correction was optimal for compression efficiency on elliptical streamtraced Busemann intakes [53]. Ding et al. used a modified von-Kárman momentum method for 2D axisymmetric compressible flow to calculate the displacment thickness along local 2D streamlines on an inward-turning intake. Results showed that the viscous-corrected surface closely matched inviscid calculations [66]. The method

was originally developed for viscous correction of hypersonic wind tunnels and was introduced by Sivells and Payne [67], [68]. This last BLVC method is implemented on the INlet and described in the design section.

2.3 Inward Turning Modular Intakes

The construction of hypersonic vehicles is a challenging endeavor due to the coupled structural, aerodynamic, and propulsion problems encountered at high speeds. This often requires careful engine-airframe integration to preserve weight margin and reduce total heat loads. As speed increases, the capture area of the intake must be scaled up to provide enough oxidizer for combustion to provide meaningful thrust. The intake becomes a significant fraction of the vehicle's frontal cross sectional area. As such, inlet shape becomes an important design constraint to the overall design of the aircraft [69], [70]. To rectify this problem, streamtracing routines have been developed to provide more flexibilty to high speed aircraft designers. Streamtracing routines provide custom shape 3D intakes based on known 2D contours for a specific design point. Streamlines solved from analytical techniques serve as the solid wall of the intake. Negating shocks and viscous effects, the wall provides the same compression and flow turning as the parent streamline. A Busemann streamline is usually the chosen contour, but custom method of characteristic solutions have also been used to create these intakes. As an added benefit, streamtracing routines create swept surfaces, which reduce internal contraction ratios that improve intake starting behavior over a range of Mach numbers [36], [39], [63], [71].

Additionally, inward turning intakes provide a variety of performance advantages compared to other intake types. Inward turning intakes provide more flow contraction than outward turning and 2D ramp intakes with the same leading flow deflection angle [72]. Inward turning intakes also retain high flow contraction after truncation, meaning that they are often shorter than other designs that provide equivalent area contraction. Shorter intakes also have smaller wetted areas, which reduce heat loads. Inward turning intakes spill little flow at on-design conditions, as the leading-edge shock is fully captured by the cowl geometry. Ramp intakes require sidewalls to prevent flow spillage, which impacts drag and

increases total pressure loss. The combination of low flow spillage and shorter intakes also plays into the lower overall drag inward-turning intakes experience [41], [69].

2.3.1 Streamtraced and Wavecatching Intakes

Historically, streamtracing was a technique used to create hypersonic waverider geometries. Streamline solutions from known 2D wedge solutions would create the classic caret wing waverider [73]. Similar ideas were applied to cone solutions, where streamlines were traced downstream of a given conical shock shape [74].The lofting of several given streamlines together formed the vehicle forebody, which would become the lifting surface of the waverider. The vehicle's leading edge formed and captured the generated shock, hence the name "waverider." The flow properties of the lifting surface is known from the analytical conical flowfield. This powerful tool provides important information to the designer on the vehicle's potential L/D and drag characteristics [75].

The streamtracing method has also been applied to intake geometries, which are internal flowfield geometries. The design process is similar to waveriders. These intakes ingest or capture the leading edge shockwaves - hence the name "wavecatching." A given streamline solution, from a conical flowfield or a method of characteristics solution, is traced downstream from a capture shape. Busemann streamlines are non-dimensional and there are an infinite amount of scalable streamlines per solution. These streamlines can be scaled to fit any pre-defined shape. This enables seamless integration of the inlet within the fuselage of a flight vehicle or missile. Additionally, streamtraced inlets can take advantage of vehicle-generated shockwaves for pre-compression if designed carefully. This is especially necessary for hypersonic flight vehicles that need to minimize external drag and total wetted area due to heat loading concerns.

Streamtracing intakes use a 2D parent flowfield to construct a 3D surface. The most common 2D parent flowfield is the Busemann solution, which provides high flow compression and good downstream flow uniformity. The parent Busemann solution is commonly solved based on a specified freestream Mach number and targeted contraction ratio. A capture shape is specified, and the parent streamline is scaled to meet the outer radii limits of the

intake for all azimuthal positions. The scaling is applied equally in both the axial and radial directions. The length of the streamlines varies considerably over the azimuthal range of the intake, creating highly swept surfaces and cutbacks. These swept notches allow the flow to spill during unfavorable conditions, allowing the intake to start at lower off-design Mach numbers [71], [76], [77].

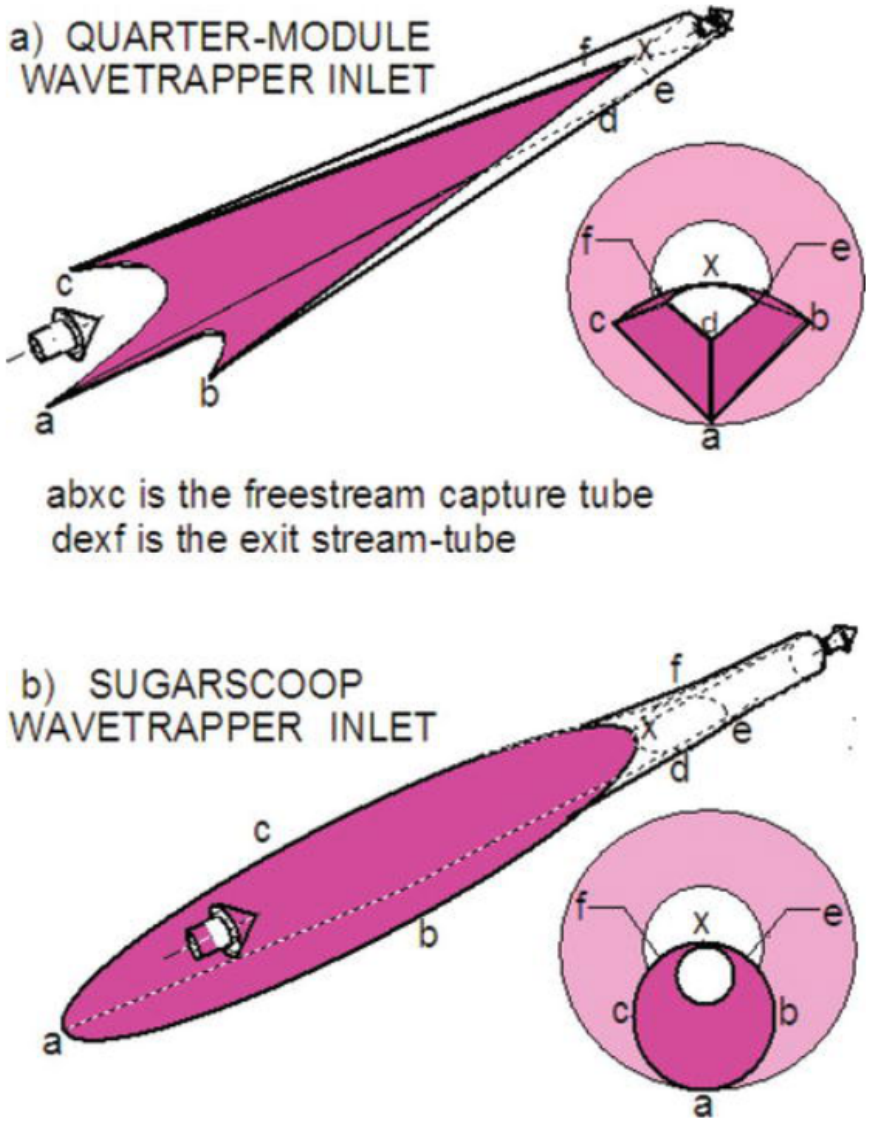

Figure 2.4. Examples of two wavetrapper intakes. © 2018, Sannu Mölder. Adapted from [42]; originally published under CC BY 3.0 license. Available from: 10.5772/intechopen.82736

The conventional Wavecatching intake family is defined by fixed exit shapes. Since the same streamline is scaled for every azimuthal location on then intake, the throat shape always retains the shape of the frontal capture plane. As an example, a triangular capture shape will always create a triangular throat, and so forth. This is not suitable for efficient combustor design, since sharp corners lead to unfavorable fluid dynamic interactions. Rounded combustor shapes are better at withstanding large pressure loads and hoop stresses than squares or triangles. Circular combustors also minimize wetted area, which reduce cooling demands in the engine [69].

Also, streamtaced designs do not exactly inherent the parent flowfield's properties. The capture shape plays a large role in determining downstream throat flow distortion and performance deviation from the parent flowfield. Streamtracing techniques may create unusable intakes because of uncontrollable area distributions. The captured flowtube area distribution along the length, including the total and internal contraction ratios, are not known a priori. Thus, iteration is often needed to converge on a suitable design that captures a targeted massflow with a relieved internal contraction required for starting. These disadvantages are areas of needed improvement in the intake design community [78].

2.3.2 Morphed Shape-Transitioned Intakes

Morphed intakes are similar to wavecatching intakes since they can create custom capture shapes. The morphed intake design methodology uses a blend of different parent flowfields to create an intake shape transition. For instance, the intake capture shape may be a rectangle, but the shape profile morphs into a circle or ellipse at the throat. This method rectifies the shape-transitioning deficiencies of the wavecatching intake methodology, but the streamline generation processes blends two or more analytically defined streamlines together. A helpful schematic shown in Figure 2.5 shows the generic procedure for creating shape-transitioned intakes.

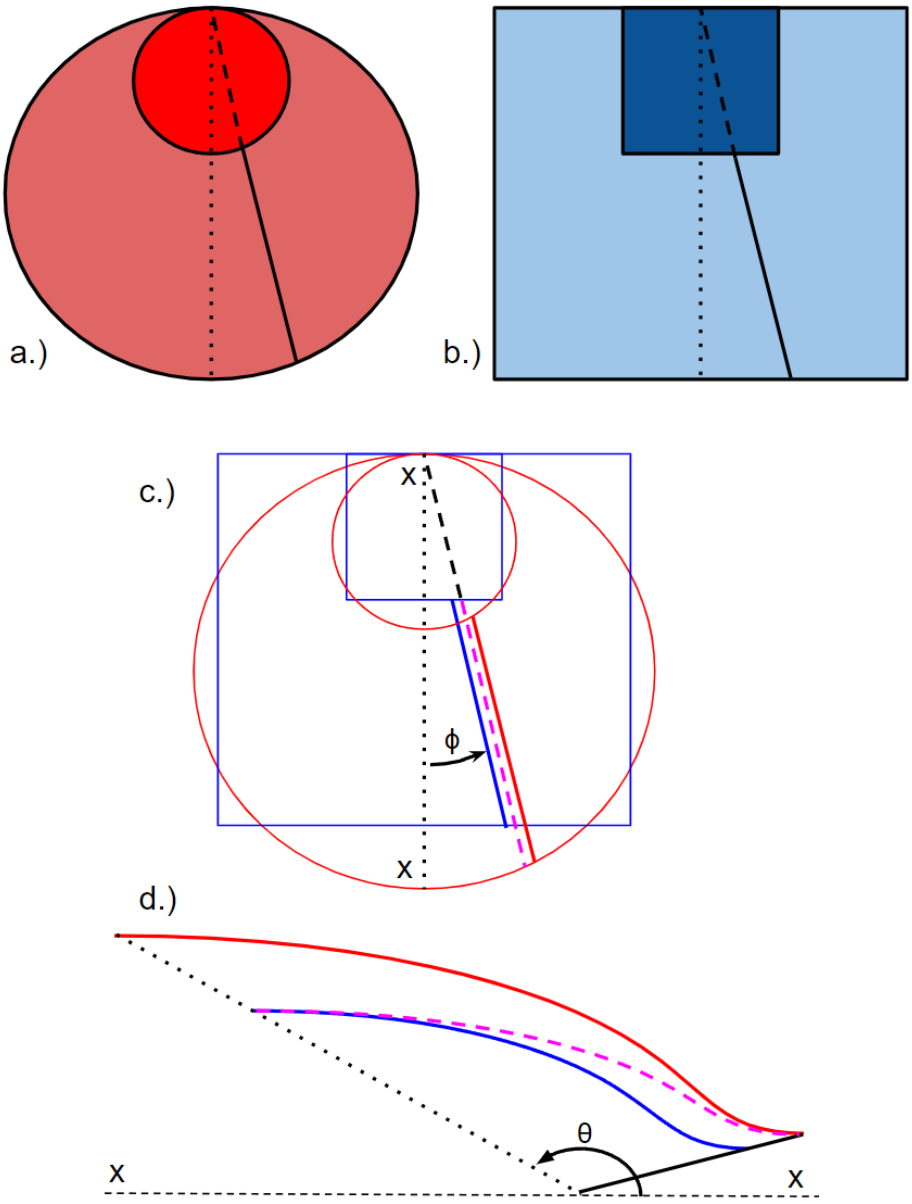

Figure 2.5. Construction method of a shape-transitioned morphed intake (c) by averaging stramlines from a circle shape (a) into a square shape (b) by a transition function that creates a new streamline (d). © 2018, Sannu Mölder. Adapted from [42]; originally published under CC BY 3.0 license. Available from: 10.5772/intechopen.82736

The shape transformation is achieved by defining a weighting function that gradually blends the capture shape into the throat shape [79]. The inherent blending of analytical solutions defines a new surface which cannot be described through the parent flowfield or

analytical techniques. Flow properties for each streamline are totally new and require CFD validation to ensure targeted performance parameters are met. The NASA Rectangular-to-Elliptical Shape Transition (REST) Intake, shown in Figure 2.6, developed by Michael Smart uses this procedure. The REST intakes were originally designed with reversed-nozzle flowfields [39]. However, newer variants rely on streamtacing from a Busemann parent flowfield to create separate capture shape and isolator shape profiles. These profiles are then averaged together to create the shape transition [80], [81].

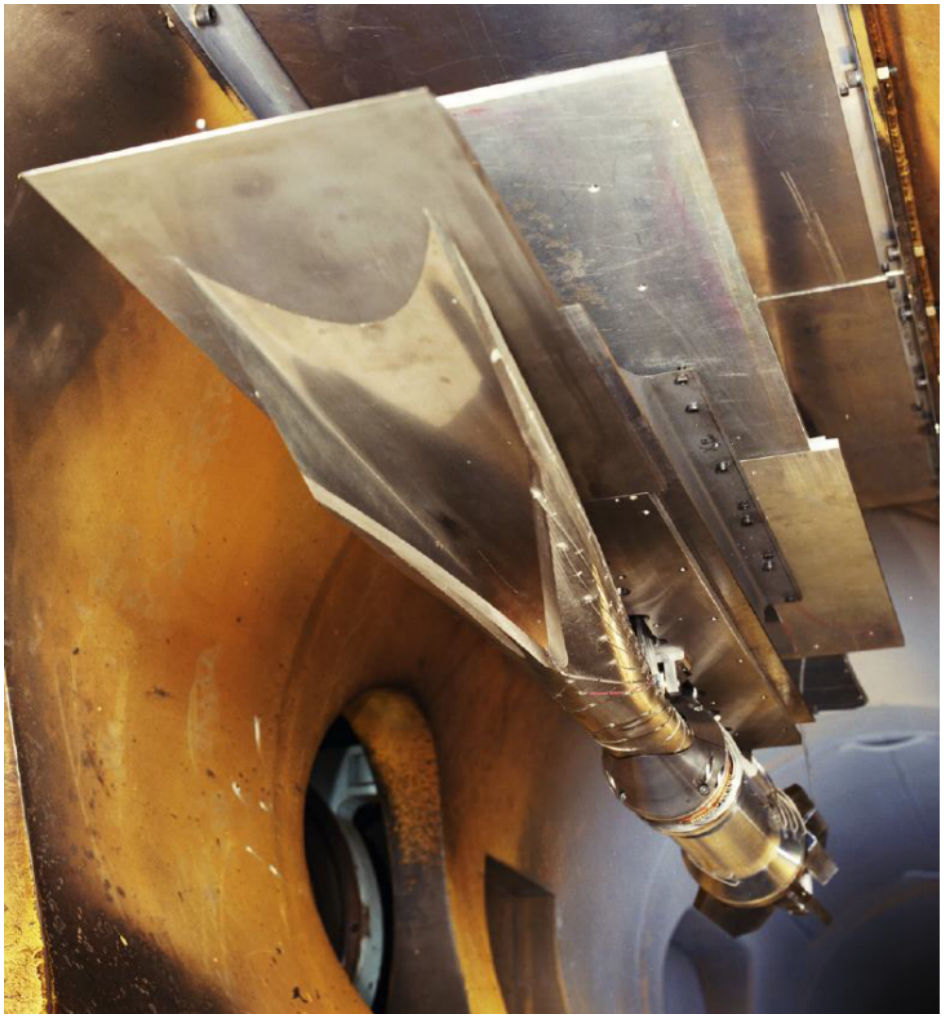

Figure 2.6. Isometric view of the shape-transitioned REST intake undergoing testing at NASA Langley [82]. Reprinted by permission of the American Institute of Aeronautics and Astronautics, Inc.

2.3.3 Osculating Cone Theory

The theory of Osculating Cones, similar to the streamtracing methodology, was first derived as a way to create waverider geometries. Waveriders were initially limited in shape when streamtraced from a singular conical flow solution. An example of a conical-flow waverider is shown in Figure 2.7a. A conical shockwave generated by a fictional cone can be traced downstream. The leading-edge shape of the waverider is then traced along the edge of the conical shock. Although more efficient than caret-style or wedge waveriders, there were a limited amount of shapes that could be generated from this method. Much work has been done to create more realistic and optimizable designs. The work of Jones and Sobieczky initially set out to solve the flowfield behind complex 3D shock shapes for more advanced waverider designs [83], [84]. A cross-stream marching method was used to solve the 3D Euler equations and define a suitable geometry. However, there were many problems bounding the problem. It was entirely possible to define a shock shape that has no physical solution. Small changes in the shock structure could cause non-physical or drastic changes in the waverider geometry. The ill-posedness of the 3D supersonic flow equations leads to stability issues that must be rectified. Thus, specific constraints must be placed on initial data or the solution space will not converge. An inverse method was discovered that essentially solved the 3D flowfield by transformation into a simpler 2D coordinate system. Here, the flow was assumed to be locally two-dimensional and irrational, and it could be solved by more robust analytical techniques [83], [85]. Simplifying the problem into a 2D coordinate system also led to better initial conditions for the 3D solver.

For a general 3D flowfield, any 2D plane where the flow is locally two-dimensional is called an osculating plane (OP). By definition, there are no pressure gradients normal to the local osculating plane. These local slices of the flowfield can be computed individually, providing inverse solutions to otherwise complex geometries and 3D shock structures. This method was extensively used for external flows with arbitrary 3D shock shapes and used only one solution from the Taylor-Maccoll equation to construct all the differently scaled streamlines. The inverse methodology was analytical simple and fast to compute, which lead to widespread adoption of the method to create external-flow waverider geometries [86].

2.3.4 Osculating Axisymmetric Theory

The Osculating Cones method was soon refined for greater control of the waverider's frontal shape. A new method allowed for arbitrary shock shapes and surface capture shapes called "inlet-capture curves" and "flow-capture tubes" (FCT), respectively. The centers of curvature for the flow-capture surface are projected and act as the local central axis. The local geometric slope of the waverider's leading edge is also carefully tailored to create shocks of similar wave angle. This allows for equal strength shocks that generate similar post-shock pressure everywhere on the vehicle. This ensures that pressure gradients do not exist and the Osculating Cone methodology can be implemented. For each central axis an assumption of local axisymmetry is made. Figure 2.7b shows how multiple Osculating Cones, with different central axes, can be defined upstream of a generalized waverider body. A unique conical flowfield is solved for each Osculating Cone by integrating the Taylor-Maccoll equations. A streamline solution within each Osculating Plane is traced downstream from the leading conical shock. The frontal "flow-capture tube" of the body is arbitrary and can be modified to optimize the waverider's shape, giving much more flexibility to designers. The local axisymmetry assumption is why this technique is called the Osculating Axisymmetric method, and it can be used to create both external waverider geometries and internally-convergent intake geometries [86]–[88].

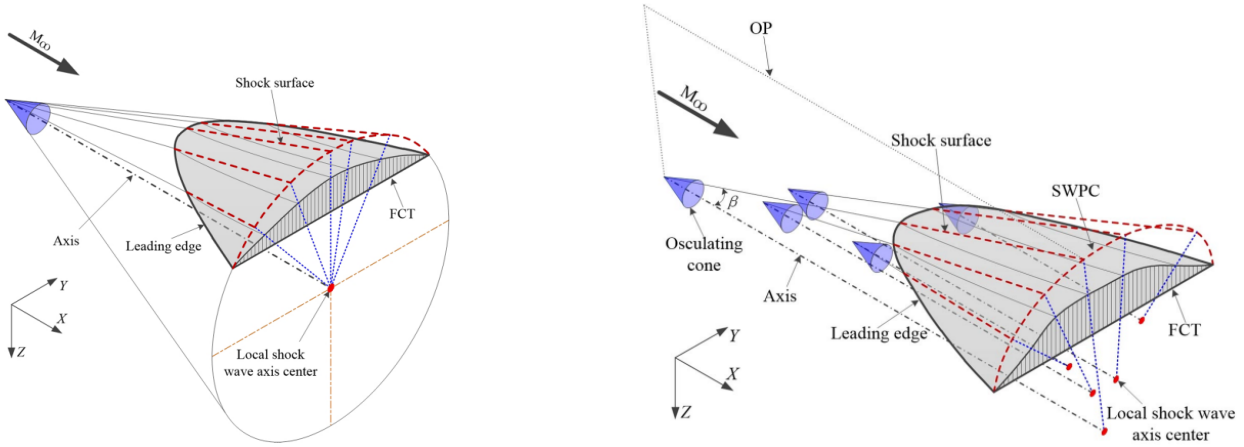

(a) Osculating cone method.

(b) Osculating axisymmetric method.

Figure 2.7. Different high-speed waverider construction methods. From ref. [89]; reprinted by permission of the American Institute of Aeronautics and Astronautics, Inc.

The potential application of Osculating Axisymmetric theory to intake design has yet to be fully realized. Strides in this realm have been made by You and Xuzhao [90], [91]. Instead of specifying a downstream shock structure, the downstream throat shape is defined with the inlet capture curve. Osculating planes are defined at discrete locations along the azimuth of the intake. Then, a streamtracing routine can solve the local 2D conical flowfield. Special care must be taken to ensure the leading edge shocks along the inlet capture curve are of equal strength. An intake shape transition is then achieved with unique streamline solutions in each osculating plane. Unlike morphed intakes, no blending is necessary and the entire flowfield is analytically defined [64], [90]–[92]. Additional information on this design methodology is presented in chapter 3.

3. STREAMTRACING DESIGN TOOL

A streamtracing intake design code was developed in MATLAB to construct the Indiana Intake Testbed. The design tool constructs inward-turning intakes with the Osculating Axisymmetric technique, which is a modified Osculating Cone method for creating arbitrary shape-transitioned waveriders. The intake design code uses these principles to construct three-dimensional, shape-transitioning, mixed compression, and inward-turning hypersonic intakes. The design tool combines several iterative functions that work in tandem to create the inner mold line (IML) of the intake's surface. Streamlines are traced through an outer capture shape and an inner throat geometry. Each streamline is a unique conical flowfield generated by the Taylor-Maccoll equations. The heart of the design code is the streamtracing routine. However, it also contains analytical performance tools and export tools for geometry and mesh generation in CAD and CFD programs. A brief description of each core function is presented in this section. Parts of this chapter are published within AIAA's 2022 SciTech conference proceedings or pending publication in AIAA's 2022 Aviation conference and the Journal of Propulsion and Power [93].

3.1 Defining the Shape Transition

The creation of a shape-transitioning inlet requires the definition of a capture shape and a throat shape. For realistic designs, the capture shape is commonly molded into the vehicle's fuselage in a rectangular fashion. The intake's throat shape is then defined as a circle or ellipse. Overall, the most common shapes for intakes include circles, ovals, squares, and rectangles. The maximal length (l) and height (h) for both the throat shape and capture shape can be specified separately. It is common to define an aspect ratio (AR) from (3.1) and substitute that in as a design parameter. The parametric superellipse family, described by equations (3.2) and (3.3), provide a quick and robust way to analytically define several of these key shapes with a few input parameters. The super-ellipse exponent (n) defines the desired shape. Historically, these equations have been used to create the REST intake family [94].

$$AR = \frac{l}{h} \tag{3.1}$$

$$x(t) = |\cos(t)|^{\frac{2}{n}} \cdot h \cdot AR \cdot sign(\cos(t)) \tag{3.2}$$

$$y(t) = |\sin(t)|^{\frac{2}{n}} \cdot h \cdot sign(\sin(t)) \tag{3.3}$$

The equations are decoupled, meaning that aspect ratio and shape are completely separate and for both the external capture shape and internal isolator shape. For example, it is possible to create a high-aspect ratio rectangular isolator (AR = 5) with a perfectly circular intake (AR = 1). Depending on the strength of the exponential factor, the rectangle's corners can be rounded to improve flow uniformity in experimental designs. A circular capture shape (AR = 1, n = 2) and a planar (rectangular) isolator with constant corner radii (AR = 2, n = 4) was defined using these equations. This shape-transition was chosen for the INlet and is presented in Figure 3.1. A rectangular isolator with flat walls allows optical access to the shock-train downstream of the intake.

After intake and isolator shapes are defined, the intake shape is modified through an iterative technique to match a desired contraction ratio. This technique uses a static offset circle, which adds a vertical height component to both the intake and isolator shape. A helpful visual is provided in Figure 3.1 for the static offset circle, intake shape, and isolator shape. Distance between capture and isolator shapes is determined implicitly from total CR. The static offset term provides a minimum centerbody radius to each streamline. This means each osculating plane solution will have a solution with a different total contraction ratio. Additionally, the offset circle is used to define a common ray that will connect the outermost edge of the isolator with a point on the intake shape. This ray defines the maximum angle of the streamtracing method with respect to the origin. It also demarcates the upper capture surface from the lower capture surface. The upper surface is defined by several modified Busemann contours that all contain unique parent flowfields. The lower surface is

constructed through a scaled-down, parallel streamline from the same solution. The parent flowfield and lower surface construction method is described in the following sections.

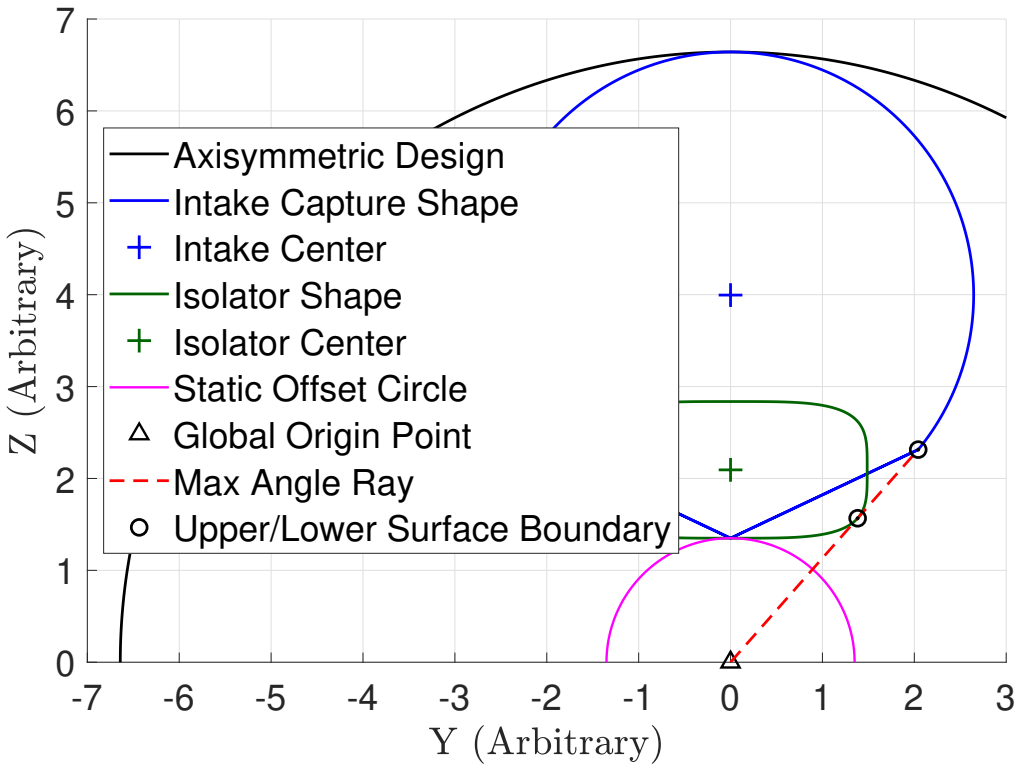

Figure 3.1. Shape-transition profile defined for the INlet Testbed.

The lower surface shape is not completely known until the streamtracing routine is completed. In order to approximate the lower surface frontal shape, straight lines are drawn from the maximum angle ray to the mid-point on the isolator wall's lower surface. This allows the program to "close" the frontal capture shape. The total contraction ratio is then calculated based on the ratio between the capture area and the isolator area. If the final CR is not within the error tolerance of the target CR, then the offset circle shape is modified. To increase the CR, the offset circle shrinks. This causes the maximum ray angle to become more steep, enlarging the capture surface. Likewise, if the offset circle grows it will shrink the capture shape. Thus, the size of the static offset circle also becomes a way to define

intake capture area and the overall contraction ratio. Also, after running the streamtracing routine, the final model CR may deviate from the target CR. At this point, if CR is a critical design factor, the initial capture shapes can be iterated to converge on an acceptable design. A list of user-defined geometric parameters are given in Table 3.1. The geometry is often normalized by the isolator's height, which is labeled here as h but also referred to as $R_\circ$ in literature referencing streamtraced Busemann inlets.

Table 3.1. User defined geometric inputs for an inlet.

Geometric Parameter	Symbol	Value
Approximated Contraction Ratio	CR_{aprox}	7
Intake Aspect Ratio	AR_{in}	1
Isolator Aspect Ratio	AR_{iso}	2
Intake Superellipse Exponent	n_{in}	2
Isolator Superellipse Exponent	n_{iso}	4
Isolator Height	$h, R_\circ$	1.8
Leading Edge Deflection Angle	δ	6^o

The second function is the definition of a centerbody radius. All Busemann solutions can be modified by a centerbody term that can alter the shape of the streamtraced curve and shock structure. The static-offset circle inherently adds radial distance to each individual Busemann contour with respect to the origin, which increases the centerbody radius. This parameter is iterable and affects the flowfield considerably. The effects of this parameter on inlet optimization are discussed in later sections.

3.2 Defining the Osculating Planes

Before the streamtracing process can begin, it is prudent to define the osculating planes at all inlet azimuthal positions. Sobiezcky proved that axisymmetric flowfield solutions, such as Taylor-Maccoll, can be used in each osculating planes to construct a full three-dimensional flowfield [83], [86]. Thus, each consecutive osculating plane contains the solution of a Taylor-Maccoll equation with different boundary conditions. Each inviscid contour is traced through the inner and outer radial bounds defined by the intake and isolator shape. As the angle of

the osculating plane changes, so does the radial boundary conditions defined by the capture and throat shapes (Figure 3.2).

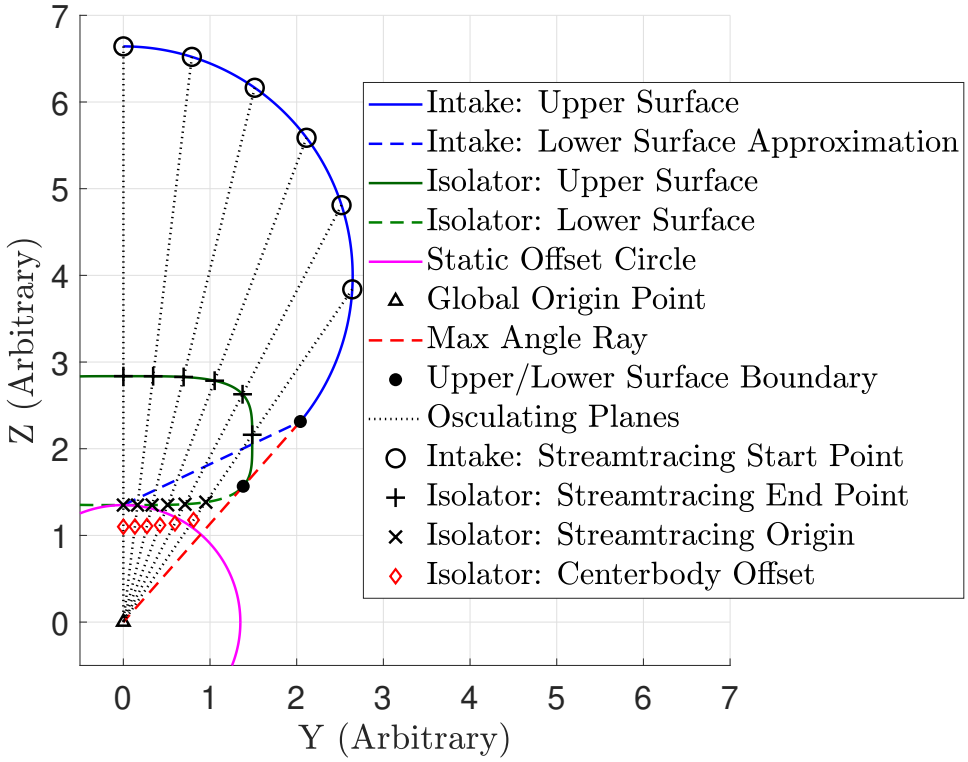

Figure 3.2. Osculating planes defined on the Indiana-Intake from the 2D base view.

In order to provide good fidelity of the intake shape, several dozen osculating planes are defined to discretize the full inlet calculation. A large amount of osculating planes also minimizes the azimuthal pressure gradients between 2D slices, ensuring that local axisymmetry holds. The origin is naturally offset from the intake and isolator shapes by the static-offset circle. Representative lines are then traced from the origin to the intake shape. These lines act as two-dimensional projections of the osculating planes. Likewise, all osculating planes for the inlet share this local origin axis. The sharing of a local axis for all osculating planes is a prerequisite for the creation of an inward-turning geometry. Additionally, the intersection points of the representative rays with the capture and isolator shapes are recorded. The outer-most capture intersection point and the outer-most isolator intersection point becomes the radial boundary limits for the Taylor-Maccoll integration scheme. The isolator

inner-most intersection point is saved for the lower-surface definition. The intake inner-most intersection point is discarded and does not contribute to the lower-surface streamtracing process. A full image presenting the osculating planes from a 3D view is seen in Figure 3.3.

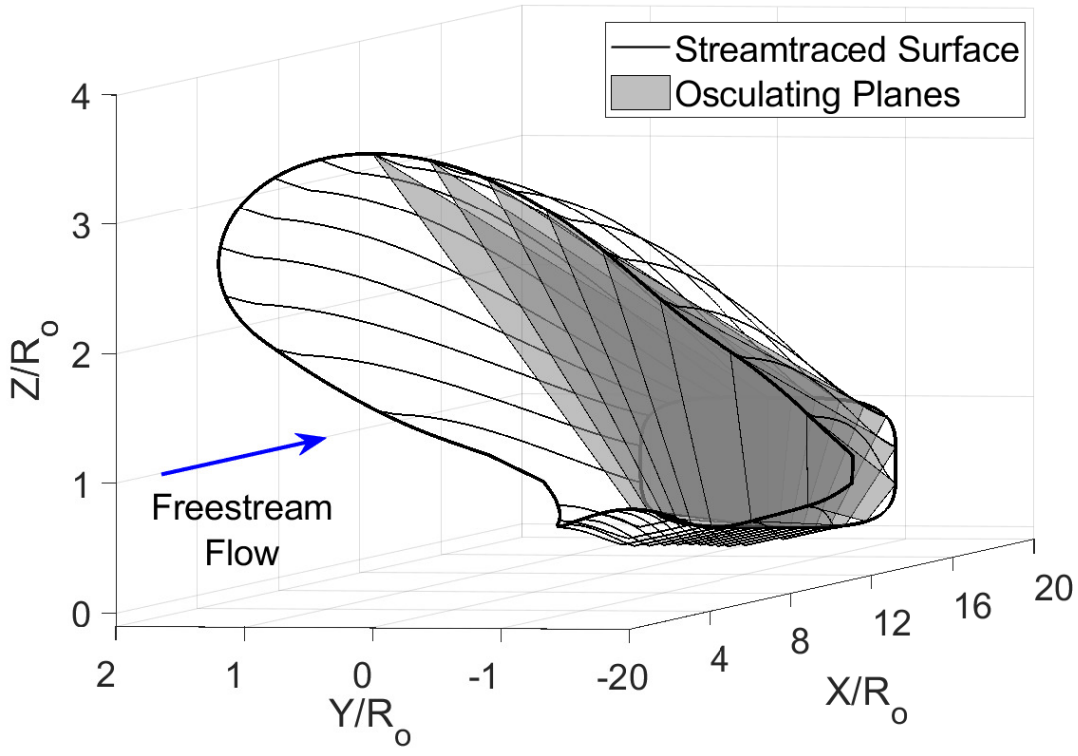

Figure 3.3. Three-dimensional view of the defined osculating planes.

3.3 Defining the Parent Flowfield

Designing a compressive internal flowfield for a hypersonic inlet relies upon the definition of a parent flowfield that compresses the flow efficiently. Historically, designers have relied upon reversed nozzle flowfields or method-of-characteristic solutions to create an inlet [7], [39]. The Taylor-Maccoll equations, which describe supersonic conical flow, can be integrated to produce internally convergent flowfields that satisfy this requirement. Mölder showed that the Taylor-Maccoll equations can be transformed from velocity space into Mach space for more intuitive analysis [36]. This set of ordinary differential equations are presented in

equations 3.4 and 3.5. The streamline equation is defined in equation 3.6. These equations are solved numerically using a Matlab fixed-step Runge-Kutta 4 solver in the streamtracing routine.

$$\frac{du}{d\theta} = v + \frac{\gamma - 1}{2} uv \frac{u + v\cot\theta}{v^2 - 1} \tag{3.4}$$

$$\frac{dv}{d\theta} = -u + (1 + \frac{\gamma - 1}{2} v^2) \frac{u + v\cot\theta}{v^2 - 1} \tag{3.5}$$

$$\frac{dr}{d\theta} = \frac{ru}{v} \tag{3.6}$$

Depending on the integration limits, the Taylor-Maccoll equations can produce four different solutions. A visual of each contour is shown in Figure 3.4. The most widely known solution is flow over a cone. This flow is external and useful for waverider design, but is not convergent or internal. However, the later three solutions are internal. The Busemann solution and Internal Conical Flow - A (ICFA) solution are internally converging and compressive. The fourth solution, Internal Concial Flow - B (ICFB), is internally expanding. The ICFA solution solves for conical flow downstream of a conical shock [45]. Unfortunately, the ICFA contour is prohibitively short and ends in a singularity. The lack of any meaningful isentropic compression limits the use of this contour by itself. The Busemann solution generates a streamline that provides adequate isentropic compression and length, making it a good candidate for intake design.

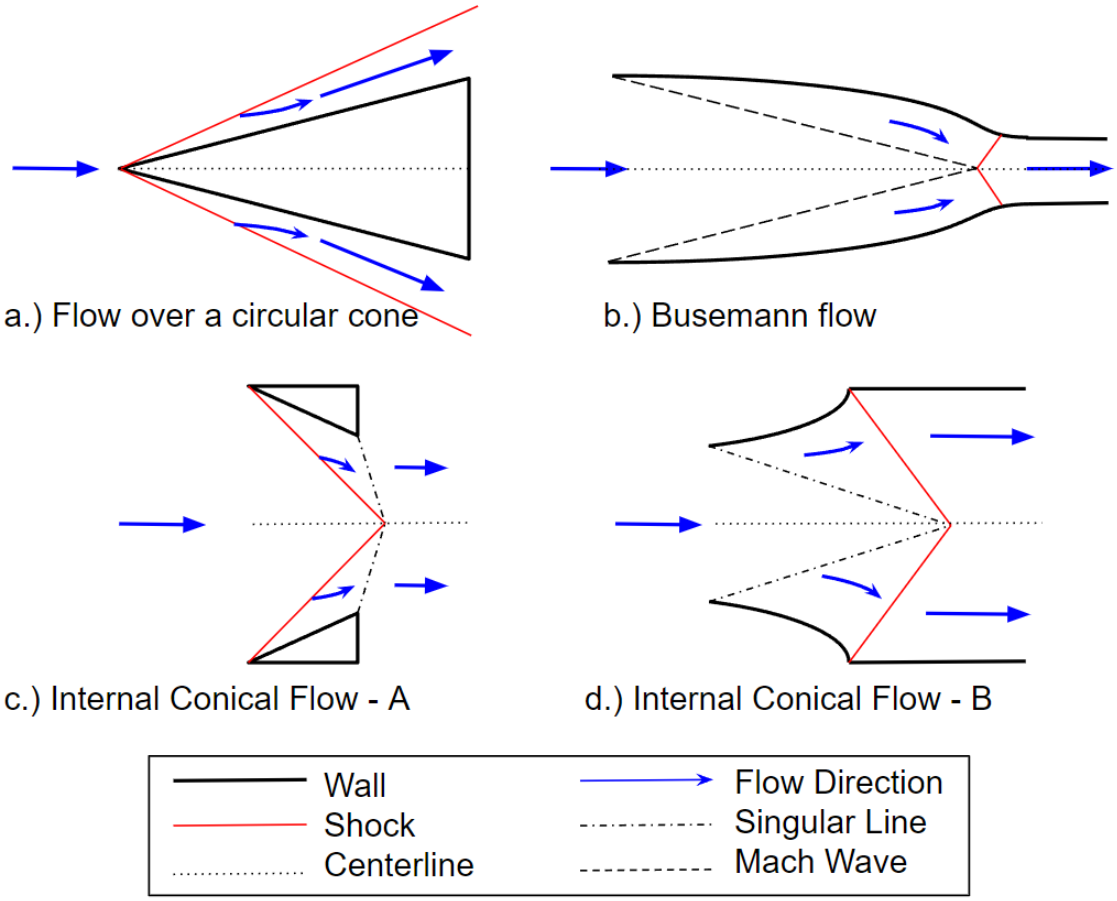

Figure 3.4. Visualization of the four solutions to the Taylor-Maccoll equations. Adapted from Mölder in ref. [45]; reprinted by permission of the American Institute of Aeronautics and Astronautics, Inc.

3.3.1 Busemann Contour Definition

The classic Busemann solution to the Taylor-Maccoll equation provides the necessary internally convergent and compressive parent streamline needed to design a high performing inward-turning inlet [44]. Unfortunately, full axisymmetric weak-shock Busemann solutions violate the Kantrowitz limit, which is discussed in Section 1.3. For this reason, three dimensional streamline traced inlet designs only use scaled Busemann solutions to generate azimuthal portions of a full intake surface. As mentioned earlier, streamtracing creates swept surfaces and cut-backs that enhance intake starting.

The Busemann solution assumes a terminal oblique shock at the isolator entrance. If designing an inlet for a ramjet, then a strong oblique-shock solution will be required to establish subsonic flow in the combustor. For a hypersonic scramjet, a weak oblique-shock solution is necessary for started supersonic flow in the downstream flowpath. Integration of the Busemann contour begins in polar coordinates beginning at the oblique shock. Figure 3.5 shows a generic untruncated Busemann contour. In this design code, a shock wave angle is specified as the initial parameter for the integration. Other design codes may use post-shock Mach numbers, total pressure recovery values, or static pressure targets as an input and back-solve the necessary shock wave angle for that condition [47]. Then, the contour is traced upstream until a freestream condition is met. Sometimes the solved freestream Mach number does not match the design condition and iteration is necessary. The inviscid streamline from any of these solutions become the contoured "wall" of the inlet.

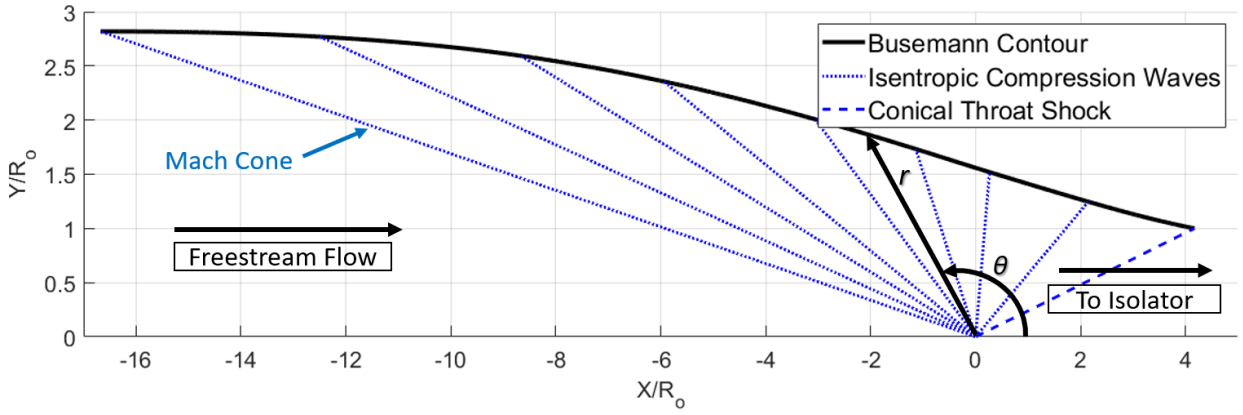

Figure 3.5. Generic untruncated Busemann contour defined with polar coordinates.

3.3.2 ICFA Contour Definition

The theory of Osculating Cones, which forms the basis of Osculating Axisymmetric Theory, states that incoming flow must be processed by shocks of equal strength in each osculating plane. This requirement prohibits the use of truncated Busemann contours due to their propensity to create curved shocks. Interestingly, the Internal Conical Flow - A solution provides a resolution to this problem. The ICFA contour is internally convergent, similarly to the Busemann solution, but it solves an axisymmetric conical flowfield behind a

straight, leading-edge conical shock [45]. A flow-relief effect acts to increase the Mach number immediately downstream of the conical shock. Figure 3.6 shows the a generic contour and its respective Mach profile.

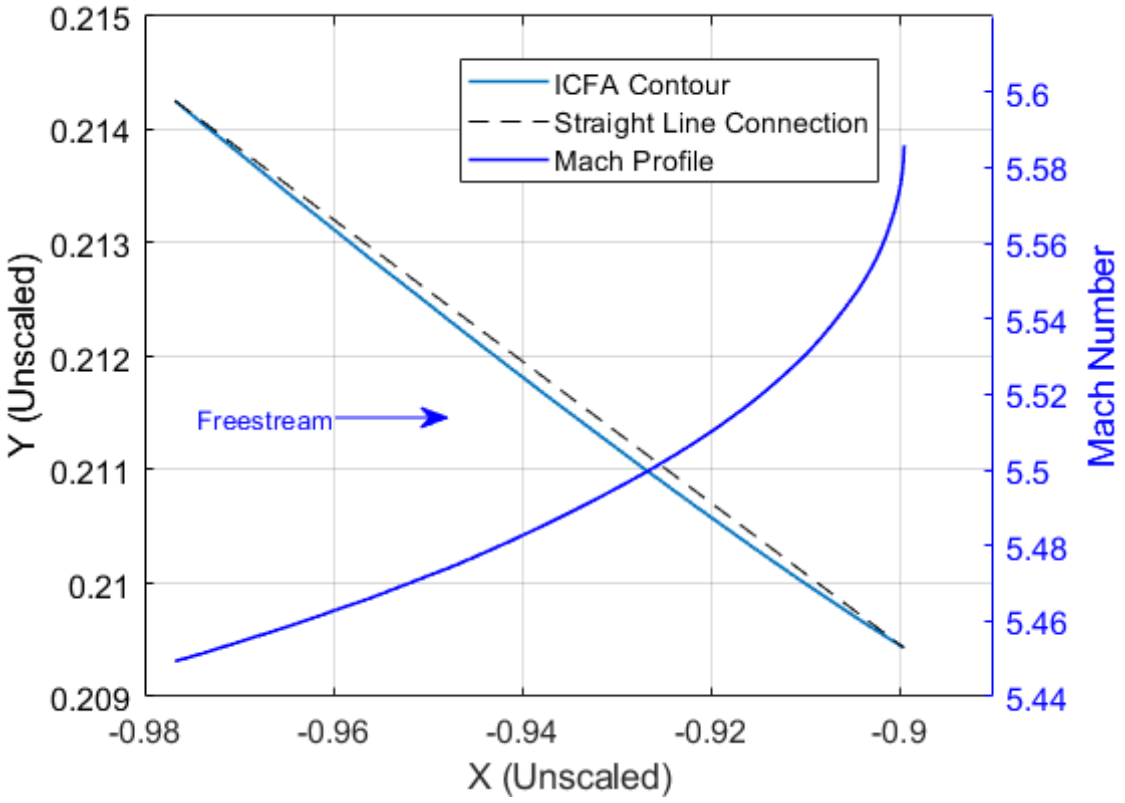

Figure 3.6. A generic ICFA contour with the Mach profile showing the 3D flow-relieving effect past the leading oblique shock.

The ICFA contour is solved by integrating the Taylor-Maccoll equations with a defined leading oblique shock wave angle and a given freestream Mach number in a polar coordinate system. Integration of the Taylor-Maccoll equations to create an ICFA solution starts from the leading oblique shock and proceeds in the downstream direction. The solution is numerically integrated until a singularity is reached at an unknown downstream ray.

The generated ICFA contour is short and provides negligible isentropic compression, so it cannot be used as the parent flowfield. However, it can be stitched to an existing parent contour, such as the truncated Busemann. Merged contours of the truncated Busemann and ICFA contour are eloquently called the Internal Conical Flow - C (ICFC) solution in

the literature. O'Brien investigated ICFA as a way to predict pressure ratios along the leading edges of truncated Busemann contours [51]. Ramasubramanian et al. investigated a physical leading edge ICFA merged with a truncated Busemann by matching individual Mach components. Geometric extensions were used to close the contours. ICFC extensions were found to improve shock placment, increase adiabatic efficiency, and reduce total pressure loss [95]. They have also been shown to significantly reduce wetted area, length, and mass spillage [41], [96]. The associated benefits to this truncation technique are well documented. It is no surprise that it is now being used in the design of waverider intake [97].

3.3.3 ICFC Merging Procedure

The combination of a Busemann streamline and an ICFA contour satisfies Osculating Axisymmetric Theory's requirements for a local 2D conical flowfield with a leading edge shock that is of equal strength in each osculating plane. Additionally, the ICFC contour reduces distortion along the inviscid flowfield's centerline. Improvements to the flowfield are heavily determined by the merging procedure. There are several flow and geometric parameters at the merging point which cannot be made to match each other simultaneously. These trade-offs include local deflection angle, termination ray, radial Mach component, theta Mach component, and total Mach number. If termination rays are matched and geometric convergence is achieved, then angular and radial Mach number may not match, as seen in Figure 3.7. There is a trade-off associated with each convergence method.

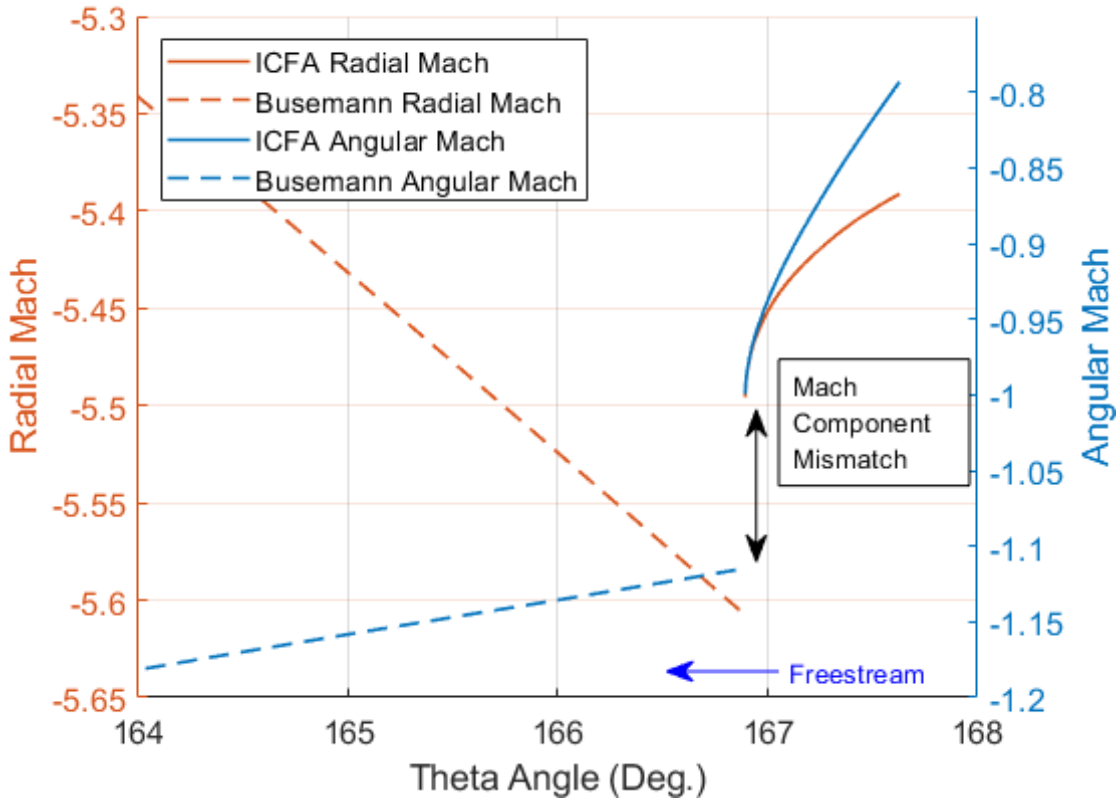

Figure 3.7. Mach component mismatch between a generic ICFA and Busemann contour in polar coordinates.

The ICFC merging procedure for the INlet was borrowed from Otto et al. [98]. This technique merges the ICFA and Busemann contours along the same polar ray, closing the geometry without extensions. A visual of the converged contour for a generic condition is shown in Figure 3.8. The geometric locations are matched at the expense of the Mach number components. To rectify this difference, a Prandtl-Meyer expansion is calculated through the turning angle of the contour mismatch. The final Mach number of the expansion is then used to find the starting Mach number of the Busemann contour. Since the turning angle and final Mach number of the Busemann streamline are coupled, iteration is necessary to converge on a solution.

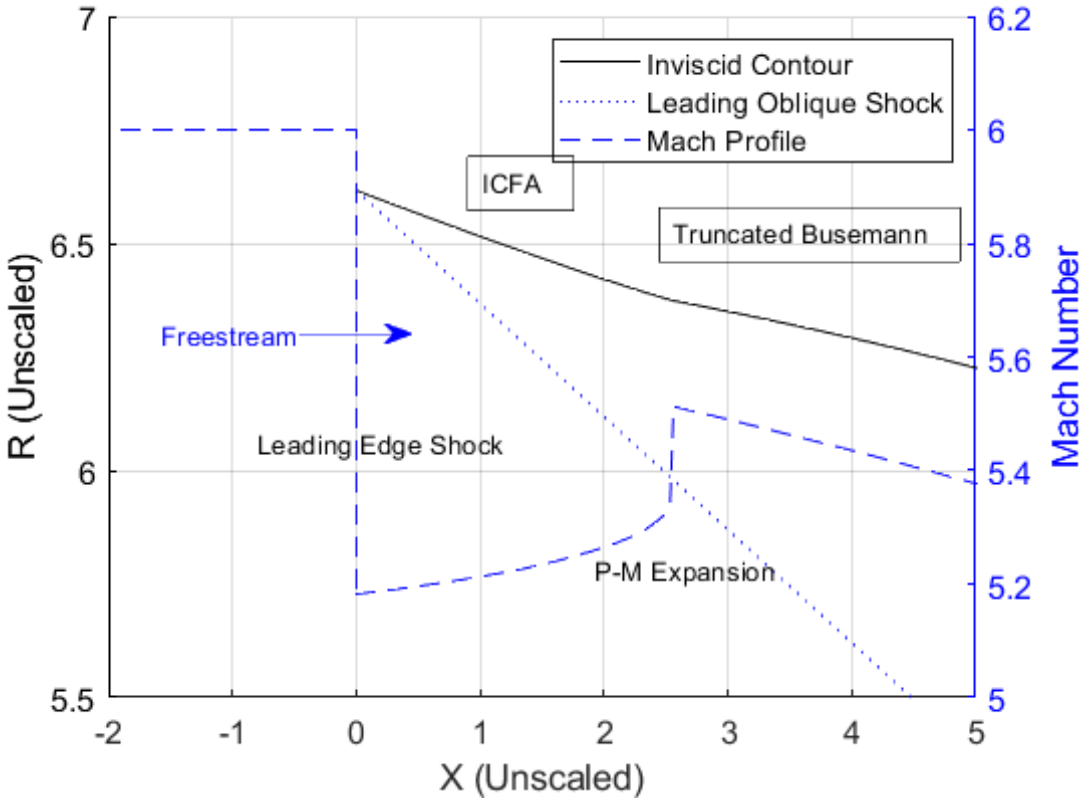

Figure 3.8. Merged ICFC contour using the Otto procedure to create the basic compressive parent flowfield [98].

This process indirectly truncates the downstream Busemann contour. It is possible that the flow expansion angle will change for different osculating planes. However, to ensure equal strength leading shocks, the same ICFA contour is used for all osculating planes. The leading edge deflection angle is defined as 6° and the freestream Mach number is 6. The leading ICFA shock directly hits the root of the Busemann throat shock. This greatly simplifies inviscid shock prediction and reduces the chance of erroneous shock reflections. Matching the centerline focal point for both shocks also simplifies the creation of the lower shock capture surface. The ICFC merging process is outlined below.

1. Define a leading edge deflection angle and freestream Mach number. The ICFA contour is defined from these quantities through the oblique shock relations.

2. Integrate the Taylor-Maccoll equations starting from the leading oblique shock in the downstream direction. Integration is halted automatically when the numerical solver encounters a singularity. The singularity occurs at the singular ray, which will be the merging point that connects the truncated Busemann contour to the ICFA contour.

3. Find and record the total Mach value at the end of the ICFA contour.

4. Guess a throat shock angle that obeys the weak-shock criterion.

5. Integrate the Taylor-Maccoll equations upstream from throat oblique shock to the recorded singular ray. This will truncate the Busemann contour. Record the Mach number of the Busemann contour at the singular ray.

6. Calculate the geometric deflection between ICFA and Busemann contours.

7. From the deflection angle, find the Prandtl-Meyer expansion angle.

8. Calculate the Mach number of flow exiting the ICFA contour as it moves through the expansion fan.

9. Compare the Mach number after the expansion with the Mach number at the leading edge of the truncated Busemann streamline. If the Mach numbers are sufficiently close, then the contour has converged.

10. If the Mach numbers do not match, iterate the process by changing throat shock angle with a secant-based numerical scheme. The process repeats until the Mach numbers converge. A fully converged profile is shown in Figure 3.9.

The ICFC creation loop is the inner-most loop in the Matlab streamtracing tool. It iterates on isolator Mach number frequently, so a secant-based numerical method is used to speed convergence. Checks on realistic isolator Mach numbers ensure physical results during the iteration process. Violations of these limits are reported in the program and automatically replaced to reset the iteration process.

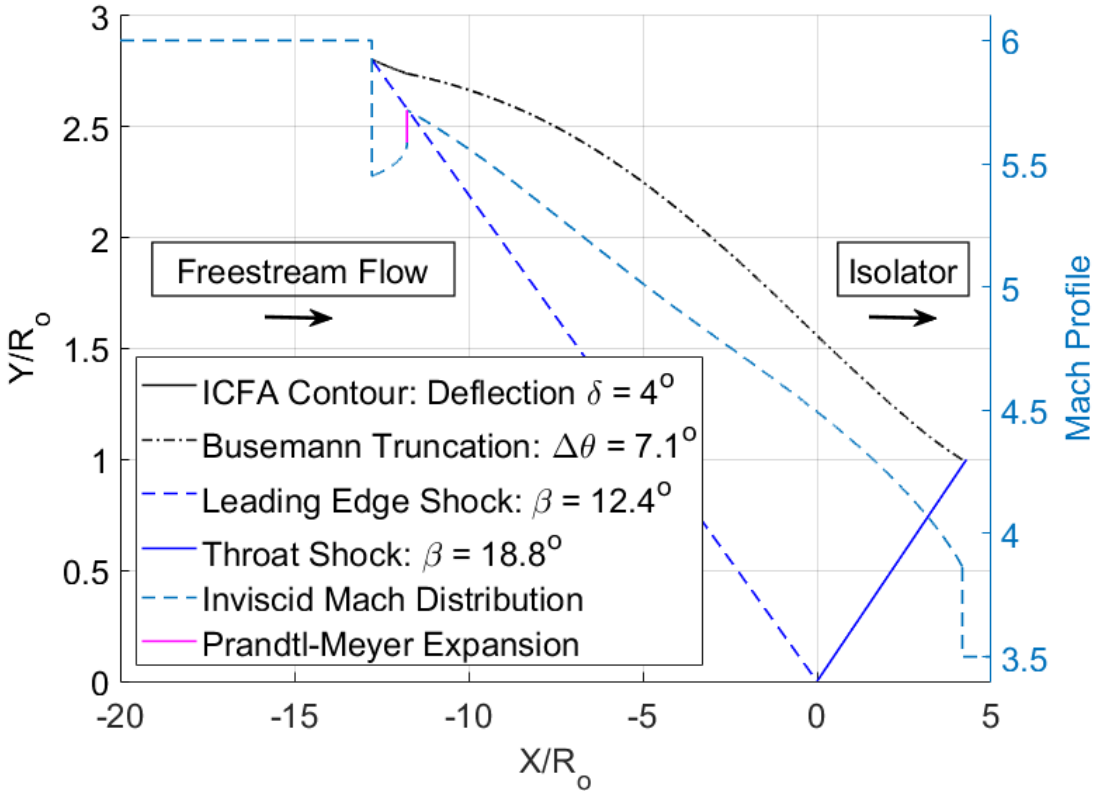

Figure 3.9. Generic ICFC contour for a Mach 6 freestream condition.

3.3.4 Geometric Streamline Merging Procedure

Fitting the ICFC contours into the geometric boundaries of each osculating plane requires a new iteration process. After the parent ICFC flowfield is initially created, the contour is shifted up or down. The last point of the contour is matched to a location at the throat. The leading edge radius is then compared to the capture shape for that osculating plane. It is common that the leading-edge radial height does not match the target. For these cases, the throat oblique-shock angle is iterated and the ICFC merging process is repeated. An example of two unique and converged ICFC solutions is shown in Figure 3.10. The two solutions do not necessarily meet the geometric target, but show how each solution provides a different amount of flow contraction.

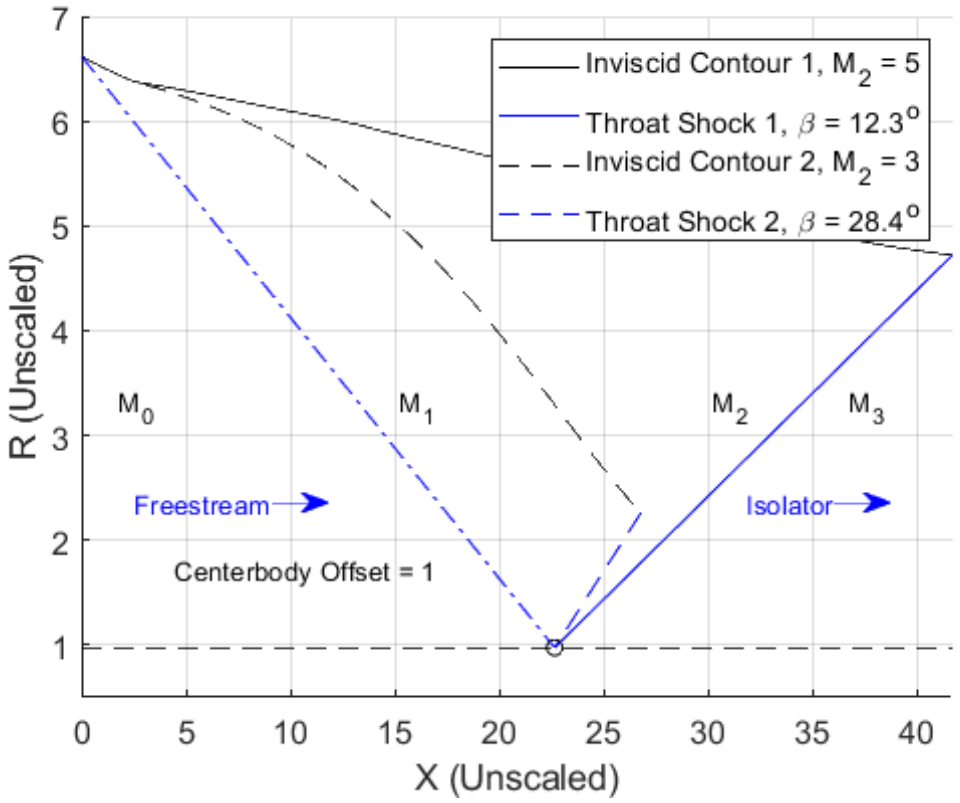

Figure 3.10. Converged ICFC contours with a constant centerbody parameter, different throat shock values, and different amounts flow contraction.

The throat Mach number and throat oblique-shock angle become independent variables that tune the local ICFC contour to fit the defined shape. Note that the contour is not scaled, as is commonly done in other streamtracing routines. Scaling the contour to fit within the radial bounds is possible, but it changes the intersection location of the leading and throat shocks for all osculating planes. Keeping the intersection point consistent for all solutions is important to create the lower surface geometry. The Busemann portion of the contour is continuously iterated (not scaled) until geometric convergence is achieved. Also note that this may cause the strength of the local Prandtl-Meyer expansion to change between osculating planes. An example of such a difference is shown in Figure 3.11.

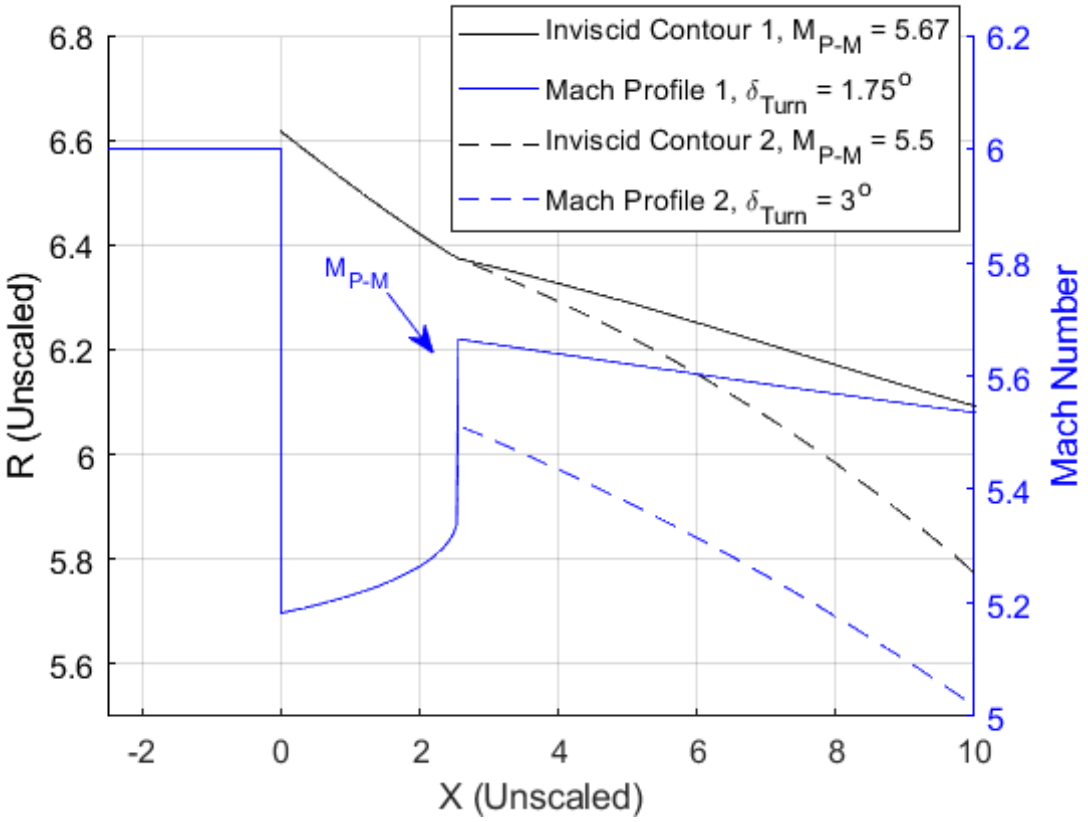

Figure 3.11. Separate ICFC solutions with different expansion Mach numbers defined by the turning angle from the downstream truncated Busemann contour.

1. Complete the ICFC merging procedure for a specific osculating plane.

2. Shift the ICFC contour to fit the inner radius point defined by the throat shape.

3. Compare the outer radius of the ICFC contour with the radius defined by the capture shape.

4. If the two radii are not within tolerance limits, then iteration will be required to converge the geometry.

5. Change the throat Mach number for that local osculating plane and resolve the ICFC contour.

6. Repeat step 1-4 until the geometry has converged. A converged solution is shown in Figure 3.12. If the solution fails to converge, save nearby neighbor quantities and interpolate these answers as initial guesses for the next round iterations. If this process does not work, then the centerbody parameter may be increased to alleviate the convergence issue.

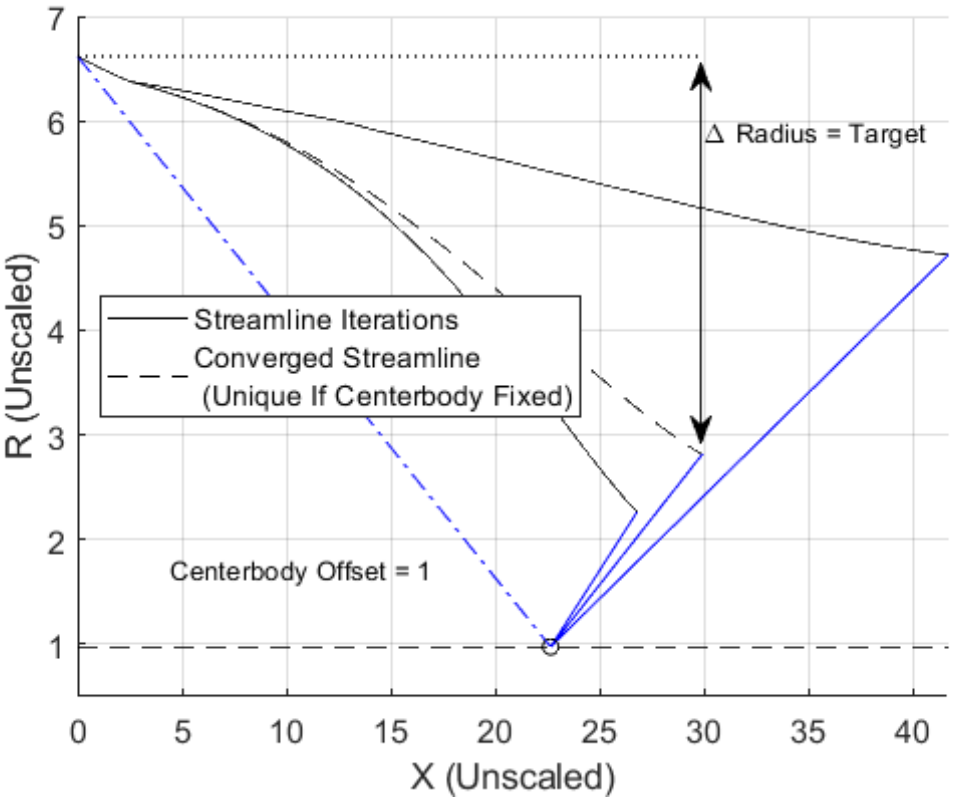

Figure 3.12. A geometrically converged ICFC parent flowfield for a local osculating plane.

The isolator Mach number is usually iterated upon several times until convergence is achieved. A secant-based numerical solver is used similarly to the ICFC merging procedure. The convergence of these loops becomes problematic when the inner and outer radial limits get close to each other. These streamtraced Busemann contours become shorter and provides less isentropic compression. Thus, to reach the target throat Mach number, the oblique shock must provide more compression than neighboring osculating planes with longer contours.

This relationship forces the shock angle to become steeper, and if it becomes too steep then it may violate the detached shock criterion for oblique shock waves. To alleviate this issue, a centerbody offset constant is added to the static offset circle radius. This constant improves the convergence of shorter contours by allowing a larger local contraction ratio and a steeper throat shock for these contours.

The results of the merging procedure for each converged osculating plane is recorded within the streamtracing routine. The local Prandtl-Meyer expansion is different in each osculating plane due to different turning angles. Figure 3.13a shows the total flow turning angle and its effect on the total Mach number. As turning angle increases, the total flow expansion increases and results in a larger total Mach number. The change in total Mach number is due to local changes in truncated Busemann deflection angle. This local change is presented in Figure 3.13b as a function of osculating plane angle. Although the polar truncation ray stays constant, the geometric deflection angle changes per individual streamline.

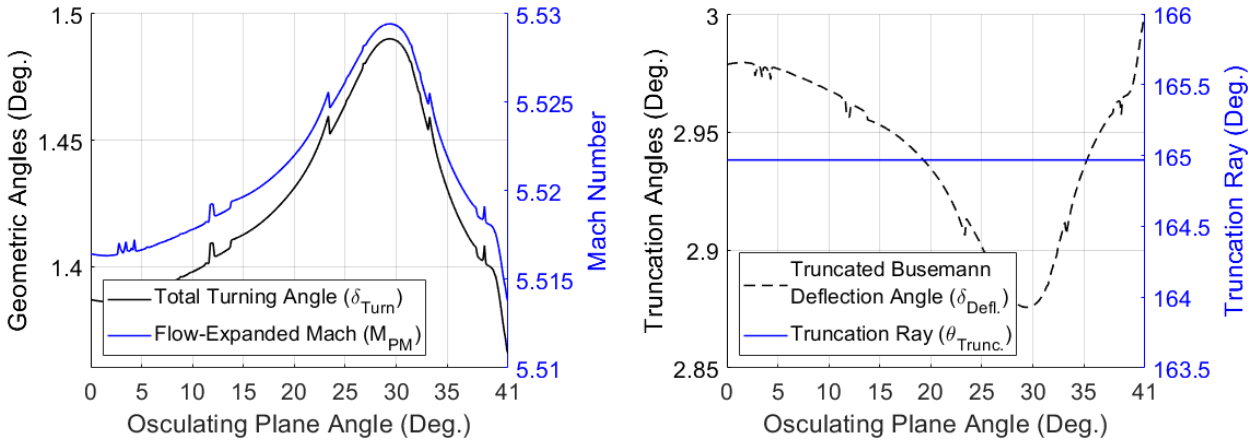

(a) Flow turning angle and total Mach number. (b) Truncated deflection angle and polar ray.

Figure 3.13. Final truncation parameters for a converged inlet.

3.3.5 Distortion Optimization Procedure

In addition to the independent variables already listed, it is possible to change the shape of an individual Busemann contour by adding a radial offset component. This radial term,

coined centerbody, can be added to the radial boundary of both the intake and isolator shapes. Although the radial distance between the capture and isolator shape is a constant, the total offset radial distance impacts the parent flowfield's shock structure. The centerbody radius influences the generation of the compressive contour. If the origin point and leading edge shock angle are held constant, smaller centerbody radii cause the throat shock to become stronger, as seen in Figure 3.14. If the throat shock angle is also held constant, then a smaller centerbody would force the Busemann contour to shrink. Thus, the centerbody radius becomes a third independent variable that acts to influence the ICFC contour and flowfield properties.

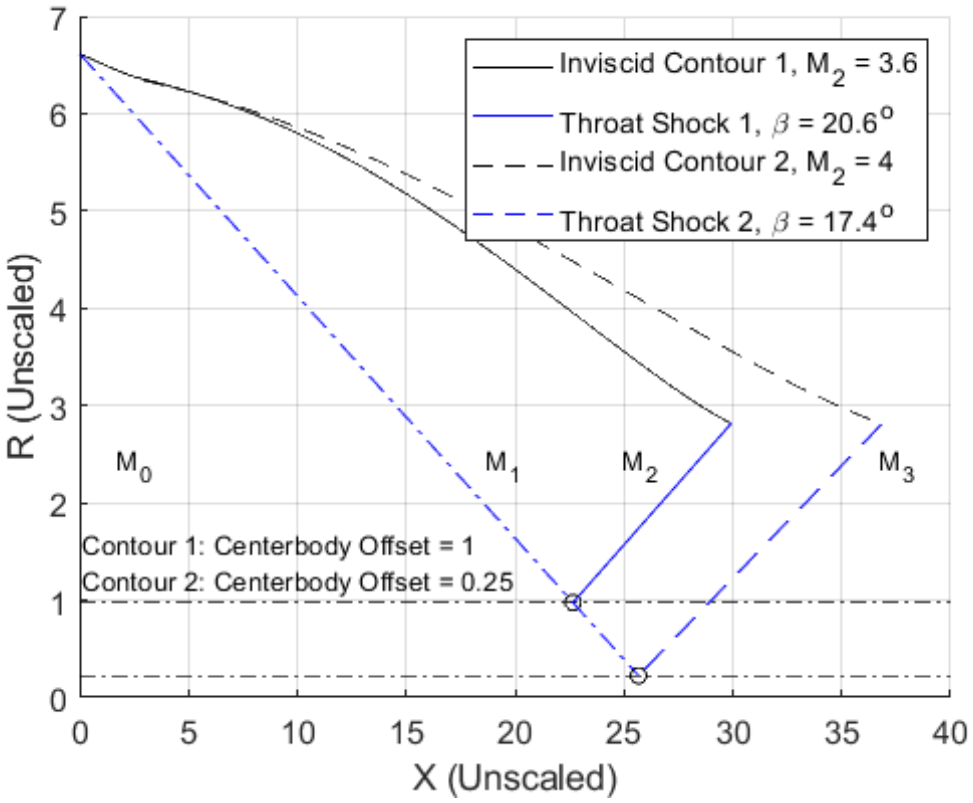

Figure 3.14. Effect of changing the centerbody parameter on a geometrically converged ICFC flowfield.

A third nested iteration loop can control this variable. The simultaneous iteration of three variables is computationally expensive and prone to faults. For the current inlet study it was deemed out-of-scope and deactivated. The benefit to activating this centerbody iteration

loop is that it holds the potential to tune isolator Mach number and downstream throat distortion. An optimization study would proceed normally to a regular inlet generation. Initial convergence of the parent ICFC contour would be conducted by varying isolator Mach number. Then, geometric convergence would be satisfied by changing shock angle of the throat shock. Finally, the addition of a changing centerbody radius would force the parent flowfield's shock structure to change while satisfying geometric constraints. Several non-unique solutions exist for each osculating plane. The variation of the centerbody parameter essential makes a sweep through these solutions. The solution that satisfies the target isolator Mach number is then recorded.

3.4 Solution Filtering

Solved contour solutions for each osculating plane are saved and analyzed for verification. The ICFC merging procedure and geometric merging procedure give solutions within a defined tolerance bound. To check these solutions, a residual plot of the relative error to the target values can be produced for a visual check. Depending on loop convergence criteria, some limits may be exceeded for specific osculating planes. In these cases, the solutions must be resolved with better initial guesses.

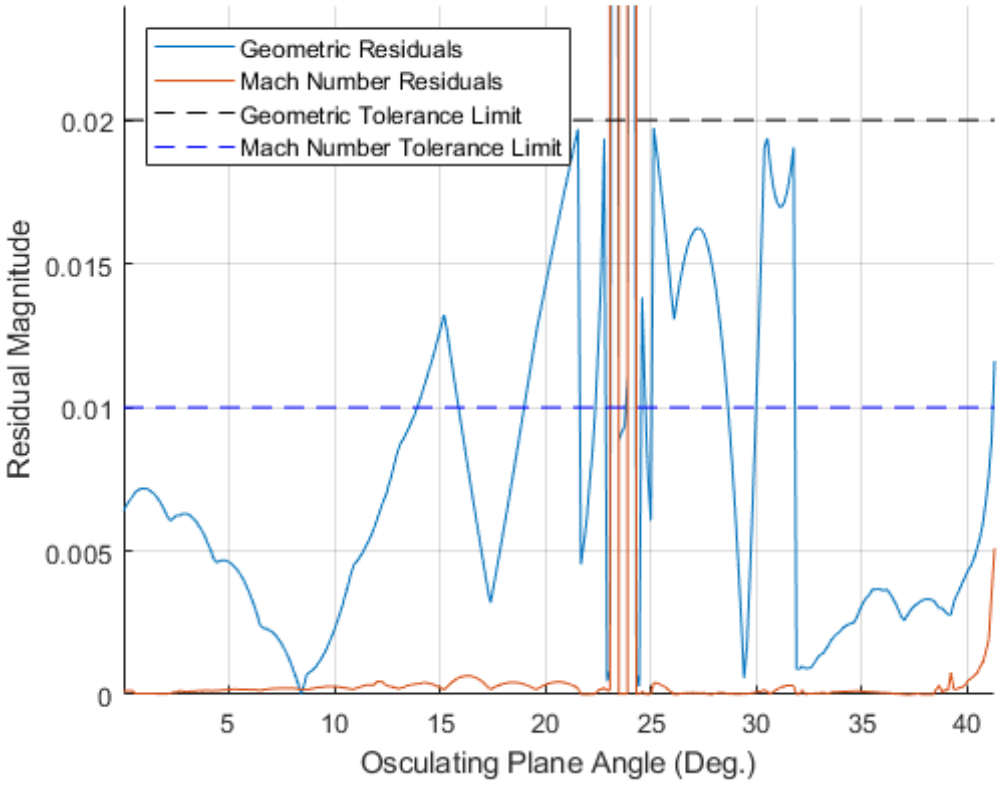

Figure 3.15. Residual plot showing the failed convergence of several parent flowfields along different osculating planes.

It is expected some osculating planes will not converge during the first calculation. After the first round of iteration, the final solutions for each osculating plane, throat shock angle and throat Mach number, are saved. If the optimization loop is activated, then the center-body term will also be saved. First, the solutions for the osculating planes which did not converge are located and removed. Solutions of nearby osculating planes are used to interpolate a guess of that local solution, for both the shock angle and throat Mach number. The solutions are passed through a Savitz-Golay smoothing filter. This moving-polynomial filter has been used in past studies to smooth inviscid contours on nozzle MoC generation codes [99]. The filter removes perturbations in the solutions brought upon by the upper and lower limits of the tolerance specifications. Shock angles and Mach numbers at the throat for each osculating plane are smoothed and then fed back as initial guesses into the program. These values directly affect the length of each 2D Busemann-derived contour. If the smoothing

filter was not applied, then the finished contour's leading-edge would look "bumpy" due to slight changes in the length of each osculating plane's contour. Examples of legacy inlet designs without the smooting filter are shown in appendix A.

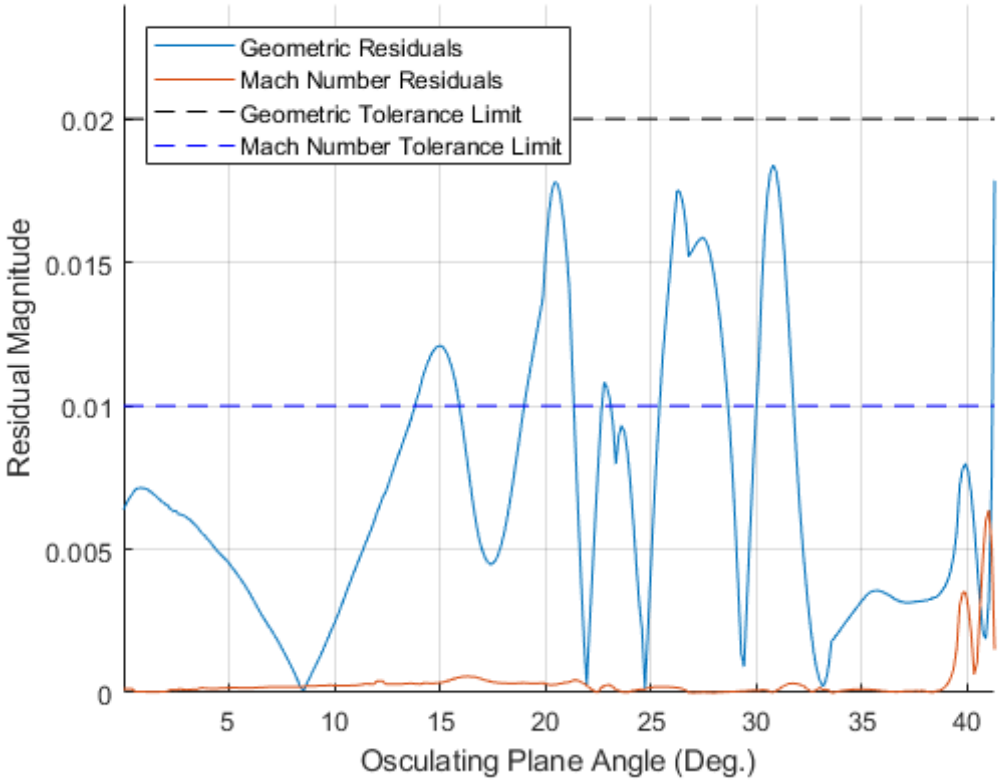

Figure 3.16. Convergence of all parent flowfields after the interpolation and smoothing step.

Since the program now has initial guesses that are close to satisfying tolerance bounds, the speed of convergence increases drastically. Osculating planes usually have contour solutions with similar values to other nearby solutions. Thus, the interpolation procedure usually solves any convergence issue. However, if persistent problems exist for a certain group of osculating planes, the centerbody offset term may be increased. This relaxes any aggressive throat shock angle solutions at the expense of longer Busemann contours.

3.5 ICFC Contour Manipulation

The accumulation of hundreds of converged flowfield contours must be reconstructed in a three-dimensional manner to create the intake surface. To do this, all converged ICFC contours are overlapped on the same two-dimensional polar coordinate plot. The solved shock intersection points for all contours are then checked against each other for anomalies. Since the leading edge and throat shock angles are known, a simultaneous set of two equations can be solved to yield the intersection point. As expected, the leading edge shock should always hit the centerline-root of the throat shock. All contours are then shifted so that their axial locations align in the same plane. This is plane is the hypothetical start of the isolator section.

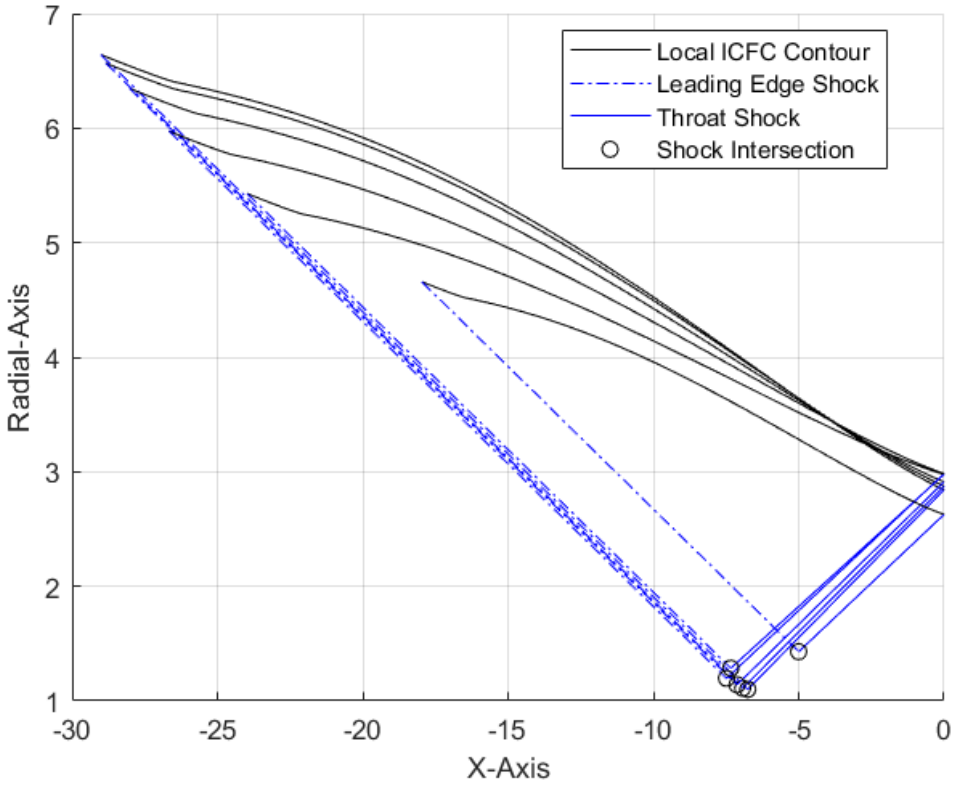

Figure 3.17. Family of geometrically converged ICFC solutions with their solved shock-intersection locations.

3.6 Capture Surface Construction

For this design code, a certain portion of the inlet is reserved to capture shocks generated by the leading edges. The shock-capture surface, or lower surface, is constructed as a means to capture all leading edge shock waves and to guide the flow into the isolator. A shock-on-lip condition ensures that on-design mass capture is sustained and predictable, which is essential for downstream components in an airbreathing engine. The lower capture surface is much shorter in length and provides little compression to the flow. If the lower surface does not provide enough area relief to the flow, other measures may be added to enhance the inlet's starting potential.

The lower surface of the INlet uses a novel construction technique and provides several inherent benefits. To make the lower surface for a certain osculating plane, the upper ICFC contour is scaled down to fit the local shock structure. This similar, inviscid parallel streamline maintains the captured flow's turning angles on both the top and bottom contour. Since each Osculating Plane contains an infinite amount of scalable streamlines from the Taylor-Maccoll equations, the capture surface is also defined from theory. However, compression waves from the upper surface will interact and bounce off the lower-surface. This will cause some flow non-uniformities and shock-mismatching downstream. The lower surface flattens out after the throat shock, which is where the flow is turned horizontally into the isolator. The inflection point where the flow is turned horizontally acts as a shock trap and is the root of the predicted throat shock.

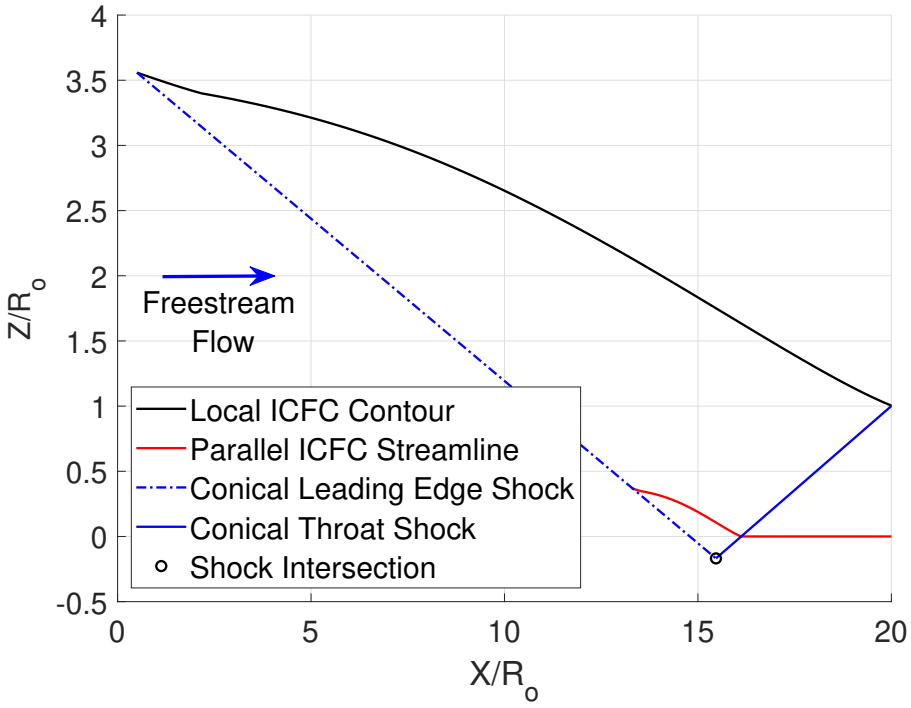

Figure 3.18. The local ICFC streamline fitted between the leading oblique shock and throat shock for a specific osculating plane.

Designing the lower surface as a scaled-down sample of the upper surface simplifies the construction process and minimizes the internal contraction ratio. Since the lower surface provides no compression to the flow, the method does not risk over-contraction. The parallel streamline also acts as a shock-trap for the throat shock, forcing the throat shock into the notch between the curved and straight sections. Since the curvature is similar on both the top and bottom surfaces, the internal area change is gradual. The lower-surface construction method does not attempt to cancel potential shocks generated by its own leading edge. These shocks will act to distort the flow and cause some amount of on-design flow spillage. The effect of these shocks will be investigated from CFD solutions in chapter 4.

3.7 Inlet Construction

Additional processing is required before the intake surface is constructed. The contours are rotated into three-dimensional space based on their original osculating plane angle. Sim-

ple geometric relationships relate the contours solved in two-dimensional Polar coordinates into three-dimensional Cartesian space. A fully constructed 3D geometry is presented in Figure 3.19. The lower-surface structure creates two separate swept cut-outs, which make the inlet both aesthetically pleasing and able to automatically operate in a spillage mode. These non-traditional cut-outs act as the cowl lip and are likely to enhance starting for both on-design and off-design Mach numbers. Since the side cowls protrude further upstream than traditional designs, the cowl shock will impinge onto the body compression surface. Based on the conditions, this may induce boundary-layer separation.

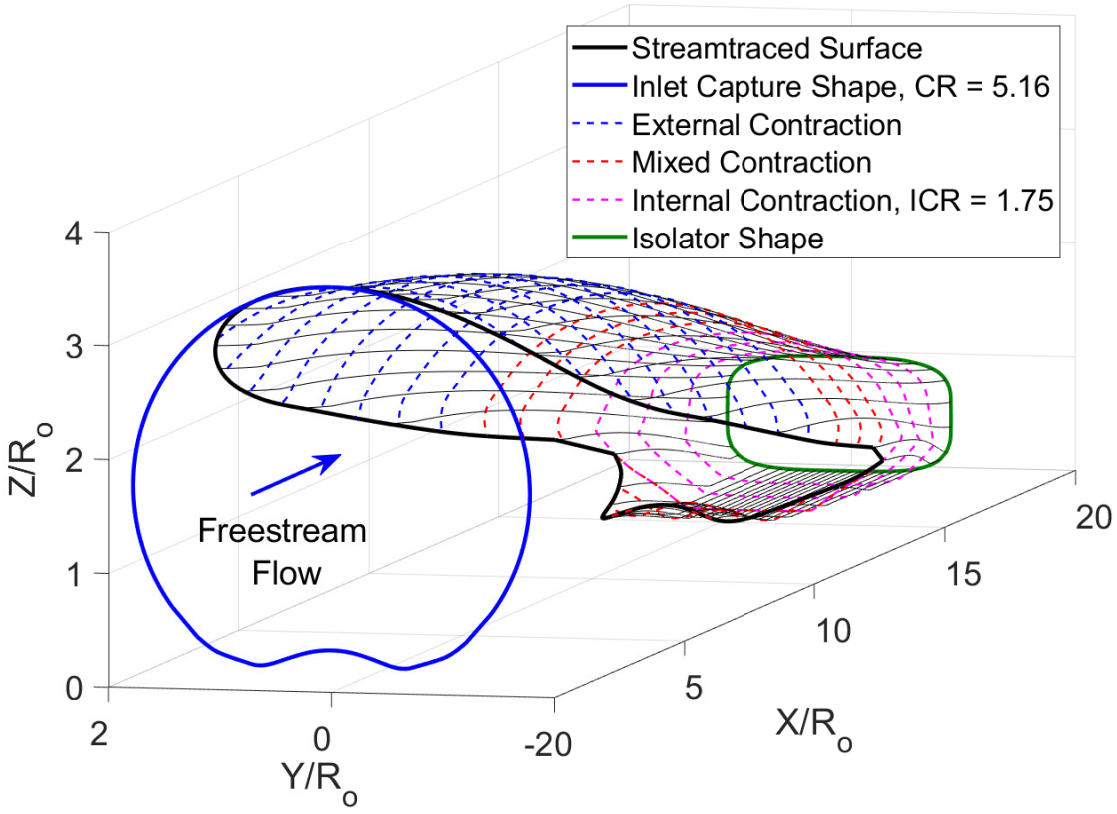

Figure 3.19. Isometric view of the INlet.

With the upper and lower surface shapes known, the external contraction and internal contraction areas can be calculated. The external contraction ratio is 5.16, which falls below the target of 7. Figure 3.20 shows a frontal projection of the INlet. It is noticeable that

the capture shape differs from the original circular design due to the lower surface, which lowers the final CR. The lower surface construction is done after the streamtracing routine for the compression surface. Also, the completed geometry is normalized by the isolator throat height $R_\circ$, providing a reference dimension for all further scaling.

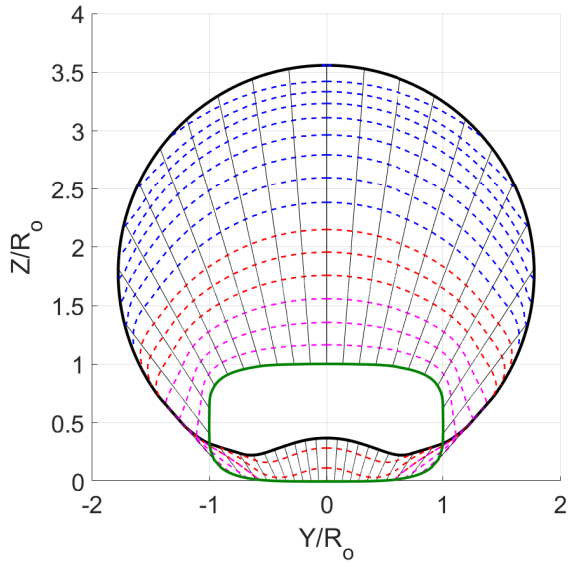

Figure 3.20. Frontal view of the INlet.

3.8 Viscous Correction Procedure

A boundary layer viscous correction was applied to each inviscid streamline by calculation of the boundary layer displacement thickness. The process used in the design code was developed by Sivells and Payne [68]. Although originally developed for axisymmeric hypersonic wind tunnels with no adverse pressure pressure gradients, the method has been shown to provide a good estimate of boundary-layer thickness for streamtraced waverider intakes [66]. The method solves the von-Kármán momentum equation for turbulent axisymmetric boundary layers, which is shown in equation (3.7). The equation can be solved by a numerical Runge-Kutta scheme similar to the Taylor-Maccoll equations. In the equation, φ is boundary layer momentum thickness, σ is the flow type ($\sigma = 1$ for axisymmetric boundary

layers), and γ is the ratio of specific heats. The shape factor H is related to the displacement thickness δ^* and momentum thickness by equation (3.8).

$$\frac{d\varphi}{dx} + \varphi[\frac{2 - M_e^2 + H}{M_e(1 + \frac{\gamma-1}{2}M_e^2)}\frac{dM_e}{dx} + \sigma\frac{1}{r}\frac{dr}{dx}] = \frac{C_f}{2}sec(\theta) \tag{3.7}$$

$$H = \frac{\delta^*}{\varphi} \tag{3.8}$$

The original von-Kármán momentum equation is first modified by Stewartson's transformation [67]. These transformations define a relationship between the transformed-incompressible (H_{tr}, φ_{tr}) and compressible (H, φ) flow quantities. They are defined in equations (3.9) and (3.10), where T_e is boundary layer edge temperature and T_o is stagnation temperature. The relationship is semi-empirical and drawn from wind tunnel correlations, making this method an approximate technique to calculate boundary layer thickness.

$$H = H_{tr}(\frac{T_o}{T_e}) + \frac{T_o}{T_e} - 1 \tag{3.9}$$

$$\varphi = \varphi_{tr}(\frac{T_o}{T_e})^{\frac{\gamma+1}{2(\gamma-1)}} \tag{3.10}$$

The stagnation temperature is quantified by its relationship to the edge temperature (T_e) and edge Mach number (M_e) in equation (3.11).

$$T_o = T_e(1 + \frac{\gamma - 1}{2}M_e^2) \tag{3.11}$$

The final transformed von-Kármán momentum equation is presented in (3.12). Properties like transformed shape factor (H_{tr}), Mach number, local radius (r), wall angle (θ), and skin friction (C_f) become functions of axial distance. Some values, like edge Mach number (M_e), temperature (T_e), and pressure (P_e) are known from inviscid parameters calculated by the streamtracing routine. To find these quantities, it assumed the freestream flow is Mach 6, freestream stagnation pressure is 160 psia, and freestream stagnation temperature is 433 K. The transformed linear first-order ordinary differential equation takes the form outlined

in equation (3.13), where $P(x)$ and $Q(x)$ are grouped terms representing quantities only a function of axial distance.

$$\frac{d\varphi_{tr}}{dx} + \frac{\varphi_{tr}}{M_{\mathrm{e}}}(2 + H_{tr})\frac{dM_{\mathrm{e}}}{dx} + \sigma\frac{\varphi_{tr}}{r}\frac{dr}{dx} = \frac{C_f}{2}sec(\theta)(\frac{T_{\mathrm{e}}}{T_o})^{\frac{\gamma+1}{2(\gamma-1)}} \tag{3.12}$$

$$\frac{d\varphi_{tr}}{dx} + \varphi_{tr}P(x) = Q(x) \tag{3.13}$$

Additionally, the transformed shape factor can be computed through a relation that incorporates heat transfer effects when the Prandtl number deviates from unity. The transformed shape (H_{tr}), or boundary-layer form factor, is then related to the incompressible flow counterpart (H_{i}) with Crocco's quadratic for the temperature distribution in the boundary layer. This is shown in equation (3.14), where T_{aw} is the adiabatic wall temperature.

$$H_{tr} = H_{\mathrm{i}}(\frac{T_w}{T_o}) + \frac{T_{aw}}{T_o} - 1 \tag{3.14}$$

The adiabatic wall temperature is defined through a recovery parameter, which is dependent on the Prandtl number (Pr) of the flow. The recovery parameter is defined in equation (3.15) and the adiabatic wall temperature in (3.16).

$$\lambda \approx Pr^{1/3} \tag{3.15}$$

$$T_{aw} = (1 + \lambda\frac{\gamma - 1}{2}M_{\mathrm{e}}^2) \tag{3.16}$$

The compressible and incompressible skin-friction coefficients can also be related through the edge and reference temperature (T^*), as shown in equation (3.17). The method used Eckhert's reference temperature relation, which is equation (3.18) [100]. The wall temperature (T_w) is a a definable parameter.

$$C_f = \frac{T_{\mathrm{e}}}{T^*}C_{f\mathrm{i}} \tag{3.17}$$

$$T^* = 0.5T_w + 0.22T_{aw} + 0.28T_\mathrm{e} \tag{3.18}$$

Additionally, the shape factor of the incompressible flow can be calculated from the incompressible skin-friction value and shown to reduce into equation (3.19).

$$H_\mathrm{i} = \frac{1}{1 - 7\sqrt{C_{f\mathrm{i}}/2}} \tag{3.19}$$

Next, an approximate method developed by Kármán and Schoenherr to find the average incompressible skin-friction coefficient is introduced in equation (3.20). The relation is drawn from experimental relations and is for an approximately adiabatic wall condition. The semi-empirical relation uses the incompressible Reynolds number (Re_X), which is itself defined in equation (3.21). The skin-friction semi-empirical relation was found to be in good agreement with the data for Reynolds numbers in the range of $10^5 - 10^9$.

$$C_{f\mathrm{i}} = \frac{0.088(log_{10}\mathrm{Re}_X - 2.3686)}{(log_{10}\mathrm{Re}_X - 1.5)^3} \tag{3.20}$$

$$Re_X = [\frac{\frac{\mu^* \mathrm{Re}_x^*}{\mu_o}}{log_{10}\frac{\mu^* \mathrm{Re}_x^*}{\mu_o} - 2.3686}][\frac{(log_{10}\frac{\mu^* \mathrm{Re}_x^*}{\mu_o} - 1.5)^3}{(log_{10}\mathrm{Re}_x^*)^2} - 0.8686] \tag{3.21}$$

The viscosity term (μ) is definable through Sutherland's law, which is in equation (3.22).

$$\mu = 1.458 * 10^{-6}\frac{T^{1.5}}{T + 110.4} \tag{3.22}$$

The incompressible Reynolds number Re_X is defined in terms of a reference Reynolds number Re_x^* and a length-dependent Reynolds number Re_x. These relations are defined in (3.23) and (3.24).

$$\mathrm{Re}_x^* = \frac{T_\mathrm{e}}{T^*}\frac{\mu_\mathrm{e}}{\mu^*}\mathrm{Re}_x \tag{3.23}$$

$$\mathrm{Re}_x = \frac{P_\mathrm{e} M_\mathrm{e} x}{\mu_\mathrm{e}}\sqrt{\frac{\gamma}{RT_\mathrm{e}}} \tag{3.24}$$

Integration of the differential equation proceeds simultaneously with the evaluation of the axial-dependent quantities. Certain conditions may cause numerical instabilities, such as non-continuous boundary layer edge properties or near-zero Reynolds numbers. Sibulkin introduced a distance correction for the Reynolds number during the first integration step [101]. The distance correction is developed for wind-tunnel nozzles and incorporates the local wall radius (r^*) and radius of curvature (R^*) terms. This correction was similarly adapted for intake boundary layer developement along leading edges. The correction is shown in equation (3.25).

$$x^* = \sqrt{\frac{\gamma + 1}{2} r^* R^*} \tag{3.25}$$

The streamtracing design code incorporates smooth pressure transitions through shocks and uses the leading-edge correction to avoid numerical instabilities. All streamlines are transformed from a three-dimensional coordinate systems into two-dimensional systems to ease curvature and radial distance calculations. Edge properties are known everywhere and are fed into the Runge-Kutta solver. The calculated displacement thickness is applied in the outward normal direction of each local 2D curve for both the upper and lower surfaces. A 100% displacement thickness correction is used, although the percentage can be altered for future studies to study performance factors. A sample of a 100% correction is shown in Figure 3.21a. A sample boundary-layer displacement thickness calculation is shown in Figure 3.21b. The growing adverse pressure gradient causes a slight decrease in the displacement thickness near the throat.

The effect of the viscous correction procedure causes a deviation in the intake's internal area profile from area constriction due to the boundary layer on each streamline. The geometry change can be visualized with Figure 3.22a. The boundary layer also changes the expected throat profile. The corrected and uncorrected INlet throat profiles are shown in Figure 3.22b. Notice the boundary layer growth varies azimuthally due to length of the parent streamline, causing the effective wall to curve. Since straight walls are preferred for optical access, then a throat transition to a more adequate shape will be required.

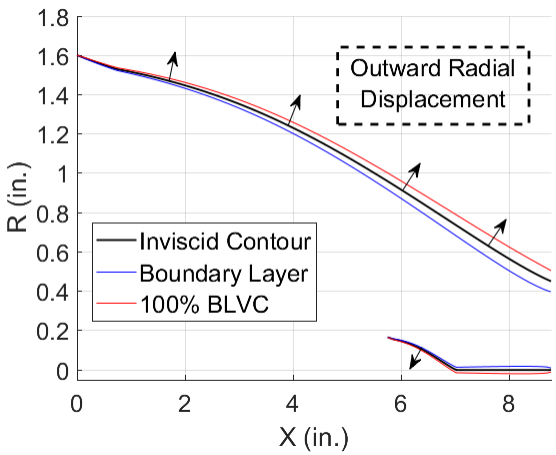

(a) Corrected and uncorrected streamlines.

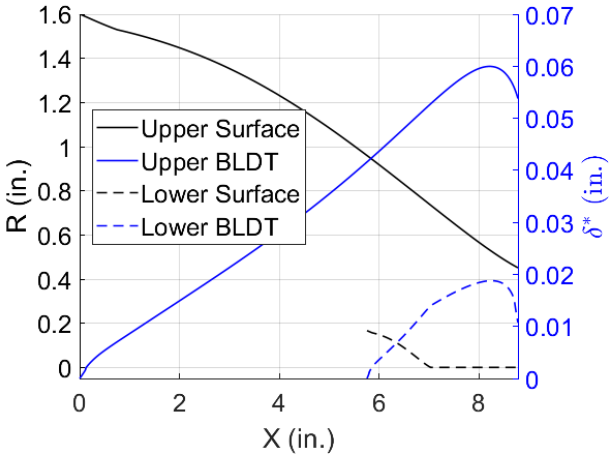

(b) Upper and lower surface BLDT profile.

Figure 3.21. Growth of a compressible and turbulent boundary layer along the 0°osculating plane of a 12% scaled INlet with a total pressure of 160 psia.

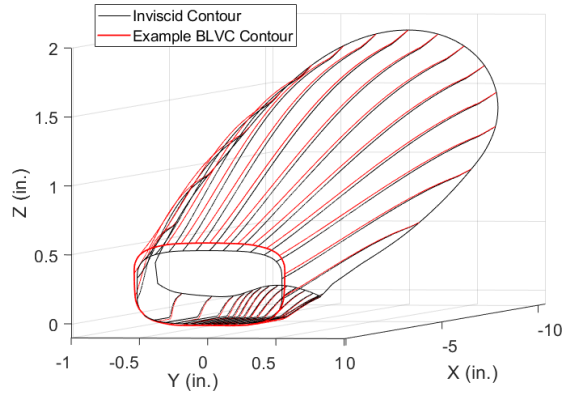

(a) Isometric view of an applied BLVC.

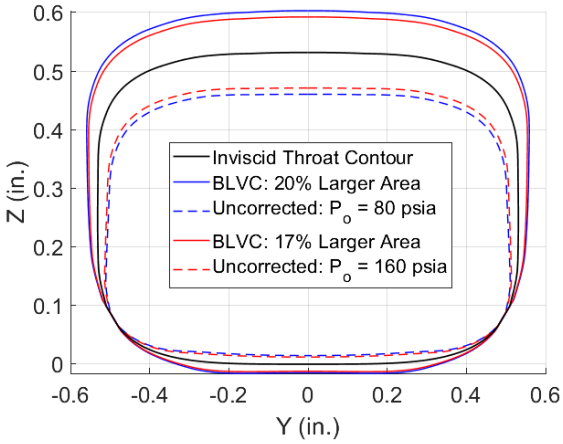

(b) Corrected and uncorrected throat profiles.

Figure 3.22. Geometry changes for a 12% scaled model with applied BLVCs.

3.9 Throat Transition

The viscous correction procedure displaces the original position of the inviscid streamlines at the intake throat. Since the streamlines vary in total length, the total displacement thickness at the throat varies along each osculating plane. This creates a highly non-uniform throat profile that deviates from the planned rectangular isolator shape. To rectify this

issue, a mathematical function was defined to transition the throat profile into a geometry suitable for experiments. Straight walls in the isolator were a paramount design driver, as they allow flat windows to provide optical access for schlieren, pressure-sensitive paint (PSP), and temperature-sensitive paint (TSP) studies. The reference throat geometry is presented in Figure 3.23.

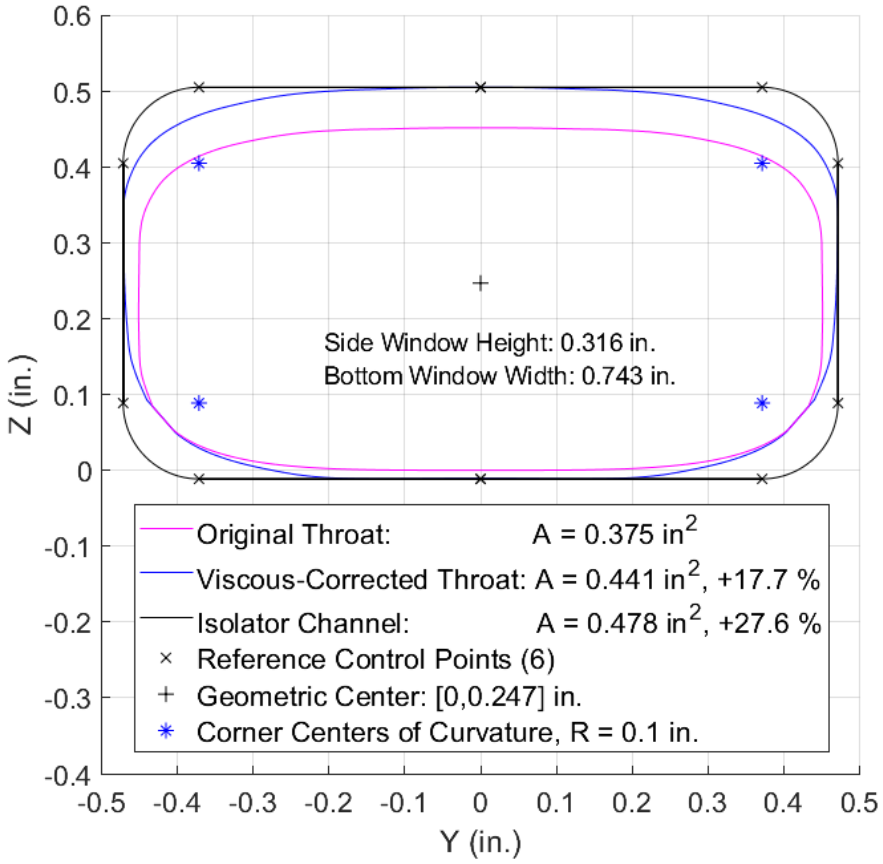

Figure 3.23. The defined throat transition with flat sidewalls in the isolator for future optical studies.

The new throat geometry is defined by the maximum width and height from the viscous-corrected throat. Control points are extended outward to create the straight walls, and the corners are rounded from a circular-arc function. The geometric center is defined and expanding rays are drawn to intersect the inner and outer shape (Figure 3.24). The coordinates

of these points are recorded. Point coordinates along the same ray will be blended together to create a shape transition.

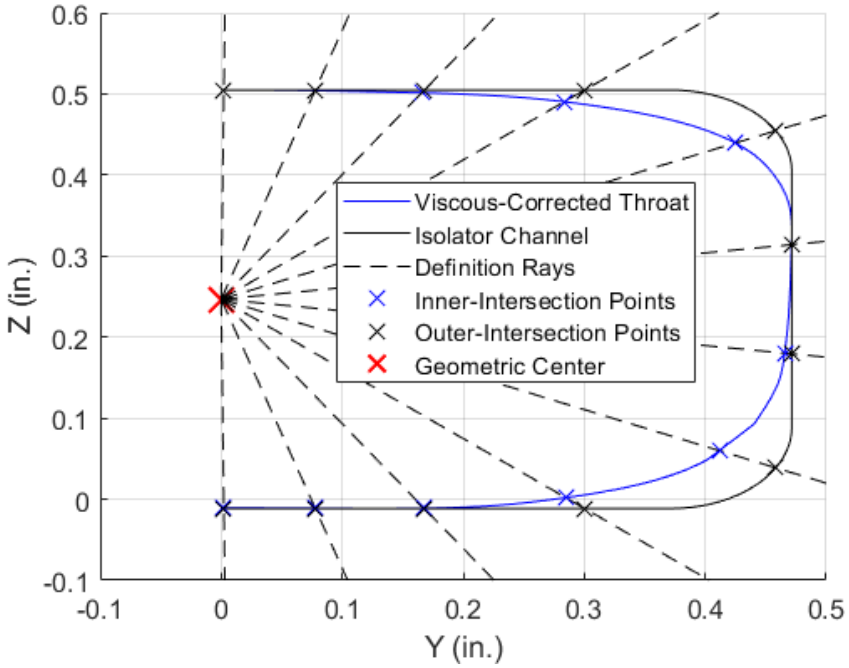

Figure 3.24. Drawn rays that will define the mathematical transition between the intake and the isolator for a 12% scale model.

The shape transition between the viscous-corrected throat and the final control shape is accomplished through a smoothing function. This mathematical relationship was used by Smart in the generation of the REST intake for shape transition [79], [94]. It smoothly transitions one real-valued parameterized curve into another. The aggressiveness of transition is handled by a user-defined exponential factor (α). These equations were modified to blend the Y-Z throat components into each other over a specified axial distance. For future studies, the first and second derivative of the throat and intake surfaces can be matched. The viscous-correct throat coordinates are grouped in f_{vct} and the reference geometry throat coordinates into f_{rgt}. The smoothing function $E(x)$ specifies the amount of transition per axial slice moving downstream. These functions are presented in equations (3.26) and (3.27).

$$f(x,y,z) = [f_{vct}(y,z)]^{1-E(x)}[f_{rgt}(y,z)]^{E(x)} \tag{3.26}$$

$$E(x) = (\frac{x - x_{vct}}{x_{vct}})^{\alpha}, \alpha > 0 \tag{3.27}$$

The final three-dimensional points are then saved into excel-csv files for export into both CAD and CFD meshing programs. A visual representation of the transition is shown in Figure 3.25. The shape transition can also be analytically defined based on a polynomial fit along each angular ray. It is up to the designer to specify what type of fit best matches the generated transition. This will depend on the amount of axial slices and the aggressiveness of the transition. For this case, a linear interpolation was defined ($\alpha = 0.5$). The coefficients of each curved-fit polynomial are also exportable via csv-file for analytic surface replication.

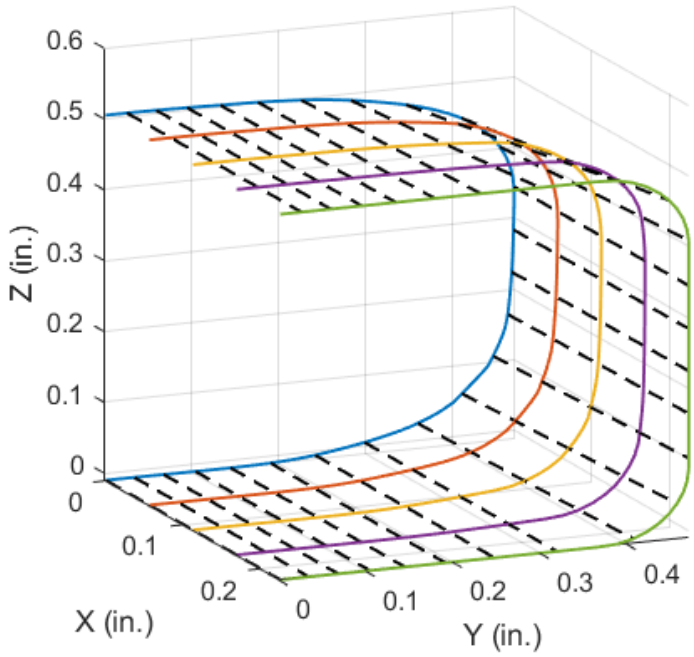

Figure 3.25. Isometric view of the throat transition region with starting shape, ending shape, and three intermediate axial profiles.

3.10 Intake Sectional Profile

The INlet's unconventional shape-transitioned design means the amount of flow contraction must be accurately estimated. The intake's captured streamtube is compressed by several 2D conical flowfields. Each flowfield provides a different amount of isentropic

compression and flow turning. To better quantify the rate of streamtube compression, the intake's effective capture area is computed from the leading edge to the throat, which is displayed in Figure 3.26. This axial streamtube constriction is separated into four major regions. These are called the external contraction, mixed contraction (cowl region), internal compression, and throat region. The leading edge of the external compression region dictates shock placement. The cowl region captures the leading shock wave and allows for flow spillage at off-design conditions. The internal compression region is critical for self-starting ability, and the throat region transitions the intake into the defined isolator shape.

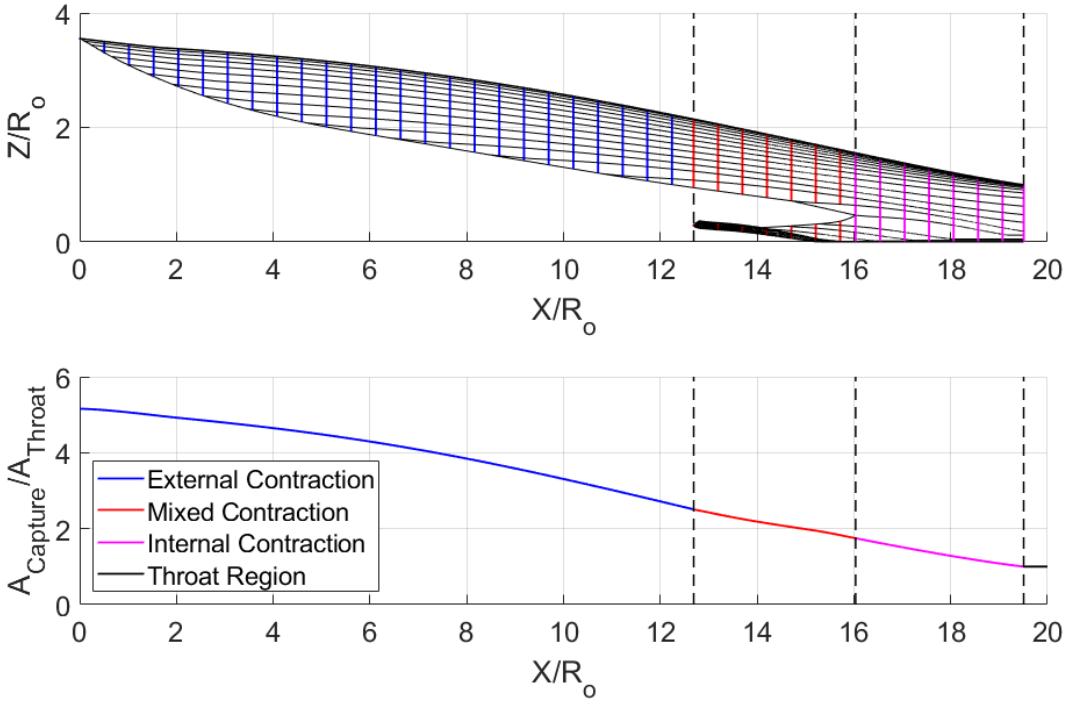

Figure 3.26. Side view and contraction profile of the inviscid-uncorrected INlet.

3.11 Intake Starting Limits

An important part of the design process is to verify that the final geometry can start under a Mach 6 freestream condition. As a first-order estimate, the Kantrowitz limit is used as a conservative baseline to estimate the possibility that the intake will a establish supersonic core flow within the isolator. To do this, the streamtracing code determines the

start of the internal contraction, which is where the flow can no longer spill overboard. This region is usually called the cowl-region of the intake. The INlet has two cowls, and flow can spill from either side of the intake. The area ratio between the cowl and throat regions is then calculated. Also, the Mach number at the cowl is computed from a 1D area-averaging technique from all osculating planes. Using these quantities, the intake is mapped onto a startability plot with cowl Mach number computed from an analytical technique and two CFD solution sets (Figure 3.27). While the intake exceeds the Kantrowitz criterion, it is still above many empirical relations for 3D intakes. From this data, it was determined that the intake would have a high probability to self-start at the design condition.

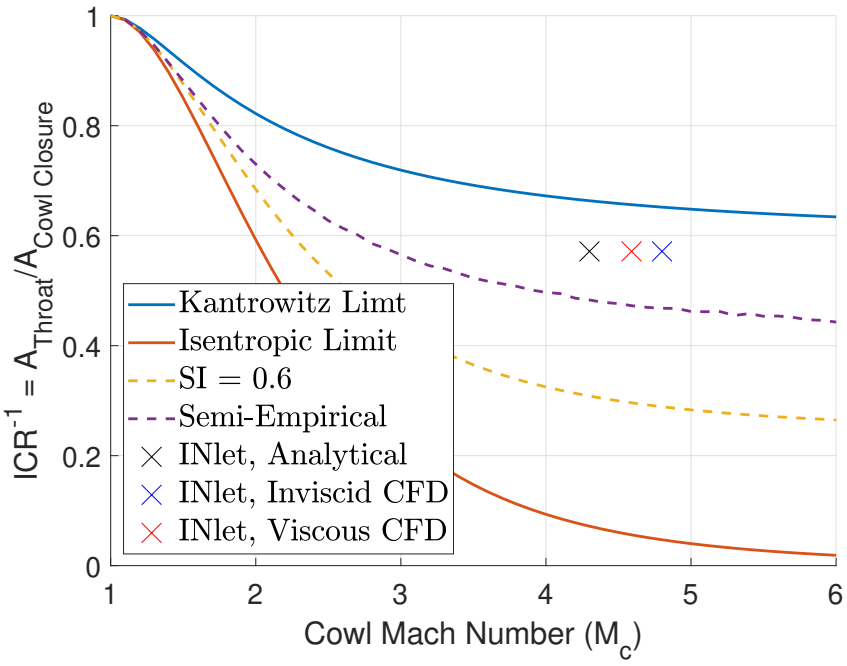

Figure 3.27. Starting contraction limit of the INlet.

3.12 Blunting Methodology

The streamline-tracing program creates inviscid contours with infinitely sharp leading edges. To make the contours better represent an inlet with real world thickness, a blunting tool was created for users to define a specified leading edge radius for all upper and lower surface streamlines. A blunting method developed by O'Brien sought to preserve the original

total contraction ratio of the intake [58]. This method shifted and recalculated the parent flowfield by a specified amount dictated by the leading edge radius and leading truncation deflection angle. Additionally, the blunting edge was defined based on a tangent condition to the leading points on the contour. The stagnation streamline, which impacts the blunt leading edge, would coincide at the same location as the inviscid, sharp contour starting position and preserve contraction ratio between streamlines. Unfortunately, integrating this method into the streamtracing code was computationally expensive and complex. Additionally, for small leading edge radii, the change in total contraction ratio is minimal. A similar method was implemented that did not re-solve the parent streamline but did preserve the blunted tangency condition. This analytical technique was key to avoiding CAD complexities stemming from rounding swept leading edges. The O'Brien method is shown in Figure 3.28 and shows the difference in parent flowfields. Note how the blunt leading edge is parallel to the intake contour and not the freestream stagnation streamline.

The blunting construction method creates an arc which attaches to the intake surface at the same inclination as the local streamline. This means that the arc is tangent to the local contour. This blunting function ensures that CAD geometries and CFD programs process the same blunt geometry as it was analytically defined. An arc or spline profile, containing several points in 3D space, is exported to these programs. For consistency, a 0.04 inch blunted leading edge was defined on all INlet model scales. This method was especially useful because the leading edge for each streamline was inclined at 6° relative to the freestream due to the inherent ICFA contour deflection.

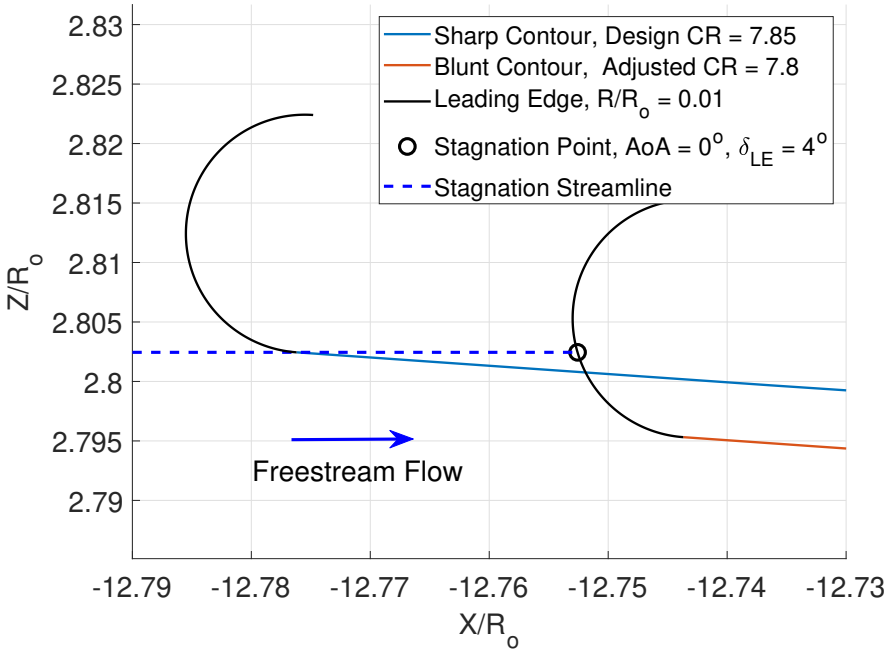

Figure 3.28. Leading edge blunting methodology taken from O'Brien et al. [58].

3.13 Outer Mold Line Definition

The outer-mold line (OML) of the intake can also be specified for easier surface generation in CAD programs. The frontal profile of the INlet is circular-like, so an elliptical OML can be defined around the geometric center of the inlet capture shape. The parametric parameters for the INlet are shown in Figure 3.29a. An ellipse was chosen as the best-fit shape to enclose the downstream body. The OML ellipse is defined by the maximum width and height of the frontal INlet shape. There is a noticeable amount of extra material near the intake throat region. This extra material is later used for fasteners and guide pins. These points are exportable via excel csv-file to define a spline-fit in CAD for the mechanical design. A reference CAD image in Figure 3.29b shows the final frontal profile of a 12% INlet model based from the imported spline profiles.

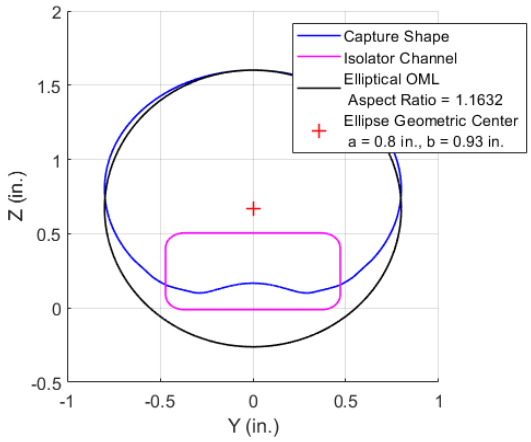

(a) Parametrically defined OML.

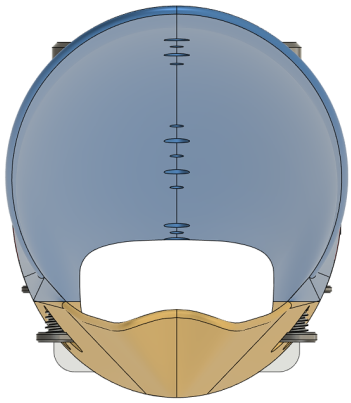

(b) Frontal profile of the 12% CAD model.

Figure 3.29. Frontal view of the INlet elliptical outer-mold line.

3.14 Data Post-Processing

Since thousands of points are stored for each plane, a resampling-downsampling script takes the solutions curves and makes them manageable for export. The resampling function takes input contours with non-linearly spaced vectors and outputs clean geometric vectors with equal spacing in the axial-direction. Equidistant axially-spaced vectors improve geometric mesh creation in CFD programs and spline formation in CAD programs. The downampling script simply reduces the total amount of stored points to a manageable amount. Leading edge and throat point locations are recorded separately to avoid edge-aliasing from the resampling filter. The designer must accept some resolution loss when implementing these sampling techniques.

The fidelity of the IML depends on the physical scale of the geometry and possible machining tolerances. The geometric vectors are saved into table format for excel csv-file export. Excel tables are transferable into CAD programs to create point clouds. Community developed tools in Autodesk Fusion 360 allow designers to import csv-files for spline generation from point clouds. Figure 3.30 shows how the inward-turning surfaces of the inlet are defined from spline point profiles. The splines are lofted together to create surfaces which are then converted into solid objects. A set of splines can be automatically imported and lofted to form the inner contoured-wall of the inlet. The same point cloud can be passed into an i-j-k

format converter, which allows different CFD software to reconstruct the original streamline surfaces.

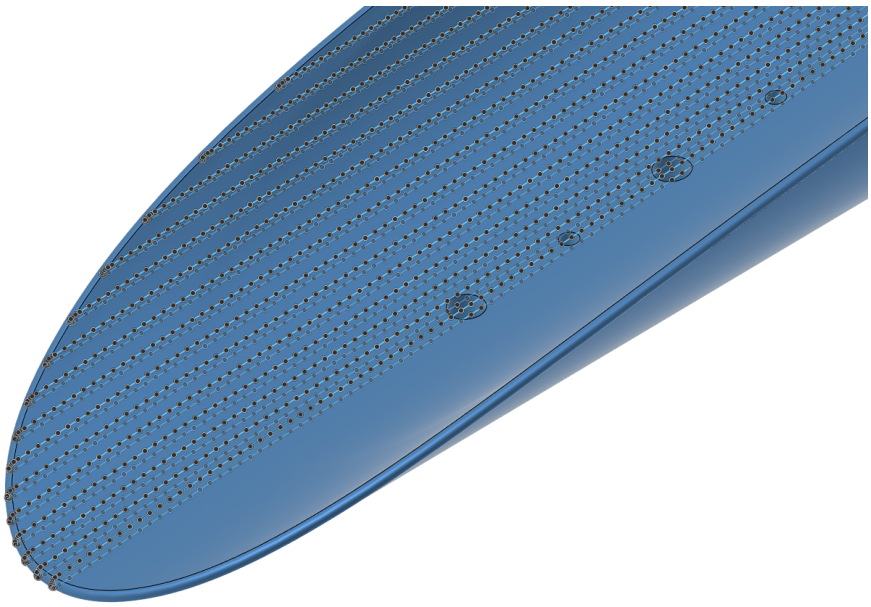

Figure 3.30. Splines used for swept-surface model generation in Autodesk Fusion 360.

3.15 Overview

The code inputs are split into geometric shape and freestream flow properties. For geometric shape, intake and isolator shapes are generated by specifying individual superellipse exponential-factors and aspect ratios. Additionally, the user can define a target total contraction ratio. The total contraction ratio may vary substantially after a full geometric iteration, so a check must be made to re-calculate the total CR on all final inlets. The lower surface frontal projection is usually much larger than the approximated straight-line projection. It might be useful to guess a total CR 15%-25% larger than the design CR to speed convergence if it is a design parameter. The leading edge deflection angle, which specifies the strength of the leading shock, must also be defined by the user. A centerbody offset term is also definable to alleviate convergence issues. However, this term does not play a role in the intake or isolator projected cross-sectional shapes. An overview of the code block diagram is shown in Figure 3.31. It outlines the high-level view of the triple iteration loop

that is computed for each osculating plane. It is expected that hundreds of Taylor-Maccoll calculations are performed during the creation of a new inlet geometry. A blunting tool is available for exporting curves into CAD software and does not play a part in the inlet iteration process. The total inlet can also be independently scaled after construction. The scaling process preserves the specified leading edge radii. However, the viscous correction procedure is length dependent and must be run for each new model scaling.

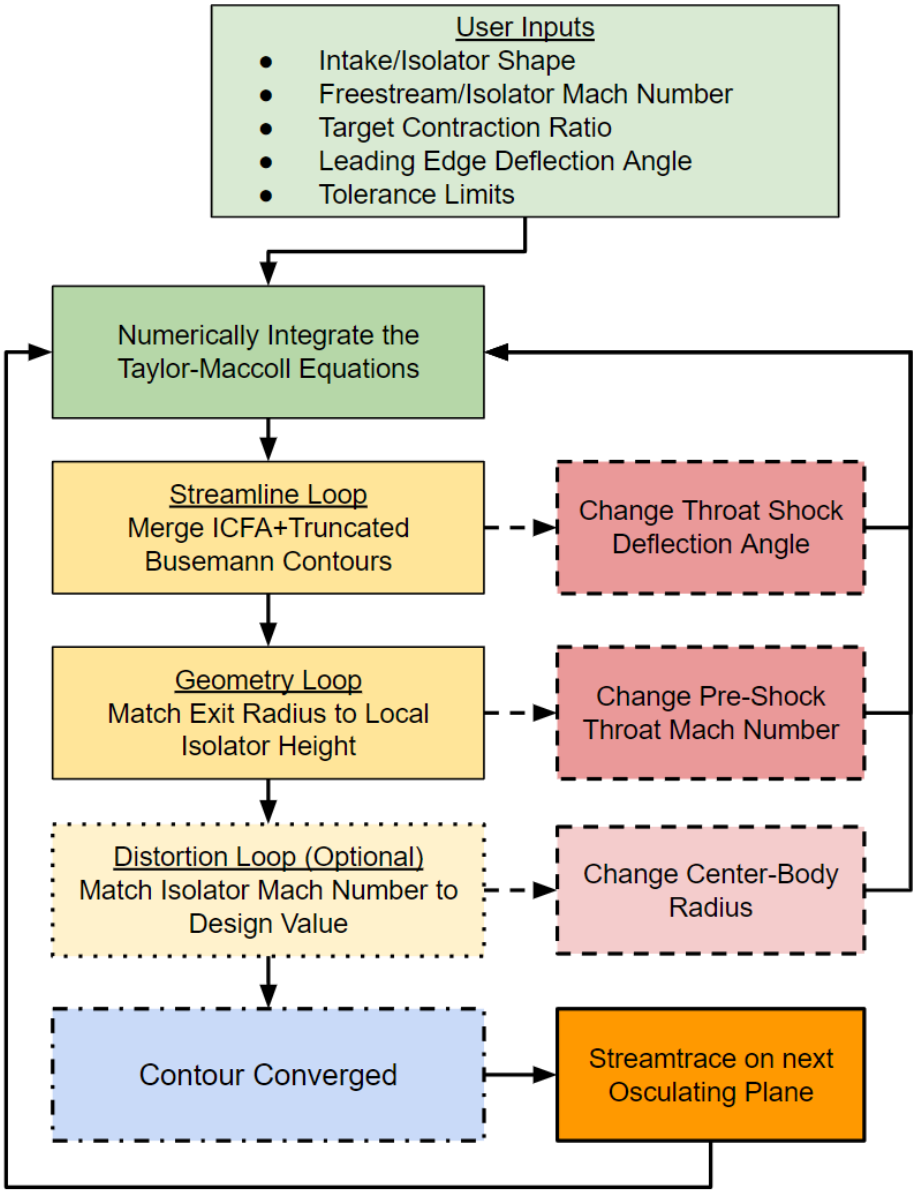

Figure 3.31. High level code block diagram of the streamtracing routine.

User defined flow properties include freestream Mach number and a targeted isolator Mach number. The isolator Mach number does not play a role if the optimization process is not activated. The optimization procedure varies throat Mach number for each osculating slice, potentially allowing for a more uniform Mach profile at the throat. Tunnel stagnation pressure and temperature can also be used to calculate inviscid pressure distributions and temperature profiles. These are useful for calculating boundary-layer edge properties which can be used to estimate boundary layer thickness along the intake shape. Tunnel conditions also play a role in calculating other inviscid criteria such as total inlet mass flow rate, total pressure recovery, and inlet efficiency terms.

The Matlab streamtracing routine iterates on several solution sets to achieve a desired convergence criteria. The radial distances and offsets, which are the geometric targets, are arbitrarily defined based on the given shape. This means that the code can be modified to create external geometries, such as waveriders, or more complex asymmetrical intake shapes. These additional capabilities were not pursued for the current project. The current streamtracing routine file contains over 6,000 lines of code.

4. INTAKE FLOWFIELD ANALYSIS

The streamtracing design code contains several analysis tools that can be helpful for determining the theoretical upper-limit of inlet performance. It contains several functions that can determine shock locations, internal pressures, and inviscid efficiency parameters. These analytically-based tools are then compared against CFD results to determine areas of performance loss. Although internal pressure data was taken from a blockage model test campaign, the blockage models are not representative of the final geometry, which includes a different throat transition, a smaller lower capture surface, and an applied viscous correction. Thus, blockage model test results are separately presented in Chapter 6.

All analysis tools developed in the streamtracing design code assume an on-design, steady-state condition for a Mach 6 freestream flow at 0° AoA. Any static pressure or static temperature values will inherently assume a nominal wind tunnel stagnation pressure of 160 psia and a total stagnation temperature of 433 K. The inviscid 3D CFD results are computed with the Create-AV Kestrel code [102], [103]. For viscous computations, the Spalart-Allmaras Turbulence model was used and the boundary layer was considered turbulent everywhere on the intake surface. The computations were performed by graduate student Andrew Shuck from Dr. Jonathan Poggie's computational group at Purdue University. More details on the computational methods, including a grid convergence study, are presented in Noftz et al. [93]. The input parameters for the CFD solution are presented in Table 4.1. Parts of this chapter also appear in AIAA's 2022 SciTech conference proceedings from the same paper. A version of this chapter and the 2022 SciTech paper are pending publication by the AIAA Journal of Propulsion and Power.

Table 4.1. CFD input flow conditions.

Flow Parameter	Value
Mach	6
Freestream Velocity	873 m/s
Freestream Pressure	480 Pa
Freestream Temperature	52.8 K
Unit Reynolds Number	8.08E6 /m

4.1 1D Performance Quantities

Streamtube analysis is a common method for evaluating intake performance. The captured streamtube is compressed from the area contraction provided by the intake. Since the geometry and incoming flow properties are known, the state of the streamtube can be tracked throughout the length of the intake. The analytical technique assumes a shock-on-lip condition, where the incoming flow is always swallowed. This 100% mass capture assumption is a first-order estimation of the intake's upper-bound of operation. The main streamtube can be divided into several smaller streamtubes defined from the frontal area projection between osculating planes (Figure 4.1). The total amount of compression from each streamtube is tracked as it passes into the inlet. For reference, CFD quantities are presented alongside the analytical prediction to determine loss mechanisms, which may occur to shock misalignment, viscous effects, or flow spillage.

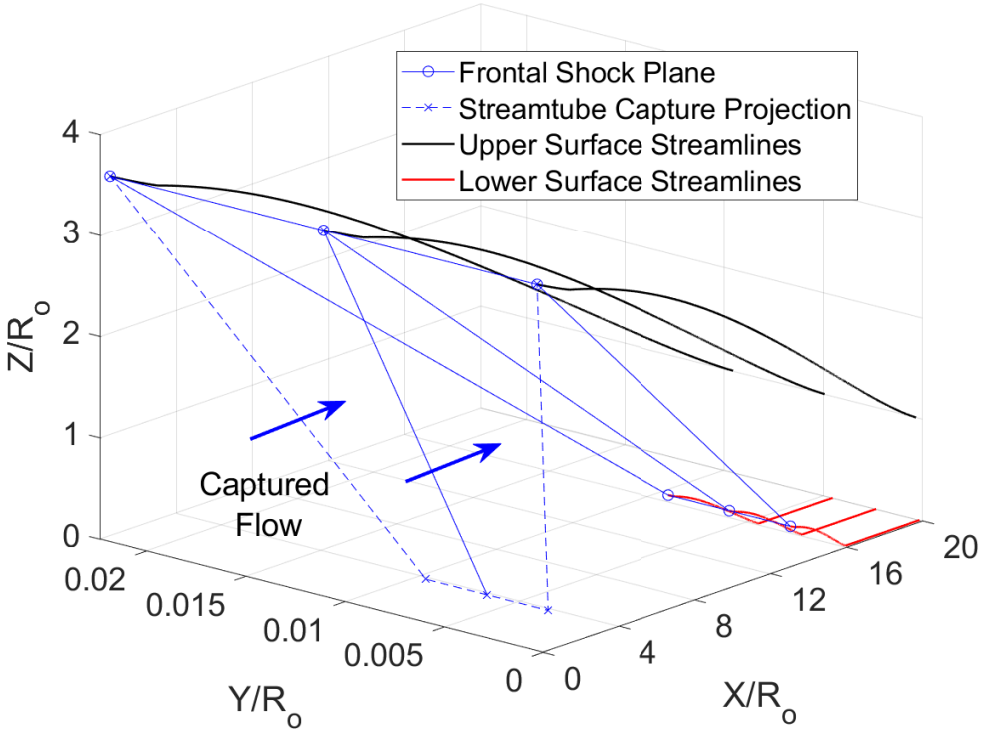

Figure 4.1. Example of streamtube discretization between osculating planes for the area-averaging analysis method.

There are several quantities of interest that provide insight to the behavior of the intake. Table 4.2 compares quantities from the analytical method with CFD derived values. Certain parameters, such as compression ratio and pressure recovery, are common quantities to determine how well the intake compresses the flow while mitigating losses. Viscous effects and shock misalignment usually act to reduce total pressure recovery under real-world conditions. Additionally, mass capture efficiency is important for determining possible losses due to flow-spillage for the on-design condition. The full 3D INlet was analyzed with inviscid analytical techniques, inviscid CFD, and viscous CFD solutions. The analytical technique provides an upper-limit on intake performance since it does not account for viscous or flow spillage effects. From these solutions, the self-starting performance and other flow compression efficiency parameters can be estimated. The analytical technique calculates 1D flow quantities through an area-averaged approach. Flow along each streamtube is appropriately weighted based on its frontal capture area in the streamtracing routine. Quantities taken from CFD results are calculated from an area-averaged approach.

The compiled list of quantities calculated from the different methods are shown in Table 4.2. It is immediately noticeable that the analytically computed compression ratio drastically over-estimates the CFD results. Loss of compression hints at on-design flow spillage, which is verified by the mass capture efficiency parameter. Nearly 20% of the incoming streamtube's massflow is exiting the intake before the start of the internal contraction. Possible loss mechanisms are discussed later in this section. Additionally, the viscous compression ratio is larger than the inviscid CFD compression ratio. The formation of a boundary layer acts to constrict the intake's core flow, which increases the pressure rise while decreasing cowl and throat Mach numbers. The studied INlet model does not have a viscous-corrected surface profile.

4.2 Streamtube Pressures

The compression of the ingested streamtube is an important quantity that ensures the intake is effectively capturing and decelerating flow. It is possible to track the captured streamtube and its compression level over the length of the intake. A visual representa-

Table 4.2. 1D Flow quantities taken at the intake's throat.

Flow Property	Symbol	Analytical	Inviscid CFD	Viscous CFD
Compression Ratio	P/P_∞	23.73	9.50	11.10
Total Pressure Recovery	$P'_\circ/P_\circ$	0.93	0.86	0.69
Cowl Mach Number	M_c	4.30	4.80	4.59
Throat Mach Number	M_3	3.38	4.09	3.60
Mass Capture Efficiency	$\dot{m}_{captured}/\dot{m}_{throat}$	1.00	0.83	0.80

tion of the ingested streamtube is provided in Figure 4.2. To accomplish pressure tracking, an analytical technique solves the locations of isobars for a purely conical flowfield in each osculating plane. The intersection point of the isobar with each downstream axial slice determines the pressure value for that point. Using this method, a structured grid is created for each slice of the axial flowfield. The pressure field is constructed from grid points with equal spacing and a constant amount of points per normalized unit distance. This prevents the skewing of results during averaging calculations. Since no Busemann isobars ever pass the conical throat shock in asymmetric flow, the method only estimates axial pressures up to the leading edge of the conical throat shock. To simplify calculations, Mach reflections and interactions are neglected. Thus, the calculated flowfield will deviate from CFD predictions downstream of the lower capture surface. However, the calculation still provides a first-order approximation of predicted pressures within the external contraction zone. To calculate streamtube pressure ratios from CFD solutions, several axial slices are defined in Tecplot. Freestream pressures are filtered out from the axial slices to isolate the compressed streamtube. The pressures slices are then averaged through a area-weighted approach and plotted from the leading edge to the throat.

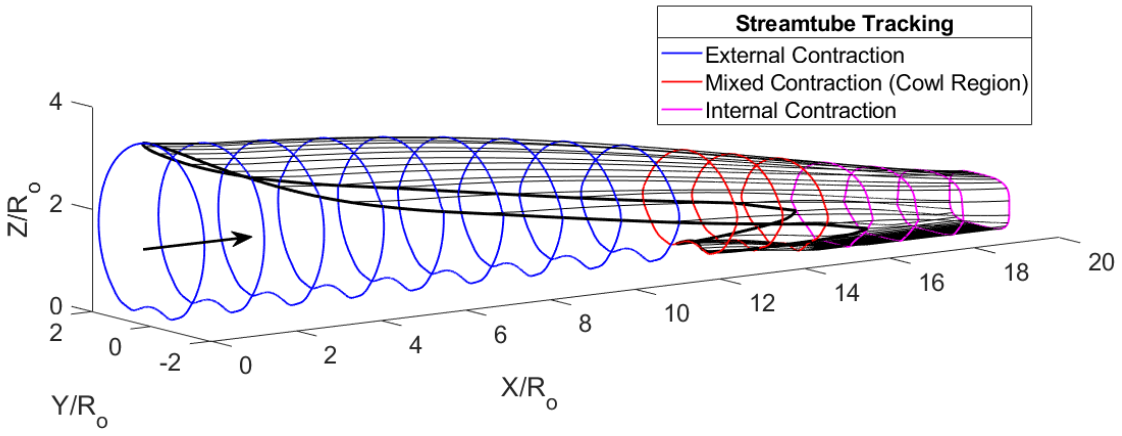

Figure 4.2. Streamtube constriction within the INlet.

A comparison plot of the calculated streamtube pressures are shown in Figure 4.3. The external contraction section shows gradual compression of the captured streamtube for all solutions. The analytical solution over-predicts the pressure rise through the leading oblique shockwave. However, the CFD solutions eventually exceeds the analytical prediction before the end of the external contraction. Interestingly, the CFD solutions show a plateau in pressure rise in the mixed contraction section while the analytical solution predicts a steep pressure rise. It is likely that the intake is failing to contain the streamtube, and it is escaping overboard in this region. Once the streamtube is ingested into the internal contraction, the pressure begins to rise considerably. The delay in the expected pressure rise is one reason for the loss in overall compression from the CFD results.

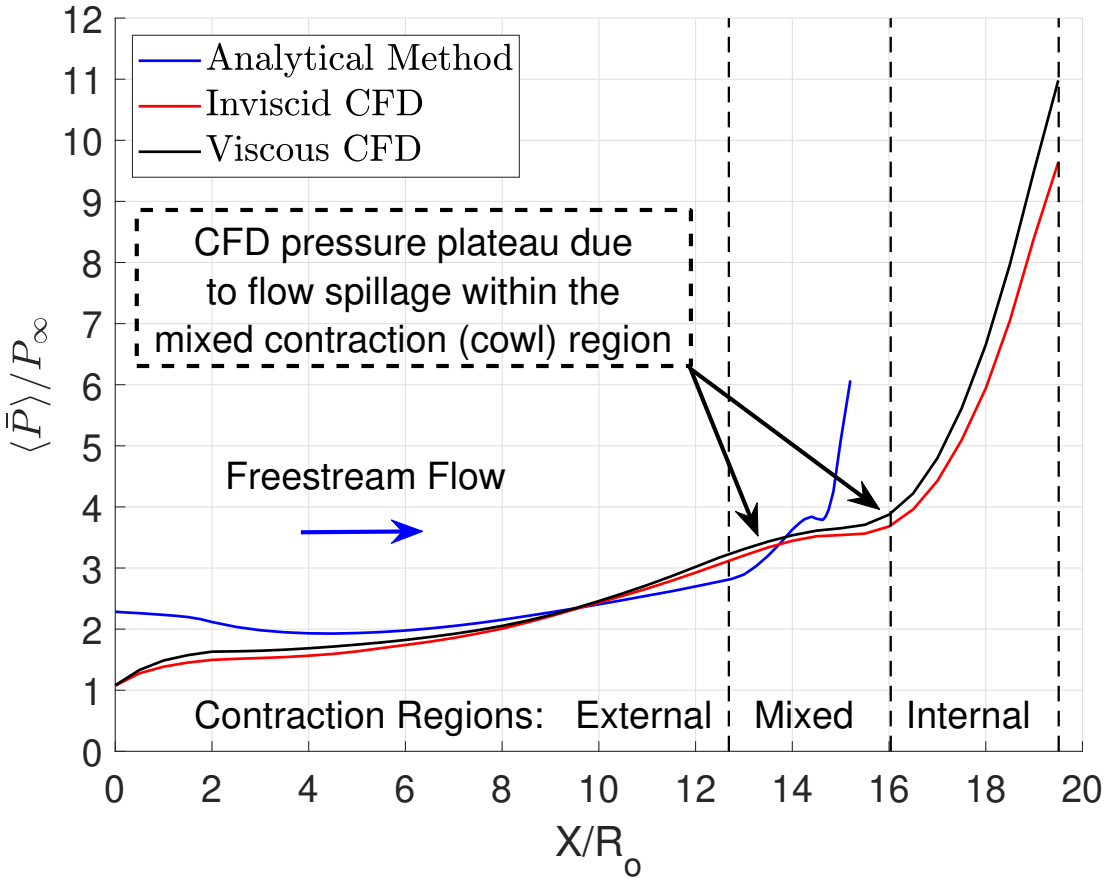

Figure 4.3. Captured streamtube compression as a function of distance from the leading edge with area-averaged and time-averaged reported pressures.

Instead of analyzing streamtube pressures, the surface pressures along different azimuthal rays can be extracted for comparison. The centerline 0° osculating plane streamline was used as a baseline case in Figure 4.4. The analytical, inviscid CFD, and viscous CFD pressure ratios were plotted as a function of distance from the leading edge. Theory compares well with CFD solutions in the external contraction region up to $X/R_\circ = 10$. After this, a rapid drop in surface pressure is observed through the internal contraction section. The pressure loss mechanism is due to a break-down in osculating axisymmetric theory that is described later in this section. The inviscid CFD calculation also predicts a drop in pressure near the throat. This is due to a corner expansion from the throat shock missing the throat shoulder. Downstream CFD pressures flucuate due to shock impingement on the isolator wall.

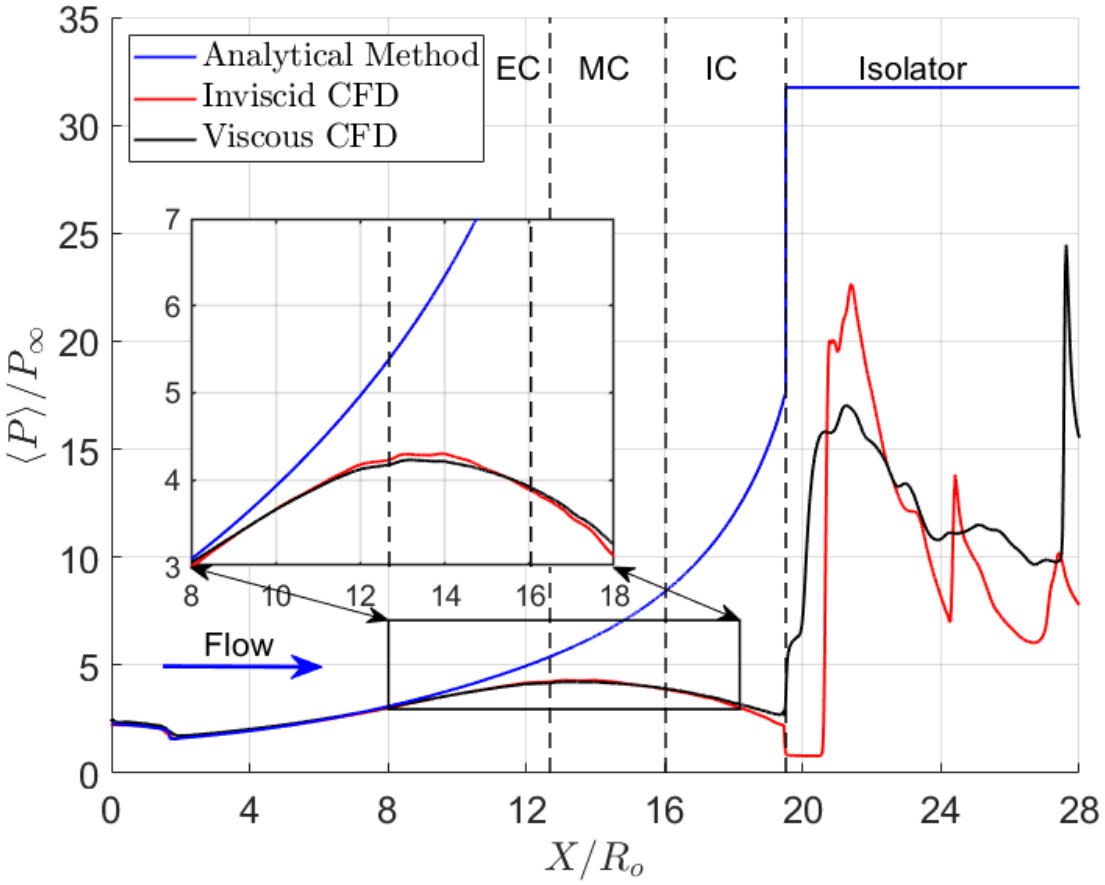

Figure 4.4. Time-averaged surface pressure ratios along the 0° osculating plane from three separate solution sets.

4.3 Flow Property Profiles

The flow properties of each streamline are known from the solutions to the Taylor-Maccoll equations. As such, it is easy to recreate wall profiles of flow quantities for the entire compression surface. Also, since the isentropic compression waves are trackable by the streamtracing routine, axial slices and cuts of the flowfield can be made for qualitative or quantitative comparison to computational results. Although raw results are in the form of Mach number, this quantity is easily convertible into pressure ratios or temperature ratios from the isentropic relations for a compressible gas. If freestream stagnation properties are known, such as pressure or temperature, then these ratios can be converted into static pressure and static temperature fields.

4.3.1 Inviscid Wall Profiles

The surface Mach number profile for the intake surfaces are known from the analytical method and inviscid CFD solution. The frontal profile of these contours is presented in Figure 4.5. The analytical and CFD profile show a clear gain in Mach number at the ICFA and truncated Busemann merging point for all osculating planes. The strength of this expansion also appears consistent for all osculating plane angles. However, the Mach profiles near the throat deviates significantly. The CFD solution shows Mach 5 flow at the throat shoulder, while the analytical technique shows Mach 3.5 flow near the throat region. It appears that the CFD throat shock misses the throat shoulder, causing flow corner-turning and expansion at the throat. This is caused by a shallower shock angle, which is observable in Figure 4.10 since the shock enters the isolator. A complex bow shock in the cowl region is also noticeable in the CFD solution.

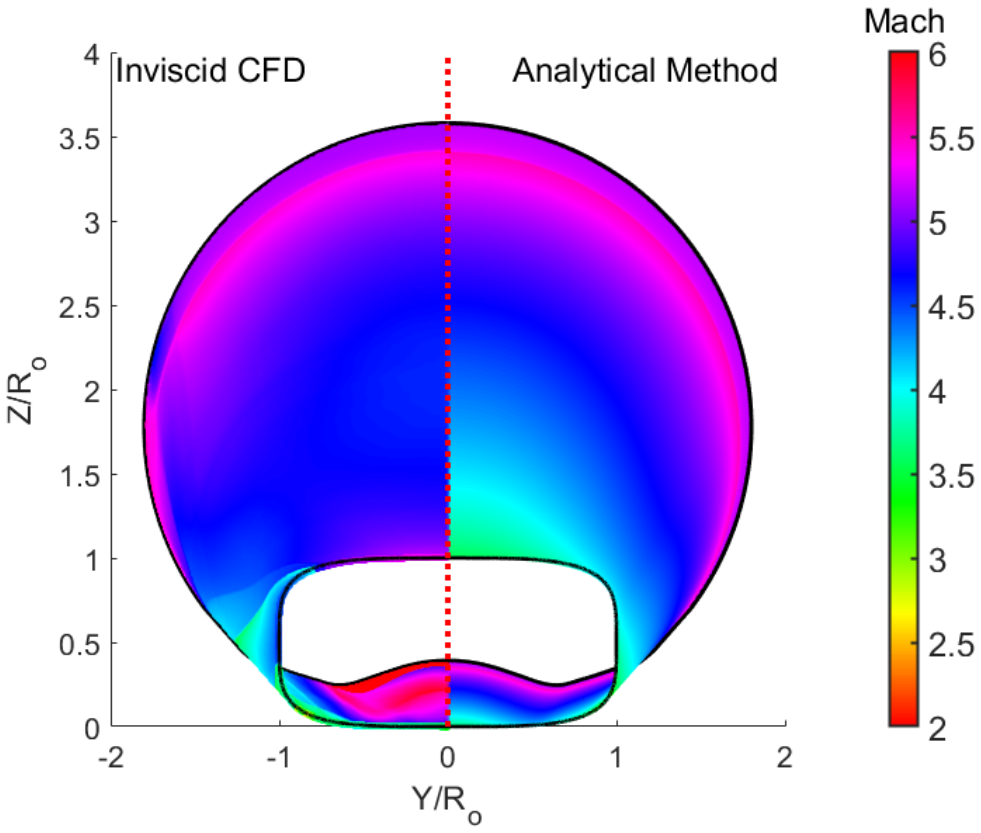

Figure 4.5. Surface Mach number profile for both the analytical method (right) and the CFD solution (left)

A frontal pressure profile of the intake is presented in Figure 4.6. The logarithmic colorbar reveals a steep change in the predicted pressure ratios near the throat. This loss of compression may be due to large azimuthal pressure gradients that violate osculating axisymmetric theory. The osculating plane streamlines near the centerline are predicted to provide the most flow compression. This means the high-pressure flow would travel to regions of lower pressure, which are the osculating planes along the edge of the intake. Such pressure gradients would route the flow overboard in the mixed contraction "cowl" region of the intake.

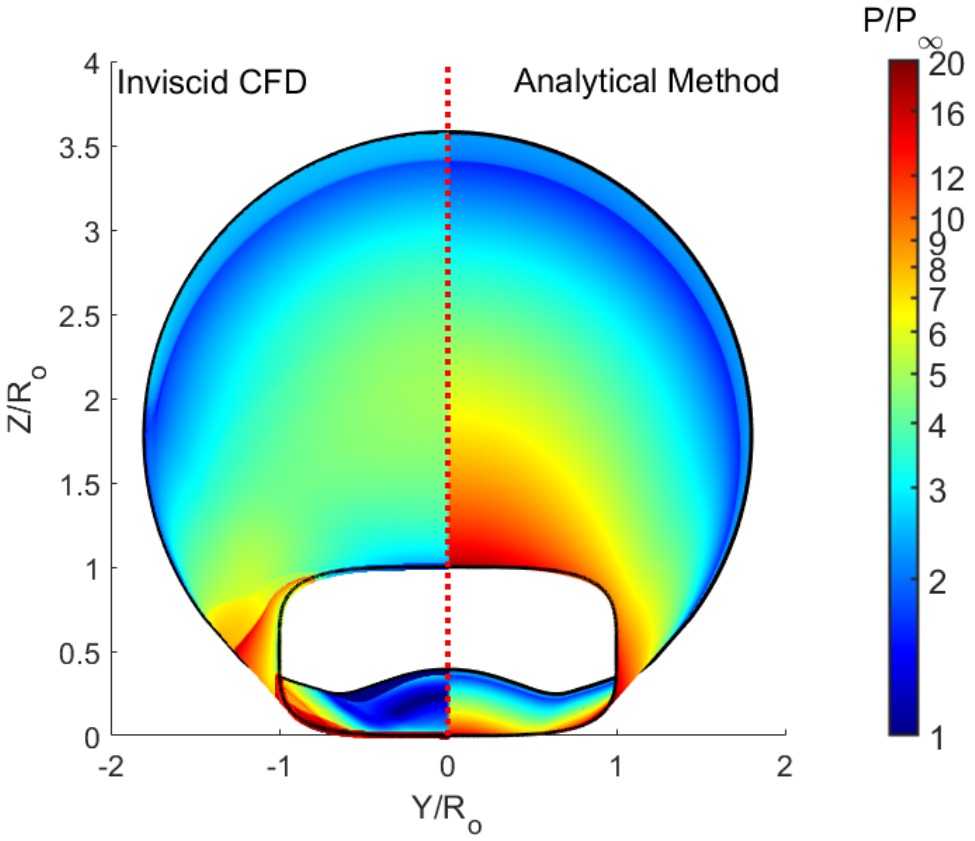

Figure 4.6. Surface pressure ratio profile for both the analytical method (right) and the CFD solution (left)

The osculating axisymmetric assumption assumes that no azimuthal pressure gradients exist between 2D slices of the flowfieled. There is reason to expect a break-down of this assumption as the expected pressures along nearby streamlines start to diverge. This quantity can be analyzed by comparing the relative error between the analytical and inviscid CFD

solutions, which is plotted in Figure 4.7. Under-prediction of surface pressures is shown by a positive gain in percentage, while an over-prediction is shown by a negative gain in percentage. The colorbar scale is limited from -100% to +100% on the plot to exaggerate the difference in solutions. A loss of pressure is present near the intake's throat in the internal contraction region. Meanwhile, there is a gain in expected pressure near the cowl region along the steepest osculating plane solutions. A possible reason for this difference is a gain in shock strength near the cowl region. A gain in shock strength would cause the shock shape itself to change, which would then allow flow spillage.

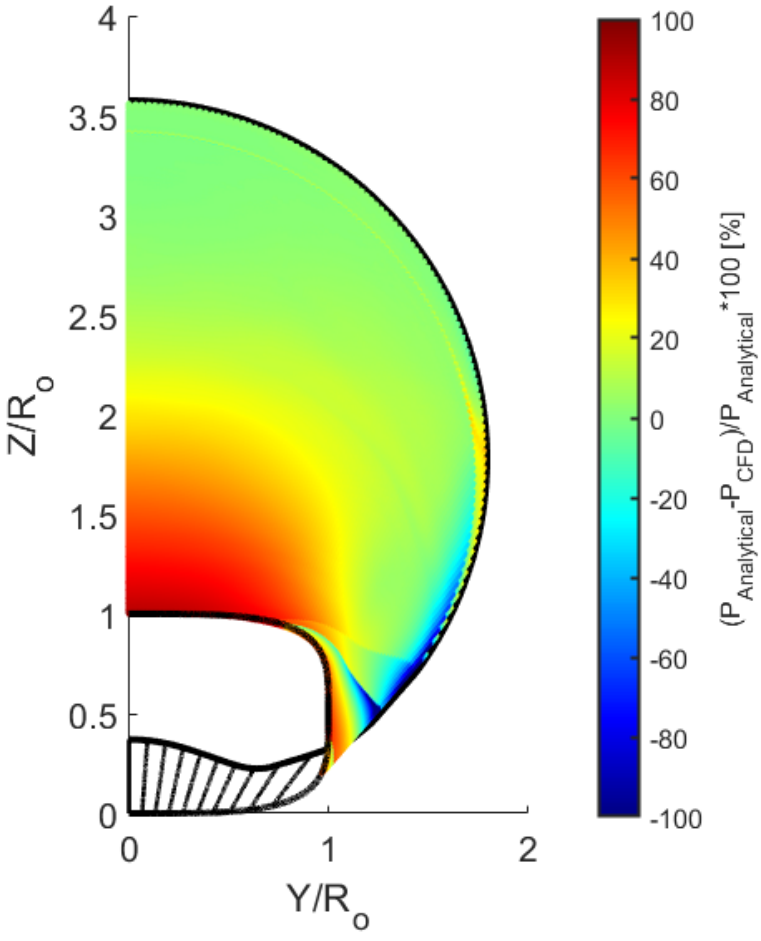

Figure 4.7. Percentage difference in pressure ratios between inviscid CFD and anayltical techniques from -100% to +100%

4.3.2 Inviscid Slice Profiles

Three-dimensional flow features can be deduced from the axial Mach slices presented in Figure 4.8. These axial Mach profiles provide insight into the compression process of the intake. The analytically predicted shock waves are shown on both plots as reference. The analytical solution shows high flow uniformity near the throat with the exception of the osculating planes along the edge of the intake. The inviscid CFD solution shows a leading edge shock reflection off the lower shock-capture surface. This shock-reflection disrupts the downstream compression process and creates downstream flow distortion. The CFD shock structure along the edge of the intake also starts to bow outwards, deviating from the shock shape predicted from theory. Overall, the analytical solution provides good estimation of flow properties for the external contraction portion of the intake. Changes in shock shape, shock reflections, and sidewall effects begin to heavily affect CFD results in the mixed contraction region. These interactions cause deviations from the analytically predicted flowfield.

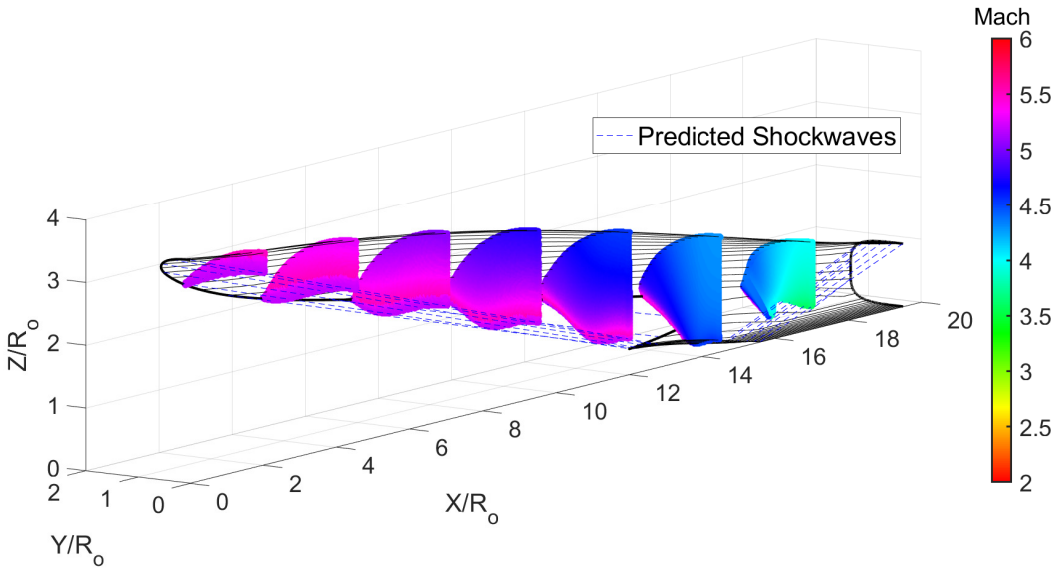

(a) Analytical Solution

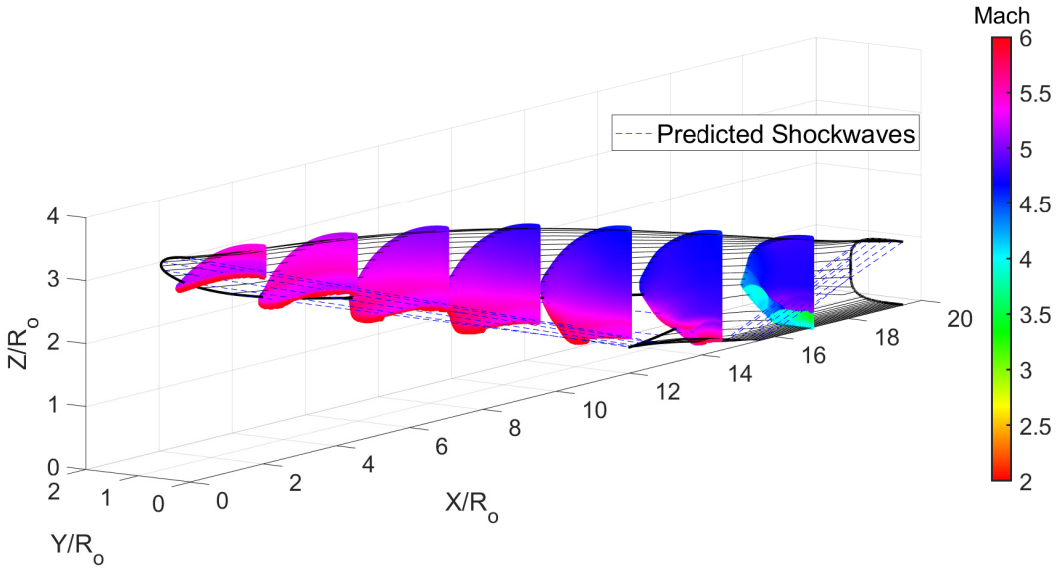

(b) Inviscid CFD

Figure 4.8. Theoretical shock shape and Mach contours for different axial slices: $X/R_\circ = [2, 4.5, 7, 9.5, 12, 14.5, 17]$.

4.4 Leading Shock Alignment

The shape of the leading edge shockwave is vitally important to the performance of any inlet system. Shock-on-lip condition ensures that the incoming streamtube is completely ingested and that no flow is routed overboard. If the leading shock misses the lower lip,

then high-pressure air may escape, leading to a loss in mass capture and a drop in expected pressure rise. The INlet uses a parallel streamline to capture the generated leading-edge shockwave for each osculating plane. However, as discussed in the "Practical Design Considerations" section in 2.2, the shock shape can change due to effects from viscous boundary layers and leading-edge blunting.

A shock structure plot is presented in Figure 4.10 to analyze shock-on-lip condition for different osculating planes. The set of osculating planes chosen for the study is presented in Figure 4.9. To create these plots, a CFD slice of pressure for each osculating plane is exported into Matlab. The leading oblique shock can the be defined and compared to the inviscid prediction by the pressure contour. The pressure contours are logarithmic for all osculating planes. The colorbar range is chosen to highlight shock structure. For osculating axisymmetric theory to hold, the leading edge shock strength needs to remain equal for all osculating planes. It is clear from all osculating planes at 0°, 10°, 20°, and 30° that the predicted shock shape stays consistently close to theory. However, a break-down in this structure occurs somewhere between the 30° and 40° OP angle. A smaller colorbar pressure range was chosen to highlight the high-pressure region ahead of the predicted shock. This does not occur within the other osculating plane solutions. The shock shape near the edge is influenced by two possible mechanisms. The first mechanism is the bow-shock created by the sidewall, which will push the shock forward. The second effect is the rapid change in contour length and isentropic compression along edge solutions. The contour at the 40° OP angle is nearly half the length of the 30° OP angle. The rapid reduction in length likely causes azimuthal pressure gradients on the sugar-scoop surface that would route the flow overboard. This results in a violation of the osculating axisymmetric assumption. With a bowed shock shape in the cowl region, the flow is free to spill and escape the inlet.

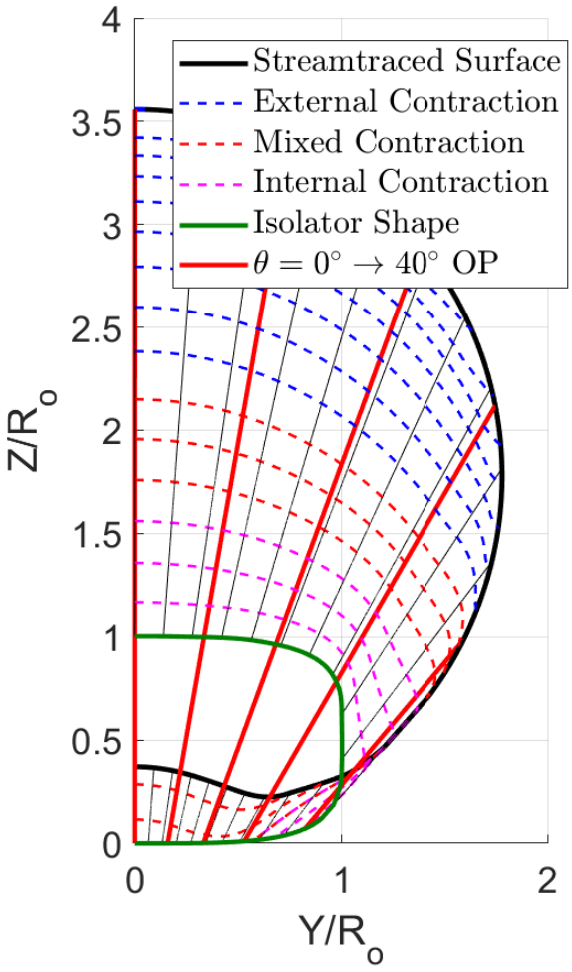

Figure 4.9. Locations of the $0°, 10°, 20°, 30°$, and $40°$ osculating planes on the INlet.

Throat shock location can also be deduced from the pressure contours. The shock root for both methods align at the same location. However, the CFD inviscid shock is more shallow and appears curved. Since the shocks are shallower than predicted, they miss the top of the throat shoulder and enter the isolator region. Complex conical SWBLI will occur along the top wall in the isolator region due to the shock pattern.

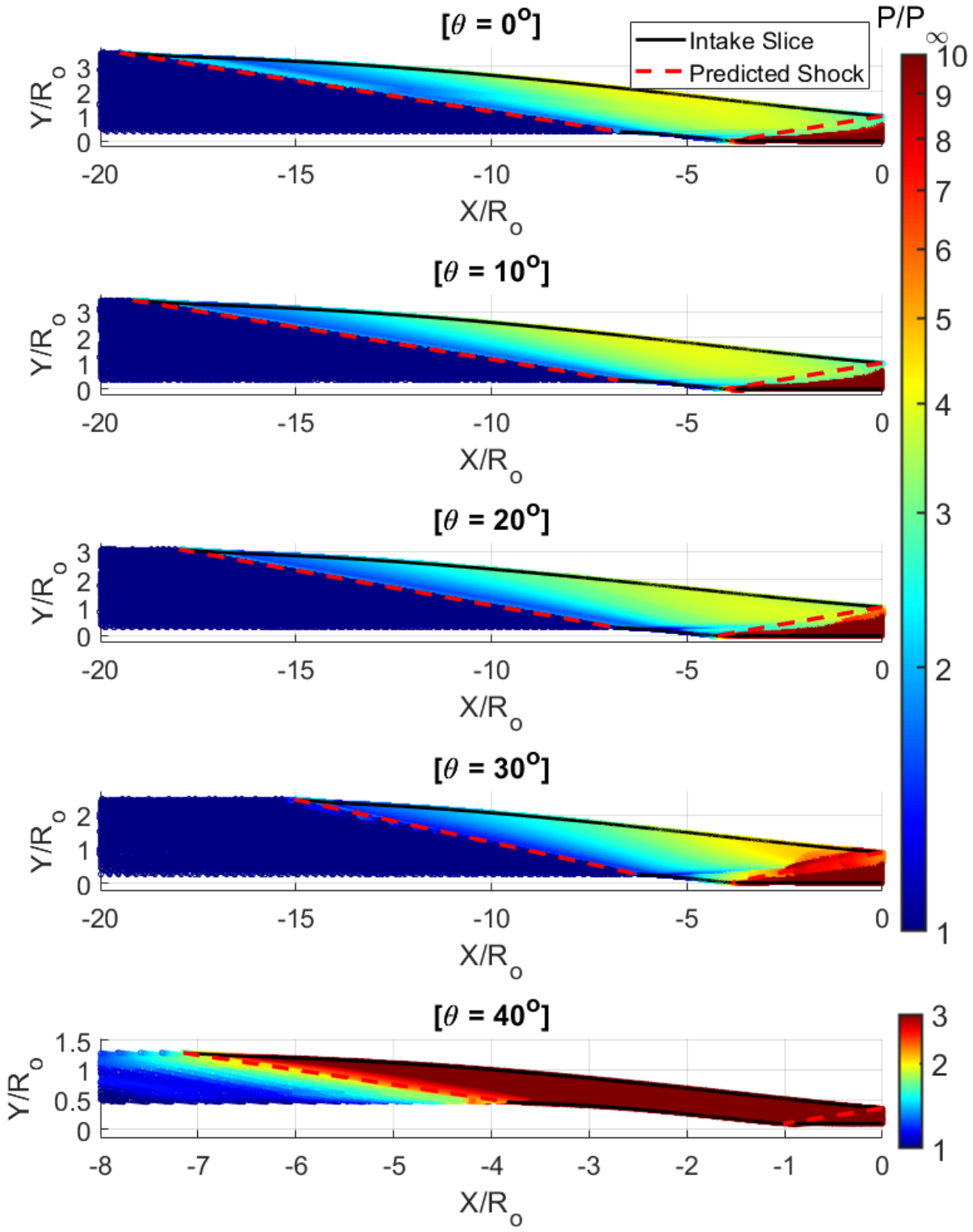

Figure 4.10. Comparison of inviscid CFD pressures with predicted shock locations for different osculating planes.

4.5 Throat Shock Profile

The changes in the predicted intake flowfield also influence the location of the 3D throat shock. Inviscid and viscous CFD solutions clearly show the shock impingement location from wall pressure contours in Figure 4.11. The throat shock impinges downstream of the throat's shoulder, causing flow expansion around the corner. Since the shocks are shallower than predicted, they also do not provide as much compression. The inviscid and viscous CFD solutions predict that the area-averaged isolator Mach number to be 4.09 and 3.60, respectively. Both of these values are much larger than the analytically predicted Mach 3.38 isolator core flow. If the flow is not decelerated to the expected Mach number, then it is possible that throat shocks will deviate from the expected strength predicted by the conical flow assumption. Shock wave boundary layer interactions and their locations are of great interest for future experiments with the INlet model.

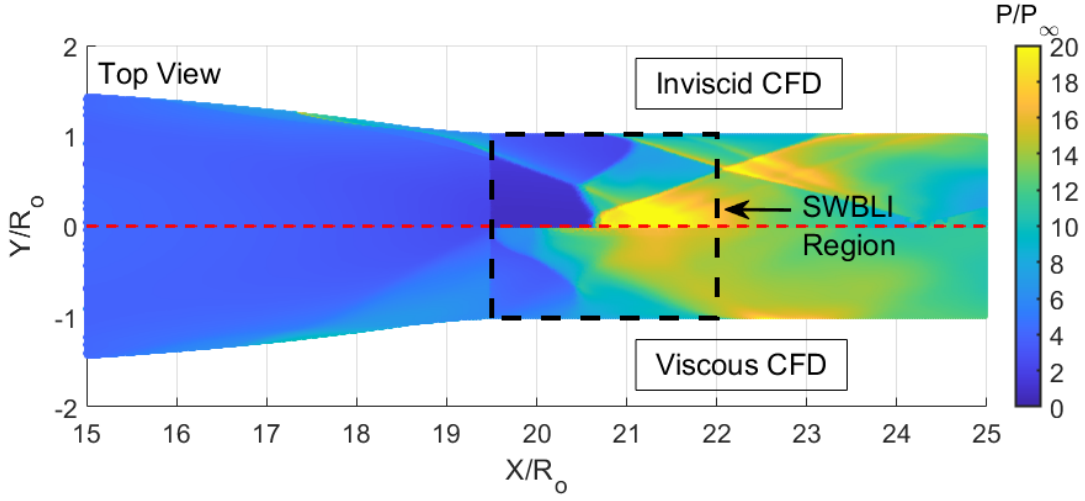

Figure 4.11. CFD solutions of the wall pressure contour of the INlet throat region.

4.6 Görtler Number Map

Inward-turning intakes are constructed with concave walls of high curvature to turn and route the captured flow into the isolator. As the boundary layer develops along these curved streamlines, the local wall curvature may induce a centrifugal instability. This occurs when

the boundary layer thickness is comparable to the radius of curvature. The centrifugal forces act to create a pressure variation in the boundary layer that leads to the formation of Görtler vortices. Görtler vortices may also lead to boundary layer transition from the growth of instabilities caused by the vortices. The Görtler number, equation (4.1), compares the effect of centrifugal forces to viscous effects. The Görtler number is defined from the momentum-thickness Reynolds number (Re_Θ), the local radius of curvature (R_C), and the local momentum thickness of the boundary layer (Θ).

$$G_\Theta = Re_\Theta \sqrt{\frac{\Theta}{R_C}} \tag{4.1}$$

A Görtler map can be constructed for the Indiana Intake using local wall curvature and flow properties from the 2D axisymmetric boundary layer method. With the Görtler number known everywhere on the intake's compression surface, it is possible to use general estimates to predict locations of vortex formation and expected boundary layer transition. Figure 4.12 shows two maps. The top map shows the contour of the Görtler number up to 0.3, which is the value where vortices are expected to form. This occurs at $X/R_\circ = 12$, or roughly two-thirds down the length of the intake. Van Wie in *Scamjet Propulsion* reports a rule-of-thumb for boundary layer transition when $G_\Theta > 8$ [104]. To make the transition location clear on the intake, the bottom map limits the colorbar at $G_\Theta = 10$. From this estimation, transition is likely to occur at $X/R_\circ \approx 17.5$ along the sugar-scoop, before flow enters the throat.

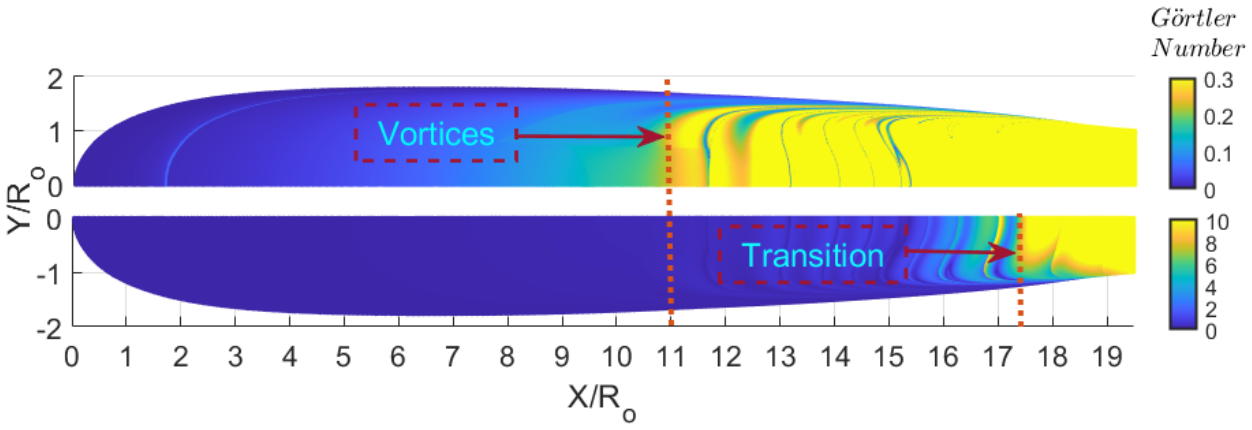

Figure 4.12. INlet Görtler number map with two separate colorbar limits.

4.7 Shockwave Induced Boundary Layer Separation

High speed intakes usually have some form of throat shock which turns the incoming flow to become parallel with the isolator. The strength of the throat shock or cowl-body shock is a primary factor in the likelihood of local boundary layer separation. Correlations exist for turbulent boundary layers that estimate the maximum strength of these shocks before a separation event occurs. For the INlet, each osculating plane's throat shock varies in strength and angle. The pre- and post-shock Mach numbers are known from the construction process, which allows the calculation of the separation limit. These Mach numbers are plotted for all osculating planes in Figure 4.13a. Shock angles are shown in Figure 4.13b as reference. The 0° osculating plane is the centerline streamline and the 41° osculating plane is nearest the cowl enclosure. As expected, large shockwave angles at the throat lead to lower post-shock Mach numbers. A three-dimensional half-view of the inlet shock structure is presented in Figure 4.15. Predicted leading edge shocks are focused at the lip of the shock capture surface to ensure maximum on-design mass capture. The throat shocks in each osculating plane vary in strength, but are designed to intersect the throat shoulder in all solutions.

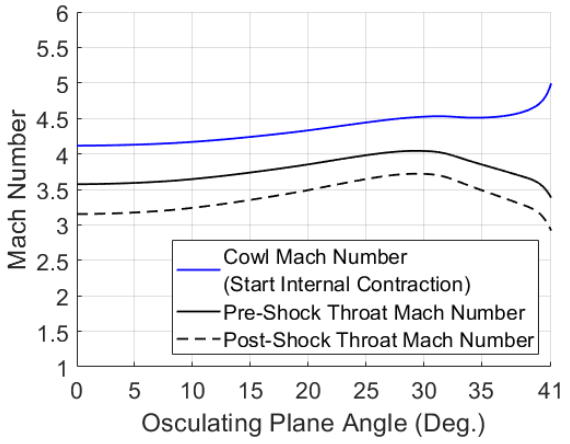

(a) Mach numbers at the cowl and throat.

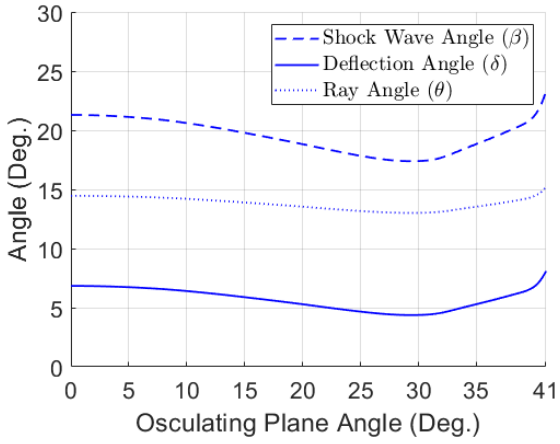

(b) Shockwave angles at the throat.

Figure 4.13. Theoretical shockwave parameters at the throat for all osculating planes.

Shock wave boundary layer interactions are usually defined as either two-dimensional or swept. The conical throat shock formed within inward-turning intakes cannot be classified through either definition. Thus, conical shock interactions are classified as a "mixed"

interaction [39]. Incipient separation caused by a mixed SWBLI can be estimated by the correlations developed by Korkegi, which modifies the 2D and swept separation correlations with the normal Mach component (M_N) past a shock [105]. The correlation is based on data with freestream Reynolds numbers between $10^5 - 10^7$. The pressure rise through a shockwave that would cause incipient separation is shown in equations (4.2) and (4.3).

$$\frac{P_{i+1}}{P_i} = 1 + 0.3(M_N)^2, M_N < 4.5 \tag{4.2}$$

$$\frac{P_{i+1}}{P_i} = 0.17(M_N)^{2.5}, M_N \geq 4.5 \tag{4.3}$$

With the shock strengths known at the throat, the pressure rise at the throat for all osculating planes can be calculated. This provides a comparison against the correlation. Figure 4.14b shows that the pressure rise for throat shocks in the different osculating planes each exceed their respective value expected for separation. However, previous CFD analysis shows that the throat shock are weaker than those predicted here. The weaker shocks predicted by CFD would lessen the risk for separation. For reference, the pressure rise through the leading edge shocks and isentropic compression streamlines are shown for all osculating planes in Figure 4.14a. Although leading and throat shock strength remain relatively equivalent across the domain, the amount of isentropic compression does not. The large variation in isentropic compression between streamlines likely leads to azimuthal pressure gradients and rotational flow. This difference in streamline compression is especially noticeable along the 30° - 41° osculating planes. Such drastic changes in compression may violate the osculating axisymmetric assumption.

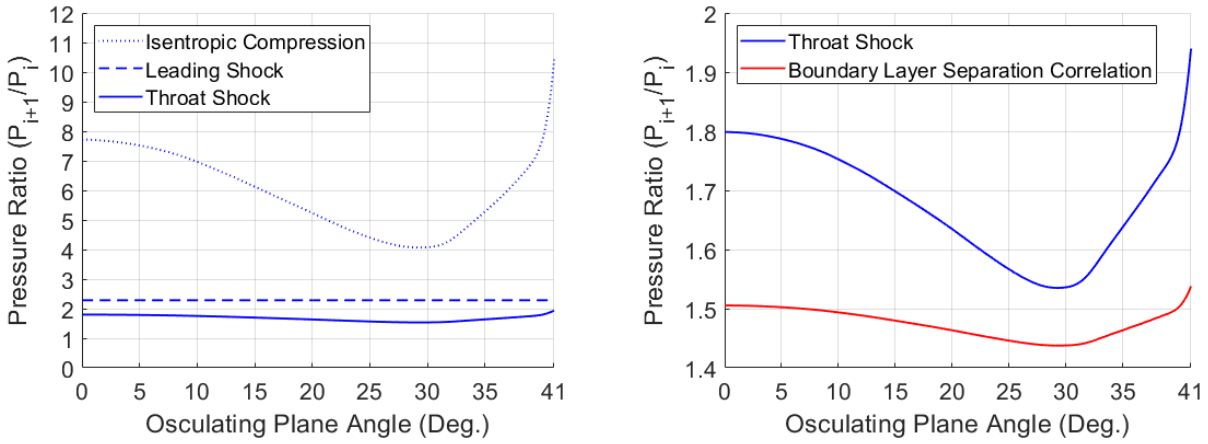

(a) Pressure rise of different inlet components.

(b) Boundary layer separation criterion.

Figure 4.14. Recorded pressure ratios from analytical calculations.

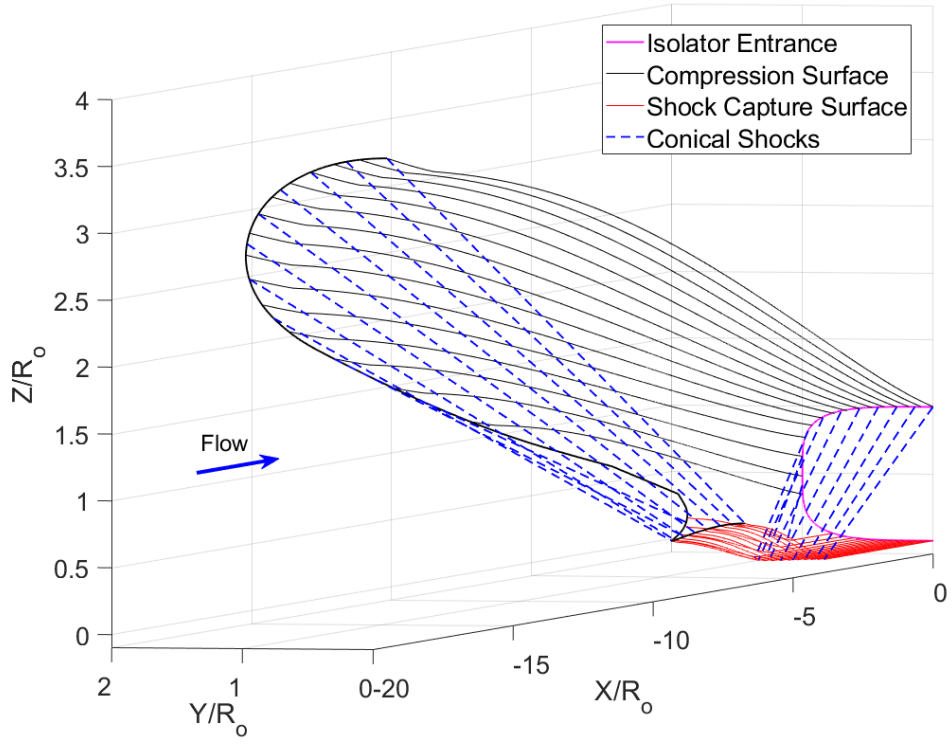

Figure 4.15. Theoretical inlet shock shape.

5. EXPERIMENTAL METHODS

This chapter details the experimental equipment and models used during the blockage testing campaign. Two blockage models were constructed by a third-party vendor through a 3D printing process. These models were subsequently tested in the Purdue hypersonic quiet tunnel. Mean pressures and pressure fluctuations were recorded from sensors placed along the internal flowpath of the model. In-depth details of the facility, sensors, data collection techniques, and the blockage models are presented below. A portion of this chapter was previously published within AIAA's 2022 SciTech conference proceedings [93].

5.1 Facility

The Boeing-AFOSR Mach 6 Quiet tunnel is a Ludwieg tube style hypersonic wind tunnel (Figure 5.1) with a 9.5 inch diameter test section. The tunnel achieves extremely low freestream disturbance levels (quiet flow) through several mechanisms. A boundary-layer bleed slot near the throat section can be activated to remove the turbulent boundary layer that forms in the contraction section. This allows a new laminar boundary layer to reform at the throat. Sections of the nozzle nearest the throat are polished to a mirror finish. Polished surfaces remove roughness elements which can trip the nozzle wall boundary layer. The nozzle contour is also designed to mitigate large changes in curvature, hence the lengthy portion of the diverging section. This suppresses the formation of Görtler vortices, which may amplify instabilities and cause transition to turbulence [106]. When the tunnel has established Mach 6 quiet flow, the normalized pitot pressure fluctuation levels are ≈0.01%, which is comparable to flight. If the bleed slots are closed, the tunnel operates in a noisy condition, and the pitot pressure fluctuations are ≈2-4% [107]. The turbulent boundary layer that forms on the nozzle wall during noisy operation is thicker than the laminar boundary layer under quiet flow. The freestream Mach number drops to 5.8 due to constriction of the core flow during noisy runs.

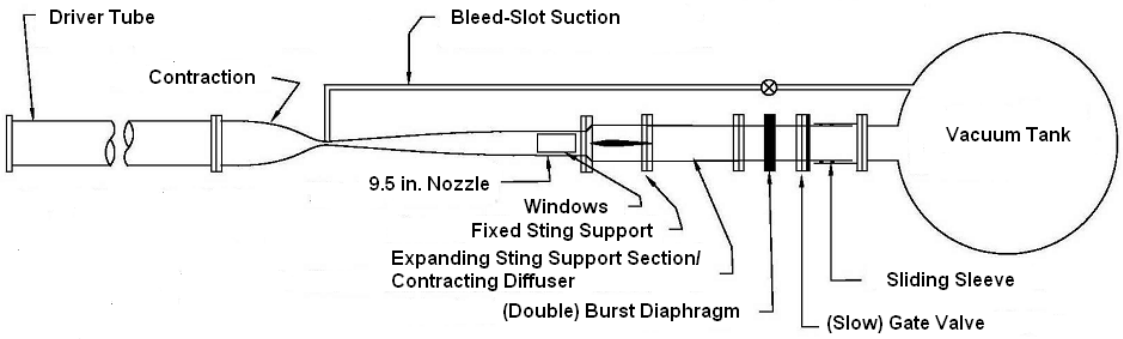

Figure 5.1. Schematic of the Boeing-AFOSR Mach 6 Quiet Tunnel.

The tunnel has an operability range from sub-atmospheric to 260 psia. A Sullair 60 HP compressor provides high pressure air up to 140 psia, and a Corken D-291 boost pump provides air compression up to 260 psia. The incoming air is filtered several times for particulates that could scratch the polished nozzle. A dryer also removes moisture in the compressed air that could condense from rapid expansion in the test section. The compressed air is then passed through a 30 kW circulation heater before entering the driver tube. The driver tube itself is restively heated by a set of four 10V-750A power supplies in parallel configuration. To avoid condensation or liquefaction of the air during expansion to Mach 6, the air is constantly warmed to a targeted stagnation temperature of 160 °C.

Maximum stagnation pressure that achieved quiet flow (max quiet) for the blockage entries was near 160 psia or a freestream Reynolds number of $11.5 \times 10^6/m$. The wind tunnel operates by pressurizing the upstream driver tube, nozzle, test section, and diffuser to a desired stagnation pressure. A tunnel run is activated by bursting a set of two diaphragms in quick succession. Downstream of the diaphragm section, a 400 ft^3 vacuum tank provides the pressure differential to start the tunnel. A typical quiet run lasts between 2-3 seconds, and a noisy run lasts between 4-6 seconds. During a run several expansion fans will travel through the driver tube, dropping the stagnation pressure during each pass. This also drops the freestream Reynolds number over the duration of run. The tunnel may unstart early due to high vacuum tank pressures or large blockages from wind tunnel models. Lower stagnation pressure runs are especially susceptible to earlier and mid-tunnel unstart.

5.2 Tunnel Diagnostic Sensors

There are several sensors that monitor the state of the tunnel during a run. An upstream pressure sensor in the subsonic contraction section of the nozzle provides stagnation pressure readings. This XTEL-190-500A Kulite pressure transducer is known as the contraction Kulite (CK). It detects the reflected expansion waves in the driver tube that cause drops in stagnation pressure during a run. As such, the stagnation pressure readings from this sensor can be used to calculate the time-dependent freestream Reynolds number. There is also a nozzle wall Kulite (NWK) that tracks the static wall pressures near the test section. This Kulite is an ETL-79-HA-DC-190 model that can measure static pressures and provide its own signal amplification. During start-up, the nozzle wall pressure transducer sees a drastic drop in pressure. The data acquisition system and bleed slot fast-valve is triggered from the signal's drop in voltage. In addition to triggering, the nozzle wall transducer can help detect unstart behavior by recording any abnormal spikes in pressure during a run. Both the contraction and nozzle wall Kulites require calibrations in their respective pressure ranges to be later used in quantitative calculations.

Another pressure sensor is located near the diaphragm section. This sensor is a Paroscientific Model 740 Digiquartz Portable Standard pressure gauge, which can measure pressures up to 300 psia. It provides real-time readouts of the pressurized tunnel sections. The Digiquartz sensor is also used to calibrate the contraction, nozzle wall, and model Kulite pressure transducers. The last tunnel diagnostic sensor is a hot film (HF) located near the nozzle exit and adjacent to the nozzle wall Kulite sensor. This is a Dante 55R45 hot film sensor that can detect fluctuations by measuring boundary-layer shear stress. The hot film signal is sent to a Bruhn-6 anemometer with a Wheatstone bridge. The bridge is balanced by manually setting the input to half the operating resistance of the hot film, which is 8.77 Ohm. The HF output signal is a good qualitative measure to detect tunnel unstart, nozzle wall boundary-layer separation, and turbulent or laminar boundary layers based on the intensity of signal fluctuations.

5.3 Tunnel Flow Conditions

The freestream flow properties of the tunnel change throughout a run due to the periodic drop in stagnation pressure from reflected expansion waves. The flow is quasi-static between reflections, but it is still necessary to track quantities such as stagnation temperature, stagnation pressure, and freestream Reynolds number. The initial stagnation temperature ($T_{o,\mathrm{i}}$) is known from a thermocouple located at the end of the driver tube. Also, the initial stagnation pressure ($P_{\circ,\mathrm{i}}$) is known from the Digiquartz pressure gauge. The contraction Kulite also measures time-dependent stagnation pressure ($P_{\circ}(t)$) throughout a run. From these quantities, it is possible to calculate the time-dependent stagnation temperature ($T_o(t)$) and static temperature ($T(t)$) from the isentropic relation given in equations (5.1) and (5.2).

$$T_0(t) = T_{0,\mathrm{i}} \left(\frac{P_0(t)}{P_{0,\mathrm{i}}} \right)^{\frac{\gamma-1}{\gamma}} \tag{5.1}$$

$$T(t) = T_0(t)(1 + \frac{\gamma - 1}{2} M^2) \tag{5.2}$$

Dynamic viscosity is found from Sutherland's Law for air, which assumes an ideal gas. The relation is shown in equation (5.3). The reference parameters are given as $T_{ref} = 273.15$ K, $S_k = 110.4$ K, and $\mu_{ref} = 1.716 \cdot 10^{-5} \frac{kg}{m*s}$.

$$\mu(t) = \mu_{ref} \left(\frac{T(t)}{T_{ref}} \right)^{\frac{3}{2}} \frac{T_{ref} + S_k}{T(t) + S_k} \tag{5.3}$$

Since stagnation temprature, static temperature, static temperature, and dynamic viscosity are known quantities, it is possible to calculate the freestream unit Reynolds number. The time-dependent equation for time-dependent Reynolds number is given in equation (5.4)

$$\mathrm{Re}_{\infty}(t) = \frac{P(t)M}{\mu(t)} \sqrt{\frac{\gamma}{RT(t)}} \tag{5.4}$$

5.4 Data Collection

A Data Acquisition System (DAQ) handles all data recording, input triggers, and output alarms. The Gen7i Genesis High-Speed DAQ by HBM can record signals from 56 sensors simultaneously from 7 separate data cards with 8 channels each. If necessary, a slaved Gen7ta can be tether to the Gen7i to increase the total amount of sensor channels. The Gen7i has 6 fast 14/16-bit GN8103B DAQ cards that record up to 25 MHz. There are also 2 slower 18-bit GN815 cards that reduce the noise floor but only sample up to 2 MHz. Tunnel diagnostic sensors for the blockage experiments were recorded on the GN8103B cards while the signals from the model Kulite sensors were recorded on the low-noise GN815 cards. All sensors, diagnostic or model, were recorded at a sample rate of 2 MHz during the blockage model test campaign.

5.5 Jet Injection System

The jet injection system was designed for massflow blowing or suction experiments within the BAM6QT. For this experiment the injection system was used to provide the isolator back-pressure required to unstart the 9% scale Indiana Intake blockage model. A schematic is presented in Figure 5.2 which is referenced from Dally and Edelman [108].

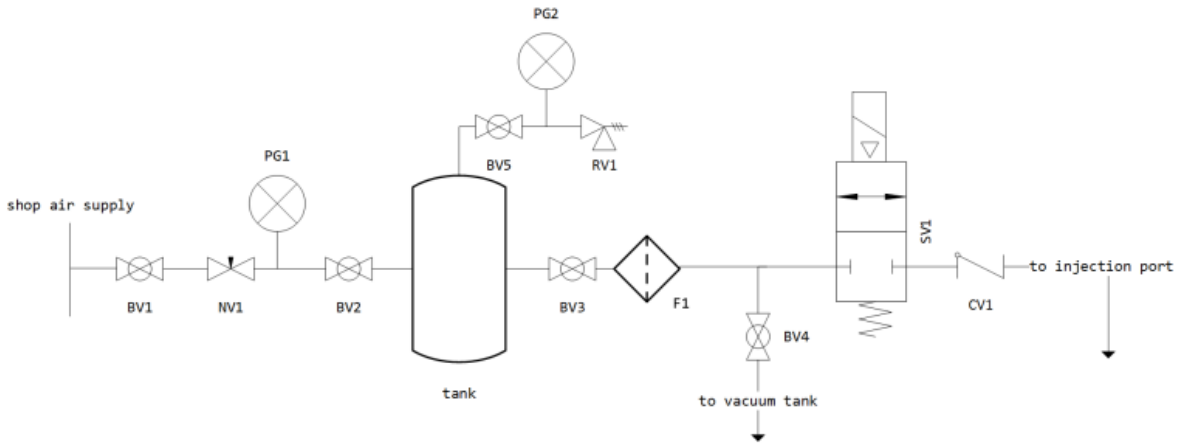

Figure 5.2. Jet system schematic, taken from Dally and Edelman [108].

High pressure air from the ASL machine shop is routed through two ball valves (BV1, BV2) and a needle valve (NV1) before entering the 4.5 gallon plenum tank. The needle valve and pressure gauge (PG1) allow an operator to determine how much air has entered the tank. A separate plenum pressure gauge (PG2) and a pressure-relief valve (RV1) are also connected to the plenum tank. To conduct a massflow blowing experiment, the downstream ball valve (BV3) must be open. High pressure air then travels through the air filter (F1), soleniod (SV1), and check-valve (CV1) before entering the tunnel. A 5/16 inch nylon tube is routed from the check valve, through a sealed Conax fitting, and into a quick-disconnect port on the blockage model. The solenoid is operated by a power system which activates based on 5V step-inputs from a signal generator. If the solenoid is triggered accidentally or early, then the check-valve will hold back high-pressure tunnel air, preventing back-flow. The check valve only opens if downstream air has dropped below 0.5 psia. Care must be taken to check for leaks within the system's piping network. No throttle exists, so massflow is calculated from starting stagnation pressure. The nylon tubing is especially susceptible to kinks that may restrict the massflow rate. The function generator, an Agilent 33220A model, controls the on-off state of the solenoid. It can be programmed to produce custom waveforms of various frequencies, offsets, delays, or shapes. A custom 5V peak-to-peak square wave was programmed as the trigger to the solenoid. The signal generator would send this signal after receiving an external trigger from the HBM DAQ. The square wave was delayed by 0.75 seconds to allow the tunnel to successfully start before injecting air. The square-wave signal would last 1.25 seconds, providing ample time to investigate quasi steady-state injection effects within the model. A full procedure for the system is presented in appendix B.

5.6 Blockage Models

Two Indiana Intake models were constructed for blockage testing within the BAM6QT. The first model was scaled similarly to the 9% scaled HIFIRE-6 202E public release model. The scaling is based on throat height. This sugar-scoop intake model was loaned to Purdue University by the Air Force Research Laboratory during the summer of 2020. Pictures of the blockage models mounted in the BAM6QT are shown in appendix C. Preliminary results

Table 5.1. INlet blockage model dimensions.

	Small	Medium
Scale (%)	9	14
Throat Height $R_\circ$ (in.)	0.34	0.53
Throat Width (in.)	0.68	1.06
Corrected Throat Height (in.)	0.44	0.73
Intake $X/R_\circ$	19.5	19.5
Intake Length (in.)	6.66	10.34
Isolator $X/R_\circ$	15	15
Isolator Length (in.)	5.10	7.95
Nozzle $X/R_\circ$	5	5
Nozzle Length (in.)	1.70	2.65
Total Length (in.)	13.46	20.94

showed that the BAM6QT successfully started with the intake geometry over a variety of starting stagnation pressures and different angles of attack. Due to instrumentation difficulties and the proprietary restrictions of sharing the model's geometry, those results cannot be presented. These restrictions were partial motivation for the creation of an open-source geometry for scientific study. The second intake model was scaled similarly to a 14% HIFIRE-6 geometry. Results of the blockage studies are presented in chapter 6. These blockage models were based on an early version of the streamtracing design code. Due to a change in the program, these preliminary models have an over-sized lower lip surface, so pressure measurements and performance may deviate from the finalized model due to changes in geometry and shock structure. Table 5.1 compares different dimensions of the two INlet blockage models.

These preliminary models were constructed without a boundary layer correction to the intake's upper surface contour. The low momentum fluid in a boundary layer effectively shrinks the core flow area of the captured streamtube at the intake's throat, artificially increasing the internal contraction ratio. Sufficient boundary layer growth may lead to flow over-contraction, potentially causing unstart [55]. To mitigate this phenomenon, the throat of the blockage models were enlarged to decrease the analytically defined internal contraction ratio. The throat was enlarged where the top compression surface connects with the isolator.

It was enlarged by 0.20 inches for the medium model and 0.10 inches for the small blockage model. Although enlarging the throat may cause off-nominal performance, this modification was deemed necessary to effectively study self-starting characteristics of the inlet until a full viscous correction could be developed.

5.6.1 Tunnel Starting Feasibility

In order to estimate the starting capability of the models within the tunnel, a wind tunnel starting correlation was used. The plot in Figure 5.3 shows a historical correlation for hypersonic wind tunnel start conditions using the frontal projected areas of models. The correlation is primarily based on axisymmetic, slender models. However, the intake models are neither axisymmetic or slender. Additionally, they contain inner flow paths that may interact to unstart the tunnel. The correlation is only an approximate estimate of possible tunnel startability. Pope describes that other factors, like model pitch, non-conformal windows, boundary layer separation, boundary layer thickness, and shock wave boundary layer interaction that all play a role in determining tunnel startability [109].

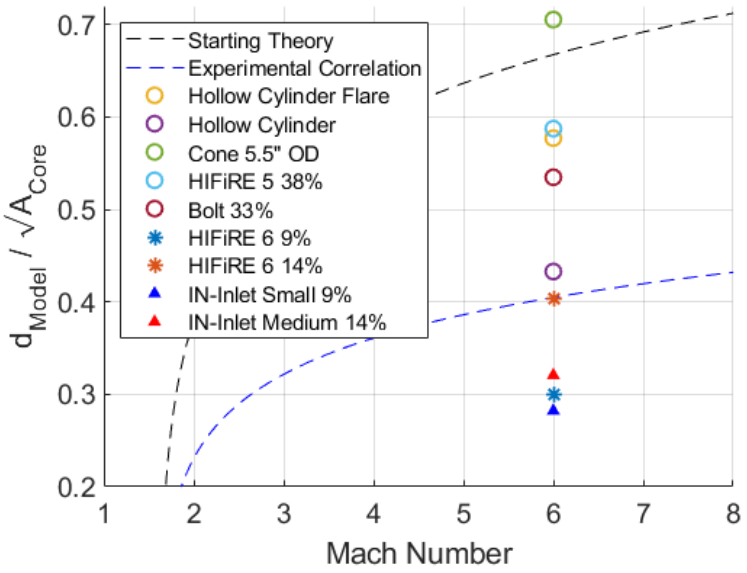

Figure 5.3. Wind tunnel starting correlation for different BAM6QT models. Reproduced from Pope [109].

5.6.2 Pressure Transducers and Signal Conditioning

The blockage models are outfitted with XCE-062-15A (0.3 inch length) and XCE-SL-062-15A (0.1 inch short-length) Kulite pressure transducers. These sensors detect changes in pressure from a piezoresistive silicon diaphragm with a Wheatstone bridge, which is mechanically stopped to prevent damage at high pressures. Kulite pressure transducers can measure both pressure fluctuations and mean pressures down to ≈0.3 psia. However, calibrations have shown that a linear response can provide accurate mean pressures down to ≈0.1 psia. The diaphragms are either protected by a perforated cover (B-screen) or a single hole (A-screen). Although the B-screen variants provide more protection from particulates, the screen drops the resonant frequency of the sensor housing. A-screen variants are preferred because more spectral content is unaffected by the sensor's higher resonant frequency (>200 kHz), but are more vulnerable from particle impacts. All blockage model sensors are A-screen variants unless noted otherwise. The sensors are excited by a custom signal conditioner box that amplifies AC signals by 10,000 or DC signals by 100. A stand-alone 10 channel conditioning box was used for the blockage model Kulite sensors. An in-situ calibration was performed for all Kulites by depressurizing the tunnel to sub-atmospheric levels. The calibration results are shown in appendix D.

5.6.3 Sensor Locations

Both blockage models were designed with eight access ports for Kulite pressure transducers. These ports were dispersed throughout the internal flowpath of the model to give indicators of inlet operation, which is shown in Figure 5.4. The location of these sensors were constrained due to internal support rods. Thus, there are sensors placed on the sidewall (S-IML), top (T-IML), and bottom portion (B-IML) of the IML. A back-pressure port (BPP) is also located within the isolator. A quick-disconnect blowing port was installed to make it easier to conduct forced-unstart experiments for comparison against started inner flow paths.

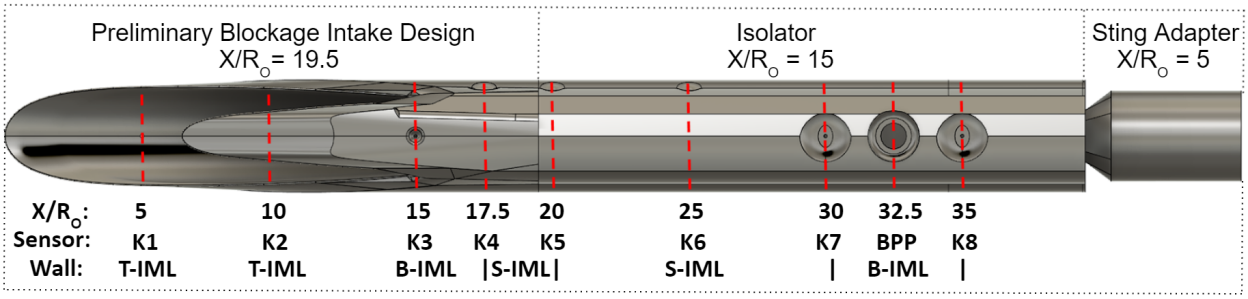

Figure 5.4. Overview of the normalized sensor locations on the INlet blockage models.

5.6.4 Construction Challenges

The two blockage models were rapidly prototyped from TriModels Incorporated with CE-221 Cyanate Ester as the chosen material. The material's high heat deflection temperature and comparable strength to ploycarbonate made it an attractive option for a blockage model [110]. Additionally, the digital light synthesis (DLS) process was able to provide good resolution on leading edges and contours without producing any stair-stepping that is innate to fused deposition modeling (FDM). Unfortunately, the baking process produced stress cracks in both models. After a finite element analysis (FEA) review, it was deemed necessary to reinforce these models. To reduce the risk of failure during a worst-case asymmetric tunnel unstart scenario, a compressive steel sleeve was wrapped around the inlet-isolator junction. Hose clamps were used to compress the sleeve around the body. In the event of failure, the sleeve would catch and hold the model together. Additional internal support rods were also drilled into the smaller model to alleviate bending stresses on the forward-most portions of the intake surface. A view of the partially installed INlet blockage model within the BAM6QT test section is shown in Figure 5.5.

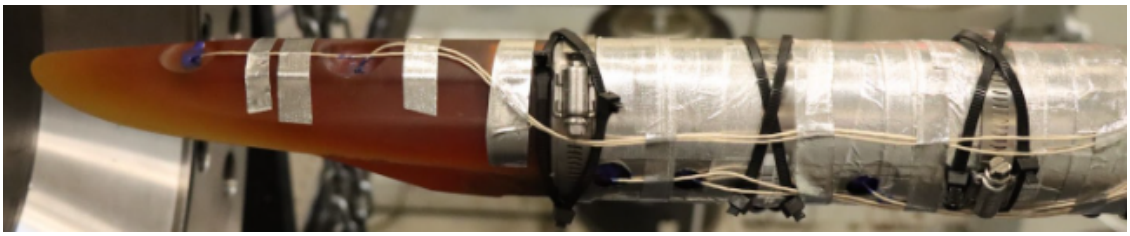

Figure 5.5. In-situ view of the 9% blockage model mounted on a sting in the BAM6QT test section with visible compressive sleeve and hose clamps.

6. BLOCKAGE TEST CAMPAIGN

The blockage test campaign was designed to test the limits of tunnel starting and the self-starting ability of the INlet blockage models. The two models were run at various freestream Reynolds numbers, sting positions, one non-zero angle-of-attack, under quiet flow, and under noisy flow. A full test matrix is provided in appendix E. Due to the compromised structural integrity of the models from internal cracks, it was deemed too risky to attempt schlieren visualization. As a precautionary measure, the sapphire windows were replaced with stainless steel blank inserts. Fortunately, both models survived installation and testing without failing. A version of this chapter is pending publication in AIAA's 2022 Aviation conference proceedings.

6.1 Tunnel Starting Analysis

Wind tunnel starting is hard to predict for irregularly shaped geometries. Experimental correlations that apply to sharp and slender conical geometries may not apply to non-axisymmetric geometries like inlets. Intake models also contain an internal flowpath that may interact with the start-up processes of a wind tunnel. It is computationally expensive to grid and solve the flowfield for an entire wind tunnel system. Blockage models are a comparably cheaper and faster method to determine a suitable size for final testing. However, care must be taken to analyze tunnel behavior with blockage models.

6.1.1 Hot Film and Nozzle Wall Pressure Traces

Tunnel diagnostic sensors, such as the hot film (HF) and nozzle wall Kulite (NWK), provide a quantitative assessment of abnormal tunnel behavior. A sample case of tunnel unstart assessment is shown in Figures 6.1 and 6.2 for the 14% model under Mach 6 quiet flow with an initial burst stagnation pressure of 170.3 psia. The uncalibrated hotfilm voltage signal is shown in Figure 6.1. The HF voltage fluctuations are computed by integrating power spectra from 0-50 kHz for 0.1 second window increments over the length of the run. The nozzle wall pressure trace in Figure 6.2 is also compared against isentropic freestream

static pressure for Mach 6 and Mach 5.8 flow. The error between the real and expected wall pressures from 0.25s to 3.5s is calculated. This array of values is then averaged together to find the average deviation of the nozzle wall pressure trace from the expected isentropic behavior. This range of time was selected to avoid start-up and shut-down behavior.

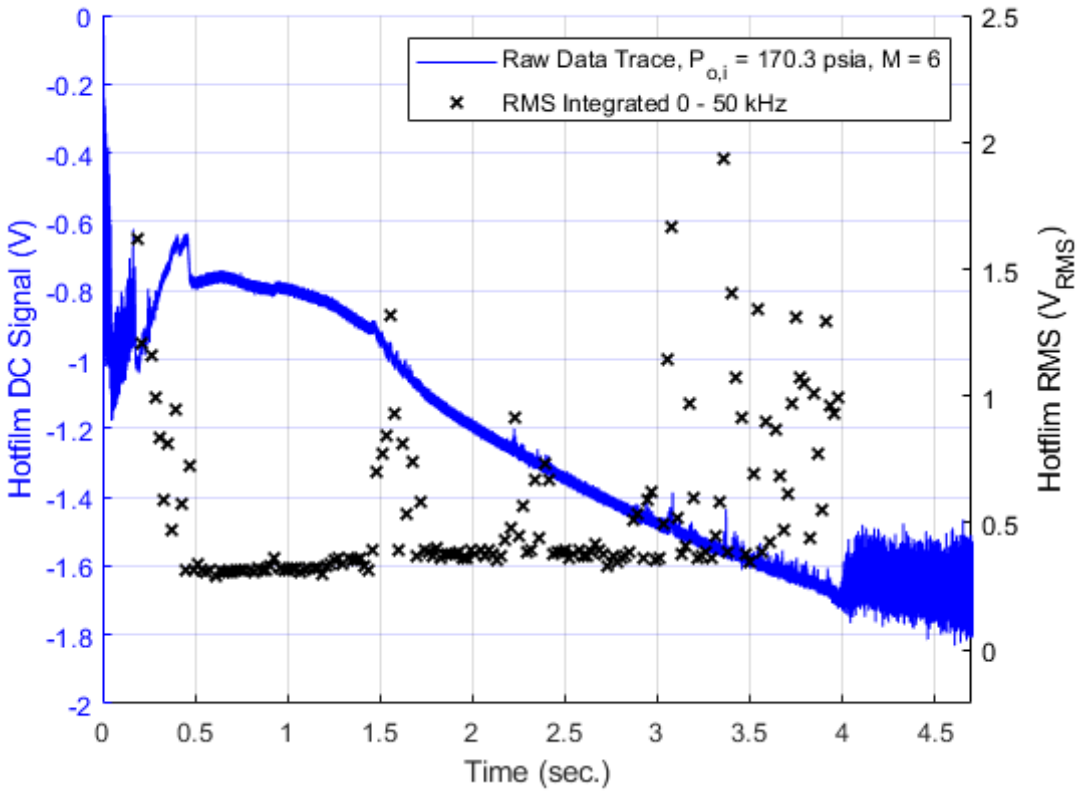

Figure 6.1. Tunnel starting analysis from hot film data for the 14% model at 0°AoA, $P_{\circ,\mathrm{i}} = 170$ psia, Mach 6 quiet flow, and in the sting-back position.

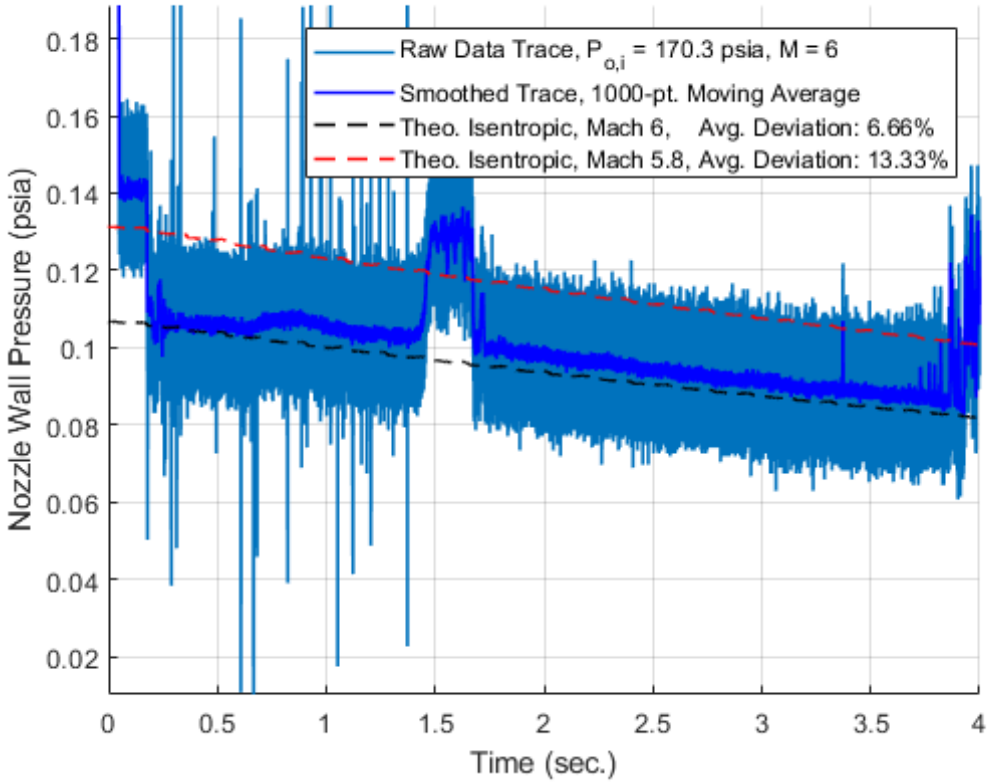

Figure 6.2. Tunnel starting analysis from nozzle wall pressure data for the 14% model at 0° AoA, $P_{\circ,\mathrm{i}} = 170$ psia, Mach 6 quiet flow, and in the sting-back position.

The nozzle wall pressure trace shows start-up behavior from 0-0.25 seconds into the run. The establishment of quiet flow occurs at 0.5 seconds and lasts until 3 seconds. A mid-tunnel unstart is observed in both the HF and NWK plots at 1.5 seconds into the run and lasts 0.25 seconds. This is likely due to nozzle wall boundary layer separating and then reattaching. After this event, the tunnel stays started until the 3.8 second mark. However, HF RMS calculations show a noticeable increase in noise starting 2.8 seconds after establishment of quiet flow. This is consistent with the "2-second rule" described by Derek Mamrol's tunnel characterization study [111]. Additional care must be taken when analyzing nozzle wall pressures. Sometimes the recorded static pressure will not match the static pressures predicted by isentropic theory for a Mach 6 freestream. Juliano showed from

pitot measurements that separation events would cause the freestream flow to drop as low as Mach 5 with initial stagnation pressures as low as 45 psia [112].

6.1.2 Reynolds Number Starting Maps

The nozzle wall pressure traces for several different tunnel runs over a Reynolds sweep can be compiled together to provide a better understanding of tunnel startability. These starting maps show abnormal behavior in the nozzle wall pressures as a function of freestream Reynolds number. Two maps are presented in this section for the medium 14% scale blockage model. The medium blockage model had worse starting performance than the 9% blockage model. The starting maps for all freestream flow conditions, sting positions, and scale models are presented in appendix F.

The first starting map in Figure 6.3 is for the medium model at 0° AoA under Mach 6 quiet flow with the model moved back the maximum amount. Five tunnel runs were conducted at various starting stagnation pressures. Vacuum tank pressures were recorded to be under 15 torr for each run. The 1,174 kPa (170.3 psia) and 896 kPa (129.9 psia) runs show a momentary mid-tunnel unstart occurring due to nozzle wall boundary layer separation. The flow cannot be considered Mach 6 steady-state during these unstart events. This stresses the importance of a tunnel starting analysis proceeding data analysis. Additionally, sustained tunnel unstart is seen for the tunnel runs below a starting 594 kPa (86.1 psia) stagnation pressure. The average deviation of the theoretical isentropic pressures and the measured pressures are above 70% for these cases.

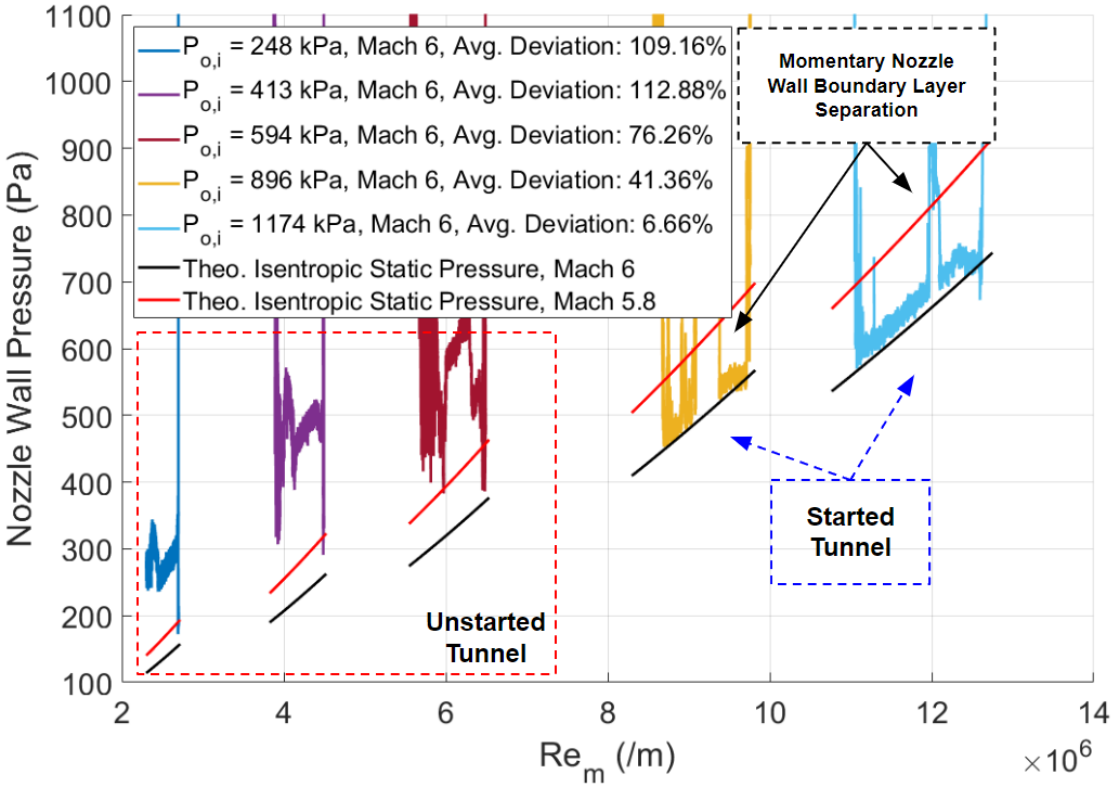

Figure 6.3. Tunnel starting map for the 14% model under Mach 6 quiet flow at 0°AoA and the furthest model position from the throat.

The second starting map shows the 14% model under the same conditions except at a 6° AoA. Increasing the angle of attack of a wind tunnel model effectively increases its frontal area, causing a larger blockage in the tunnel. Figure 6.3 shows the Reynolds sweep conducted for this orientation. Interestingly, tunnel starting improves for the 595 kPa (86.3 psia) case. Also, no mid-tunnel unstart was observed at the highest Reynolds number run. This shows that other factors beyond frontal blockage area influence tunnel starting.

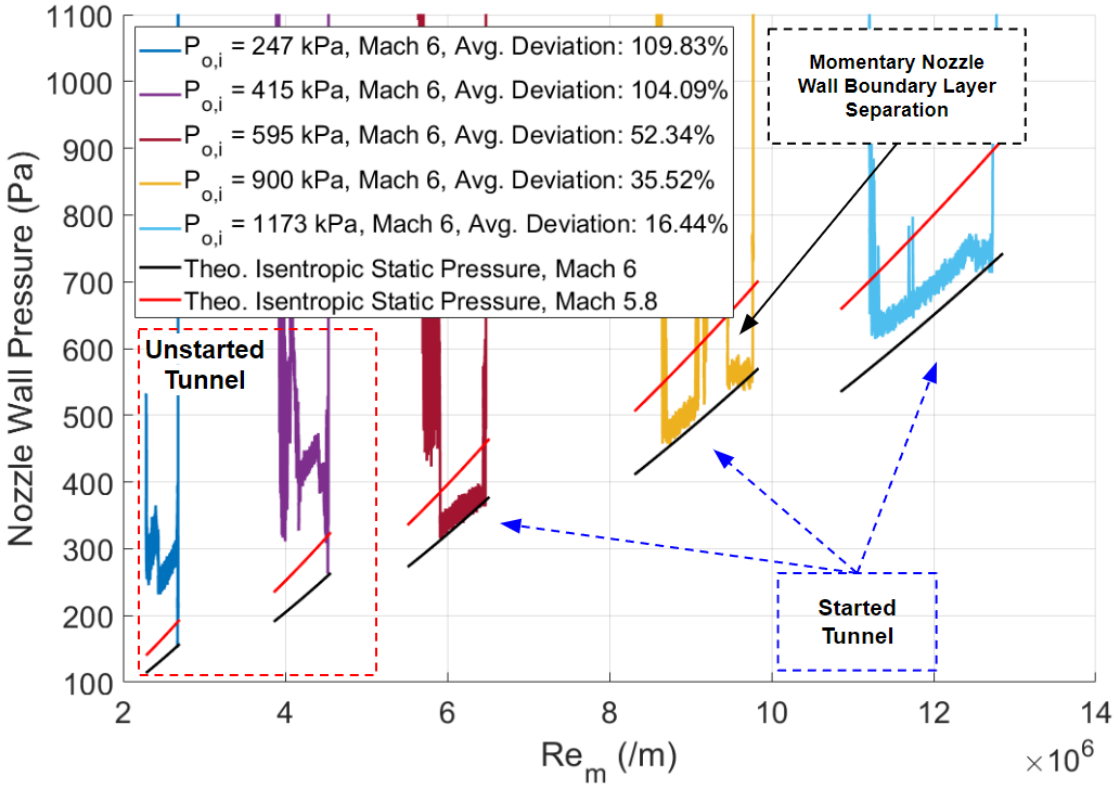

Figure 6.4. Tunnel starting map for the 14% model under Mach 6 quiet flow at 6°AoA and the furthest model position from the throat.

The results of these starting maps show that the 14% model appears to unstart the tunnel at freestream Reynolds numbers below $8 \cdot 10^6/m$. Interestingly, tunnel starting issues disappear completely for noisy flow conditions at all Reynolds numbers tested. For the 9% model, the tunnel starts consistently across all Reynolds numbers tested under quiet and noisy flow conditions. Only one tunnel run with the 9% model unstarted early due to abnormally high vacuum tank pressure. The results of the tunnel starting analysis influenced the scaling of the final intake model, which is based on an intermediate 12% scale. This was determined to be the best compromise between model length, structural strength, viewing area, and tunnel startability.

6.2 Intake Starting Analysis

The second objective of the test campaign was to conduct a preliminary study on the self-starting characteristics of the INlet blockage models. The blockage models were designed with an over-sized lower lip because of an error in the streamtracing code. Due to this deviation from the target geometry, the experimental results cannot be directly compared to the benchmarked CFD results and are omitted from this analysis. Also, there were tunnel starting difficulties at low freestream Reynolds numbers ($Re_m < 9.0 \cdot 10^6/m$) for the 14% scaled blockage model, so only data from Reynolds number cases above this value are presented.

Intakes are designed to compress freestream flow for downstream components in an air breathing engine. For a scramjet, the establishment of supersonic flow in the isolator is essential. Determining the state of the ingested flow can be determined through static pressure measurements. Initial analysis of the intakes was accomplished by calculating the mean flow pressures along the IML Kulite sensors for verified started tunnel conditions. The mean pressures were calculated over 200,000 points (0.1 seconds) of data centered around the targeted Reynolds number condition. These results were then normalized by the theoretical freestream static pressure predicted by isentropic theory per the respective tunnel condition.

6.2.1 Pressure Profiles

Internal flowpath static pressures were recorded from Kulite pressure transducers. The locations of the Kulites within the blockage models are shown in Figure 6.5 for reference. Dashed-red lines delineate the different regions of the model, which include the external contraction, internal contraction, rectangular isolator, and blended nozzle. The Kulite at $X/R_\circ = 15$ is located directly at the cowl plane, which is where incoming flow can spill overboard. During inlet unstart, a normal shock will take position at the beginning of the internal contraction, making this Kulite important for determining a started inlet state. Also, the Kulite at $X/R_\circ = 20$ is located directly adjacet to the throat, which is defined at $X/R_\circ = 19.5$ for both geometries. Depending on the model, some Kulites were excluded from the analysis due to abnormal readings or breaking during the entry. A variety of different

conditions were compared with each other to determine the startability of the INlet models. Although two separate sting positions were tested, results from the sting-forward position are omitted from this analysis due to negligible effects. This is expected since the tunnel's core flow should not be influenced by the sting position for a successfully started tunnel.

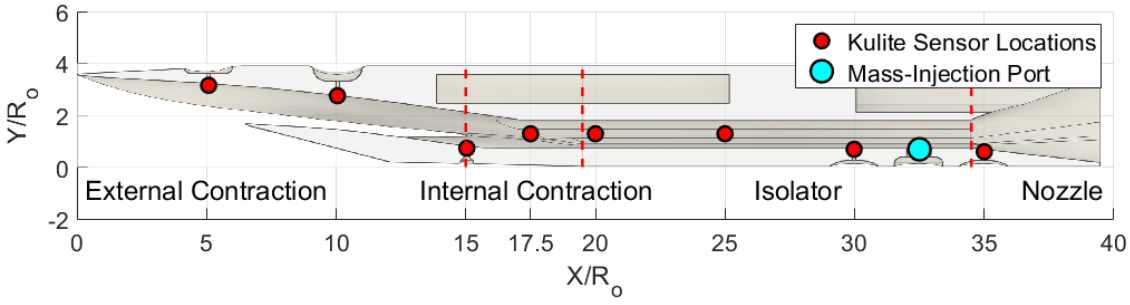

Figure 6.5. INlet blockage model schematic with labeled regions and senor locations.

The effect of model scale on internal pressures is shown in Figure 6.6. Model scale had a substantial effect on internal pressures past the $X/R_\circ = 15$ location. Pressure ratios downstream of this location were higher for the smaller 9% blockage model across two separate Reynolds numbers. It is likely the smaller model had less relative on-design spillage than the larger model, allowing for more efficient compression. The over-sized lower lip on the 14% model may also have had a more drastic effect on shock structure and flow spillage. Additionally, normalized pressures for both models appear independent of Reynolds number. Some small deviations may be explained by the difference in boundary layer thickness, which is a function of freestream Reynolds number. Lower freestream Reynolds numbers create thicker surface boundary layers that restrict and compress the core flow of the inlet to a small extent.

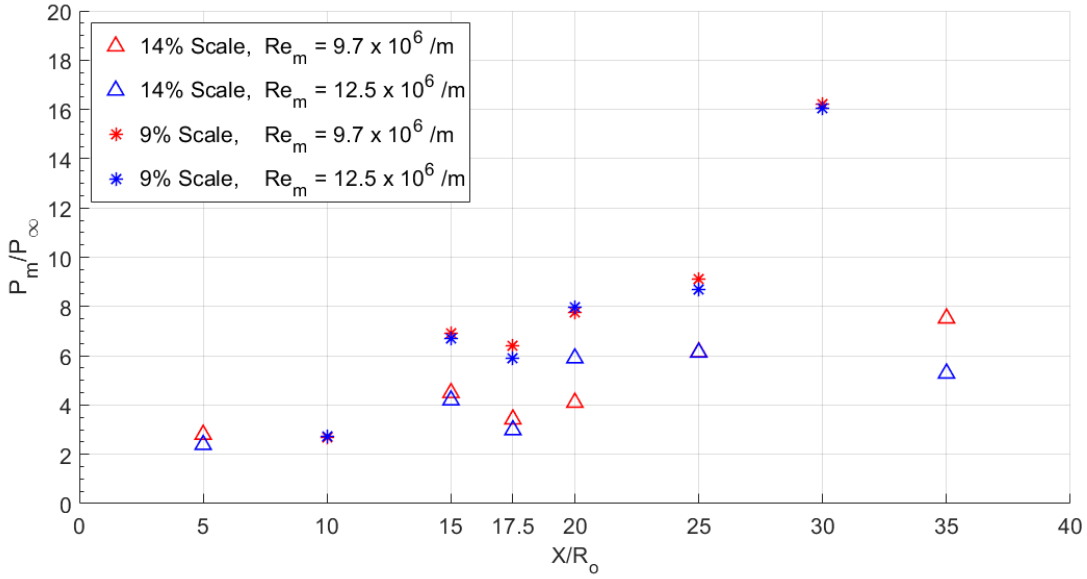

Figure 6.6. Model scale and freestream Reynolds number comparison of normalized IML static pressures for a Mach 6 quiet flow condition.

The effect of Mach 5.8 noisy flow and Mach 6 quiet flow on IML pressures of the 14% model is shown in Figure 6.7. Isolator Kulite sensors show an increase in normalized pressures past the throat region. Since the freestream Mach number has dropped, the leading inlet shockwave becomes shallower. This increase in shock angle also strengthens the shock, resulting in higher downstream pressures. This is the most likely effect that causes the increase in downstream pressures when compared to the on-design Mach 6 condition. This effect is consistent across both Reynolds number sweeps.

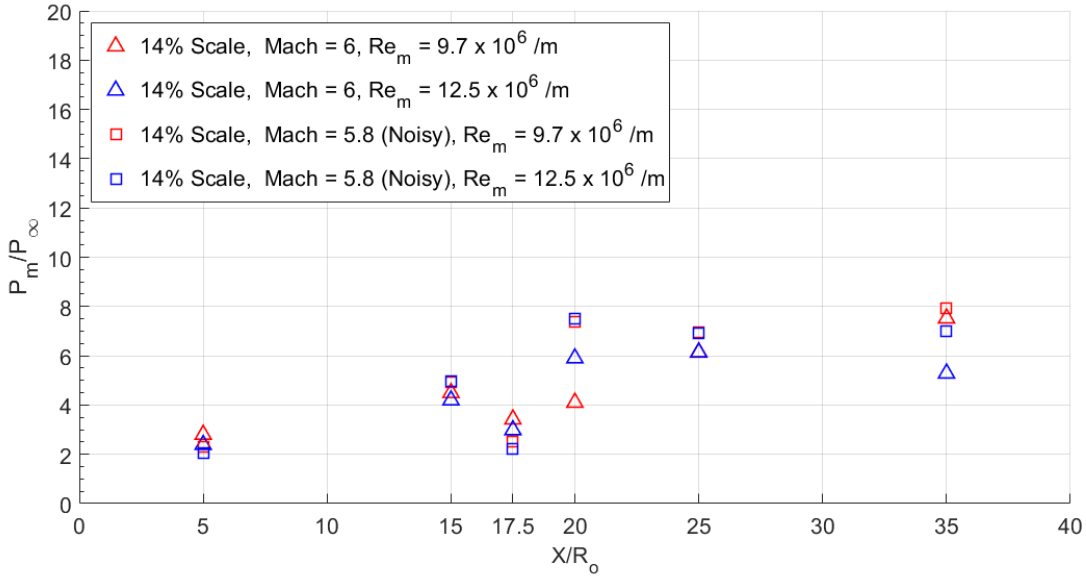

Figure 6.7. Noisy and quiet flow comparison of normalized IML static pressure for the 14% model.

Angle of attack had the most drastic change in the internal pressure ratios of the 14% model. A comparison is made between a 0° and 6° AoA case with the 14% scaled model in Figure 6.8. The 6° AoA case had a pressure gain nearly 3x the value of the 0° AoA case and 2x the Mach 5.8 0° AoA case at $X/R_\circ = 20$. Pitching the model increases the relative deflection angle of the leading shock, causing a pressure rise exceeding that of an on-design condition. This pressure rise was sustained through the isolator region. Again, measured static pressures appear mostly independent of Reynolds number. Slight deviations may occur due to a thicker boundary layer for the lower Reynolds number case. This effect is to be studied more thoroughly on the final INlet model, which has an applied viscous correction to the model's surfaces.

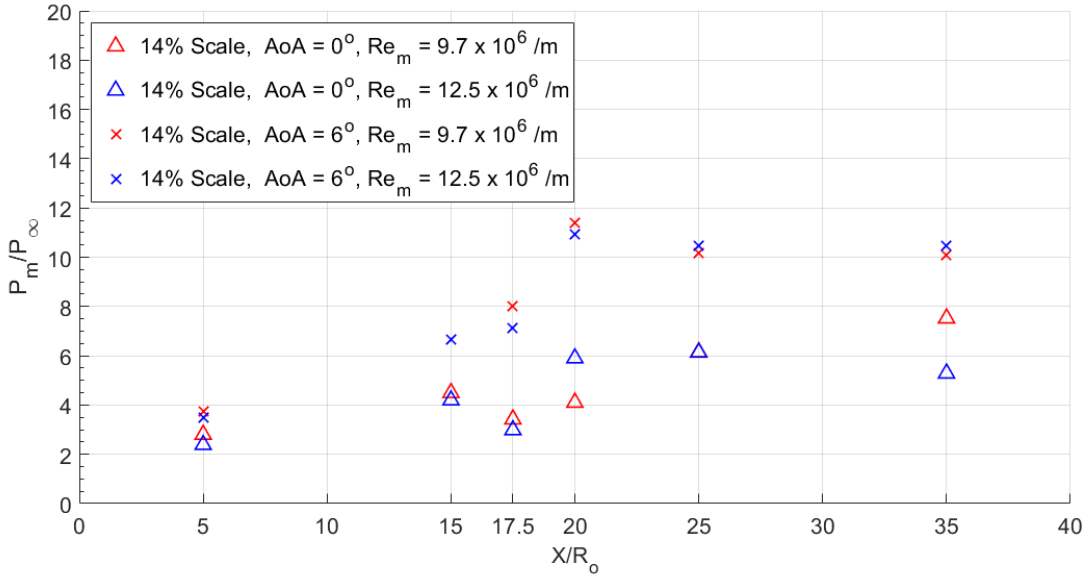

Figure 6.8. Angle of attack comparison of normalized IML static pressure for the 14% model.

The internal pressure profiles also reveal other trends about both INlet models. There appears to be a consistent drop in pressure gain at the $X/R_\circ = 17.5$ sidewall Kulite location across several different run conditions. This loss in pressure may be related to the on-design spillage phenomena discussed in previous sections. Sidewall boundary layer separation could also be a cause for this effect and requires more investigation. If flow is being spilled, then the high-pressure air is leaving the inlet and dropping the static pressure. Future schlieren studies will confirm this result and its affect on the leading shock structure. The Kulite pressure transducers in the inlet's isolator section also measure a gradual rise in static pressure. This is likely due to the isolator shock-train, which causes additional static pressure gain to the captured flow.

For a functioning high-speed inlet, the incoming flow must be compressed and remain supersonic. The pressure profiles reported here show a consistent trend of increasing mean pressures throughout the streamtube flowpath. Subsonic pressures past the throat region are indicative of an unstarted inlet and are calculated based on the 1D normal shock equations. Normal shock pressure ratios are on the order of $P_{i+1}/P_i \approx 10.3$ at Mach 3 and $P_{i+1}/P_i \approx 18.5$ for Mach 4. These ratios must be multiplied by the pressure gain ratios through the leading

oblique shock for Mach 6 flow at a 6° deflection angle ($P_i/P_\infty \approx 2.3$) and the isentropic compression from the intake's inward-turning surface. If the isentropic pressure gain is neglected, the final throat pressure ratios would be $P_m/P_\infty \approx 23.7$ and $P_m/P_\infty \approx 42.5$, for a Mach 3 and Mach 4 throat, respectively. The reported values are sufficiently below this margin, with the highest throat pressure ratio nearing $P_m/P_\infty \approx 12$ for the 6° AoA case. It is safe to assume, with these calculations, that the internal core flow is supersonic and the INlet models have successfully self-started at all reported conditions.

6.3 Forced Intake Unstart

The resiliency of intake systems to forced unstart is an important quantity that provides a safe operating margin for flight vehicles. Unstart can be simulated by choking the flow within the isolator through several different mechanisms. A mechanical blockage, such as a downstream conical plug, provides throttling capability if the plug is moved into the isolator and restricts the core flow's exit area. A thermal blockage occurs from combustion that drives the flow to a sonic condition from the Rayleigh flow condition. Also, the flow can be choked from mass-injection. This last method was used in the experiment to simulate a back-pressure condition at different freestream Reynolds numbers. The amount of flow injected into the isolator was calculated by assuming choked exit flow at the isolator's injection port. Choked flow occurs when the pressure ratio across the orifice (P^*/P_t) drops below 0.53 for the run duration. The maximum back-pressure occurs during partial unstart, which resulted in a pressure ratio of $P_{Isolator}/P_{Plenum} = 0.136$, which was safely below the limit and validated the assumption. The choked flow relation for a perfect gas is shown in equation (6.1), where P_t and T_t are stagnation pressure and temperature of the plenum gas.

$$\dot{m}_{\text{injection}} = A_{orifice} P_t \sqrt{\frac{\gamma}{RT_t}} \left(\frac{\gamma+1}{2}\right)^{-\frac{\gamma+1}{2(\gamma-1)}} \tag{6.1}$$

The jet-injection system described in chapter 5 provides a plenum of high-pressure air that can be routed into the blockage models. The stagnation pressure of the plenum (P_t) was set to a constant of 30 psig for all mass-injection studies. Total temperature of the air was taken as room temperature ($T_t = 293$ K). Due to time limitations, the mass-injection

studies were only performed on the small 9% scale blockage model. The injection system was triggered approximately 0.75 seconds after the fast-valve was activated. The delay ensures that the tunnel can sufficiently start and gives a small window to collect reference data before the mass injection begins.

6.3.1 Back-Pressure Profiles

The back-pressure study was conducted with the 9% model at 0° AoA for three freestream Reynolds numbers ($Re_m = 12.7 \cdot 10^6/m,\ Re_m = 9.7 \cdot 10^6/m,\ Re_m = 6.4 \cdot 10^6/m$) which are referred to as the high Reynolds number, medium Reynolds number, and low Reynolds number condition, respectively. All back-pressure runs were conducted at a Mach 6 quiet flow condition. The state of the internal flow path was determined through mean pressure and pressure fluctuation measurements. Mean pressures were calculated from the averaged DC pressure signal trace for a 0.1 second (200,000 point) increment. Pressure fluctuations were calculated by integrating the power spectra of the 0.1 second sampled signal over a given frequency range. A low frequency band [10 Hz - 1 kHz] and a high frequency band [1 kHz - 50 kHz] was defined. The power-spectra was integrated over these frequency bands to find the total RMS fluctuation magnitude. These pressure fluctuation values were normalized by the mean pressures for their respective location. Two states of the inlet are compared at each freestream Reynolds number condition: mass-injection active (Blowing On [Red]) or no mass-injection (Blowing Off [Blue]).

It is helpful to have a rule-of-thumb for the estimated pressure rise within the internal contraction during inlet unstart. A series of 1D pressure ratios can be solved from theoretical calculations to give this estimate. It is known that the leading oblique shock is turned by a 6° wedge angle for all osculating plane solutions. The leading shock pressure ratio is calculated as $P_{\mathrm{i}}/P_\infty = 2.3$ from the oblique shock relations. Viscous CFD shows that the captured streamtube is at Mach 4.6 at the beginning of the internal contraction. If a standing normal shock develops there, then the pressure rise estimate is $P_{Throat}/P_{\mathrm{i}} = 24.5$ from normal shock relations. If intermediate isentropic compression from the inlet surface is neglected, then the total pressure ratio is $P_{Throat}/P_\infty = 56.3$ for an unstarted inlet.

The highest Reynolds number case ($Re_m = 12.7 \cdot 10^6/m$) studied with the jet-injection system is presented in Figure 6.9. During the blowing event, the maximum back-pressure ratio in the isolator reaches $P_m/P_\infty \approx 36$. The effect is immediately noticeable when compared to the baseline blowing-off condition at locations $X/R_\circ = 25$ and $X/R_\circ = 30$. No other upstream influence appears on sensors. Although the isolator shock train moves forward, the back-pressure is not strong enough to eject it from the inlet. Interestingly, low frequency RMS content appear to dominate the unsteadiness measurements at $X/R_\circ = 25$ and $X/R_\circ = 30$ compared to pre-blowing data. Elevation in low frequency content is likely due to shock unsteadiness, which suggests shock train movement from the blowing event. RMS fluctuations upstream of $X/R_\circ = 25$ appear similar to pre-blowing data.

The second highest Reynolds number run ($Re_m = 9.7 \cdot 10^6/m$) is shown in Figure 6.10. The effect of blowing is immediately apparent from the rise in isolator pressure ratios. The pressure transducers at $X/R_\circ = 25$ and $X/R_\circ = 30$ show a jump to $P_m/P_{inf} \approx 60$. However, the throat pressure transducer at $X/R_\circ = 20$ stays below the predicted throat unstart pressure ratio of $P_{Throat}/P_\infty = 56.3$. The isolator shock train has not yet been disgorged from the inlet and the inlet remains fully started. However, increases in pressure at the $X/R_\circ = 15$ and 17.5 locations hint at change in the throat shock strength.

Analysis of the RMS pressures show an elevation of the high frequency and low frequency content above baseline at nearly all locations. One exception is the last sensor location at $X/R_\circ = 30$, which is directly ahead of the mass-injection port. Fluctuations also appear to affect the sensor at $X/R_\circ = 10$. This sensor is in the external contraction of the inlet, so any perturbations would have to travel upstream through the boundary layer. Downstream acoustic information in a scramjet isolator travels upstream, even if the inlet remains fully started.

The last jet-injection run was conducted at $Re_m = 6.4 \cdot 10^6/m$ and presented in Figure 6.11. This final case shows the most drastic changes in internal mean pressures and RMS pressures. In this case, the back-pressure resistance appears to flatten at $P_m/P_\infty \approx 60$ for most sensors within the isolator. The throat unstart pressure limit ($P_{Throat}/P_\infty = 56.3$) is nearly surpassed. The isolator shock has propagated upstream and is nearly disgorged from the inlet at $X/R_\circ = 15$, which is the start of the internal contraction. This is likely a soft

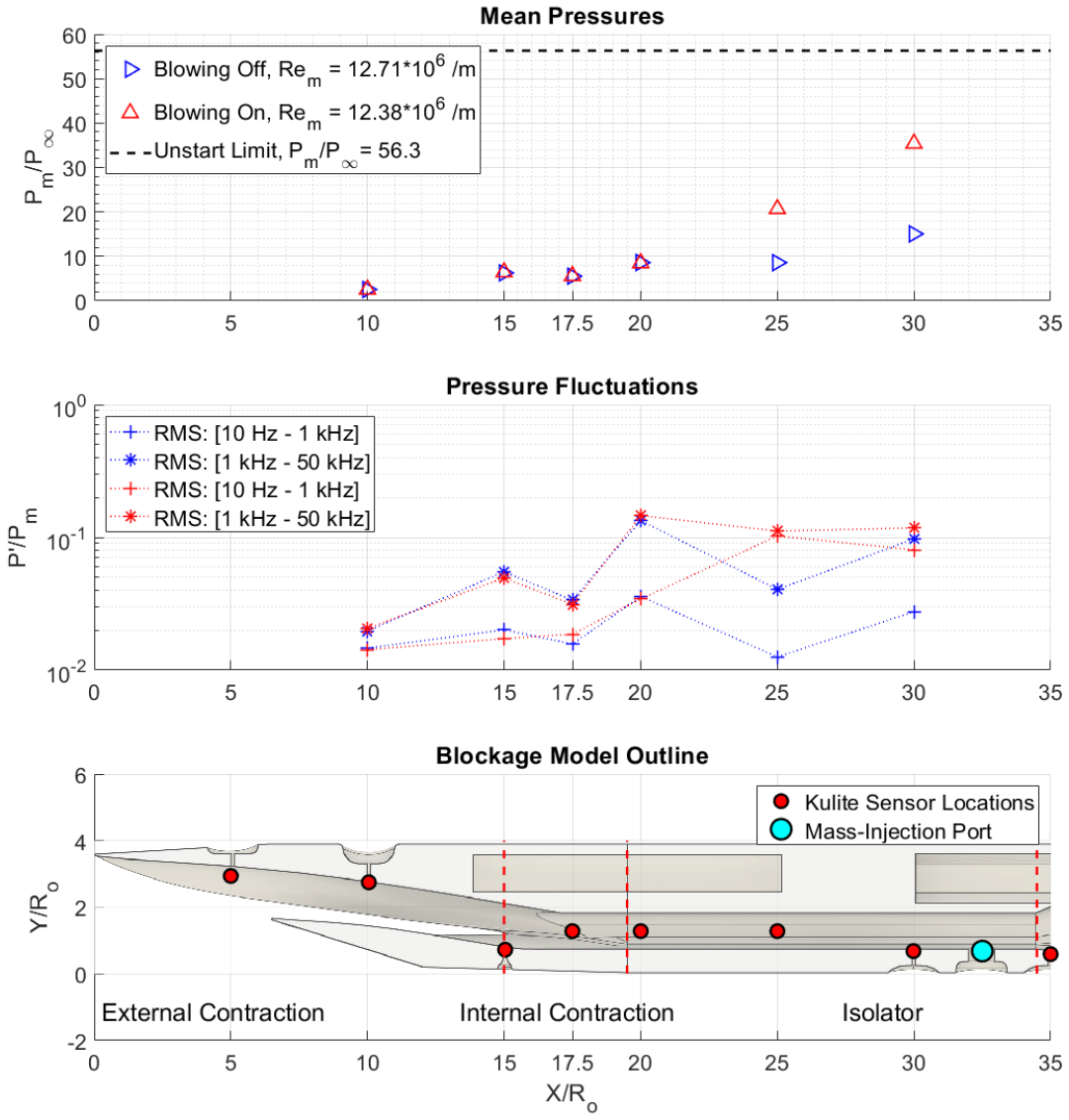

Figure 6.9. Jet-injection INlet internal flowpath analysis at $Re_m = 12.7 \cdot 10^6/m$.

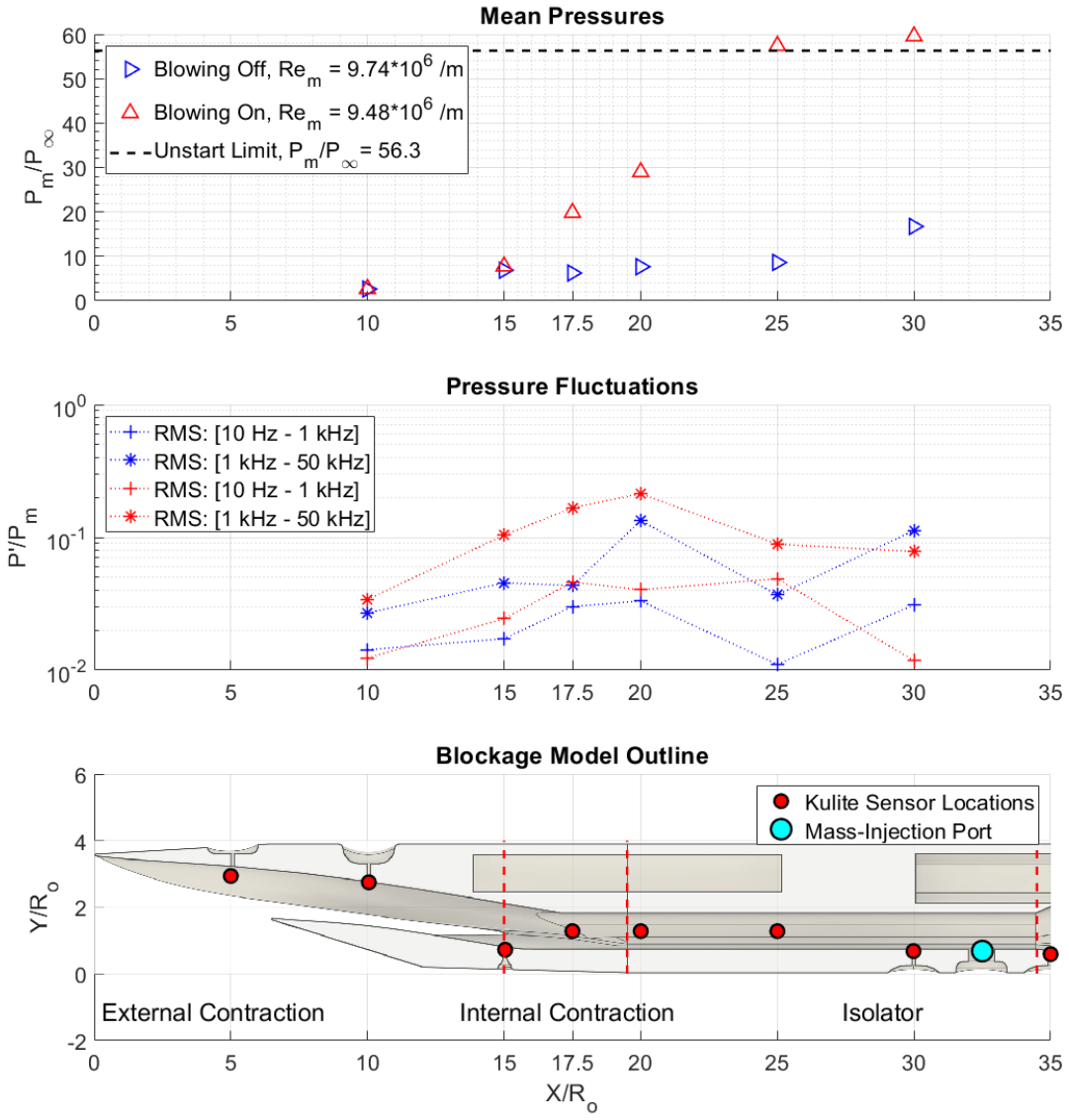

Figure 6.10. Jet-injection INlet internal flowpath analysis at $Re_m = 9.7 \cdot 10^6/m$.

intake unstart, where a mixture of subsonic and supersonic flow exits within the internal flowpath. Future schlieren photography will verify flow spillage along the side cowls.

There is an elevation in RMS pressures for all locations except for $X/R_\circ = 30$. The most drastic spike in RMS is seen at $X/R_\circ = 15$, where the blowing-on values are nearly two orders of magnitude larger than baseline. This is likely due to an unstable normal shock sitting in this region, causing unsteady flow spillage. Similar to the medium Reynolds case, fluctuations are traveling upstream and effecting RMS values at the $X/R_\circ$ =10 location. The power spectra of the Kulites during this unstart event are analyzed in the cavity resonance subsection.

6.3.2 Shock Arrival Tracking

A shock tracking code was developed to determine the speed of the leading shock in the isolator shock train during back-pressure and unstart events. The DC pressure signal from Kulites along the intake's IML was used to calculate the isolator's shock location over time. A moving-average of 40,000 points (0.02 second increments) of the DC pressure signal was computed to show large changes in static pressure. Additionally, three separate methods were used to calculate pressure fluctuations. The first two methods calculate mean-removed RMS pressure fluctuations over a 0.02 second window increments for specific frequency bands. A low frequency band [50 Hz - 5 kHz] and a high frequency band [50 Hz - 50 kHz] was defined. The power-spectra was integrated over these frequency bands to find the total RMS fluctuation magnitude. The PSDs were calculated from Welch's method with 50% window overlap and a frequency resolution of 100 Hz. A third method calculated mean-removed standard deviation of the same signal. All methods were calculated over a trailing 0.02 second window to simulate real-world detection. Pressure RMS and STD values were normalized by the mean pressure over the same time window.

It was determined that the standard deviation calculations show the clearest distinction of shock pass-over during analysis. A comparison of the three methods is provided in Figure 6.12. RMS calculations show changes from shock pass-over, but peaks are not as prominent and sometimes do not appear at all. Prominent, consistent peaks are required to for the

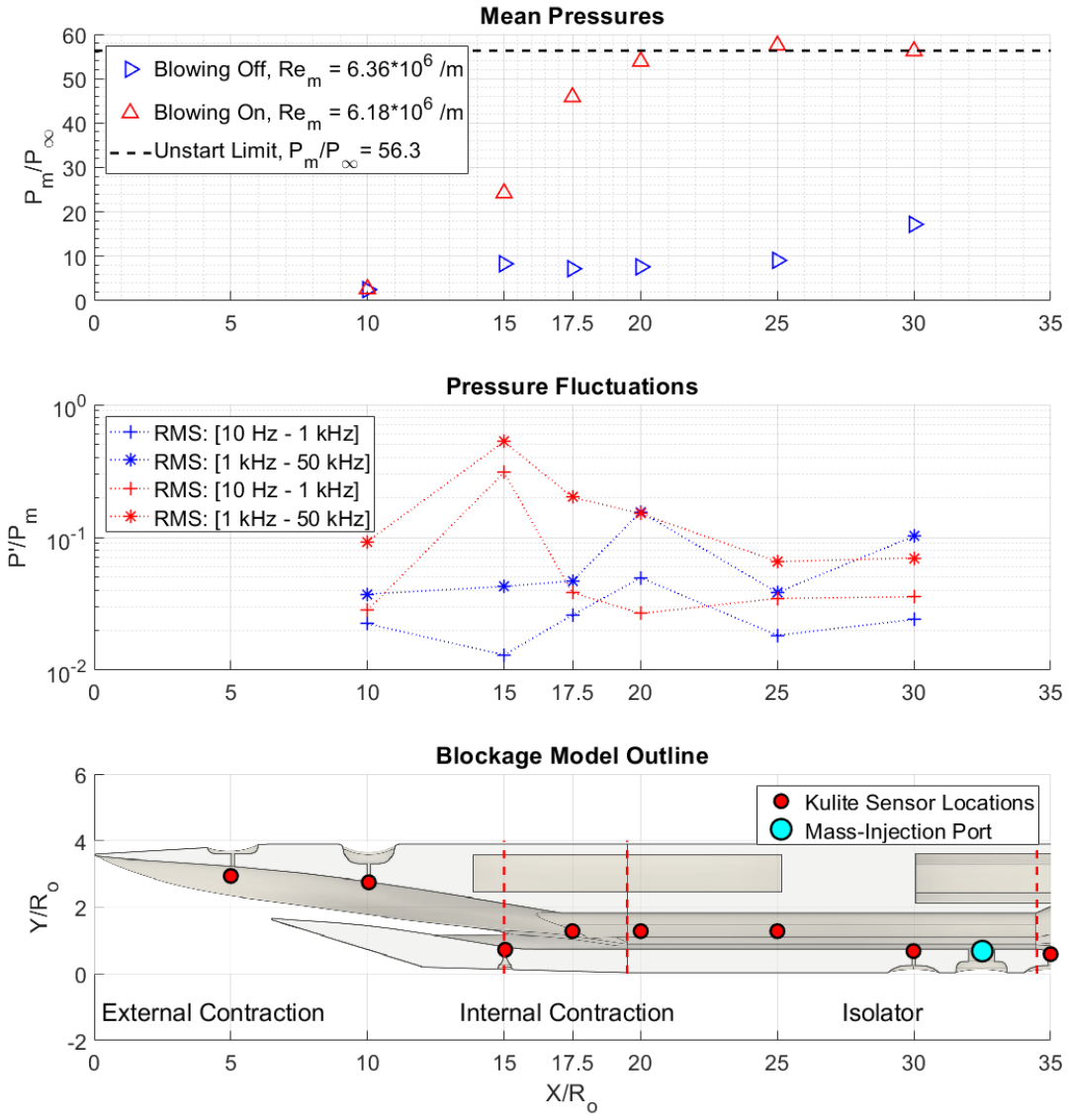

Figure 6.11. Jet-injection INlet internal flowpath analysis at $Re_m = 6.4 \cdot 10^6/m$.

Matlab peak-finding function to automatically detect the shock. The peak-finding function is fed the array of standard-deviation values for a given sensor and discriminates peaks that are larger than 3x the standard deviation of the data. The peak is located, recorded, and plotted. Sensors that do not see a clear peak are omitted from the shock arrival tracking catalog.

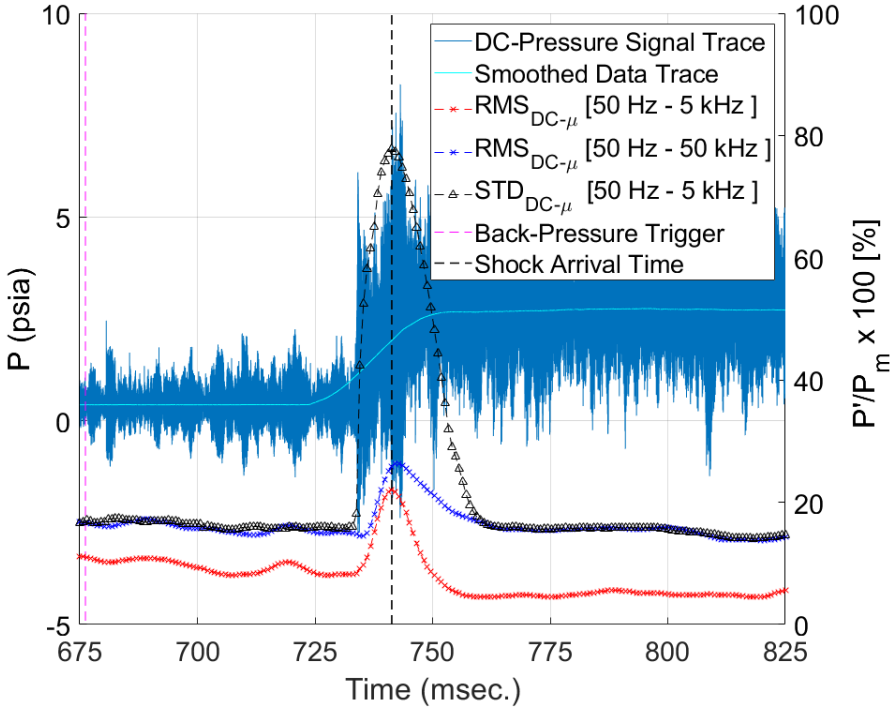

Figure 6.12. Shock arrival time comparison for Kulite 5 at $X/R_\circ = 20$ during a jet-injection event.

A sample case of the clearest unstart event is shown in Figure 6.13. All Kulites and their locations are labeled for reference. The blowing trigger is registered at time ≈ 0.676 seconds. High pressure air then travels through the tubing network into the isolator. The isolator Kulite at $X/R_\circ = 30$ is the first to see a jump in static pressure, pressure RMS, and pressure standard deviation at ≈ 0.726 seconds. The standard deviation peak is the most distinct compared to the other RMS methods. The peak finding algorithm correctly locates the center of the peak and records the time of shock pass-over. The process is repeated at other locations as the the shock continues to move upstream. Kulites at locations $X/R_\circ =$

25, 20, and 17.5 see clear peaks. Kulite sensors at $X/R_\circ = 10$ and 15 see a general jump in RMS and STD values, but they do not see a distinct peak. The sensor at $X/R_\circ = 15$ is at the beginning of the internal contraction, so any inlet unstart normal shock would sit at this location. Since this is the farthest a normal shock can move forward, it will contribute to the sustained fluctuation levels detected by the Kulite at this location. The sensor at $X/R_\circ = 10$ is in the external contraction region and likely never sees shock pass-over. However, it does detect boundary layer fluctuations traveling upstream. This explains why neither Kulite #2 or #3 see a clear peak but still see an elevation in pressure fluctuation levels. The medium and low Reynolds number shock arrival-tracking plots are cataloged in appendix G.

The standard deviation values of each sensor are shown in Figure 6.14. The plot clearly shows the shock traveling upstream in time. The shock moves quickly through the isolator, but slows down as it nears the internal contraction. Since time between peaks and distance between sensor locations are known, the average speed of the ejected shock can be calculated later. Although sensors at $X/R_\circ = 10$ and 15 do not see a shock, they do see elevated deviation values. Information from the unstart event has propagated upstream past the standing shock that sits in the cowl plane at the start of the internal contraction.

6.3.3 Unstart Detection

Although the initial plenum stagnation pressure was equivalent between runs ($P_t = 30$ psig), the speed of the shock train was not. There is a general trend of faster shock-train movement at lower freestream Reynolds numbers. Two potential effects are acting to change the speed of the isolator shock train. The first effect is the thickness of the boundary layer. A thicker boundary layer, from a lower freestream Reynolds number, may restrict the core flow area at the throat. This constriction decreases the isolator Mach number and makes it more susceptible to inlet unstart. The second effect is that the total massflow ingested by the inlet drops with lower freestream Reynolds numbers. The maximum ingested massflow of the inlet is analytically calculated by assuming 100% freestream capture of the incoming streamtube. Equation (6.2) gives the relation for massflow rate in terms of Mach number (M), static pressure (P_s), and static temperature (T_s). These terms are known from the

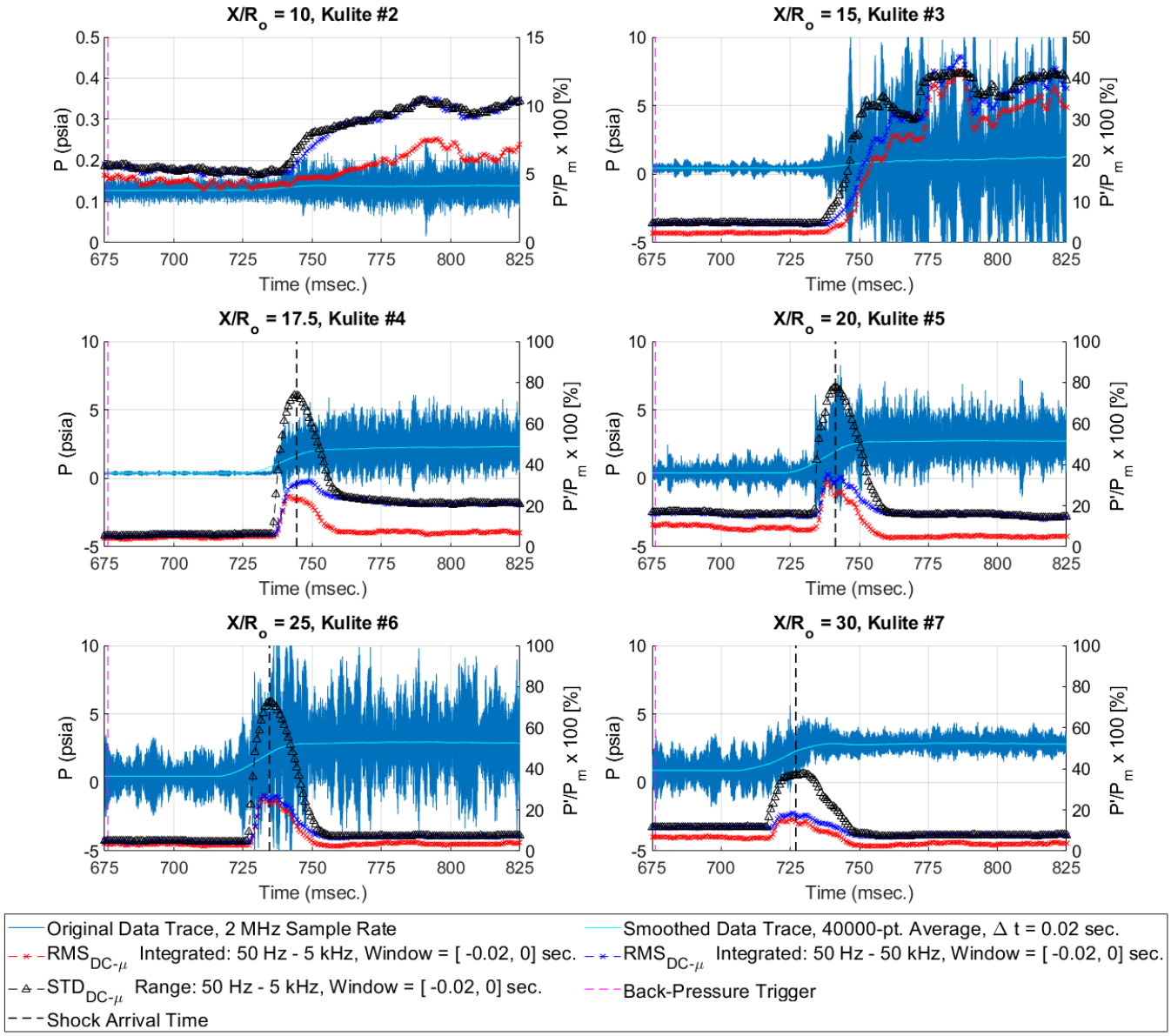

Figure 6.13. Shock arrival detection example for the INlet soft-unstart case at $Re_m = 6.4 \cdot 10^6/m$.

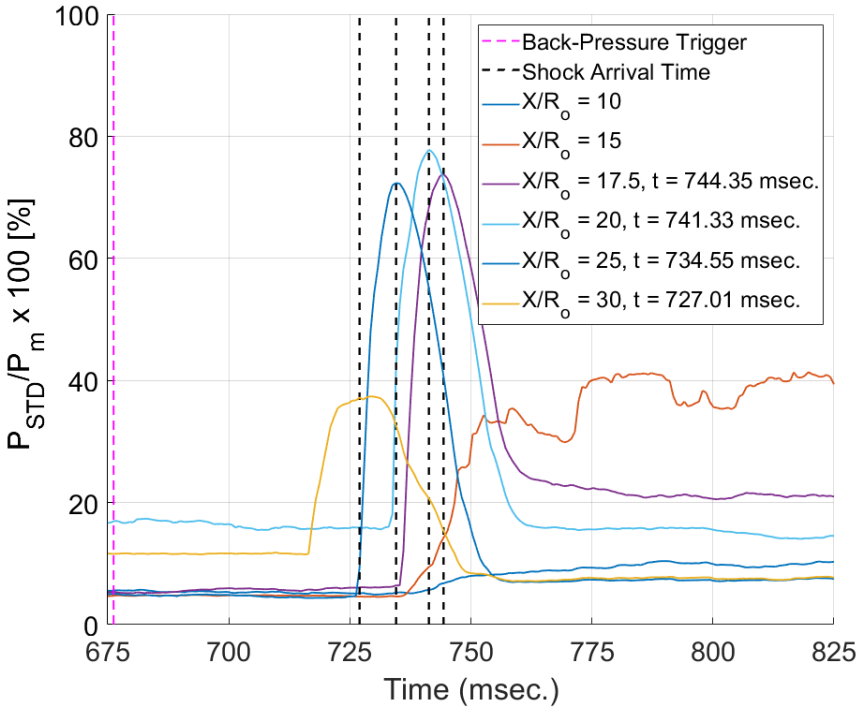

Figure 6.14. Condensed standard-deviation arrays for all Kulites from the INlet soft-unstart case at $Re_m = 6.4 \cdot 10^6/m$.

freestream tunnel conditions. A lower tunnel stagnation pressure necessarily means a lower massflow rate through the tunnel core flow and the inlet.

$$\dot{m}_{Capture_{Analytical}} = \frac{P_s}{RT_s} A_{frontal} M \sqrt{\gamma R T_s} \tag{6.2}$$

The theoretical massflow capture estimate can be compared to a reference CFD calculation. The CFD massflow rate is calculated by taking area-averaged quantities of density (ρ_{avg}) and axial velocity ($v_{x_{avg}}$) at the throat. The CFD throat area is scaled to match the 9% blockage model size. The full relation is shown in equation (6.3). The CFD solution accounts for upstream overboard mass spillage, so it will be lower than the perfect-capture estimate of the analytical prediction.

$$\dot{m}_{Capture_{CFD}} = \rho_{avg} A_{throat} v_{x_{avg}} \tag{6.3}$$

Since the amount of massflow injected in the isolator is constant throughout the jet-injection study, the only variable that changes drastically is the incoming massflow rate determined by tunnel conditions. If the ratio between the captured massflow rate and the injected massflow rate is taken as a function of shock speed, a clear trend emerges. Figure 6.15 shows that faster shock speeds occur from larger massflow rate fractions. This makes sense intuitively because there is less upstream mass and momentum to slow the forward-moving shock train. If the massflow fraction becomes too large, then the inlet-isolator system cannot accept any more air before choking. The shock train is disgorged and unstart occurs. The error bars in the plot represent the slowest and fastest shock speeds measured from the shock-tracking code. The average of all calculated shock speeds is the centered data point. A massflow ratio limit is placed at $\dot{m}_{Injection}/\dot{m}_{Capture} = 0.60$ to estimate the 9% INlet model's unstart range.

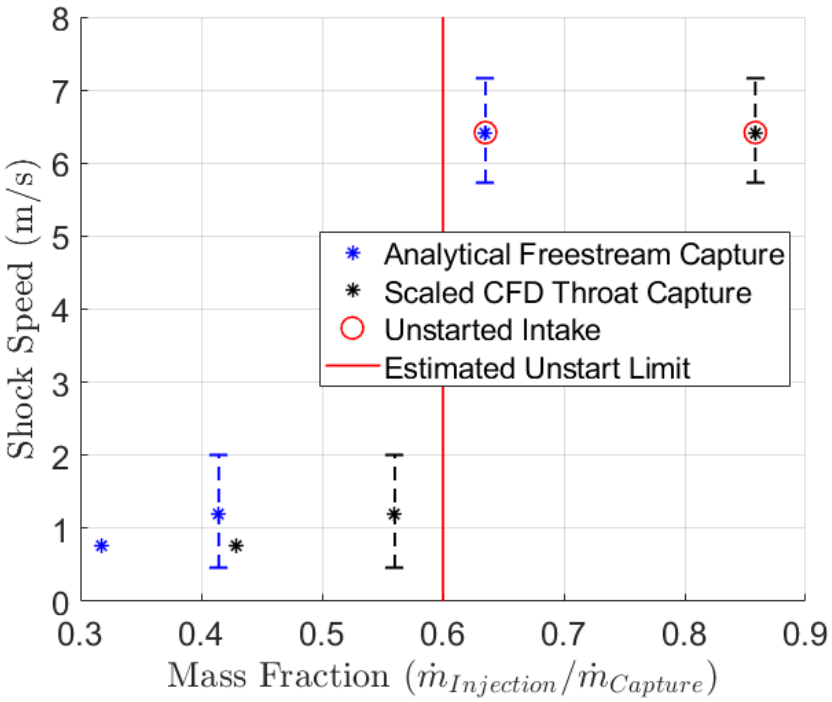

Figure 6.15. Shock speed as a function of massflow rate ratio with soft-unstart intake boundary.

6.3.4 Unstart Boundary

An unstart map for the 9% model can be constructed from two independent variables: tunnel stagnation pressure ($P_\circ$) and jet-injection plenum stagnation pressure (P_t). From these quantities, it is possible to determine the inlet massflow rate through equations (6.2) or (6.3). The injected massflow rate is similarly known from equation 6.1. The ratio of the captured massflow rate to the injected massflow rate acts as a dependent variable. The catpured massflow parameter is calculated from a scaled CFD solution. A contour plot of massflow fraction against choked injection masflow and tunnel total pressure is shown in Figure 6.16. The massflow ratio unstart limit is highlighted by a red line. Any condition to the right of this line would cause unstart, while any condition to the left would keep the inlet started. This contour map acts as an operability map for the combined tunnel and intake model system.

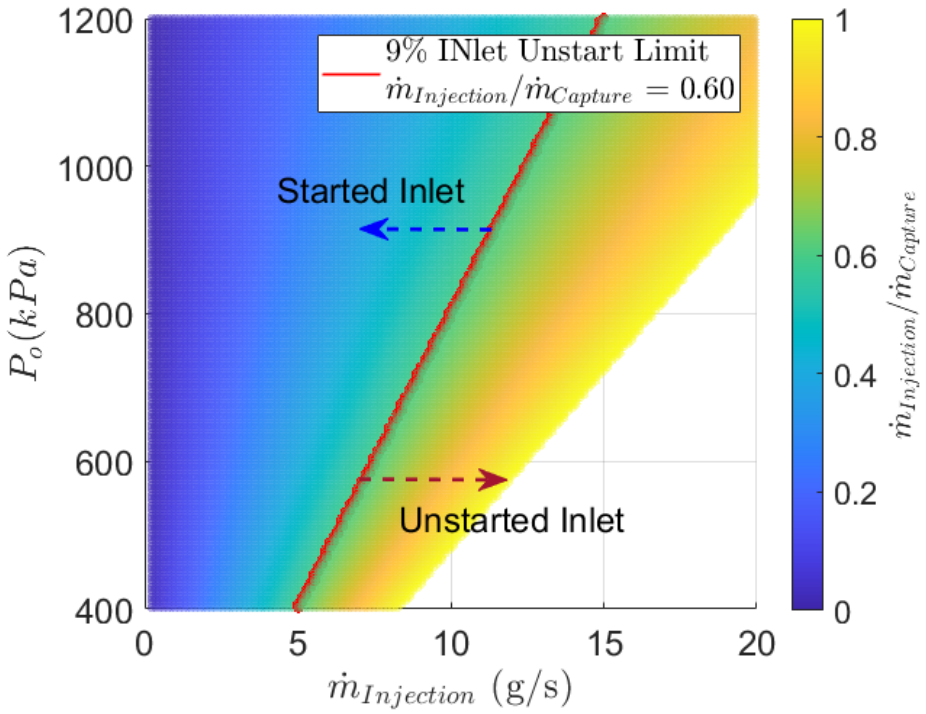

Figure 6.16. 9% INlet extrapolated startability map for various jet massflow rates, jet massflow ratios, and tunnel stagnation pressures.

6.3.5 Power Spectra Analysis

A small selection of power spectra were analyzed for the 9% scaled INlet model using Kulite DC-pressure signals. The presented power spectra were calculated over a 0.05 second data segment with Welch's method, a 200 Hz frequency resolution, and a 50% window overlap with 500 Hamming windows. The pressure signal was normalized by the local mean pressure for the time at which the data were recorded. Power spectra provide insight into frequency content of the flow within both the external contraction compression ramp and the isolator. It is expected that flow within the isolator is turbulent due to interactions with the shock train. The effects of mass jet-injection on the state of flow perturbations are shown within this section.

The first PSD presented in Figure 6.17 is for the soft-unstarted 9% INlet case during back-pressure blowing at t = 1.64 sec. The Kulites presented on the plot are all within the internal contraction or isolator regions of the intake. All sensors show highly elevated

spectra indicative of turbulent flow. The Kulite sensor located at $X/R_{\circ} = 15$ shows especially high power frequency content below 5 kHz. This sensor location sits at the beginning of the internal contraction, which is also where the standing normal shock sits during intake unstart. A large amount of shock unsteadiness and flow spillage likely contributes to the elevated power in this frequency range. Also, all displayed sensors detect frequency peaks at 180 Hz, 1.32 kHz, and 2.86 kHz. This is indicative of a universal cavity resonance within the inlet-isolator system. These frequency peaks are not detected during the blowing-off condition.

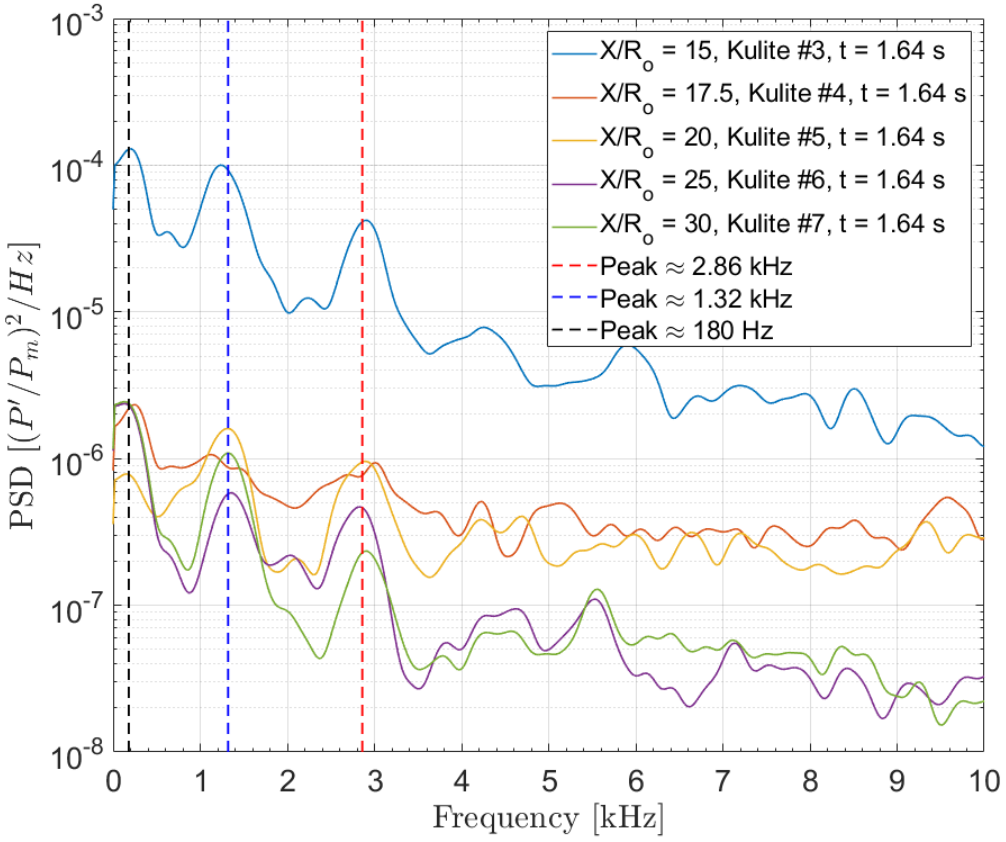

Figure 6.17. Power spectra of internal contraction and isolator Kulites for the 9% scale model during soft-unstart. [Mach 6 flow, $P_{\circ,\mathrm{i}} = 85.2$ psia]

Similar frequency peaks were detected on the external contraction Kulites during the back-pressure event. Power spectra of the external contraction Kulites are presented for run times before (t = 0.45 sec.) and during (t = 1.25 sec.) the back-pressure event in

Figure 6.18. During unstart, the spectra for Kulites #1 and #2 become elevated and several distinct peaks become apparent. Although these Kulites are sufficiently upstream of the isolator, there is acoustic information traveling upstream through the boundary layer. A peak-finding algorithm was implemented in Matlab to detect the first four peaks at least 200 Hz in width. The results coincide with the peaks detected by Kulites #3 - #7 within the isolator. The 1.36 kHz - 1.38 kHz and 2.80 kHz - 2.86 kHz peaks consistently appear on PSDs throughout the unstart event. The frequency peaks above 2.86 kHz are highly transient and disappear/reappear depending on the time analyzed.

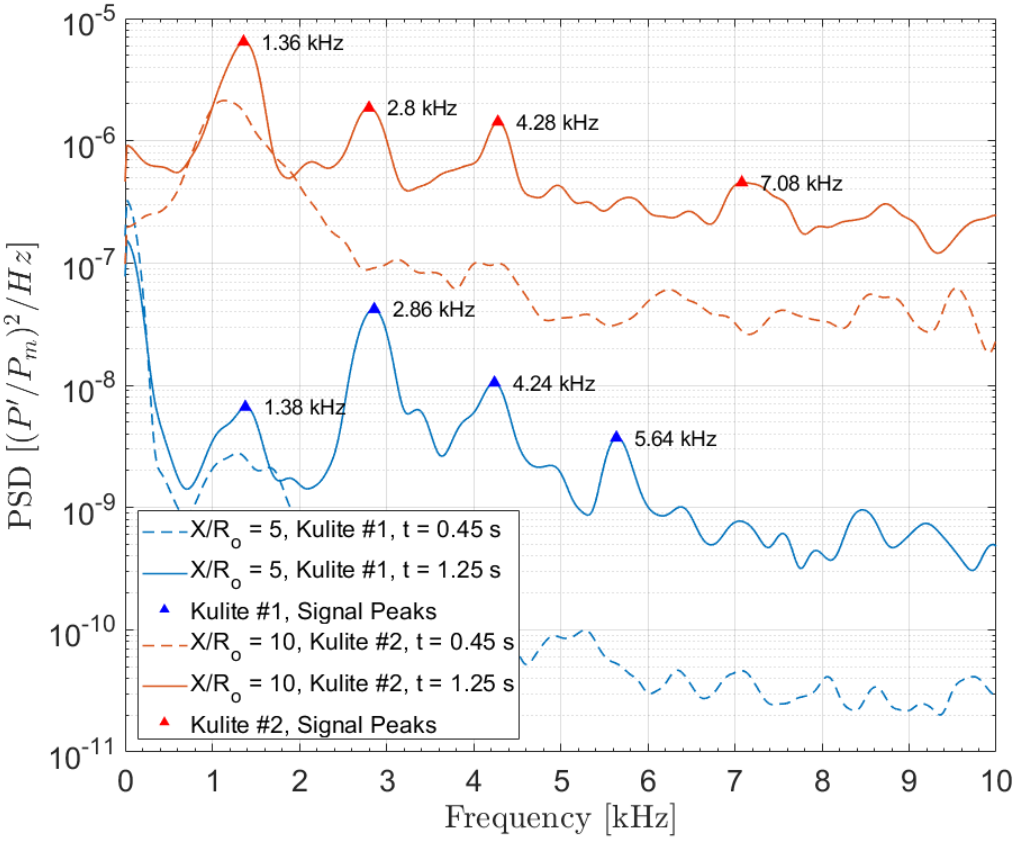

Figure 6.18. Power spectra of external contraction Kulites for the 9% scale model before and during soft-unstart. [Mach 6 flow, $P_{\circ,\mathrm{i}} = 85.2$ psia]

The peaks detected on the external contraction portion of the intake are harmonics of the main resonance detected within the isolator. The higher harmonics likely exist within

the isolator. However, the state of the turbulent boundary downstream makes it hard to discriminate these peaks from the elevated spectral content. A cavity resonance calculation was carried out to determine the theoretical frequencies for an open cavity and its harmonics. The cavity length was was determined by the distance between the start of the internal contraction and the downstream location of the back-pressure port. The BPP is the beginning of the downstream blockage from mass-injection. Figure 6.19 shows the cavity distance over a sample INlet model. A similar calculation was done by Rodi to estimate a dual-mode scramjet model unstart resonance at Mach 4 [113]. He calculated a theoretical resonance of 246 Hz while the measured scramjet resonance was close to 300 Hz, showing decent agreement between theory and reality.

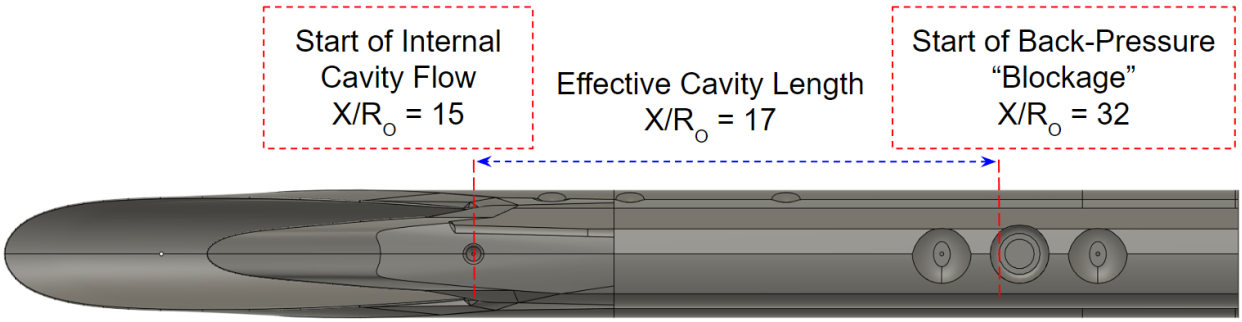

Figure 6.19. Definition of the effective cavity length for the INlet model.

Since distance is known from the dimensional throat height for the 9% model ($R_\circ = 0.34$ in, L = 0.1468 m), the calculation can be carried out from equation (6.4). The acoustic speed is calculated from the total temperature within the model's internal boundary layer (T_t = 425K [Measured] - 433K [Nominal]). Both temperatures were used in the calculation to account for uncertainty in the total temperature measurement.

$$f = n\frac{a}{2L} = n\frac{\sqrt{\gamma R T_t}}{2L} \tag{6.4}$$

Figure 6.20 shows the possible mechanisms that may cause the upstream propagation of acoustic waves. During a full unstart the flow in the isolator is subsonic. Therefore, acoustic information can travel upstream through the core flow. Additionally, information can travel upstream through the subsonic portions of the isolator boundary layer. This

information is radiated from downstream disturbances, such as massflow injection from the back-pressure port. These acoustic waves interact with the cavity and produce harmonics which are detectable by high frequency pressure transducers.

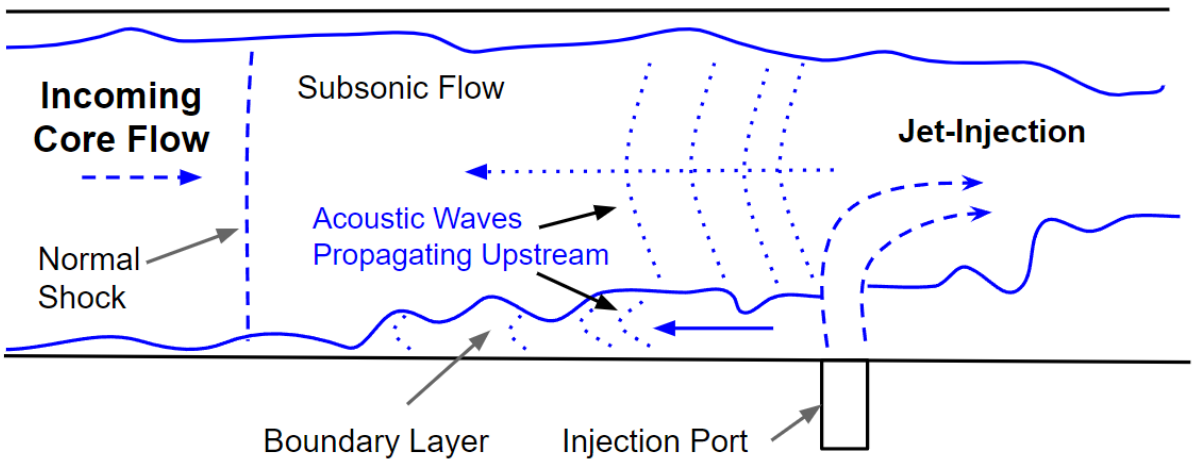

Figure 6.20. Acoustic resonances and modes of propagation in a 1D isolator.

Results of the calculations compared with the detected peaks are presented in Table 6.1. The measured peaks are in good agreement with the calculated harmonics. Future studies will seek to measure the effect of these cavity resonances on inlet buzz and boundary layer on the sugar-scoop compression surface. The lower frequency peak seen in Figure 6.17 is transient in nature and more closely matches the measurements from Rodi. However, it does not match with any of the theoretical calculations. More investigation is necessary to verify the existence of harmoincs below 1 kHz. These low frequency disturbances are likely linked to shock unsteadiness or inlet buzz.

Table 6.1. Predicted cavity resonance frequencies for the 9% INlet blockage model.

Frequencies (kHz)		
n	**Predicted**	**Measured**
1	1.41 - 1.42	1.36 - 1.38
2	2.81 - 2.84	2.80 - 2.86
3	4.22 - 4.26	4.24 - 4.28
4	5.63 - 5.68	5.64
5	7.04 - 7.10	7.08

7. CONCLUSIONS

The main effort of this project was to develop, analyze, and test an unrestricted high-speed intake within a hypersonic quiet tunnel. To achieve these goals, an in-house design code was developed to aid in the creation of a shape-transitioned intake using a novel streamtracing technique. The final geometry, named the INlet, was analyzed by theoretical techniques, inviscid CFD, and viscous CFD. Two blockage models were subsequently constructed and tested within the BAM6QT. A blockage test campaign was undertaken to catalog essential information regarding tunnel starting behavior under various conditions. Additionally, Kulite pressure transducers provided information on the state of the model's internal flowpath. The results of the blockage tests influenced the design of the final model and identified interesting flow phenomena for future study.

7.1 Major Chapter Summaries

Chapter 3 describes the comprehensive inlet design code in detail. The code creates mixed-contraction, high-speed intake geometries by streamtracing unique solutions of the Busemann flowfield through a user-defined shape transitions. The theory of osculating axisymmetry is applied to stitch many local 2D flowfields together as an approximate design method for a 3D geometry. To create the compression surface, several iteration schemes work in-tandem to iterate on three key parameters: throat shock angle, throat Mach number, and centerbody radius. The outer loop was deactivated for expediency in the current project. The lower surface is then crafted through a local parallel-streamlines technique. All inlets are inward-turning by nature of the local Busemann flowfields. The design code incorporates a boundary layer viscous correction tool to adjust the inviscid surfaces outward by the estimated displacement thickness of a compressible turbulent boundary layer. Other blunting and export tools were also developed to ease model and mesh generation in CAD and CFD programs.

Chapter 4 analyzes the INlet geometry with streamtube-tracking analytical techniques and CFD. The streamtracing code contains built-in tools to estimate inlet flow characteristics. These include 1D performance quantities taken at the throat, compression-surface

flow property contours, and axial-slice flow property contours. Inviscid and viscous CFD solutions are compared against theoretical estimates to identify performance loss mechanisms. The analytical performance calculations over-estimate streamtube flow compression and mass capture efficiency. Computational results show noticeable flow spillage and shock structure deviation from theory near the cowl regions of the intake. These results hint at a breakdown in the osculating axisymmetric assumption along the steeper osculating-plane Busemann solutions. Other analysis shows that the conical throat shock misses the throat shoulder and is weaker overall. An experimental correlation predicts possible boundary layer separation from the throat shock. Additional analysis shows that the inward-turning surface will facilitate the formation of Görtler vortices that may lead to boundary layer transition.

Chapter 6 discusses the blockage campaign test results and offers suggestions to the creation of a final model. The BAM6QT started consistently above $P_{\circ,\mathrm{i}} = 50$ psia for the 9% scale model during Mach 6 quiet flow operation. The 14% model fared worse, with the BAM6QT only starting consistently above $P_{\circ,\mathrm{i}} = 90$ psia for Mach 6 quiet flow runs. Several cases of temporary unstart and sustained unstart were cataloged for various run conditions. Interestingly, the tunnel never unstarted with the bleed-valve closed and operating in a noisy Mach 5.8 condition. The self-starting nature of the INlet models were verified by mean pressure measurements and theoretical unstart pressure limits. To force inlet unstart, a limited jet-injection study was carried out to induce a large back-pressure event within the isolator of the 9% model. The results reveal a relatively large back-pressure limit of the intake ($P/P_\infty \approx 60$) before unstart. An unstart shock-arrival code identified the speed of the shock train during all jet-injection runs. During selected back-pressure events, a cavity resonance was detected from Kulite sensors within the isoloator and the external contraction region. Acoustic information appears to travel upstream through the boundary layer during large back-pressure events.

7.2 Design Recommendations

There were several important lessons learned from the model generation process and blockage campaign. The generation of inward-turning and swept geometries in CAD and

CFD programs require special attention to export formatting, endpoint preserving down-sampling techniques, and grid/mesh generation. The over-fitting of streamline points was a common problem for both CFD meshing and CAD. A custom polyfit community developed function was required to generate the complex lofted surfaces within Autodesk Fusion 360. The model OML is also a vital design parameter that must balance tunnel blockage limits and construction practicality while achieving experimental objectives. Material choice and processing methods must be considered as well. The blockage models were rapidly prototyped from a DLS process with CE-221. The DLS process is superior to FDM techniques due to the removal of stair-stepping and improvement of resolution down to 0.03 in. Although CE-221 is as strong as Polycarbonate, the DLS curing process created stress cracks that caused parts of the blockage models to fail below FEA FoS limits during pre-testing. The rapid advancements in 3D printing techniques are promising, but there are still many hiccups to be addressed.

The final INlet geometry will be based on a 12% scale, which seeks a balance between the two blockage models. Engineering drawings and schematics of the final model are presented in appendix H. This model scaling mitigates blockage issues experienced by the 14% model while maintaining a relatively large intake surface. The leading edge of the 12% INlet neatly fits within the viewing section provided by the BAM6QT rectangular sapphire windows. This ensures good schlieren visualization of the inlet and its leading shock structure. The 12% model is also streamlined due to the material choice. It will be constructed with stainless steel, allowing thinner walls compared to the plastic blockage models. Internal sensor routing will make the design easier to manage during experiments. The model is also modular, meaning that certain parts can be easily swapped or taken apart for inspection or installation.

7.3 Future Work

The work presented herein represents the first foray into the design, analysis, and testing of a hypersonic inlet within the BAM6QT. The final INlet model is designed to study a variety of fluid dynamic phenomena. This includes, but is not limited to, hypersonic boundary-

layer transition, shock-wave boundary layer interaction, off-design inlet operability, inlet buzz, and unstart phenomena. These complicated interactions are often coupled and require a variety of analysis techniques and instrumentation to understand completely. Schlieren visualization will assist with understanding unstart shock dynamics within the inlet-isolator system. High-frequency transducers will provide insight into the spectra content of IML pressures, especially near the throat SWBLI. Possible tests with fast PSP or TSP may also provide insight to unsteady shock dynamics along the isolator wall or boundary layer instabilities on the external compression surface. A larger scaled-up model will also be designed and tested within the AFOSR Notre Dame Large Mach-6 Quiet Tunnel at the University of Notre Dame to compliment the Purdue BAM6QT test campaign.

REFERENCES

[1] E. L. Goldsmith and J. Seddon, *Practical intake aerodynamic design*. American Institute of Aeronautics & Astronautics, 1993.

[2] J. Seddon and E. L. Goldsmith, *Intake aerodynamics*. Blackwell science Oxford, 1999, vol. 2.

[3] G. Laruelle and F. Les Mureaux, "Air intakes: Role, constraints and design," in *International Council of the Aeronautical Sciences Congress*, 2002, pp. 643–1.

[4] W. H. Heiser and D. T. Pratt, in *Hypersonic Airbreathing Propulsion*, Education Series, AIAA, 1994, ch. 5. Compression System or Components, pp. 197–266.

[5] S. D. Heister, W. E. Anderson, T. L. Pourpoint, and R. J. Cassady, *Rocket propulsion*. Cambridge University Press, 2019, vol. 47.

[6] T. Cain, "Design and evaluation of high speed intakes," in *RTO-EN-AVT-195-03*, 2019.

[7] J. J. Mahoney, *Inlets for supersonic missiles*. American Institute of Aeronautics and Astronautic, 1990.

[8] J. Fabri, "Air intake problems in supersonic propulsion," *AGARD-AG*, vol. No. 27, 1958.

[9] A. Sóbester, "Tradeoffs in jet inlet design: A historical perspective," *Journal of aircraft*, vol. 44, no. 3, pp. 705–717, 2007.

[10] R. S. Fry, "A century of ramjet propulsion technology evolution," *Journal of Propulsion and Power*, vol. 20, no. 1, pp. 27–58, 2004. DOI: 10.2514/1.9178.

[11] K. K. Aminjan, "A review on the change process and the evolution of aircraft engine air intake," *International Journal of Mechanics and Design*, vol. 4, no. 1, pp. 15–22, 2018.

[12] S. Candel, "Concorde and the future of supersonic transport," *Journal of propulsion and power*, vol. 20, no. 1, pp. 59–68, 2004.

[13] C. Danforth, "Distortion-induced vibration in fan and compressor blading," *Journal of Aircraft*, vol. 12, no. 4, pp. 216–225, 1975.

[14] P. Sforza, *Theory of Aerospace Propulsion*, ser. Aerospace Engineering. Elsevier Science, 2016, ISBN: 9780128096017. [Online]. Available: https://books.google.com/books?id=GNYCDAAAQBAJ.

[15] S. R. Wellborn, B. A. Reichert, and T. H. Okiishi, "Study of the compressible flow in a diffusing s-duct," *Journal of Propulsion and Power*, vol. 10, no. 5, pp. 668–675, 1994. DOI: 10.2514/3.23778.

[16] L. D. V. Faro, "Supersonic inlets," *AGARDograph*, vol. No. 102, 1965.

[17] M. K. Smart, "Scramjet inlets," Queensland and University Brisbane (Australia) Centre for Hypersonics, Tech. Rep., 2010.

[18] M. K. Smart, "How much compression should a scramjet inlet do?" *AIAA journal*, vol. 50, no. 3, pp. 610–619, 2012.

[19] D. M. Van Wie, "Scramjet inlets," *Scramjet propulsion, Reston, VA, American Institute of Aeronautics and Astronautics, Inc., 2000,*, pp. 447–511, 2000.

[20] J. Colville and M. Lewis, "An aerodynamic redesign of the sr-71 inlet with applications to turbine based combined cycle engines," in *40th AIAA/ASME/SAE/ASEE Joint Propulsion Conference and Exhibit*, 2004, p. 3481.

[21] P. Merlin, "Design and development of the blackbird: Challenges and lessons learned," in *47th AIAA aerospace sciences meeting including the new horizons forum and aerospace exposition*, 2009, p. 1522.

[22] R. Longstaff and A. Bond, "The skylon project," in *17th AIAA International Space Planes and Hypersonic Systems and Technologies Conference*. DOI: 10.2514/6.2011-2244.

[23] J. A. Clough and M. J. Lewis, "Practical implications of integrating turbomachinery into the air turborocket," in *Turbo Expo: Power for Land, Sea, and Air*, vol. 41723, 2004, pp. 569–574.

[24] J. A. Medina, H. Patel, and B. Chudoba, "Inlet sizing of hypersonic vehicles for conceptual design," in *ASCEND 2021*. DOI: 10.2514/6.2021-4096.

[25] A. Kantrowitz and C. Donaldson, "Preliminary investigation of supersonic diffusers," *NACA Wartime Report*, vol. ACR-L5D20, pp. 1–25, 1945.

[26] J. F. Connors and R. C. Meyers, "Design criteria for axisymmetric and two-dimensional supersonic inlets and exits," Tech. Rep., 1956.

[27] A. Ferri and L. M. Nucci, "Preliminary investigation of a new type of supersonic inlet," *NACA TM*, vol. 2286, 1951.

[28] A. Ferri and L. M. Nucci, *Theoretical and Experimental Analysis of Low-Drag Supersonic Inlets Having a Circular Cross Section and a Central Body at Mach Numbers of 3.30, 2.75, and 2.45*. NACA, 1954.

[29] A. Ferri, *Scoop-type supersonic inlet with precompression surface*, U.S. Patent 2990142A, Nov. 5 1955.

[30] R. Askari and M. R. Soltani, "Symmetric and asymmetric performance investigation of a diverterless supersonic inlet," *AIAA Journal*, pp. 1–10, 2022. DOI: 10.2514/1.J061201.

[31] A. K. Flock and A. Gülhan, "Modified kantrowitz starting criteria for mixed compression supersonic intakes," *AIAA Journal*, vol. 57, no. 5, pp. 2011–2016, 2019. DOI: 10.2514/1.J057283.

[32] B. Sun and K.-y. Zhang, "Empirical equation for self-starting limit of supersonic inlets," *Journal of Propulsion and Power*, vol. 26, no. 4, pp. 874–875, 2010. DOI: 10.2514/1.46798.

[33] D. V. Wie, F. Kwok, and R. Walsh, "Starting characteristics of supersonic inlets," in *32nd Joint Propulsion Conference and Exhibit*. DOI: 10.2514/6.1996-2914.

[34] S. Molder, E. Timofeev, and R. Tahir, "Flow starting in high compression hypersonic air inlets by mass spillage," in *40th AIAA/ASME/SAE/ASEE Joint Propulsion Conference and Exhibit*. DOI: 10.2514/6.2004-4130.

[35] N. Moradian and E. Timofeev, "Starting characteristics of prandtl–meyer scramjet intakes with overboard spillage," *Journal of Propulsion and Power*, vol. 34, no. 1, pp. 189–197, 2018. DOI: 10.2514/1.B36574.

[36] S. Mölder and E. Timofeev, "Hypersonic air intake design for high performance and starting," in *RTO-EN-AVT-195*, 2019.

[37] J. Chang, N. Li, K. Xu, W. Bao, and D. Yu, "Recent research progress on unstart mechanism, detection and control of hypersonic inlet," *Progress in Aerospace Sciences*, vol. 89, pp. 1–22, 2017, ISSN: 0376-0421. DOI: https://doi.org/10.1016/j.paerosci.2016.12.001.

[38] E. J. Stephen, S. R. Hoenisch, C. J. Riggs, M. L. Waddel, M. A. Bolender, and T. E. McLaughlin, "Hifire-6 unstart conditions at off-design mach numbers," in *53rd AIAA Aerospace Sciences Meeting*. DOI: 10.2514/6.2015-0109.

[39] M. K. Smart, "Design of three-dimensional hypersonic inlets with rectangular-to-elliptical shape transition," *Journal of Propulsion and Power*, vol. 15, no. 3, pp. 408–416, 1999. DOI: 10.2514/2.5459.

[40] R. Gollan and P. Ferlemann, "Investigation of rest-class hypersonic inlet designs," in *17th AIAA International Space Planes and Hypersonic Systems and Technologies Conference*. DOI: 10.2514/6.2011-2254.

[41] Y. You, "An overview of the advantages and concerns of hypersonic inward turning inlets," 2011. DOI: 10.2514/6.2011-2269.

[42] S. Mölder, "The busemann air intake for hypersonic speeds," in *Hypersonic Vehicles-Past, Present and Future Developments*, Intech Open, 2019.

[43] K. L. Oswatitch, "Pressure recovery for missiles with reaction propulsion at high supersonic speeds (the efficiency of chock diffusers)," *NACA TM*, vol. 1140, 1947.

[44] A. Busemann, "Die achsensymmetrische kegelige überschallströmung," *Luftfahrtforschung*, vol. 19, no. 4, pp. 137–144, 1944.

[45] S. Mölder, "Internal, axisymmetric, conical flow.," *AIAA Journal*, vol. 5, no. 7, pp. 1252–1255, 1967. DOI: 10.2514/3.4179.

[46] G. I. Taylor and J. W. Maccoll, "The air pressure on a cone moving at high speeds," *Proceedings of the Royal Society of London. Series A, Containing Papers of a Mathematical and Physical Character*, vol. 139, no. 838, pp. 298–311, 1933. DOI: 10.1098/rspa.1933.0018.

[47] R. Baurle, "Busemann inlet design code," in *Taitech, Inc*, Beavercreek, OH, 2006.

[48] V. J. Babu, U. Pathak, and K. Sinhaa, "Comparative analysis of ramp-type and busemann intakes for hypersonic air-breathing engine," in *Proceedings of the 1st National Aerospace Propulsion Conference*, 2017, pp. 1–11.

[49] S. Mölder and E. Timofeev, "Hypersonic air intake design for high performance and starting," *Von Karman Institute lecture series on: Engine Intake Aerothermal Design: Subsonic to High Speed Applications*, vol. 14, 2011.

[50] A. K. Flock and A. Guelhan, "Viscous effects and truncation effects in axisymmetric busemann scramjet intakes," in *53rd AIAA Aerospace Sciences Meeting*. DOI: 10.2514/6.2015-0108.

[51] T. F. O'Brien and J. R. Colville, "Analytical computation of leading-edge truncation effects on inviscid busemann-inlet performance," *Journal of Propulsion and Power*, vol. 24, no. 4, pp. 655–661, 2008. DOI: 10.2514/1.30178.

[52] Z. Zhao and W. Song, "Effect of truncation on the performance of busemann inlet," *Canada: CCSE Modern Applied Science Journal*, 2009.

[53] T. Drayna, I. Nompelis, and G. Candler, "Hypersonic inward turning inlets: Design and optimization," in *44th AIAA Aerospace Sciences Meeting and Exhibit*. DOI: 10.2514/6.2006-297.

[54] T. O'Brien, "Viscous-optimized length-constrained axisymmetric geometries for streamline tracing," in *15th AIAA International Space Planes and Hypersonic Systems and Technologies Conference*. DOI: 10.2514/6.2008-2511.

[55] H. Ogawa, S. Mölder, and R. Boyce, "Effects of leading-edge truncation and stunting on drag and efficiency of busemann intakes for axisymmetric scramjet engines," *Journal of Fluid Science and Technology*, vol. 8, no. 2, pp. 186–199, 2013. DOI: 10.1299/jfst.8.186.

[56] K. Y. Zhang, "Research progress of hypersonic inlet inverse design based on curved shock compression system," in *20th AIAA International Space Planes and Hypersonic Systems and Technologies Conference*. DOI: 10.2514/6.2015-3647.

[57] J. D. Anderson, *Hypersonic and high temperature gas dynamics*. Aiaa, 2000.

[58] T. O'Brien and J. Colville, "Blunt leading edge effects on inviscid truncated busemann inlet performance," in *43rd AIAA/ASME/SAE/ASEE Joint Propulsion Conference & Exhibit*. DOI: 10.2514/6.2007-5411.

[59] L. Jacobsen, C.-J. Tam, R. Behdadnia, and F. Billig, "Starting and operation of a streamline-traced busemann inlet at mach 4," in *42nd AIAA/ASME/SAE/ASEE Joint Propulsion Conference & Exhibit*. DOI: 10.2514/6.2006-4508.

[60] T. O'Brien, "Viscous performance map of a blunt streamline-traced busemann inlet," in *17th AIAA International Space Planes and Hypersonic Systems and Technologies Conference*. DOI: 10.2514/6.2011-2255.

[61] Y. Xiao, L. Yue, P. Gong, and X. Chang, "Investigation on a truncated streamline-traced hypersonic busemann inlet," in *15th AIAA International Space Planes and Hypersonic Systems and Technologies Conference*. DOI: 10.2514/6.2008-2634.

[62] P. C. Walsh, R. B. Tahir, and S. Molder, "Boundary-layer correction for the busemann hypersonic air inlet," *Canadian Aeronautics and Space Journal*, vol. 49, no. 1, pp. 11–17, 2003. DOI: 10.5589/q03-003.

[63] A. Matthews and T. Jones, "Design and test of a modular waverider hypersonic intake," in *AIAA/CIRA 13th International Space Planes and Hypersonics Systems and Technologies Conference*. DOI: 10.2514/6.2005-3379.

[64] Y. You, D. Liang, and K. Cai, "Numerical research of three-dimensional section controllable internal waverider hypersonic inlet," in *44th AIAA/ASME/SAE/ASEE Joint Propulsion Conference & Exhibit*. DOI: 10.2514/6.2008-4708.

[65] F. M. White and J. Majdalani, *Viscous fluid flow*. McGraw-Hill New York, 2006, vol. 3.

[66] F. Ding, J. Liu, W. Huang, Y. Zhou, and S. Guo, "Boundary-layer viscous correction method for hypersonic forebody/inlet integration," *Acta Astronautica*, vol. 189, pp. 638–657, 2021, ISSN: 0094-5765. DOI: https://doi.org/10.1016/j.actaastro.2021.09.018.

[67] J. C. SIVELLS, "Aerodynamic design of axisymmetric hypersonic wind-tunnel nozzles," *Journal of Spacecraft and Rockets*, vol. 7, no. 11, pp. 1292–1299, 1970. DOI: 10.2514/3.30160.

[68] J. C. Sivells and R. G. Payne, "A method of calculating turbulent-boundary-layer growth at hypersonic mach numbers," Arnold Engineering Development Center, Tech. Rep., 1959.

[69] M. Bulman and A. Siebenhaar, "The rebirth of round hypersonic propulsion," in *42nd AIAA/ASME/SAE/ASEE Joint Propulsion Conference & Exhibit*. DOI: 10.2514/6.2006-5035.

[70] D. Capriotti, "Viscous optimized hypersonic waveriders," in *25th AIAA Aerospace Sciences Meeting*. DOI: 10.2514/6.1987-272.

[71] F. S. Billig and A. P. Kothari, "Streamline tracing: Technique for designing hypersonic vehicles," *Journal of Propulsion and Power*, vol. 16, no. 3, pp. 465–471, 2000. DOI: 10.2514/2.5591.

[72] A. Kothari, C. Tarpley, T. McLaughlin, B. Babu, and J. Livingston, "Hypersonic vehicle design using inward turning flow fields," in *32nd Joint Propulsion Conference and Exhibit*. DOI: 10.2514/6.1996-2552.

[73] T. Nonweiler, "Delta wing of shape amenable to exact shock-wave theory," *JR Aeronaut. Soc.*, vol. 67, pp. 521–528, 1963.

[74] J. Jones, "A method for designing lifting configurations for high supersonic speeds using the flow fields of non-lifting cones," *RAE Report No. Aero 2674*, 1963.

[75] G. Maikapar, "Bodies formed by the stream surfaces of conical flows," *Fluid Dynamics*, vol. 1, no. 1, 1966.

[76] F. Billig, R. Baurle, C.-J. Tam, and S. Wornom, "Design and analysis of streamline traced hypersonic inlets," in *9th International Space Planes and Hypersonic Systems and Technologies Conference*. DOI: 10.2514/6.1999-4974.

[77] D. V. Wie and S. Mölder, "Applications of busemann inlet designs for flight at hypersonic speeds," in *Aerospace Design Conference*. DOI: 10.2514/6.1992-1210.

[78] B. Xiong, X. Fan, and Y. Wang, "Deficiencies of streamline tracing techniques for designing hypersonic inlets and potential solutions," *Science China Technological Sciences*, vol. 63, pp. 488–495, 2019.

[79] R. Barger, "A procedure for designing forebodies with constraints on cross-section shape and axial area distribution," *NASA Technical Paper 1881*, 1981.

[80] M. K. Smart and C. A. Trexler, "Mach 4 performance of hypersonic inlet with rectangular-to-elliptical shape transition," *Journal of Propulsion and Power*, vol. 20, no. 2, pp. 288–293, 2004. DOI: 10.2514/1.1296.

[81] M. R. Rosli, M. Takahashi, T. Sato, T. Kojima, H. Taguchi, and Y. Maru, "Streamline tracing technique based design of elliptical-to-rectangular transitioning hypersonic inlet," in *31st AIAA Applied Aerodynamics Conference*. DOI: 10.2514/6.2013-2665.

[82] M. Smart and E. Ruf, "Free-jet testing of a rest scramjet at off-design conditions," in *25th AIAA Aerodynamic Measurement Technology and Ground Testing Conference*. DOI: 10.2514/6.2006-2955.

[83] H. Sobieczky, F. Dougherty, and K. Jones, "Hypersonic waverider design from given shock waves," in *Proc. First International Waverider Symposium, University of Maryland*, 1990, pp. 1–20.

[84] K. Jones and K. Center, "Waverider design methods for non-conical shock geometries," in AIAA Paper 2002-3204, American Institute of Aeronautics and Astronautics, 2002, pp. 1–14. DOI: 10.2514/6.2002-3204.

[85] K. D. Jones, H. Sobieczky, A. R. Seebass, and F. C. Dougherty, "Waverider design for generalized shock geometries," *Journal of Spacecraft and Rockets*, vol. 32, no. 6, pp. 957–963, 1995. DOI: 10.2514/3.26715.

[86] H. Sobieczky, B. Zores, Z. Wang, and Y. Qian, "High speed flow design using osculating axisymmetric flows," in *Proc. 3rd Pacific Int. Conf. on Aerospace Science and Technology*, 1997, pp. 182–187.

[87] H. Sobieczky, "On conical flow," in *2nd AIAA, Theoretical Fluid Mechanics Meeting*. DOI: 10.2514/6.1998-2594.

[88] K. Center, H. Sobieczky, and F. Dougherty, "Interactive design of hypersonic waverider geometries," in *22nd Fluid Dynamics, Plasma Dynamics and Lasers Conference*, 1991. DOI: 10.2514/6.1991-1697.

[89] X. Zheng, Y. Li, C. Zhu, and Y. You, "Multiple osculating cones' waverider design method for ruled shock surfaces," *AIAA Journal*, vol. 58, no. 2, pp. 854–866, 2020. DOI: 10.2514/1.J058640.

[90] Y. You and D. Liang, "Design concept of three-dimensional section controllable internal waverider hypersonic inlet," *Science in China Series E: Technological Sciences*, vol. 52, no. 7, pp. 2017–2028, 2009.

[91] H. Xuzhao, L. Jialing, Z. Zheng, M. Penfei, and W. Yingchuan, "Osculating inward turning cone waverider/inlet (oicwi) design methods and experimental study," in *18th AIAA/3AF International Space Planes and Hypersonic Systems and Technologies Conference*. DOI: 10.2514/6.2012-5810.

[92] Y. You, C. Zhu, and J. Guo, "Dual waverider concept for the integration of hypersonic inward-turning inlet and airframe forebody," in *16th AIAA/DLR/DGLR International Space Planes and Hypersonic Systems and Technologies Conference*. DOI: 10.2514/6.2009-7421.

[93] M. E. Noftz, A. J. Shuck, J. S. Jewell, *et al.*, "Design of an internal osculating waverider intake," in *AIAA SCITECH 2022 Forum*. DOI: 10.2514/6.2022-0064.

[94] R. J. Gollan and M. K. Smart, "Design of modular shape-transition inlets for a conical hypersonic vehicle," *Journal of Propulsion and Power*, vol. 29, no. 4, pp. 832–838, 2013. DOI: 10.2514/1.B34672.

[95] V. Ramasubramanian, M. Lewis, and R. Starkey, "Performance of various truncation strategies employed on hypersonic busemann inlets," in *16th AIAA/DLR/DGLR International Space Planes and Hypersonic Systems and Technologies Conference*. DOI: 10.2514/6.2009-7249.

[96] Z. Fengyuan and G. Huang, "A preliminary overview analysis on the internal waverider inlets for ramjet," in *21st AIAA International Space Planes and Hypersonics Technologies Conference*. DOI: 10.2514/6.2017-2420.

[97] F. Zuo, G. Huang, and C. Xia, "Investigation of internal-waverider-inlet flow pattern integrated with variable-geometry for tbcc," *Aerospace Science and Technology*, vol. 59, pp. 69–77, 2016.

[98] S. E. Otto, C. J. Trefny, and J. W. Slater, "Inward-turning streamline-traced supersonic inlet design method for low-boom, low-drag applications," in *51st AIAA/SAE/ASEE Joint Propulsion Conference*. DOI: 10.2514/6.2015-3700.

[99] R. L. Gaffney, "Design of a pulse-facility nozzle using the rotational method of characteristics," *Journal of Spacecraft and Rockets*, vol. 43, no. 6, pp. 1216–1224, 2006. DOI: 10.2514/1.20193.

[100] E. R. Eckert, "Survey on heat transfer at high speeds," Minnesota University, Tech. Rep., 1961.

[101] M. Sibulkin, "Heat transfer to an incompressible turbulent boundary layer and estimation of heat-transfer coefficients at supersonic nozzle throats," *Journal of the Aeronautical Sciences*, vol. 23, no. 2, pp. 162–172, 1956.

[102] D. R. McDaniel and T. Tuckey, "Hpcmp create^{TM}-av kestrel new and emerging capabilities," in 2020-1525, American Institute of Aeronautics and Astronautics, 2020. DOI: 10.2514/6.2020-1525.

[103] S. A. Morton and D. R. McDaniel, "Hpcmp create^{TM}-av kestrel architecture capability and future direction," in 2018-0025, American Institute of Aeronautics and Astronautics, 2018. DOI: 10.2514/6.2018-0025.

[104] E. Curran and S. Murthy, *Scramjet propulsion*. AIAA, 2001, vol. 189.

[105] R. H. Korkegi, "Comparison of shock-induced two- and three- dimensional incipient turbulent seperation," *AIAA Journal*, vol. 13, no. 4, pp. 534–535, 1975. DOI: 10.2514/3.49750.

[106] S. P. Schneider, "Development of hypersonic quiet tunnels," *Journal of Spacecraft and Rockets*, vol. 45, no. 4, pp. 641–664, 2008.

[107] L. E. Steen, "Characterization and development of nozzles for a hypersonic quiet wind tunnel," M.S. thesis, Dec. 2010.

[108] M. Dally and J. Edelman, "Aae 520 class report: Generic scramjet forebody transition at mach 6," May 2015.

[109] A. Pope and K. L. Goin, *High-speed wind tunnel testing*. New York: Wiley, 1965.

[110] *Ce 221*, Doc 103474-00, Rev F, Carbon-3D Data Sheet, Jan. 2012.

[111] D. V. Mamrol, "Characterization of the quiet flow freestream and a flat plate model in the boeing/afosr mach 6 quiet tunnel," M.S. thesis, Nov. 2021.

[112] T. J. Juliano, "Nozzle modifications for high-reynolds-number quiet flow in the boeing/afosr mach-6 quiet tunnel," M.S. thesis, Dec. 2006.

[113] P. E. Rodi, S. Emami, and C. A. Trexler, "Unsteady pressure behavior in a ramjet/scramjet inlet," *Journal of Propulsion and Power*, vol. 12, no. 3, pp. 486–493, 1996. DOI: 10.2514/3.24061.

A. LEGACY INLET ITERATIONS

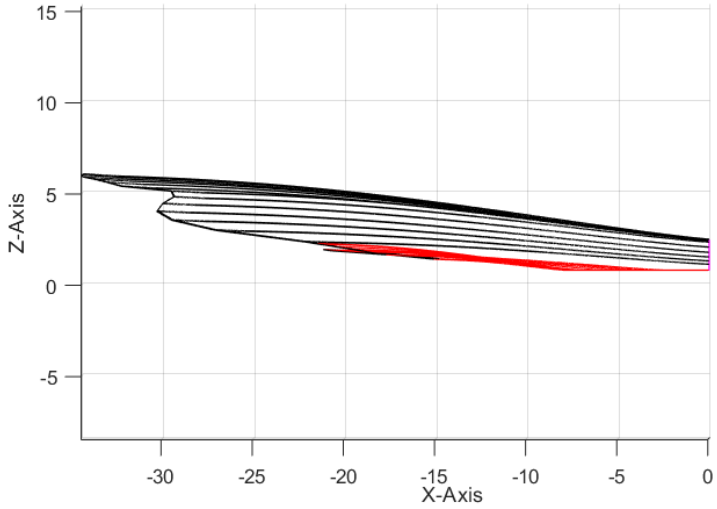

Figure A.1. Legacy inlet iteration with unsmoothed solutions, resulting in a jagged leading edge.

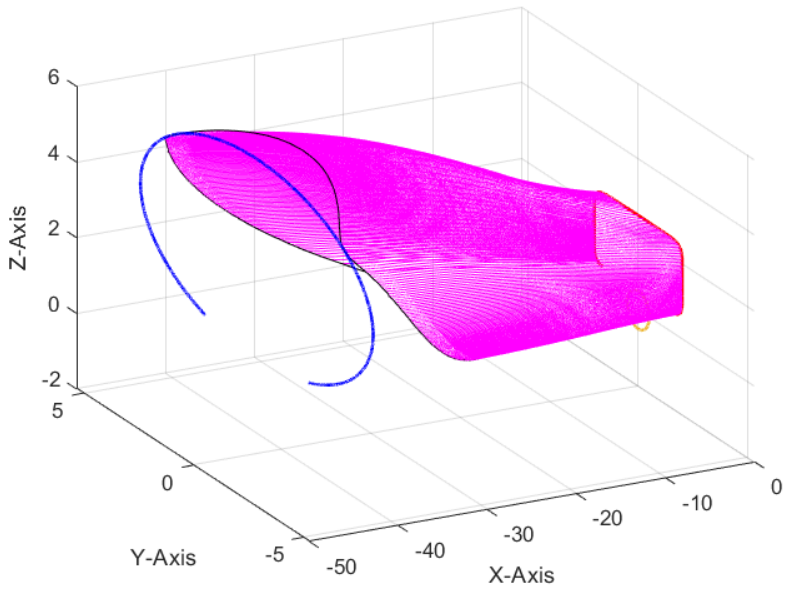

Figure A.2. Legacy inlet iteration with an optimzed and smooth upper surface but no lower shock-capture suface.

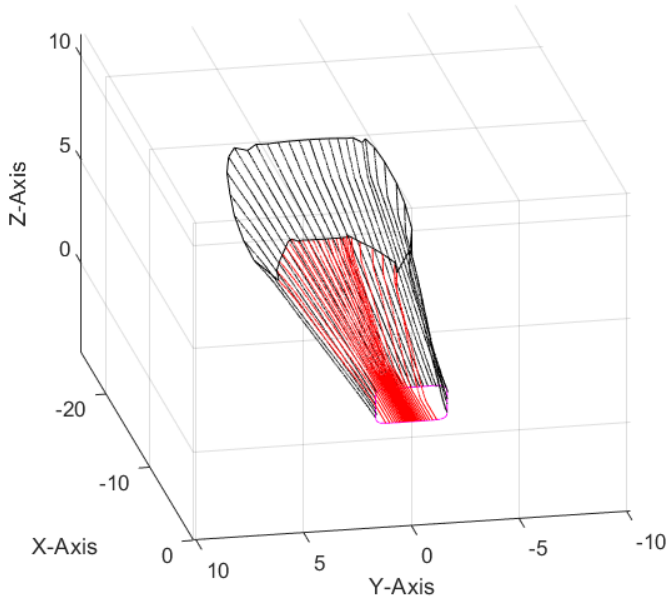

Figure A.3. Legacy inlet design without smoothed solutions and an over-sized shock capture surface.

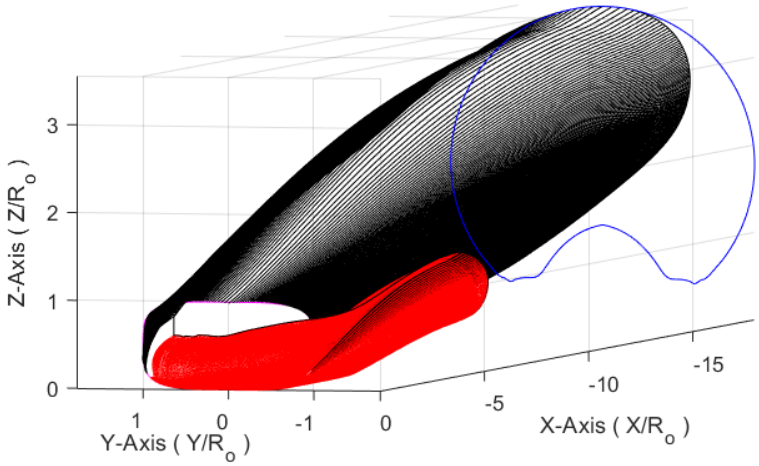

Figure A.4. Legacy inlet design with smoothed solutions and an over-sized shock capture surface.

B. JET INJECTION PROCEDURE AND SYSTEM

1. Open BV5 before the start of the experiment. Verify the tank is unpressurized with PG2. If PG2 does not work, open RV1 to ensure the tank is empty. Close BV4 if it is open.

2. Connect the DAQ alarm-out cable to the Agilent signal generator. Make sure the DAQ sends alarm-out triggers based on drop of NWK voltage. Create a custom waveform 5V square-wave on the Agilent signal generator and connect it to the solenoid power box. Check that the DAQ-Agilent-Solenoid system correctly triggers.

3. Use high-pressure 5/16" nylon tubing to connect the jet-injection system to the model within the BAM6QT. A special Conax fitting is available to pass this tube into the tunnel. Check that the Conax provides a good seal without pinching the tubing.

4. Open BV1 and BV2 before the jet-injection experiment. The line will become pressurized with air from the ASL machine shop. Pay attention to hissing sounds that may indicate leaks in the system.

5. Use NV1 and PG1 to fill the plenum tank to the desired pressure. Close NV1 and BV2 to isolate the plenum tank from the fill line.

6. Verify the tank is pressurized to the desired level with PG2. If pressure is too high, then RV1 can be opened slightly by-hand to drop the tank pressure.

7. To prime the system for triggering, turn on the solenoid power box and single the Agilent signal generator. Check that the power box is connected to both the solenoid and the Agilent signal generator.

8. Prior to running, open BV3 so that plenum air can flow through the filter, solenoid, check-valve, and pressure tubing.

9. Trigger the system by bursting the tunnel diaphragms. The DAQ will trigger the Agilent signal generator. The Agilent signal generator will output a 5V square wave that will activate the solenoid power box. The solenoid will open and air will flow into the tunnel.

10. Close BV3 at the end of the run. Empty the plenum tank by opening RV1 by-hand. If another run is planned, the tank can be refilled by repeating steps 4 - 9.

11. When the jet-injection system is no longer needed, BV1 can be closed to cut-off the air supply. Open NV1, BV2, BV3, and BV5 so all lines are connected. Open RV1 to eject any residual high pressure air in the system.

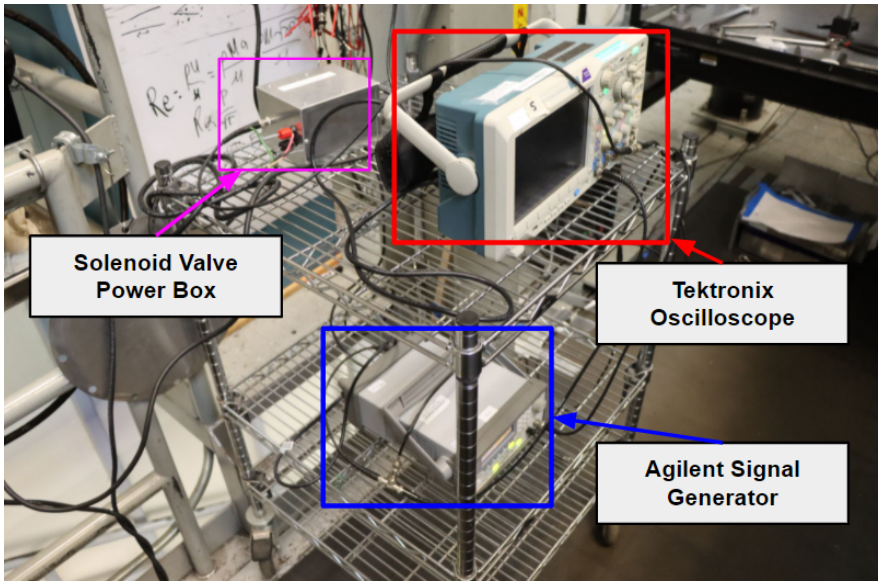

Figure B.1. Jet injection triggering system for the blockage model test campaign.

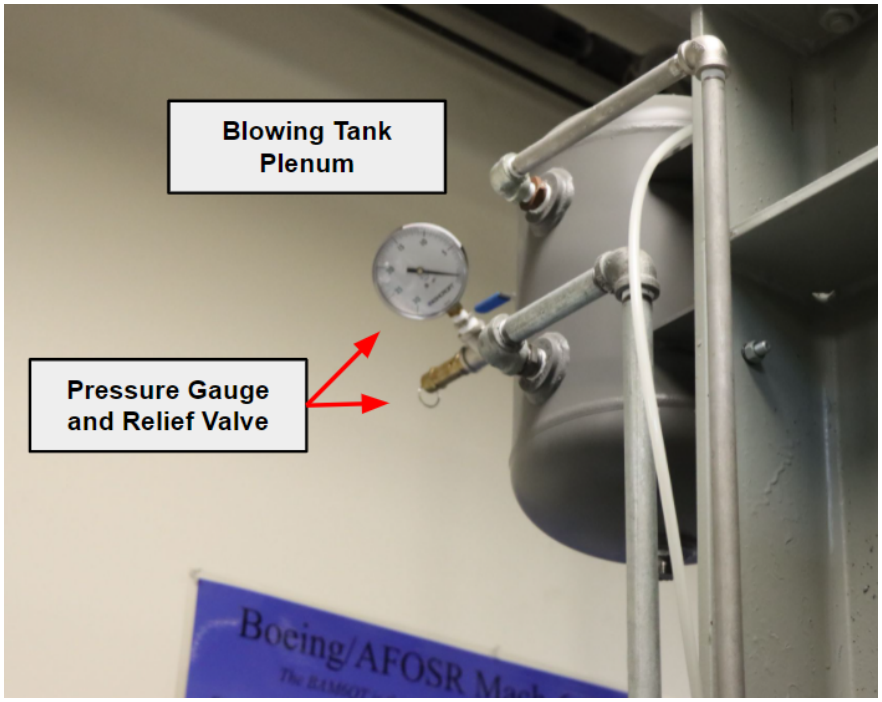

Figure B.2. Jet injection plenum tank and supporting equipment.

C. INDIANA INLET BLOCKAGE MODELS

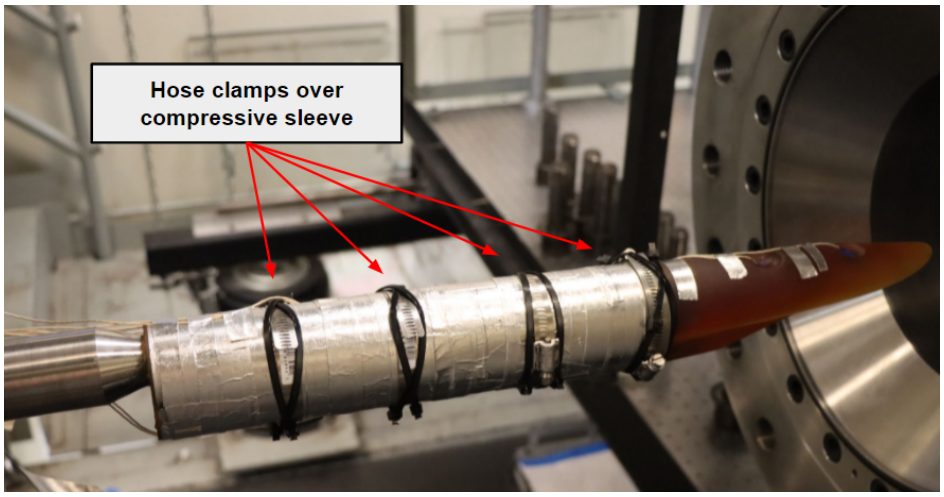

Figure C.1. The 14% INlet model in the BAM6QT section.

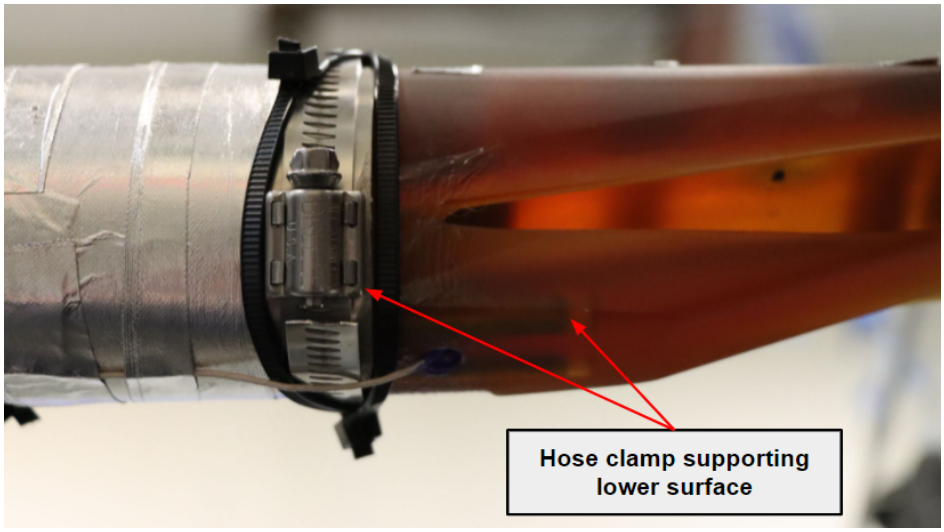

Figure C.2. Forward section of the 14% INlet model.

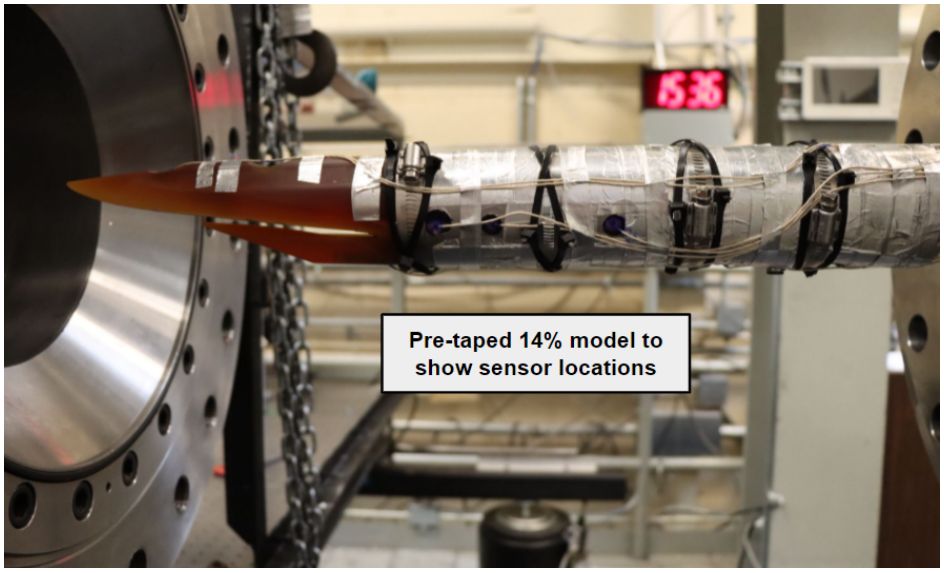

Figure C.3. The 14% INlet model with intentionally exposed Kulite sensor wires.

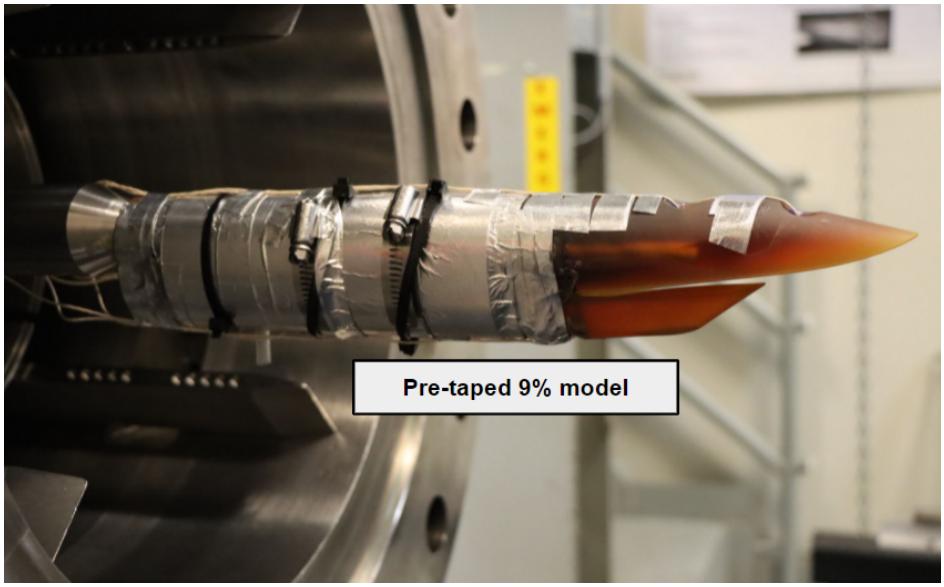

Figure C.4. The 9% INlet model in the BAM6QT section.

D. SENSOR CALIBRATIONS

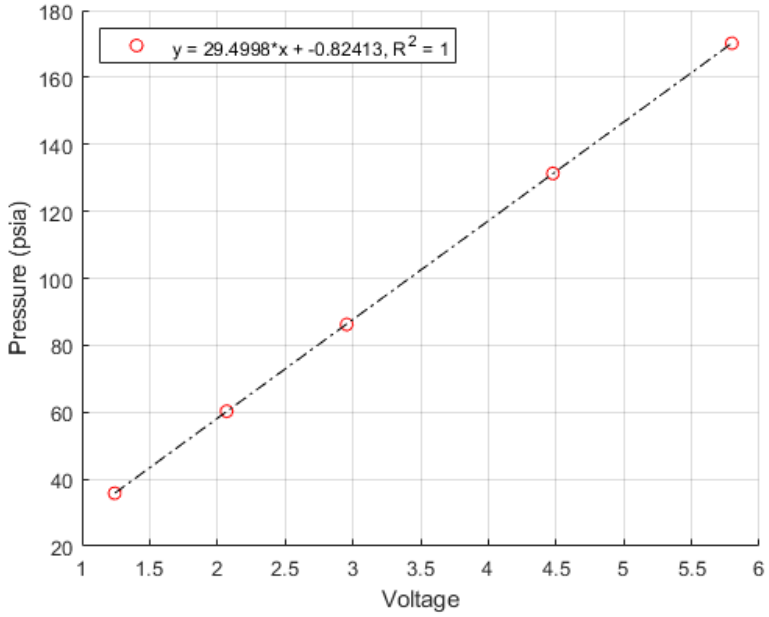

Figure D.1. Contraction Kulite calibration.

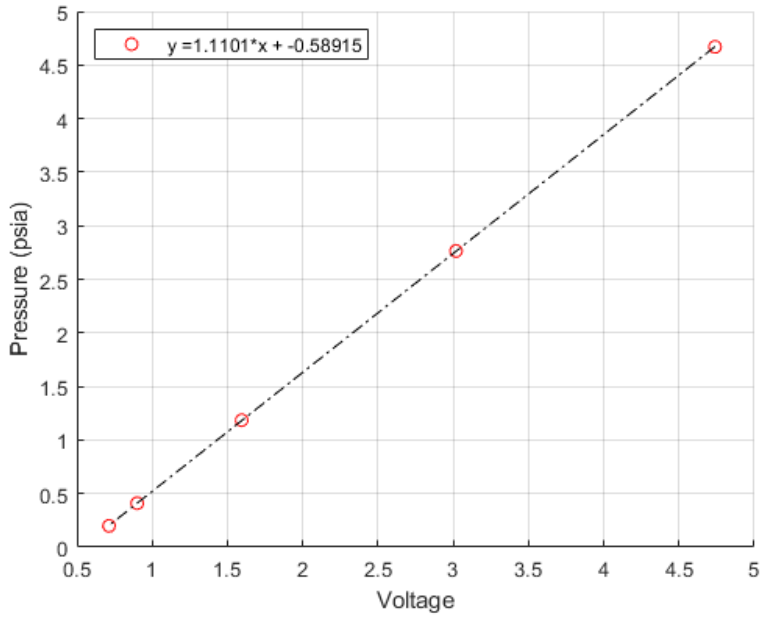

Figure D.2. Nozzle wall Kulite calibration.

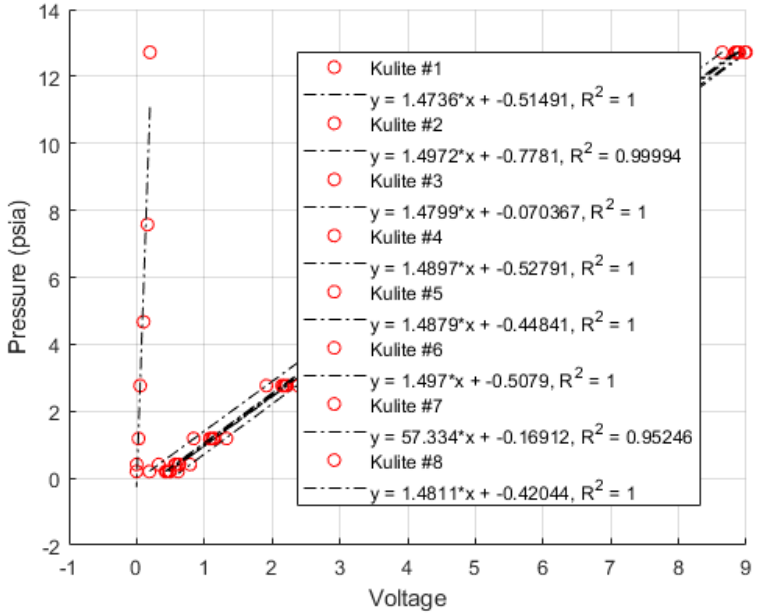

Figure D.3. 14% scale model Kulite calibrations.

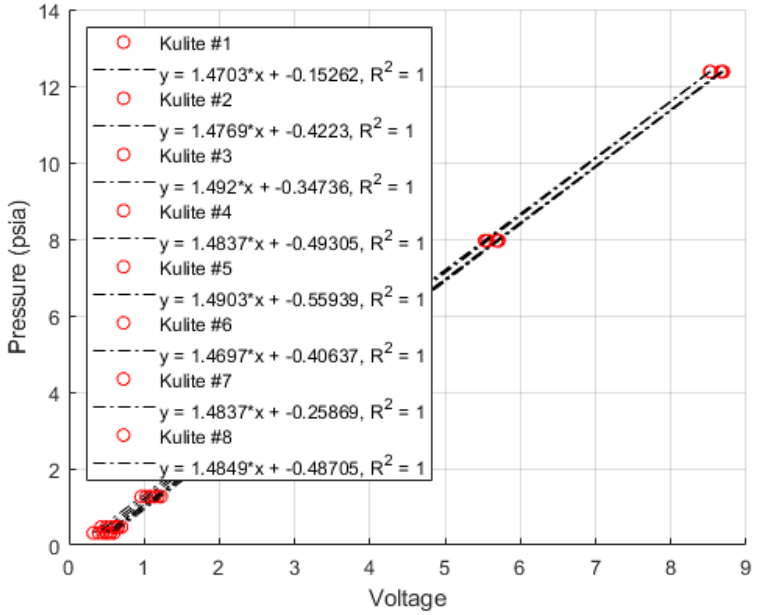

Figure D.4. 9% scale model Kulite calibrations.

E. BLOCKAGE CAMPAIGN RUN MATRIX

Table E.1. Blockage campaign run log. [Part 1, 9/30/2021-10/9/2021]

Run #	**Target (psia)**	$P_{o,\mathrm{i}}$ **(psia)**	$T_{o,\mathrm{i}}$ **(°C)**	**Vacuum (torr)**	**Quiet? (Y/N)**	**AoA** (^{o})	**BP? (Y/N)**	**Model Scale**
1	40	35.80	151.7	2.13	Yes	0	No	14%
2	65	60.30	151.8	2.70	Yes	0	No	14%
3	95	86.20	153.7	3.45	Yes	0	No	14%
4	145	131.30	153.5	7.75	Yes	0	No	14%
5	185	170.20	154	15.10	Yes	0	No	14%
6	40	35.90	155.3	4.32	No	0	No	14%
7	65	59.90	154.7	7.42	No	0	No	14%
8	95	86.50	154.2	8.79	No	0	No	14%
9	145	130.50	152.7	7.23	No	0	No	14%
10	185	170.50	153.3	14.90	No	0	No	14%
11	40	35.90	153.1	2.26	Yes	0	No	14%
12	65	59.90	153.7	7.57	Yes	0	No	14%
13	95	86.10	152.2	5.81	Yes	0	No	14%
14	145	129.90	153	9.77	Yes	0	No	14%
15	185	170.30	155.4	4.82	Yes	0	No	14%
16	40	35.60	151.8	11.40	No	0	No	14%
17	65	59.56	152.6	7.97	No	0	No	14%
18	95	86.30	152	5.00	No	0	No	14%
19	145	130.80	156.4	5.66	No	0	No	14%
20	185	170.20	156.3	12.60	No	0	No	14%
21	40	35.8	154.7	1.72	Yes	6	No	14%
22	65	60.20	152.7	6.87	Yes	6	No	14%
23	95	86.30	153.4	11.10	Yes	6	No	14%
24	145	130.50	153.7	4.10	Yes	6	No	14%
25	185	170.1	153	3.98	Yes	6	No	14%
26	40	35.15	149.2	2.05	Yes	0	No	9%
27	65	59.70	151.1	3.00	Yes	0	No	9%
28	95	85.30	150.2	9.62	Yes	0	No	9%
29	145	130.20	153.1	6.96	Yes	0	No	9%
30	185	169.50	152.9	12.50	Yes	0	No	9%

Table E.2. Blockage campaign run log. [Part 2, 9/30/2021-10/9/2021]

Run #	**Target (psia)**	$P_{o,\mathrm{i}}$ **(psia)**	$T_{o,\mathrm{i}}$ **(°C)**	**Vacuum (torr)**	**Quiet? (Y/N)**	**AoA** (^{o})	**BP? (Y/N)**	**Model Scale**
31	40	35.15	35.1	1.95	Yes	0	Yes - 30 psig	9%
32	65	59.70	149.2	5.14	Yes	0	Yes - 30 psig	9%
33	95	85.50	149.6	7.98	Yes	0	Yes - 30 psig	9%
34	95	84.80	156.5	6.59	Yes	0	Yes - 30 psig	9%
35	145	130.40	156.1	6.56	Yes	0	Yes - 30 psig	9%
36	95	85.2	152	3.29	Yes	0	Yes - 30 psig	9%
37	145	130.7	152	7.65	Yes	0	Yes - 30 psig	9%
38	65	60.25	150.3	26.90	Yes	0	Yes - 30 psig	9%
39	185	170.8	152.1	6.92	Yes	0	Yes - 30 psig	9%
40	37	34.7	147.8	49.70	Yes	0	Yes - 30 psig	9%

F. BAM6QT STARTABILITY MAPS

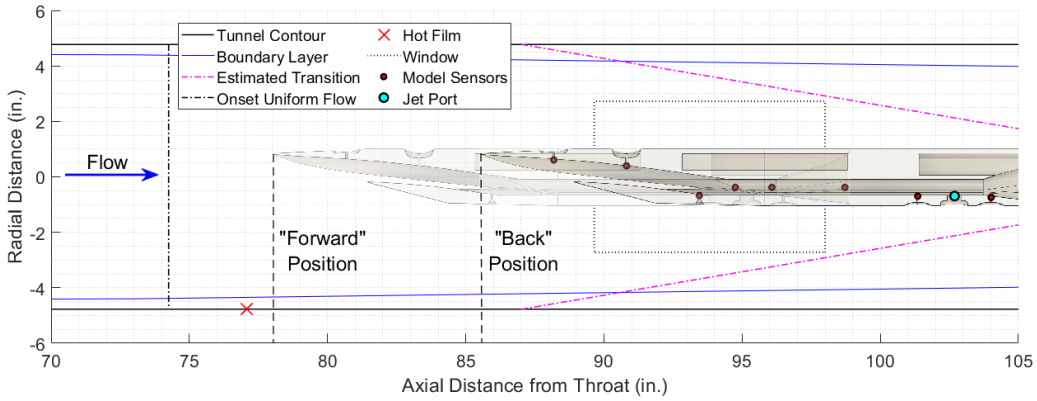

Figure F.1. INlet 14% scale model positions.

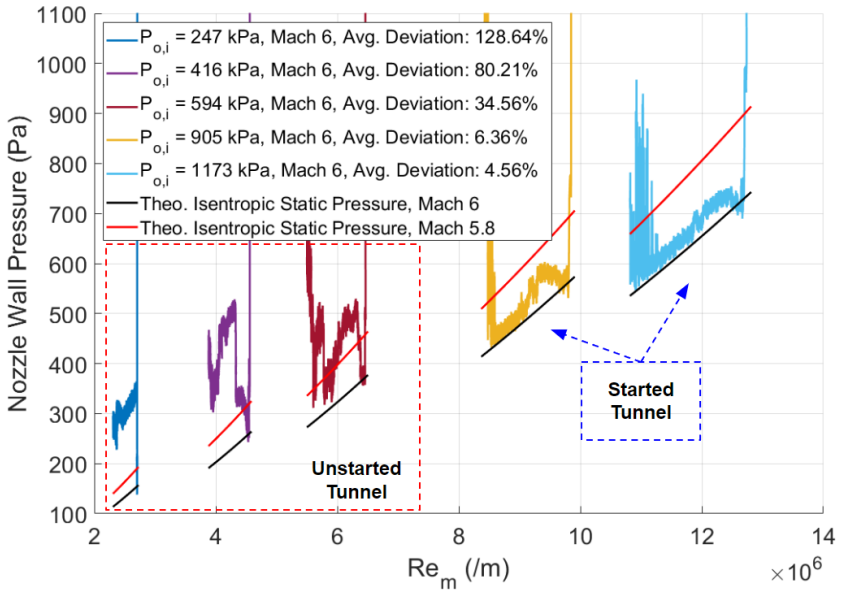

Figure F.2. Tunnel starting map for the 14% model under Mach 6 quiet flow at 0°AoA and the sting-forward position.

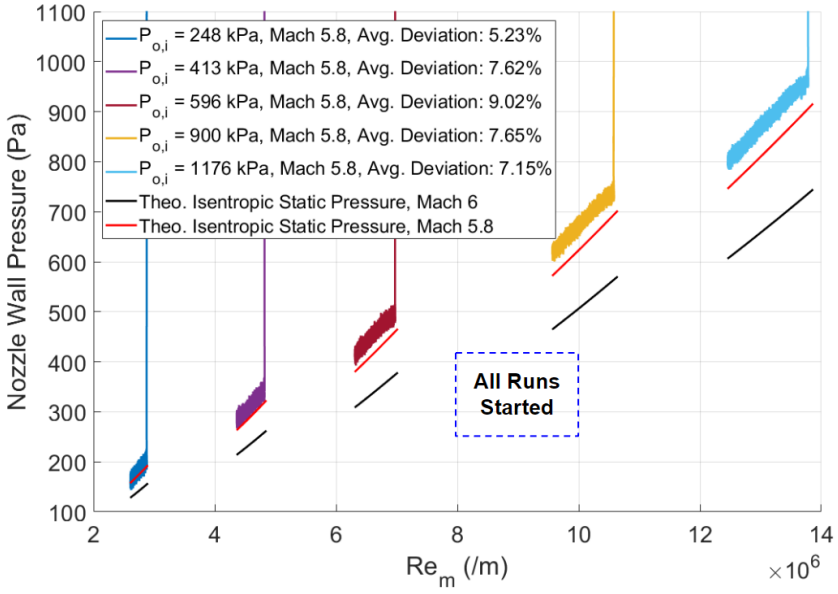

Figure F.3. Tunnel starting map for the 14% model under Mach 5.8 noisy flow at 0°AoA and the sting-forward position.

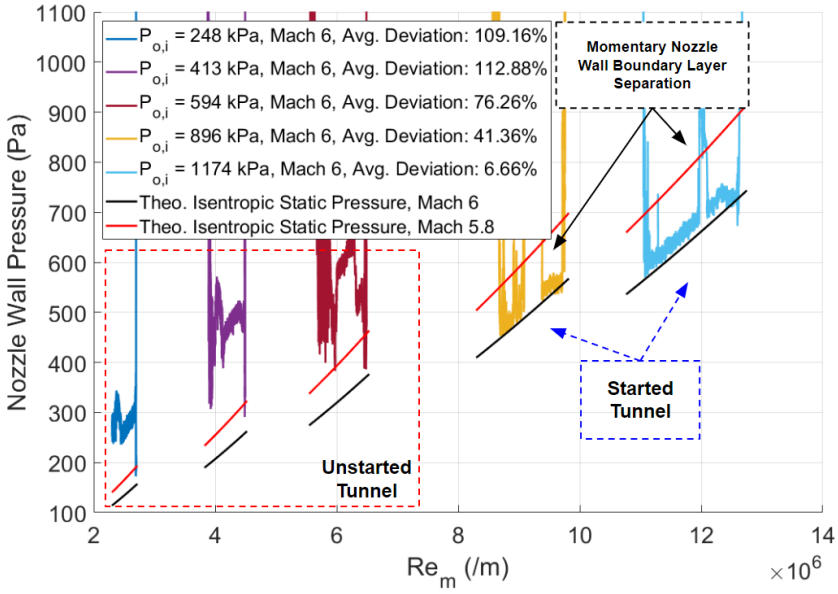

Figure F.4. Tunnel starting map for the 14% model under Mach 6 quiet flow at 0°AoA and the sting-back position.

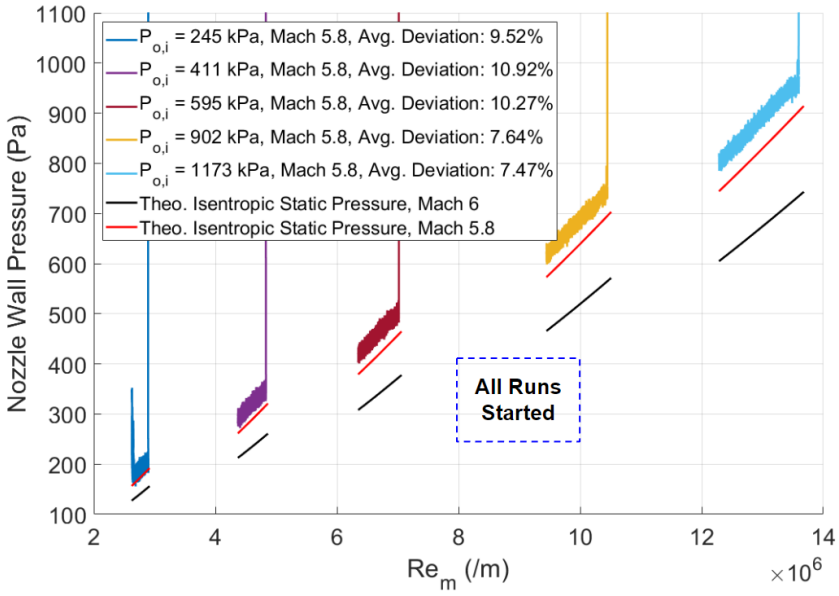

Figure F.5. Tunnel starting map for the 14% model under Mach 5.8 noisy flow at 0°AoA and the sting-back position.

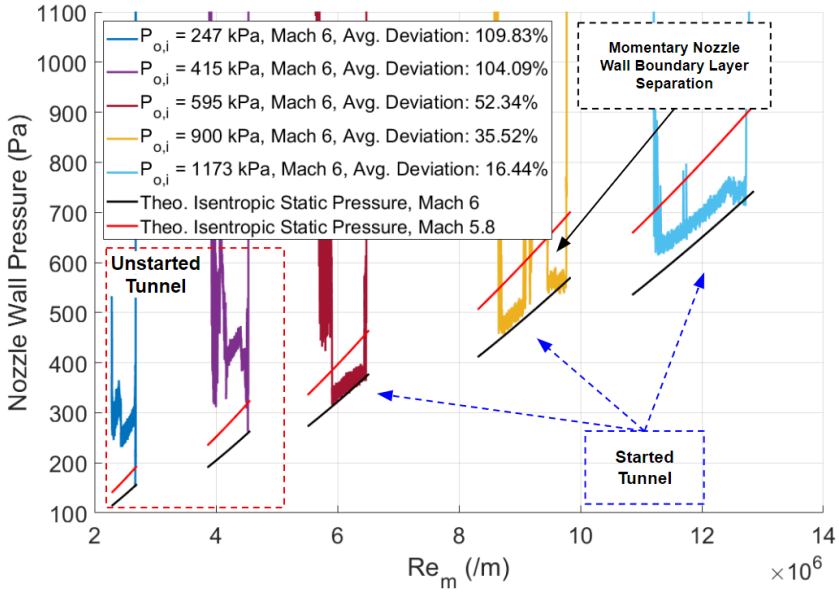

Figure F.6. Tunnel starting map for the 14% model under Mach 6 quiet flow at 6°AoA and the sting-back position.

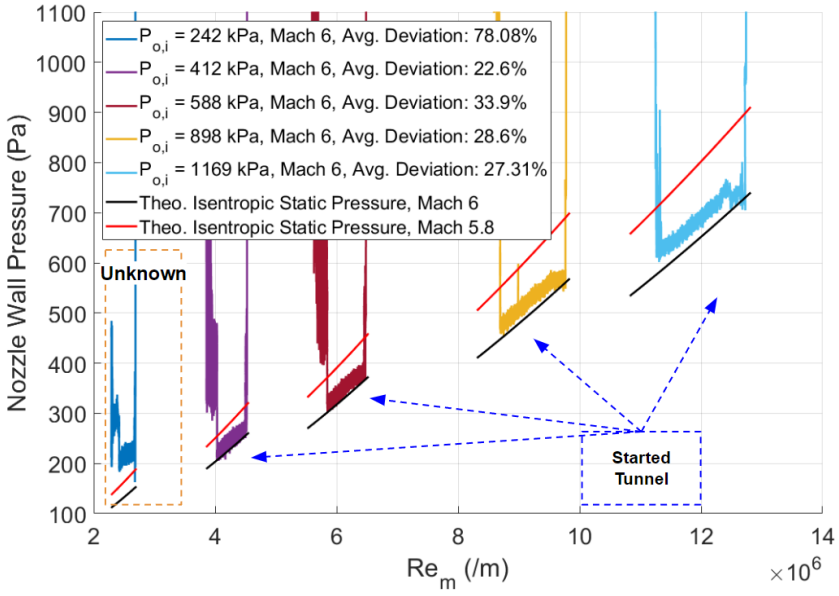

Figure F.7. Tunnel starting map for the 9% model under Mach 6 quiet flow at 0°AoA and the sting-back position.

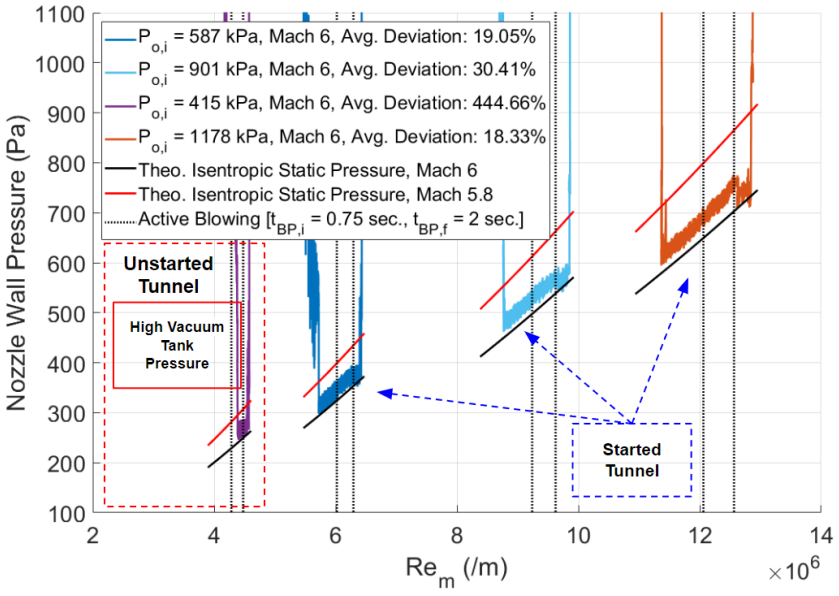

Figure F.8. Tunnel starting map for the 9% model under Mach 6 quiet flow at 0°AoA, with back-pressure, and the sting-back position.

Table F.1. Tunnel Startability Matrix for Mach 6 Quiet Flow

Freestream Reynolds Number	**9% Scale AoA=0° Sting-Back Quiet Flow**	**14% Scale AoA=6° Sting-Back Quiet Flow**	**14% Scale AoA=0° Sting-Forward Quiet Flow**	**14% Scale AoA=0° Sting-Back Quiet Flow**
$\approx 12.5 \cdot 10^6/m$	Yes	Yes	Yes	Momentary
$\approx 10 \cdot 10^6/m$	Yes	Yes	Yes	Momentary
$\approx 6.5 \cdot 10^6/m$	Yes	Yes	No	No
$\approx 4.5 \cdot 10^6/m$	Yes	No	No	No
$\approx 3 \cdot 10^6/m$	Momentary	No	No	No

Table F.2. Tunnel Startability Matrix for Mach 5.8 Noisy Flow

Freestream Reynolds Number	**14% Scale AoA=0° Sting-Forward Noisy Flow**	**14% Scale AoA=0° Sting-Back Noisy Flow**
$\approx 12.5 \cdot 10^6/m$	Yes	Yes
$\approx 10 \cdot 10^6/m$	Yes	Yes
$\approx 6.5 \cdot 10^6/m$	Yes	Yes
$\approx 4.5 \cdot 10^6/m$	Yes	Yes
$\approx 3 \cdot 10^6/m$	Yes	Yes

G. SHOCK ARRIVAL TRACKING EXAMPLES

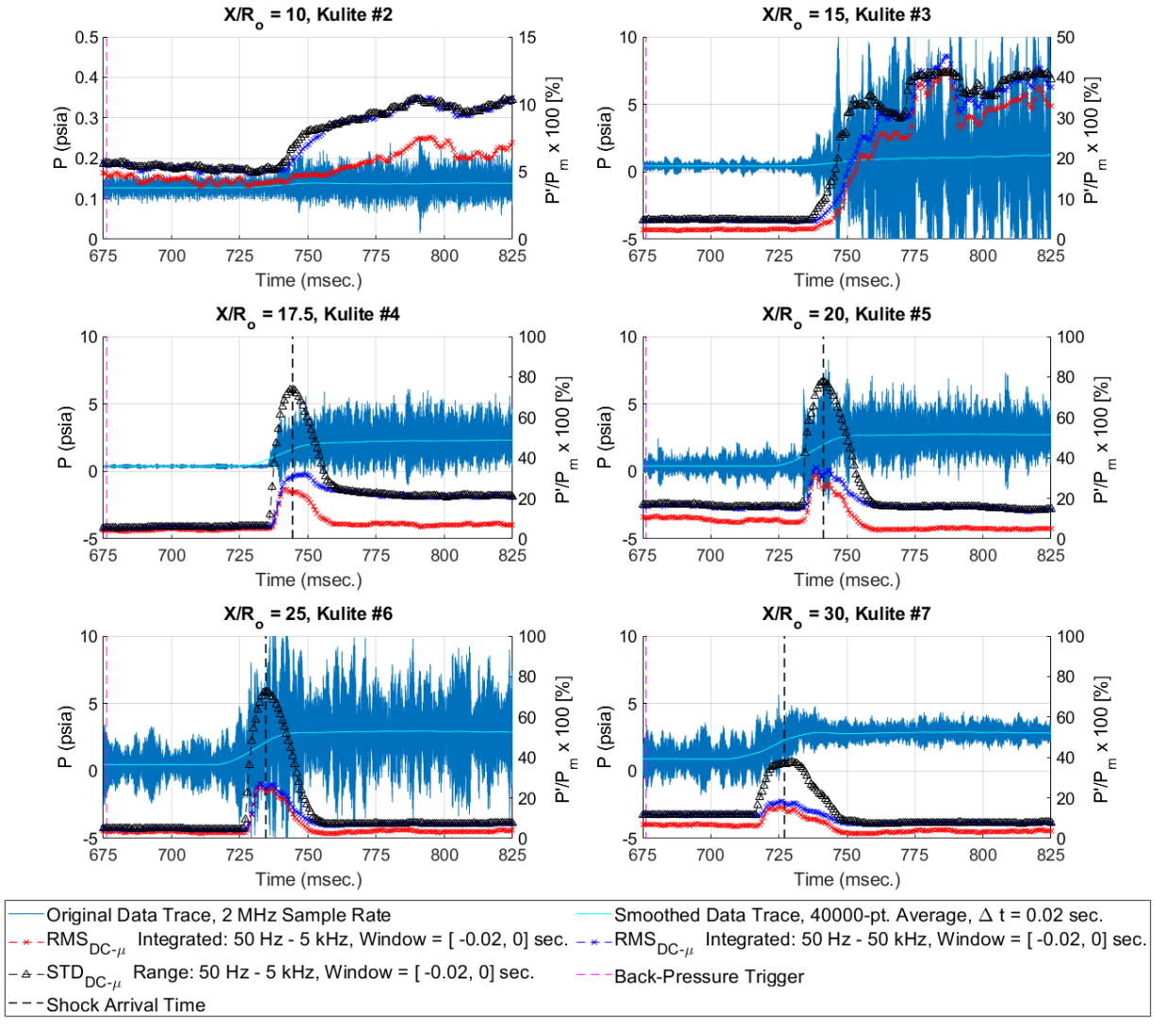

Figure G.1. Shock arrival tracking for a back-pressure event with the 9% scaled model. Tunnel conditions: Mach 6 quiet flow, $P_{o,\mathrm{i}} \approx 85$ psia.

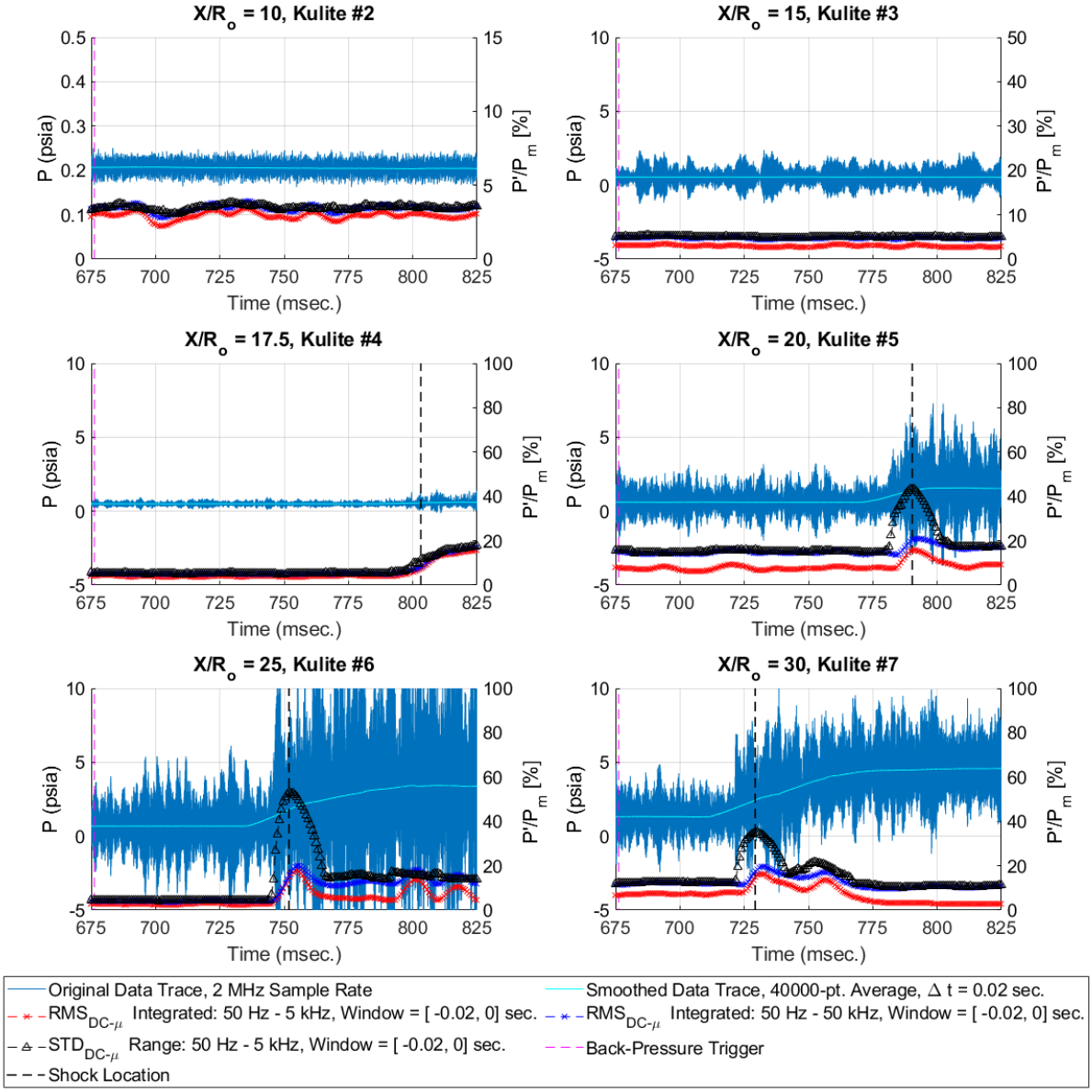

Figure G.2. Shock arrival tracking for a back-pressure event with the 9% scaled model. Tunnel conditions: Mach 6 quiet flow, $P_{o,\mathrm{i}} \approx 130$ psia.

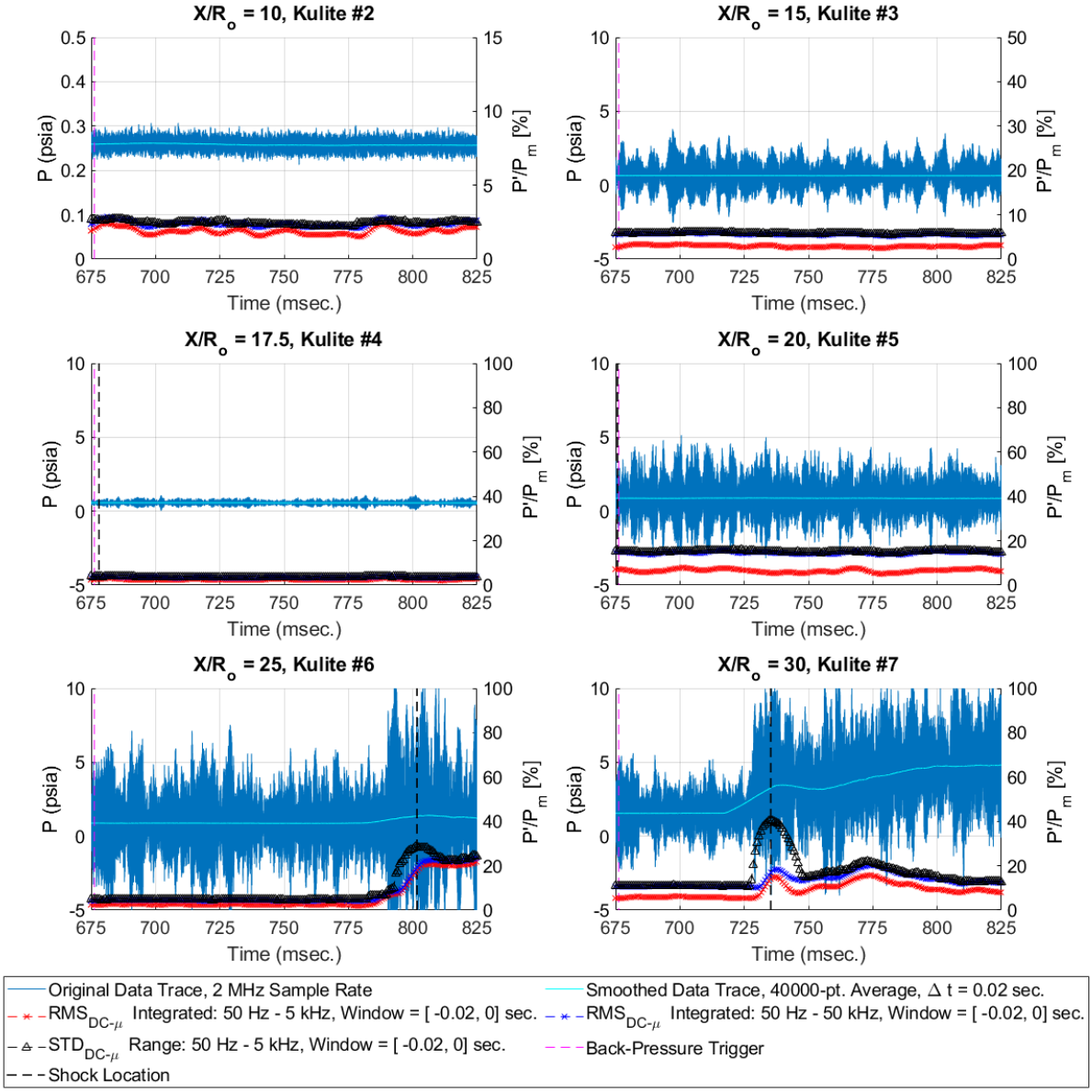

Figure G.3. Shock arrival tracking for a back-pressure event with the 9% scaled model. Tunnel conditions: Mach 6 quiet flow, $P_{o,\mathrm{i}} \approx 170$ psia.

H. 12% INDIANA INLET MODEL DRAWINGS, ASSEMBLY, AND LOAD CALCULATIONS

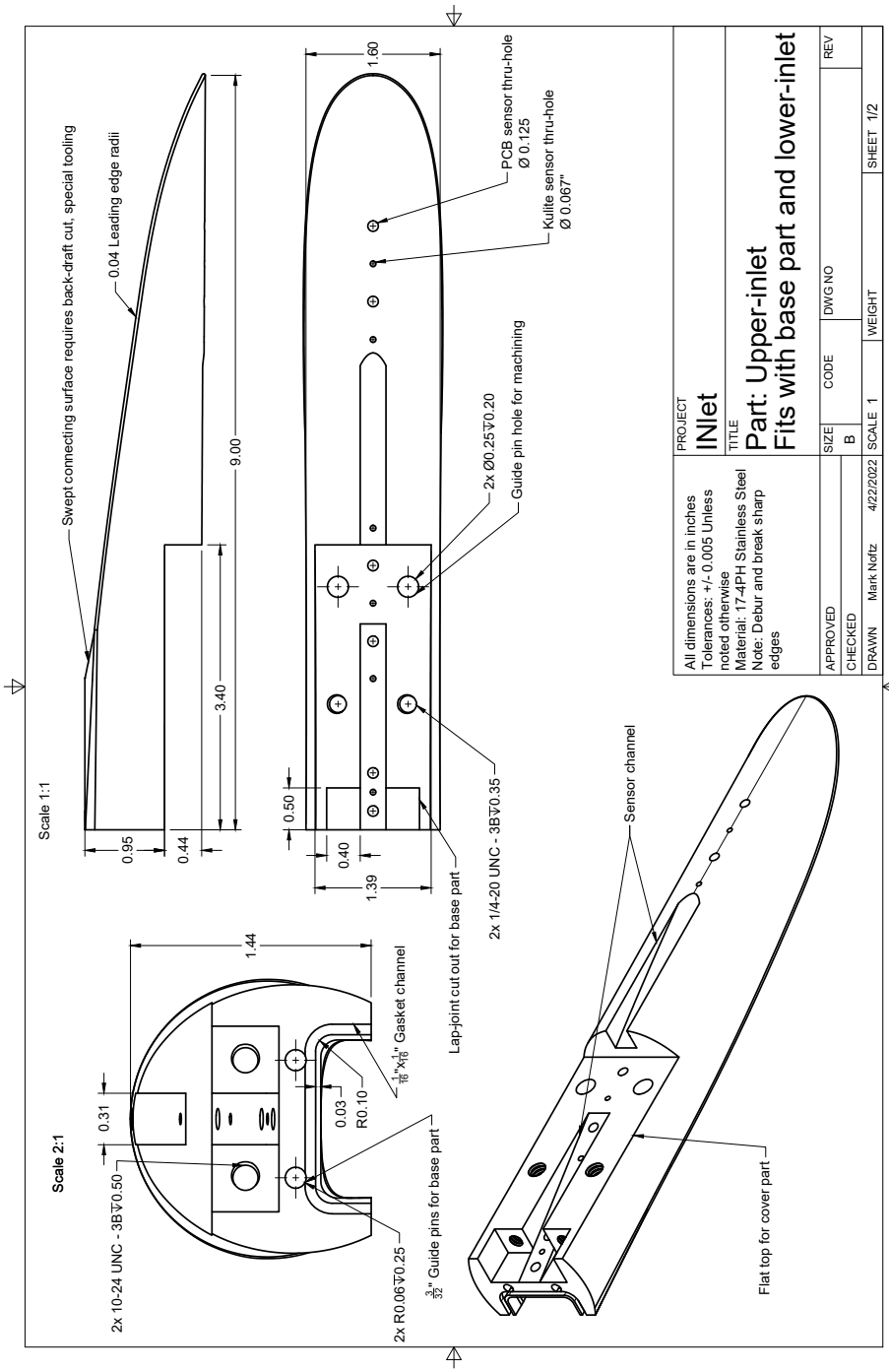

Figure H.1. Upper inlet (compression surface).

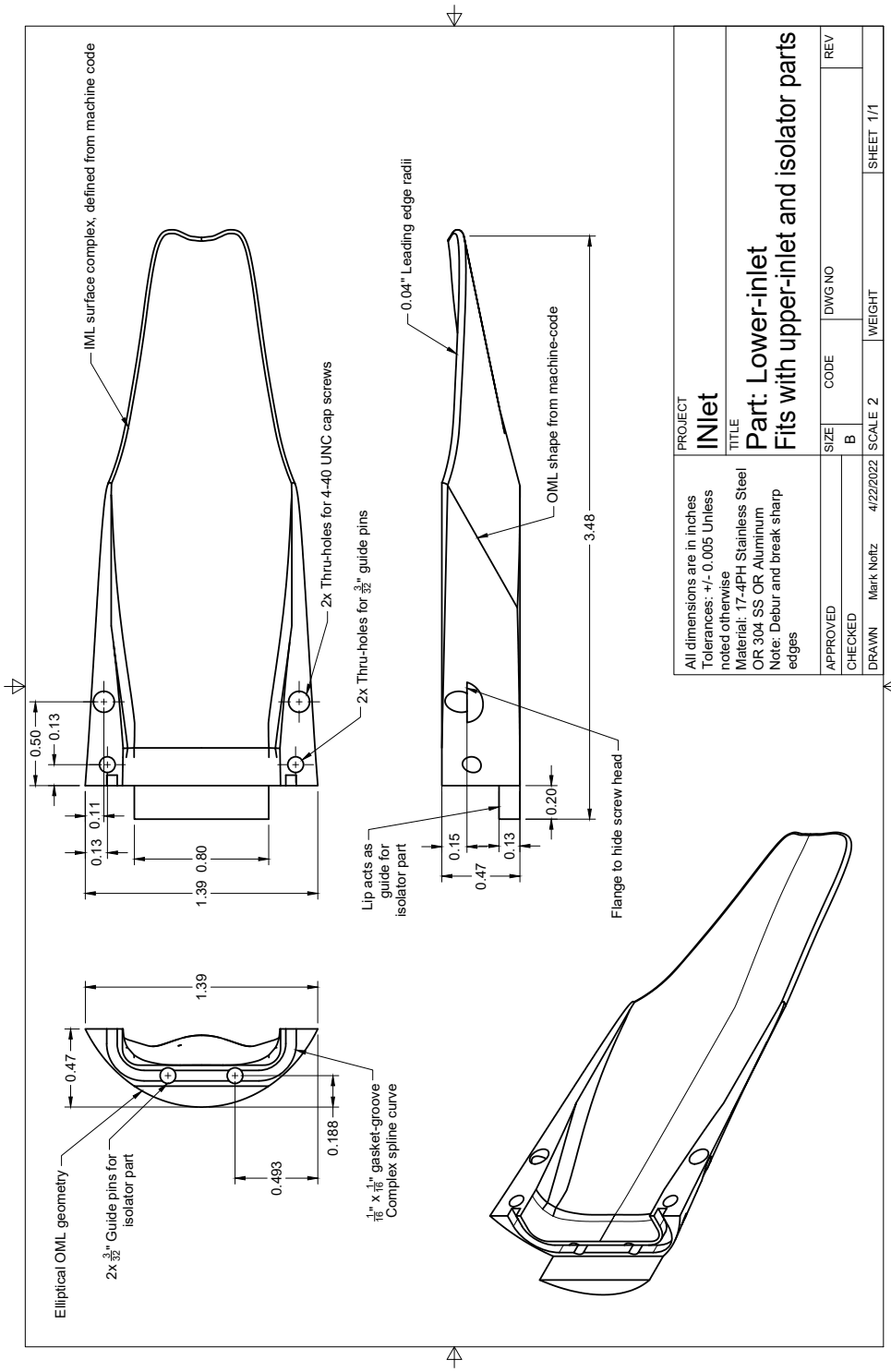

Figure H.2. Lower inlet (capture surface).

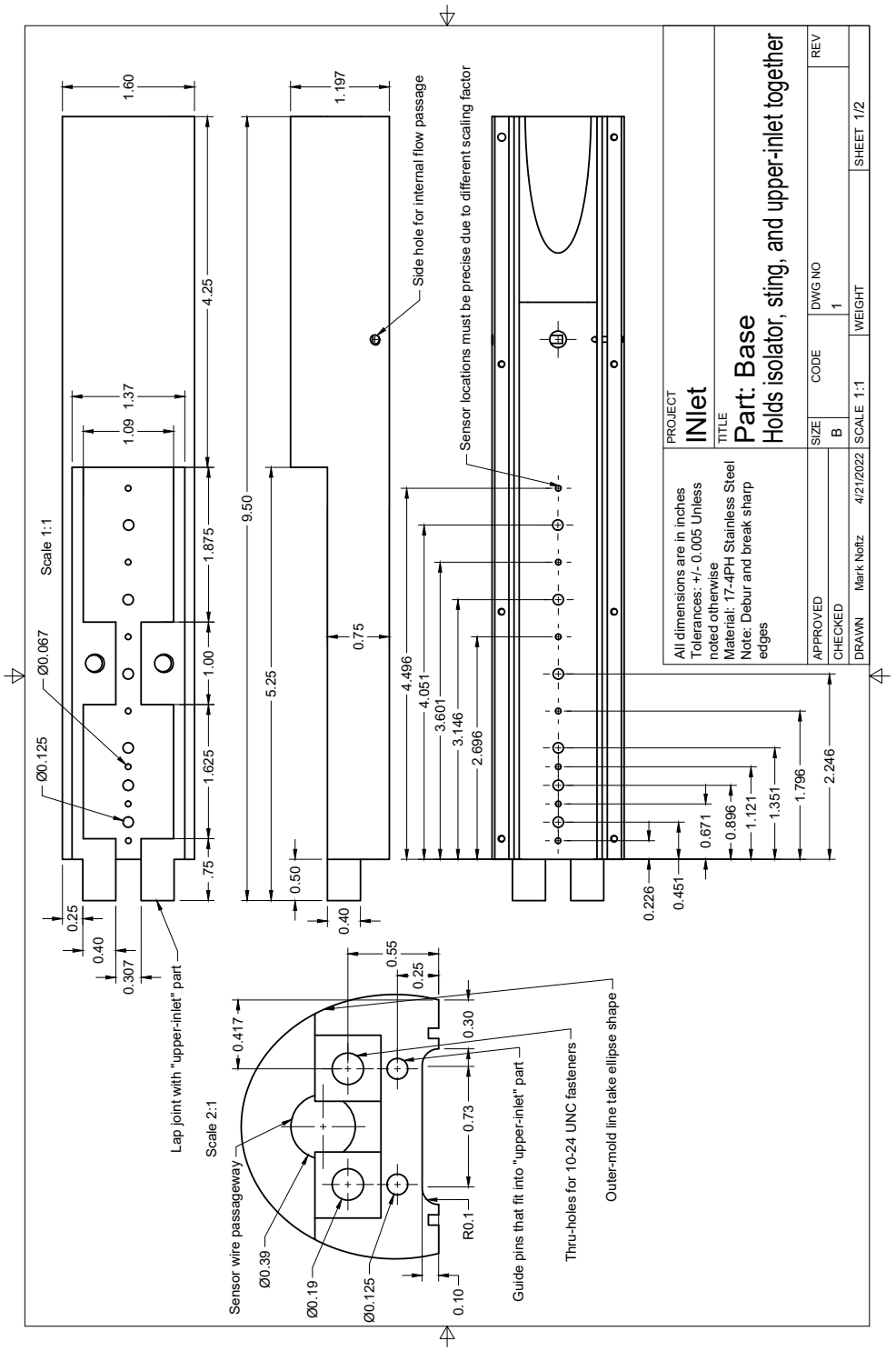

Figure H.3. Upper isolator (base component).

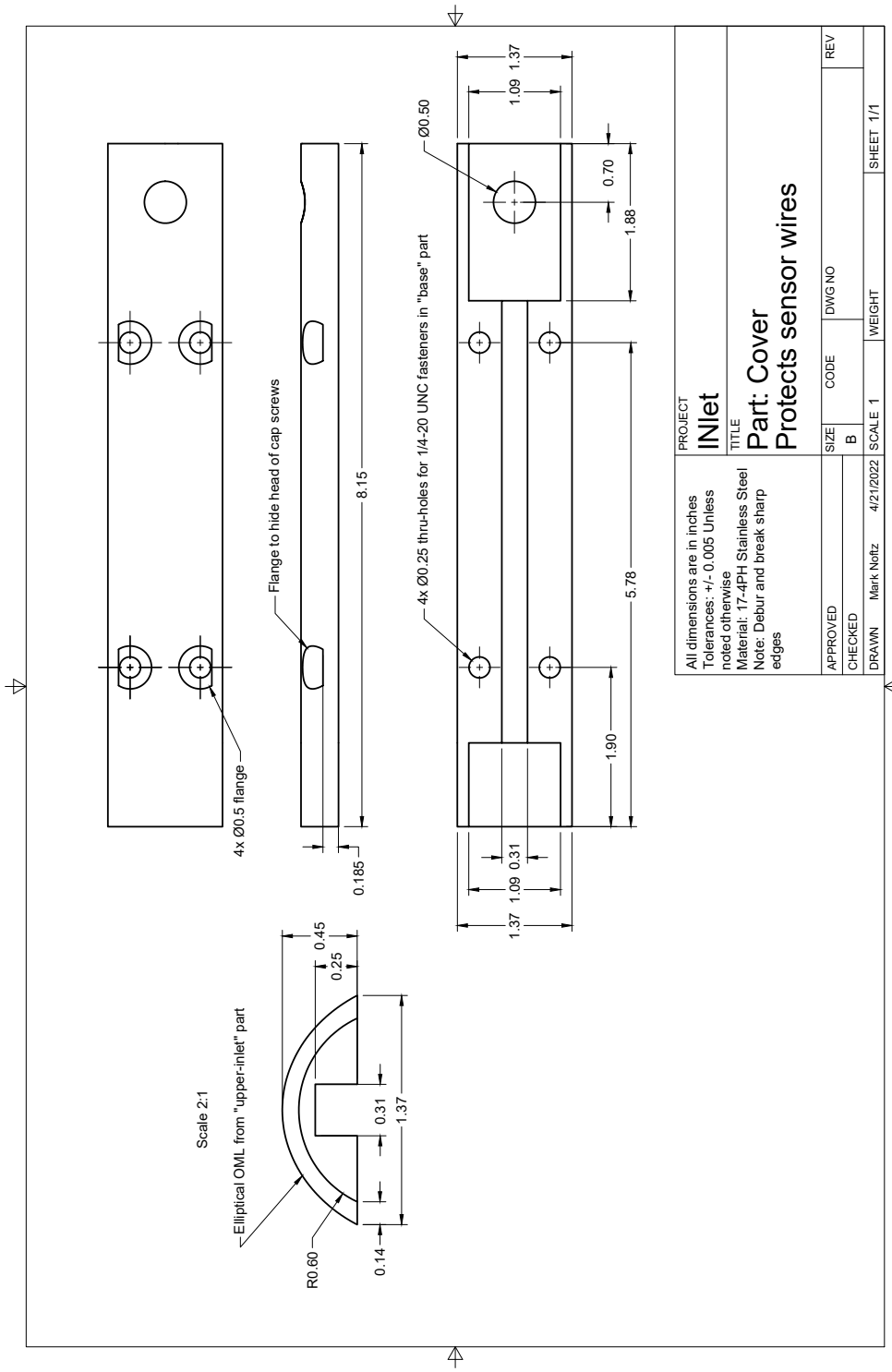

Figure H.4. Sensor cover (strongback).

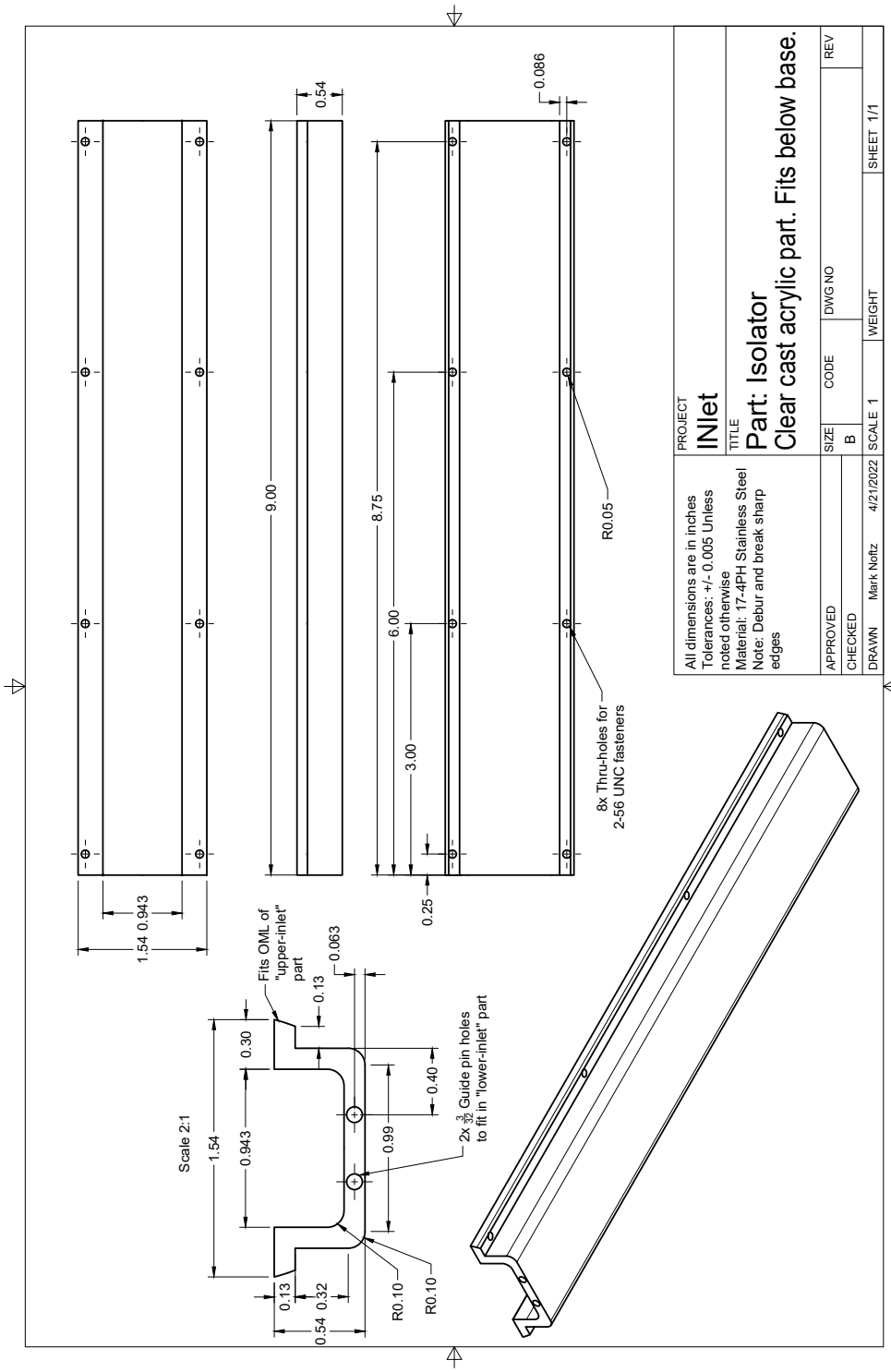

Figure H.5. Lower isolator (C-channel).

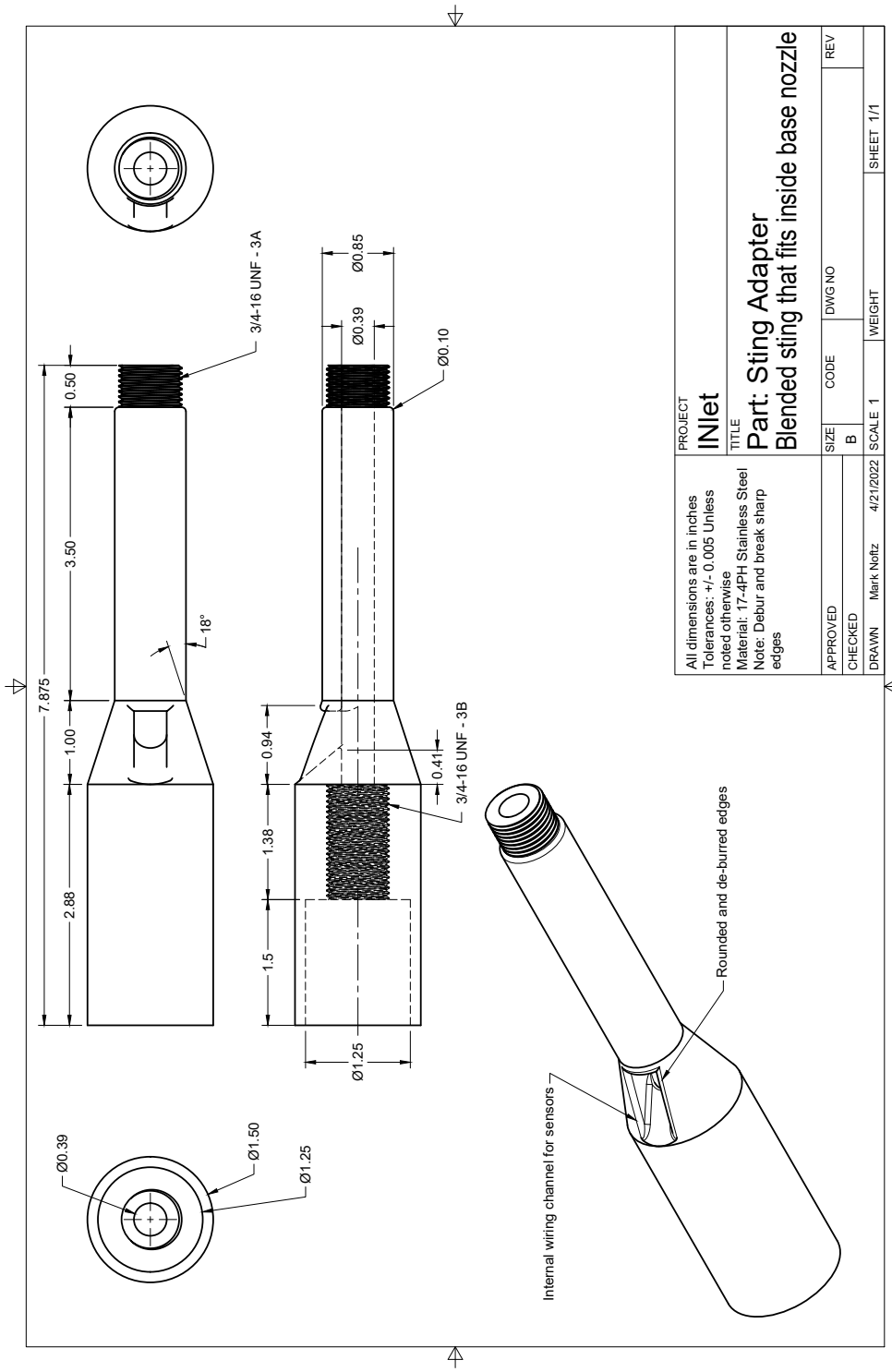

Figure H.6. Blended sting adapter.

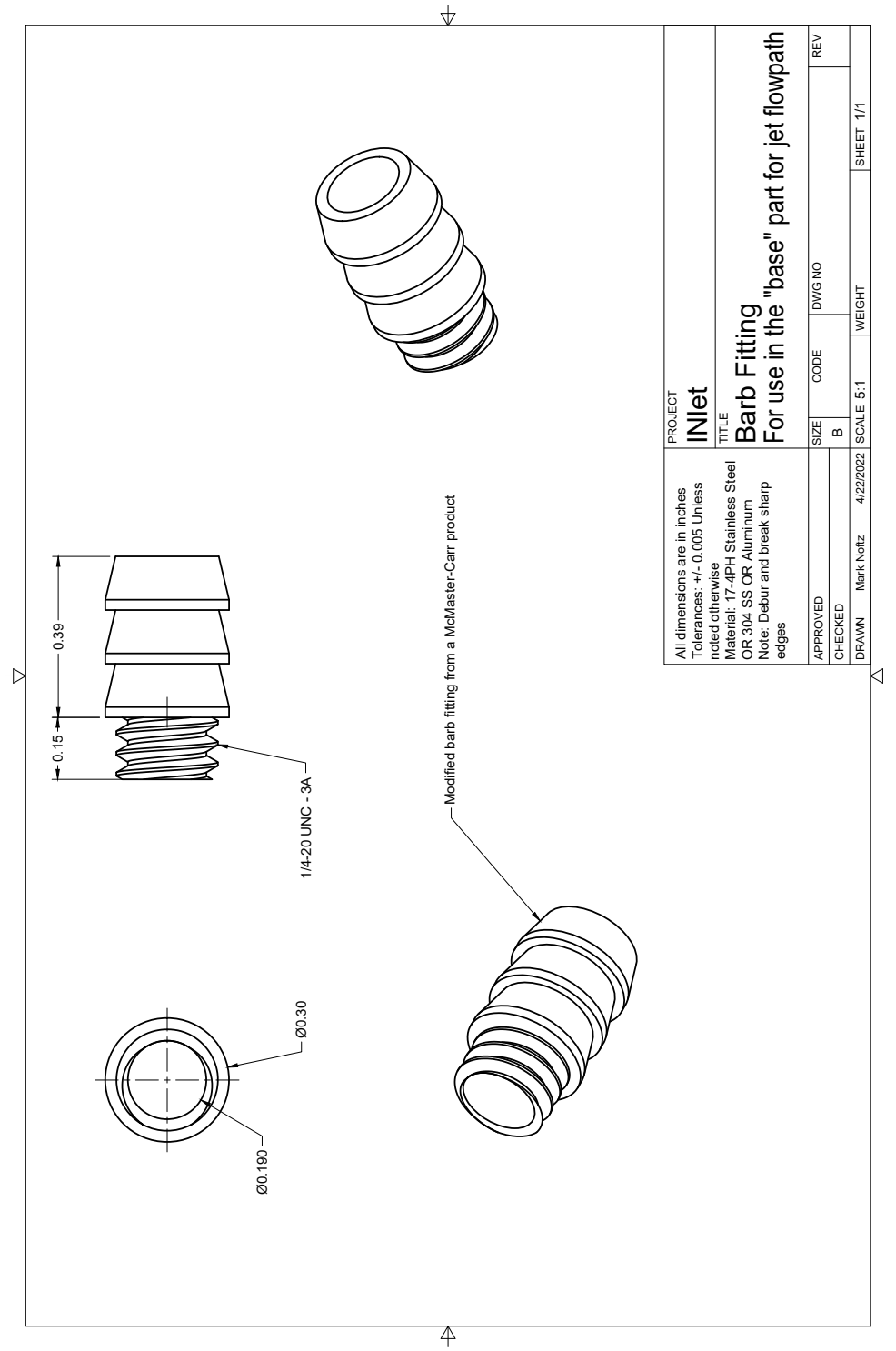

Figure H.7. Custom barb fitting for back-pressure studies.

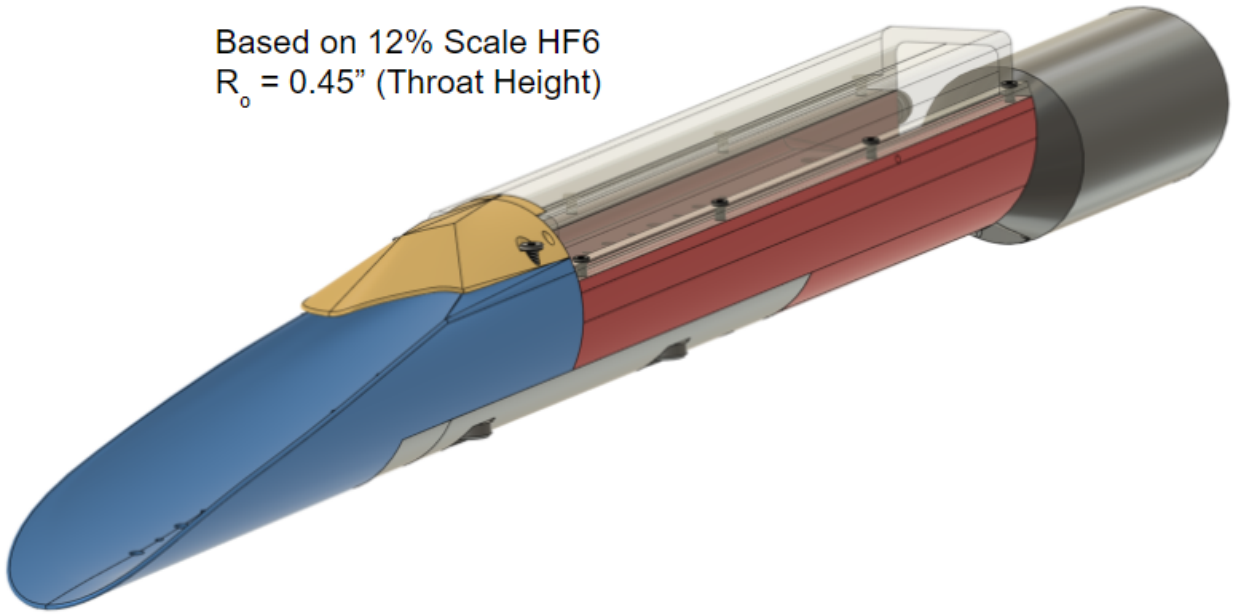

Figure H.8. Isometric view of the 12% INlet model.

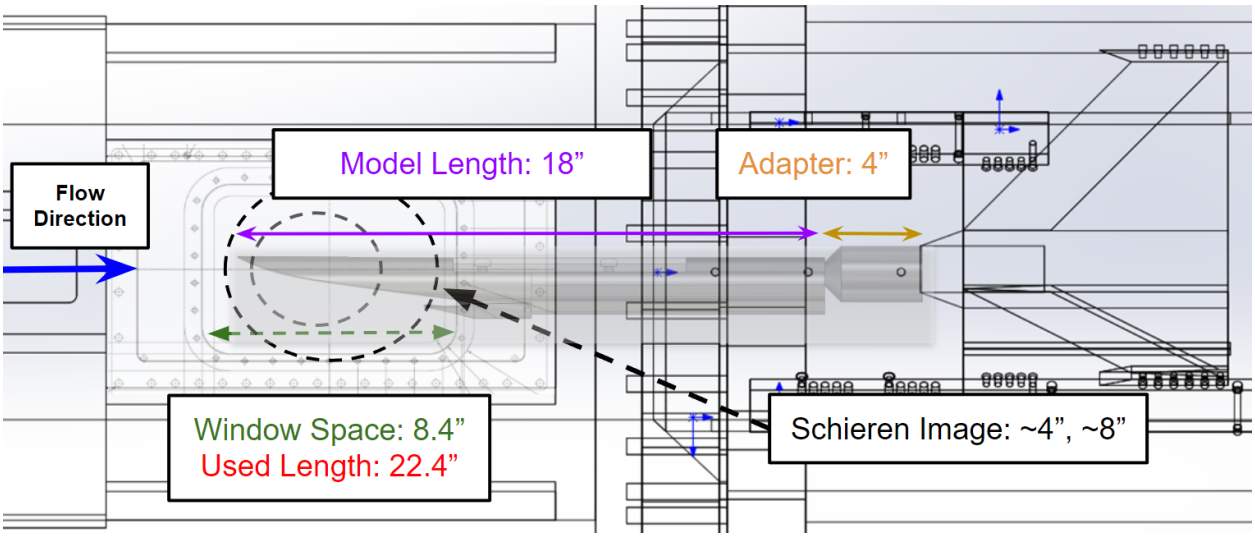

Figure H.9. 12% INlet model in the BAM6QT test section.

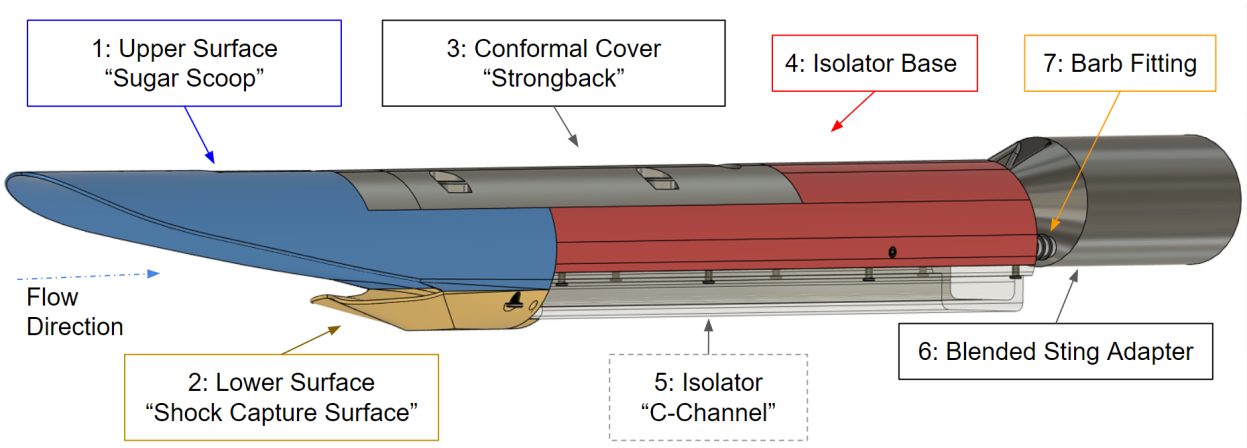

Figure H.10. Labeled components of the final model.

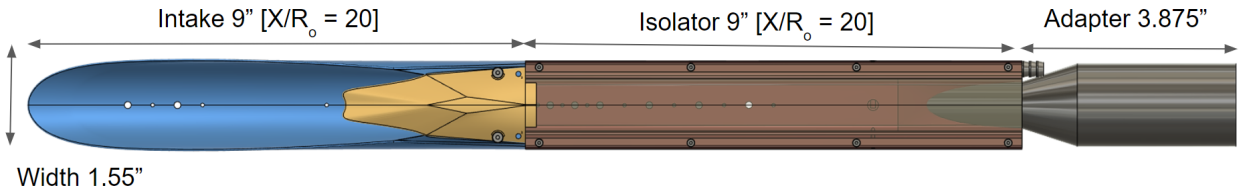

Figure H.11. Dimensions of the inlet, isolator, and sting.

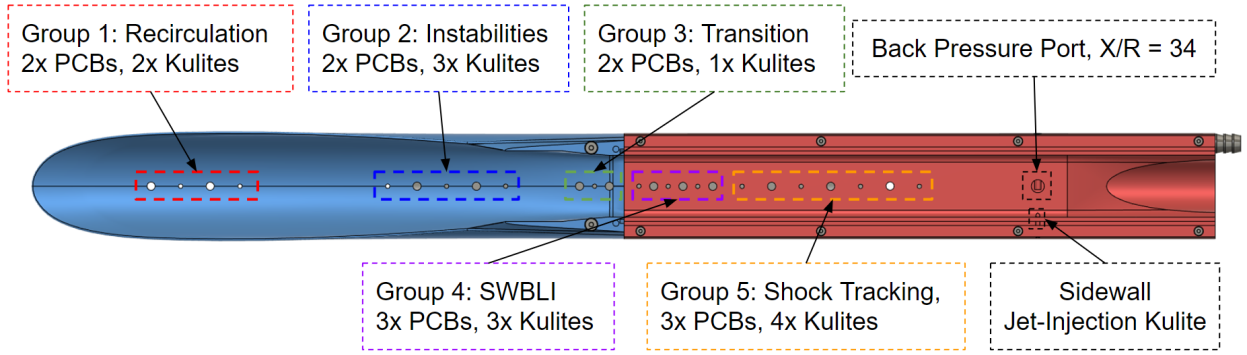

Figure H.12. Sensor groupings based on suspected flow phenomena.

- Worst case unstart loading
  - Body Material: 304 Stainless Steel, Yield Strength = 110 ksi
  - Mach = 5.8, Normal Shock, Po = 240 psia, Ps = 7.83 psia
  - Lower Surface Area = 2.6 in^2, Upper Surface Area = 12 in^2
  - Worst-Case Load = 20.4 lbf + 93.6 lbf = 114 lbf
  - 4-40 Cap Screw, C12.9, Stress Area 0.006 in^2
- Load Calculation
  - Proof Load = 110 ksi*0.8*0.006 in^2 = 528 lbf
  - Clamp Load = 528*0.75 = 396 lbf
  - FOS = (2x396) lbf/114 lbf = **6.9**
- Assumes 304-SS threads will fail first

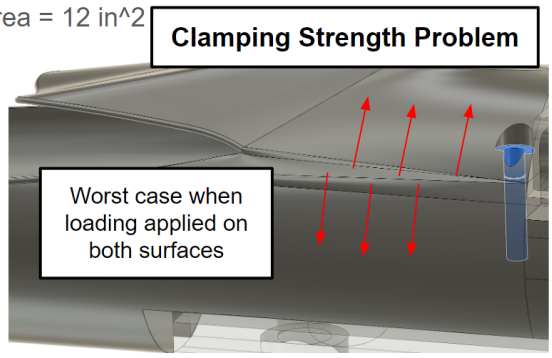

Figure H.13. Upper-lower inlet fastener load calculation.

- Worst case unstart loading
  - Body Material: 304 Stainless Steel, Yield Strength = 110 ksi
  - Mach = 5.8, Normal Shock, Po = 240 psia, Ps = 7.83 psia
  - Upper Surface Area = 12 in^2
  - Worst-Case Load = 93.6 lbf
  - 10-24 Cap Screw, C12.9, Stress Area = 0.017 in^2
- Load Calculation
  - Proof Load = 110 ksi*0.8*0.017 in^2 = 1496 lbf
  - Shear Calculation: 110 ksi*0.6*0.017 in^2 = 1122 lbf
  - Clamp Load = 1122 lbf*0.75 = 842 lbf
  - FOS = (842 *2) lbf/93.6 lbf = **18**
- Assumes 304-SS threads will fail first

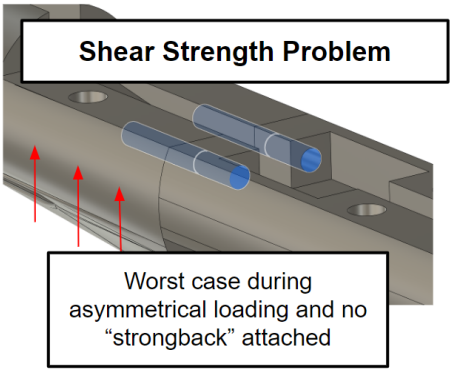

Figure H.14. Upper inlet-base fastener load calculation.

- Worst case unstart loading
  - Body Material: 304 Stainless Steel, Yield Strength = 110 ksi
  - Mach = 5.8, Normal Shock, Po = 240 psia, Ps = 7.83 psia
  - Lower-Flat of Channel = 8.4 in^2, Pressure pulling out acrylic C-channel
  - Worst-Case Load = 65.8 lbf
- Load Calculation
  - 2-56 Cap Screw, C12.9, Stress Area = 0.003in^2
  - Proof Load = 110 ksi*0.8* 0.003in^2 = 264 lbf
  - Clamp Load = 264 lbf*0.75 = 198 lbf
  - FOS = (8x198) lbf/65.8 lbf = **24**
- Assumes 304-SS threads will fail first

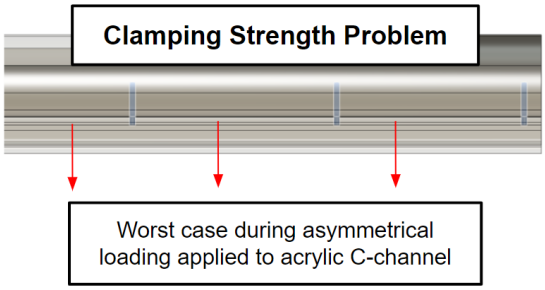

Figure H.15. Base-isolator fastener load calculation.

- Worst case unstart loading
  - Mach = 5.8, Normal Shock, Po = 240 psia, Ps = 7.83 psia
  - Upper Surface Area = 12 in^2, Isolator Top Surface Are = 13.75 in^2
  - Worst-Case Load = 93.6 lbf + 108 lbf = 201.6 lbf
  - Hollow Sting: OD = 0.85", Sting ID = 0.39"
  - Assuming V = 202 lbf, M = 202 lbf*9in = 1818 lbf-in
- Load Calculation
  - ***Bending Stress,*** Hollow Rod
    - Sigma = M*y/I, y=0.85 in., I=0.199 in.^4, Sigma = 6.8 ksi
    - FOS = 110 ksi/6.8 ksi = **25.7, (if 2x long, 12.8)**
  - ***Shear Stress*** for Hollow Rod
    - Tau = V*Q/(I*b), Q = 0.326 in.^3, b =0.7 in., Tau = 260 psi
    - FOS = 110 ksi/260 psi = **421**

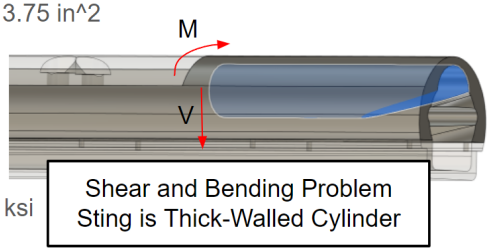

Figure H.16. Sting adapter load calculation.

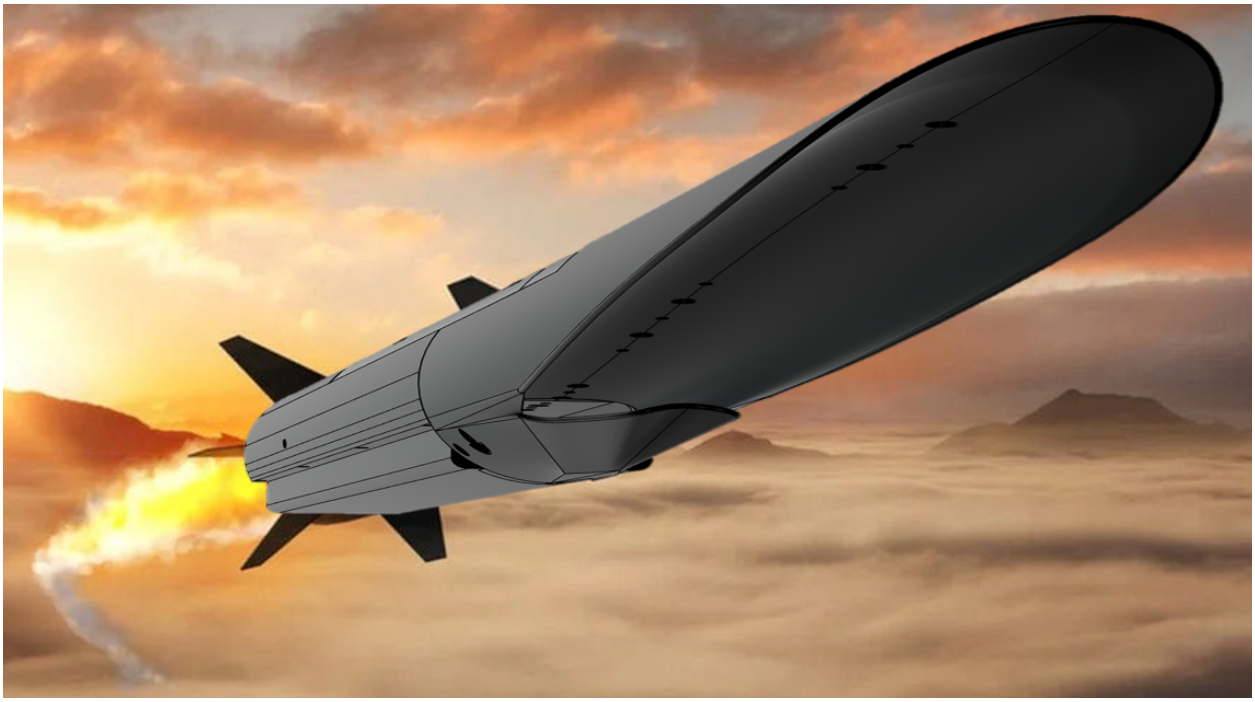

Figure H.17. The INlet taking to the skies.